CRANFIELD UNIVERSITY

NASER ALSAYEGH

INVESTIGATION ON THE PERFORMANCE OF NANOFLUIDS DUE TO PREPARATION EFFECTS AND OPERATIONAL CONDITIONS

SCHOOL OF AEROSPACE, TRANSPORT AND MANUFACTURING

Doctor of Philosophy
Academic Year: 2017 - 2019

Academic Supervisor: Dr. Joao A. Teixeira, and Prof. Pericles Pilidis
Technical Supervisor: Dr. Abdulmajid Addali

CRANFIELD UNIVERSITY

SCHOOL OF AEROSPACE, TRANSPORT AND MANUFACTURING

Doctor of Philosophy

Academic Year 2017 - 2019

NASER ALSAYEGH

INVESTIGATION ON THE PERFORMANCE OF NANOFLUIDS DUE TO PREPARATION EFFECTS AND OPERATIONAL CONDITIONS

Academic Supervisor: Dr. Joao A. Teixeira, and Prof. Pericles Pilidis
Technical Supervisor: Dr. Abdulmajid Addali

This thesis is submitted in partial fulfilment of the requirements for the degree of PhD

DECLARATION

No portion of the work referred to in the thesis has been submitted in support of an application for another degree or qualification of this or any other university or other institute of learning.

Naser Alsayegh

ABSTRACT

Nanofluids are advanced type of fluids that are produced by dispersing nanoparticles within a non-dissolving liquid. In heat transfer applications, these suspensions have shown to be superior to conventional heat transfer fluids in terms of thermal performance because of their enhanced effective thermal properties. The effective thermal conductivity of nanofluid depends on several factors, such as the preparation method employed, particles concentration, colloidal stability, thermal conductivities of both basefluid and solid particles used, … etc. Furthermore, the suspension effective thermal conductivity can only have a value within the range of the added nanoparticles (highest) and the hosting fluid (lowest) thermal conductivities. Thus, to obtain an optimum effective thermal conductivity for a certain mixture with minimum degradation in the aforementioned property, the nanofluid needs to be homogeneously dispersed while sustaining its short and long-term stability. This is one of the main challenges seen today with such type of advanced fluids. Moreover, the nanofouling effect associated with these suspensions in operational conditions is another important factor that needs to be focused on, as it tends to change the surface wettability behaviour depending on the fluid and deposited surface properties, and hence can increase or decrease the heat transfer performance of the system.

To address the previous challenges, the thesis at hand investigates the effect of nanofluid fabrication approach on its stability and pH value, and explores the influence of deposited particles of similar surface materials on the wettability behaviour of the surface. In order to achieve this, a two-step controlled temperature approach was used to fabricate the nanofluids at different set of fixed temperatures using a bath type ultrasonicator. The as-prepared suspensions were then characterised in terms of changes in pH value and stability using a pH meter and the sedimentation photograph capturing method, respectively. In addition, an electron beam physical vapour deposition technique was used to form nanoscaled layers on surfaces of similar materials to the evaporant source, so that a reflection of the nanofouling build-up on surfaces can be obtained, after which the wettability was examined, through a goniometer device, by varying the extracted liquid conditions.

The results have shown that increasing the nanoparticles concentration had caused the fluid alkalinity level to increase, while the rise in nanofluid sonication temperature had led to a decrease in its pH value, and vice versa. Furthermore, a general correlation was developed to predict the changes in pH value for similar fabricated suspensions, which illustrated an overall accuracy of ~92% in its prediction capability. The shelving-life evaluation of aluminium – water dispersion has showed that the nanofluids fabricated via the two-step controlled temperature approach at 30^{o}C had better short and long-term stabilities than the ones produced by the conventional method. Moreover, the wettability behaviour of aluminium surfaces was seen to depend on the deposited aluminium film thickness, surface characteristics, and water properties; but in general, the water of pH 7 has demonstrated a tendency to enhance the hydrophilicity of the surface, while water of lower and higher pH values were seen to have the opposite outcome. On the other hand, the wettability behaviour of copper or stainless steel surfaces has shown to greatly depend on the surface topographical structure compared to the attached liquid properties.

Keywords:

Colloidal; pH correlation; stability; surface roughness; two-step fabrication method; wettability.

ACKNOWLEDGEMENTS

First and foremost, I would like to take this opportunity to thank God for guiding me throughout my life. I would like to also thank my family for being beside me during my good and bad times. To my amazing two sons, Dr. Osamah Alsayegh and Dr. Laith Alsayegh, thank you for making this world a better place for me and your mother.

I would like to express my sincere gratitude to the Kuwait Institute for Scientific Research (KISR) for funding and supporting this research throughout my PhD program here at Cranfield University, UK. I would also like to thank my supervisors, Dr. Joao, Dr. Abdulmajid, and Prof. Pilidis for providing a positive environment for me to conduct my research.

To you all, I extend my deepest and sincere appreciation.

Thank you very much.

Naser

TABLE OF CONTENTS

LIST OF FIGURES

Chapter 2

Chapter 3

Chapter 4

Chapter 5

Chapter 6

Chapter 7

Chapter 8

APPENDIX B

LIST OF TABLES

Chapter 1

Chapter 2

Chapter 3

Chapter 4

Chapter 5

Chapter 6

Chapter 7

Chapter 8

APPENDIX A

APPENDIX B

LIST OF ABBREVIATIONS

Al	Aluminium
AC	Air conditioning
ACA	Average contact angle
AFM	Atomic force microscopy
Ag	Silver
Al_2O_3	Alumina
ANL	Argonne National Laboratory
ASNSS	Arc spray nanofluid synthesis system
BAC	Benzalkonium chloride
BZC	Benzethonium chloride
CA	Contact angle
CH_3COCH_3	Acetone
CHF	Critical heat flux
CMIS	Committee machine intelligent system
CNC	Computer numerical control
CNTs	Carbon nanotubes
Cryo-EM	Cryogenic electron microscopy
CTAB	Cetyl trimethyl ammonium bromide
Cu	Copper
CuO	Copper oxide
Cu_2O	Copper(I) Oxide

DIW	Deionised water
DLS	Dynamic light scattering
DSC	Differential scanning calorimeter
DTAB	Dodecyltrimethylammonium bromide
DW	Distilled water
EB-PVD	Electron beam physical vapor deposition
EB-SFF	Electron beam solid freeforming
EDS	Energy dispersive x-ray spectroscopy
EG	Ethylene glycol
Fe	Iron
H_2O	Water
HCl	Hydrochloric acid
HCTAB	Hexadecyl trimethyl ammonium bromide
HEs	Heat exchangers
HLB	Hydrophilic/lipophilic balance
H_S	Average sediment height
H_T	Total liquid height
HTC	Heat transfer coefficient
HTF	Heat transfer fluids
IBAD	Ion beam assisted deposition
KISR	Kuwait Institute for Scientific Research
Mg	Magnesium

MHS	Maximum height of surface
MWCNTs	Multi-walled carbon nanotubes
NaHMP	Sodium hexametaphosphate
NAM	Nanotechnology and Advanced Materials
NaOH	Sodium hydroxide
NPs	Nanoparticles
OA	Oleic acid
PCNTs	Presitine carbon nanotubes
PTFE	Polytetrafluoroethylene
PVP	Polyvinylpyrrolidone
Re	Reynold number
RH	Relative air humidity
RMSH	Root mean square height
RMSR	Root mean square roughness
SDBS	Sodium dodecylbenzene sulfonate
SDS	Sodium dodecyl sulphate
SEM	Scanning electron microscopy
SHR	Sediment height ratio
Si	Silicon
SiO_2	Silicon dioxide
Sku	Surface kurtosis
SOCT	Sodium octanoate

SS	Stainless steel
Ssk	Surface skewness
TBHQ	Tert-Butylhydroquinone
TCNTs	Treated carbon nanotubes
TEM	Transmission electron microscopy
TH66	Therminol 66
Ti	Titanium
TiO_2	Titanium dioxide
VEROS	Vacuum evaporation onto a running oil substrate
XRD	X-ray diffraction
XRF	X-ray fluorescent
Zn	Zinc
ZSN	Zeta sizer nano

Chapter 1 Introduction

1. Introduction

1.1 Background

Nanofluids are an advanced category of fluids that can be fabricated by homogeneously dispersing particles of less than 100 nm in a non-dissolving basefluid [1]. They were originally discovered and named by Choi and Eastman in 1995, through their research work at Argonne National Laboratory (ANL) [2]. Their primary motivation at that time was to solve the problem associated with suspensions made of dispersed microparticles in basefluids, as these types of fluids were seen to clog small passages due to the formation of large sized agglomeration of particles. Furthermore, the aforementioned two researchers have theoretically known beforehand that reducing the dispersed particles size to the nanoscale would enlarge the particle exposed surface area to the surrounding, and thus increasing the colloidal overall thermal conductivity [2,3]. Following their success, many researchers started to explore and develop this class of engineered fluid via modifying their production route, enhancing the suspension stability, and improving the colloidal thermal conductivity [4,5]. As of today, nanofluids are seen to have potential usage in a wide range of fields, including the energy sector, construction and building, transportation, medical sector, … etc [6-13].

Despite the promising achievements that nanofluids were able to deliver to the scientific community, there are still some obstacles that need to be overcome before this category of fluids can be industrially accepted. For example, the preparation phase of the colloidal is considered to be one of the greatest challenges, as this stage can strongly influence the fluid stability and effective thermophysical properties [5,14]. Meaning that, if the fabrication process used was not well planned before being executed, the chances of an unstable nanofluid being produce is likely to occur and as a result of that the thermophysical properties of the suspension will gradually degrade with time due to the separation of particles from the hosting basefluid. In addition, the commonly employed two-step fabrication method that relies on an ultrasonic bath type device, has been reported to rise the as-prepared nanofluid temperature and that this increase in temperature is governed by the surrounding atmospheric conditions and the sonicator working power [1,15]. Thus, it is highly unlikely that similar nanofluids will be produced through the conventional two-step route without simultaneously fabricating the products at the same conditions. On the operational scale, many researchers have experienced scale formation, also known as nanofouling, on the surfaces (e.g. heat pipes) over which the nanofluids flow over [16]. Such observation is related to the flowing nanoparticles (NPs)

becoming deposited on the surface, and hence to the fact that a layer of NPs builds-up and modifies the wettability nature of the surface with time. The overall system performance is therefore affected by the newly introduced thin film, and this process may be manipulated in order to obtain a positive outcome.

In this context, this research explores the effect of nanofluid fabrication approach on its stability and pH value, and determines the wettability behaviour of nanofouled surfaces. A controlled temperature two-step approach was employed to increase the number of fixed parameters used in fabricating the suspensions. The nanofluids pH value was then measured to drive a relation between the NPs materials type and concentration, sonication bath temperature, and pH value. This relation was afterwards used to develop a general correlation that can predict the pH value of nanofluids that are fabricated within the same range of the conducted experiments. Moreover, the sedimentation settling behaviour of the colloidal was characterised by monitor the samples via the sedimentation photograph capturing method to determine the stability of the as-prepared nanofluids with time. Finally, the change in wettability was investigated by measuring the liquid – solid static contact angle of surfaces before and after being deposited with different thicknesses of similar materials. The temperature and pH value of the liquids employed for the contact angle experiments were varied to illustrate their effect on the results.

1.2 Project development

The research work presented within this document was sponsored by the Kuwait Institute for Scientific Research (KISR), Nanotechnology and Advanced Materials (NAM) program, in the form of a PhD scholarship in order to determine and find potential solutions for nanofluids at both preparation and operation phases. Early stage training on fundamentals of conducting research, usage of equipment's, and health and safety procedures were provided by Cranfield University and KISR/NAM.

1.3 Aim and objectives

It is hypothesised that through a better understanding of the influence of nanofluids fabrication procedure on the suspension stability and pH value, and the changes in surface wettability behaviour caused by the fouled layer, that such category of advanced fluids can be promoted for usage in industrial scale heat transfer applications. Therefore, the aim of this thesis is to examine the effect of nanofluids preparation approach on their stability and pH value, and to

investigate the wettability behavior of surfaces deposited with particles of similar surface materials. Accordingly, a series of objectives were identified as following:

1- To conduct an intensive literature review on the thesis research topic;
2- To design and set up an ultrasonicator working station with the capability of controlling the device bath temperature for fabricating nanofluids via the two-step controlled and uncontrolled temperature methods;
3- To measure the pH value of the produced stainless steel (SS) 316L, copper(I) oxide (Cu_2O), and aluminium (Al) water based nanofluids, and develop a validated correlation for predicting the nanofluids pH value based on the NPs material, concentration, and fixed preparation temperature;
4- To compare between the conventional and controlled temperature fabrication methods of the as-dispersed Al NPs in water in terms of stability, using the sedimentation photographic capturing method; and
5- To study the wettability behaviour of nanocoated and uncoated SS 316L, copper (Cu), and Al substrates using different controlled liquids conditions.

1.4 Thesis structure

This thesis takes the form of a series of chapters formatted as papers, which are either published or submitted for review. Starting from the second chapter to the seventh, the titles used for the chapters are those of the original papers along with each journal the papers were submitted to. All chapters/papers were written by the primary author, Naser Alsayegh (professionally known as Naser Ali) and edited by Dr. Joao A. Teixeira (main supervisor). The majority of the experimental work was conducted by Naser Alsayegh with some contribution from Feras Al-Zubi (KISR/NAM) in chapter 5/paper 4 and chapter 7/paper 6; Ehab Shaban (KISR/NAM) in chapter 5/paper 4; Ismail Behbehani (Ministry of Public Works, Materials Department) in chapter 5/paper 4; Maryam Saeed (KISR/NAM) chapter 7/paper 6; Ahmad Sedaghat (Isfahan University of Technology, Department of Mechanical Engineering) chapter 7/paper 6; and Husain Bahzad (Imperial College London, Department of Chemical Engineering) chapter 7/paper 6. The structure of the thesis is presented below, and a summary of the working plan is shown in Table 1.1.

Chapter 2/paper 1 – covers most of the available literature on nanofluids history, types, preparation methods, stability, thermophysical properties, and future challenges. This was done in order to identify the gap in knowledge, and hence justify the conducted research at hand.

Ali, N.; Teixeira, J.A.; Addali, A. A review on nanofluids: Fabrication, stability, and thermophysical properties. *J. Nanomater.* **2018**, *2018*, 33. DOI: 10.1155/2018/6978130.

Chapter 3/paper 2 – examines the changes in pH value caused by the two-step controlled sonication bath temperature method for nanofluids fabricated from dispersing SS 316L, Cu_2O, and Al in water. The fixed sonication temperatures employed were from 10°C to 60°C, and the particles concentration were in the range of 0.1 – 1.0 vol.%. The study was conducted to understand how such fabrication method would affect the pH value of the as-prepared nanofluids, and thus can lead to the development of a theoretical pH correlation. Ali, N.; Teixeira, J.A.; Addali, A. New pH Correlations for Stainless Steel 316L, Alumina, and Copper(I) Oxide Nanofluids Fabricated at Controlled Sonication Temperatures, *J. Nano. Res.*, **2019**, *58*, 125-138. DOI: 10.4028/www.scientific.net/JNanoR.58.125.

Chapter 4/paper 3 – addresses the significance role of the fabrication approach on the nanofluid stability, where dispersed particles of Al (0.1 – 1.0 vol.%) in water were given as an example. A comparison between the suspensions produced by the conventional method and the controlled temperature approach (10°C – 60°C) was performed in order to identify the optimum nanofluids stability fabrication procedure. Ali, N.; Teixeira, J.A.; Addali, A. Aluminium Nanofluids Stability: A Comparison Between The Conventional Two-Step Fabrication Approach And The Controlled Sonication Bath Temperature Method, *J. Nanomater.*, In Press.

Chapter 5/paper 4 – outlines the wettability results of coating Al surfaces with Al using an electron beam physical vapor deposition technique and varying the in contact liquid properties. The aim of this chapter is to demonstrate the wettability relation between the fluid and the surface when the deposited particles forms layers of different thicknesses on the surface. Ali, N.; Teixeira, J.A.; Addali, A.; Al-Zubi, F.; Shaban, E.; Behbehani, I. The effect of aluminium nanocoating and water ph value on the wettability behavior of an aluminium surface. *Applied Surface Science* **2018**, *443*, 24-30. DOI: 10.1016/j.apsusc.2018.02.182.

Chapter 6/ paper 5 – This work is similar to the previous one (i.e. chapter 5/paper 4), except that in this research Cu was selected for both the substrate and depositing material. The reason behind selecting Cu is because it is a very favourable element in heat transfer applications, thus investigating its wettability changes can be of high interest to the industry. Ali, N.; Teixeira, J.A.; Addali, A. Effect of Water Temperature, pH Value, and Surface Roughness on the Wettability Behaviour of Copper Surfaces Coated with Copper Using EB-PVD Technique, *J. Nano. Res.*, In Press.

Chapter 7/paper 6 – Similar to the previous two chapters, this part of work investigates the wettability changes of SS 316L. The SS deposition method used in this research was the first of its kind, where the thin films of SS were fabricated via an electron beam physical vapor deposition procedure. The wettability behaviour of the surface was then shown using the same route employed for chapter 5/ paper 4 and chapter 6/paper 5. Ali, N.; Teixeira, J.A.; Addali, A.; Saeed, M.; Al-Zubi, F.; Sedaghat, A.; Bahzad, H. Deposition of stainless steel thin films: An electron beam physical vapour deposition approach. *Materials* **2019**, *12*, 571. DOI: 10.3390/ma12040571.

Chapter 8 – General Discussion, This chapter provides an overall discussion towards the two research questions from this study, can the nanofluid fabrication method change the pH value and the stability of the suspension? and is it possible to use the associate nanofouling effect towards the benefit of the heat transfer application?

Chapter 9 – Conclusions and Future Work, This chapter lists the key findings of the research work conducted in this thesis and provides recommendations on how future investigations can expand the understanding of current knowledge on nanofluids preparation and implementation.

Table 1.1. Summary of working plan.

Chapter/ paper	**Objective/s**	**Area of focus**	**Journal**	**Status**
2/1	1	Literature on nanofluids	Journal of Nanomaterials	Published
3/2	2 and 3	Characterisation of changes in nanofluids pH value caused by fabrication method and correlation development	Journal of Nano Research	Published
4/3	2 and 4	Comparison between conventional and controlled temperature fabrication approaches in terms of nanofluids stability	Journal of Nanomaterials	In Press
5/4	5	Wettability evaluation of Al surfaces deposited with Al thin films	Applied Surface Science	Published

6/5	5	Wettability evaluation of Cu surfaces deposited with Cu thin films	Journal of Nano Research	In Press
7/6	5	Wettability evaluation of SS 316L surfaces deposited with SS thin films	MDPI Materials	Published

1.5 Contribution to knowledge

The contribution to knowledge that this research work provides to the scientific community can be summarised through the following points:

1- A new pH correlation for nanofluids that are fabricated using the two-step controlled sonicator bath temperature approach was developed and validated;
2- An innovative approach for changing the sedimentation mechanism in suspensions that are fabricated via the two-step controlled sonicator bath temperature method was introduced;
3- An approach for modifying surfaces wettability behaviour was provided; and
4- A new method for depositing stainless steel thin film was introduced.

References

1. Ali, N.; Teixeira, J.A.; Addali, A. New ph correlations for stainless steel 316l, alumina, and copper(i) oxide nanofluids fabricated at controlled sonication temperatures. *J. Nano. Res.* **2019**, *58*, 125-138.

2. Choi, S.U.S.; Eastman, J.A. Enhancing thermal conductivity of fluids with nanoparticles. In *Conference: 1995 International mechanical engineering congress and exhibition, San Francisco, CA (United States), 12-17 Nov 1995; Other Information: PBD: Oct 1995*, Argonne National Lab., IL (United States): 1995; p Medium: ED; Size: 8 p.

3. Lee, S.; Choi, S.U.S. Application of metallic nanoparticle suspensions in advanced cooling systems. *American Society of Mechanical Engineers, Materials Division (Publication) MD* **1996**, *72*, 227-234.

4. Eastman, J.A.; Choi, U.S.; Li, S.; Thompson, L.J.; Lee, S. In *Enhanced thermal conductivity through the development of nanofluids*, Proceedings of the 1996 MRS Fall Symposium, Pittsburgh, PA, United States

Boston, MA, USA, 1997; George, E.P.; Gotthardt, R.; Otsuka, K.; Trolier-McKinstry, S.; Wun-Fogle, M., Eds. Materials Research Society: Pittsburgh, PA, United States

Boston, MA, USA, pp 3-11.

5. Ali, N.; Teixeira, J.A.; Addali, A. A review on nanofluids: Fabrication, stability, and thermophysical properties. *J. Nanomater.* **2018**, *2018*, 33.

6. Ilyas, S.U.; Pendyala, R.; Shuib, A.S.; Marneni, N. A review on the viscous and thermal transport properties of nanofluids. In *International Conference on Process Engineering and Advanced Materials, ICPEAM 2012*, Trans Tech Publications Ltd: Kuala Lumpur, 2014; Vol. 917, pp 18-27.

7. Shanthi, R.; Anandan, S.S.; Ramalingam, V. Heat transfer enhancement using nanofluids an overview. *Therm. Sci.* **2012**, *16*, 423-444.

8. Wen, D.S.; Lin, G.P.; Vafaei, S.; Zhang, K. Review of nanofluids for heat transfer applications. *Particuology* **2009**, *7*, 141-150.

9. Vekas, L.; Bica, D.; Avdeev, M.V. Magnetic nanoparticles and concentrated magnetic nanofluids: Synthesis, properties and some applications. *China Particuology* **2007**, *5*, 43-49.

10. Reddy, K.S.; Kamnapure, N.R.; Srivastava, S. Nanofluid and nanocomposite applications in solar energy conversion systems for performance enhancement: A review. *Int. J. Low Carbon Technol.* **2017**, *12*, 1-23.

11. Sheikholeslami, M.; Ganji, D.D. Chapter 1 - application of nanofluids. In *Applications of semi analytical methods for nanofluid flow and heat transfer*, Sheikholeslami, M.; Ganji, D.D., Eds. Elsevier: 2018; pp 1-44.

12. Mansoury, D.; Faramarz, I.D.; Kiani, A.; Chamkha, A.J.; Sharifpur, M. Heat transfer and flow characteristics of al2o3/water nanofluid in various heat exchangers: Experiments on counter flow. *Heat Transfer Eng* **2018**, 1-36.

13. Chamkha, A.J.; Molana, M.; Rahnama, A.; Ghadami, F. On the nanofluids applications in microchannels: A comprehensive review. *Powder Technol.* **2018**, *332*, 287-322.

14. Mukherjee, S.; Mishra, P.C.; Chaudhuri, P. Stability of heat transfer nanofluids – a review. *ChemBioEng Reviews* **2018**, *5*, 312-333.

15. Song, Y.Y.; Bhadeshia, H.K.D.H.; Suh, D.-W. Stability of stainless-steel nanoparticle and water mixtures. *Powder Technol.* **2015**, *272*, 34-44.

16. Estellé, P.; Cabaleiro, D.; Żyła, G.; Lugo, L.; Murshed, S.M.S. Current trends in surface tension and wetting behavior of nanofluids. *Renewable Sustainable Energy Rev* **2018**, *94*, 931-944.

Chapter 2

Publication 1: A Review on Nanofluids: Fabrication, Stability, and Thermophysical Properties

(Ali, N.; Teixeira, J.A.; Addali, A. A review on nanofluids: Fabrication, stability, and thermophysical properties. *J. Nanomater*. **2018**, *2018*, 33. DOI: 10.1155/2018/6978130)

A Review on Nanofluids: Fabrication, Stability, and Thermophysical Properties

A B S T R A C T

Nanofluids have been receiving great attention in recent years due to their potential usages, not only as an enhanced thermophysical heat transfer fluid but also because of their great importance in applications such as drug delivery and oil recovery. Nevertheless, there are some challenges that need to be solved before nanofluids can become commercially acceptable.

The main challenges of nanofluids are their stability and operational performance. Nanofluids stability is significant important in order to maintain their thermophysical properties after fabrication for a long period of time. Therefore, enhancing nanofluids stability and understanding nanofluid behaviour are part of the chain needed to commercialize such type of advanced fluids.

In this context, the aim of this article is to summarize the current progress on the study of nanofluids, such as the fabrication procedures, stability evaluation mechanism, stability enhancement procedures, nanofluids thermophysical properties, and current commercialisation challenges. Finally, the article identifies some possible opportunities for future research that can bridge the gap between in lab research and commercialisation of nanofluids.

Keywords: Nanofluids; fabrication approach; stability evaluation; stability enhancement; thermophysical properties; challenges.

1. Introduction

Fluids of different types are usually used as heat carriers in heat transfer applications. Such applications where heat transfer fluids (HTF) have an important role are heat exchanging systems in power stations [1], cooling and heating systems in buildings [2], vehicles air conditioning (AC) system in transportations [3], and cooling systems of most of the processing plants [4]. In all of the aforementioned applications, the HTF's thermal conductivity has a strong influence on the efficiency of the heat transfer process and with it the overall efficiency

of the system. For such reason, researchers have continuously worked on developing advanced HTFs that have significantly higher thermal conductivities than conventionally used fluids [5].

Considerable efforts were made on heat transfer enhancement through geometrical modification up to today [6] but were all constrained by the low thermal conductivity of the heat transfer fluids used. However, In 1995, Choi developed a newly innovative class of heat transfer fluids that depends on suspending nano scale particles of metallic origin with an average particle size of less than 100 nm into conventional heat transfer fluids and gave such type of fluids the term “Nanofluids” [5]. In other words, the term nanofluid is used to describe a mixture containing nano scale particles of average size less than 100 nm with any basefluid that does not dissolve the particles hosted by it.

The idea of dispersing solids in fluids was first proposed by Maxwell via his theoretical work more than 120 years ago [7]. It was later used to disperse mm and/or µm sized particles in fluids by Ahuja in 1975, Liu et al. in 1988, and researchers at Argonne National Laboratory (ANL) in 1992 [8-12]. Their work depended on the high thermal conductivity of metals at room temperature compared to fluids (i.e. order of magnitude higher in thermal conductivity). For instant, at room temperature, copper has a thermal conductivity 3000 and 700 times greater than that of an engine oil and water, respectively. The same difference in thermal conductivity cohabit between liquids, since metallic liquids have much higher thermal conductivity than non-metallic ones. Fig. 2.1 illustrates the thermal conductivities of different organic materials, heat transfer fluids, metals, and metal oxides at 20^{o}C [13]. Therefore, by suspending metallic particles in a fluid its thermal conductivity is expected to be enhanced.

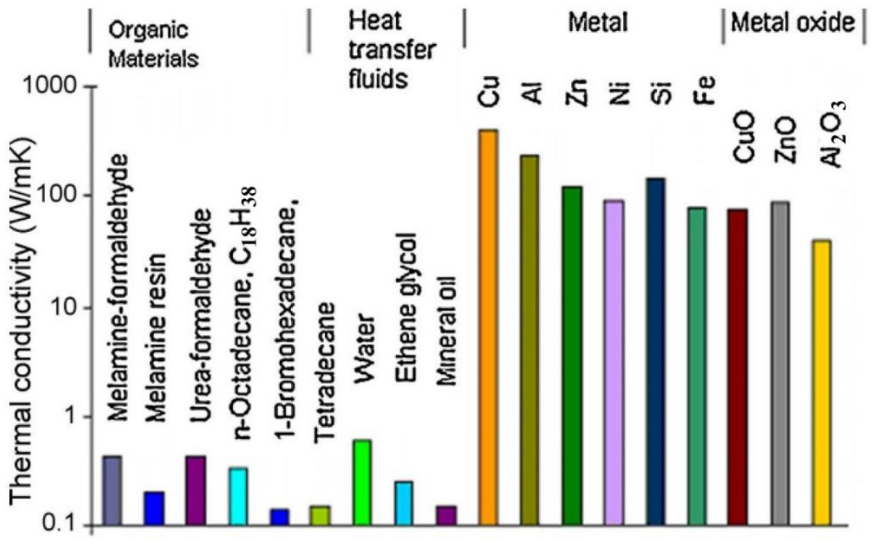

Fig. 2.1. Thermal conductivity comparison of common polymers, liquids, and solids.

One of the problems that arises from using fluids containing µm sized particles is the clogging of small passages caused from the large agglomeration of the solid particles, making it therefore hard to employ in heat transfer equipment's fitted with small passages. On the other hand, nanofluids are believed to surpass such obstacle due to containing small enough particle size which can flow smoothly through such channels (i.e. they will not block flow passages). Another advantage of using nanoparticles is that they have an extremely large surface area over which the heat transfer mechanism between the particle and its surrounding takes place. For such reason, decreasing the size of particles from mm and µm down to nm would extremely largen the surface area and with it the enhancement in heat transfer. In the year 2000, Xuan and Li redefined the term nanofluids to include any nano scaled particles of metallic, non-metallic, and polymeric origin mixed with a non-carcinogenic basefluid [12]. They also stated that the effective thermal conductivity can be increased by more than 20% by adding concentration of nanoparticle as low as 1–5 vol% to the basefluid and that the enhancement get effected strongly by the particles shape, particle dimensions, added volume fractions in the basefluid, particles thermophysical properties, and so forth. The term 'effective' was introduced to describe the thermophysical property of nanofluids and to differ between the thermophysical properties of the basefluid itself and the newly formed fluid that consist of the basefluid and its dispersed nanoparticles [14]. Fig. 2.2 highlights the main parameters that influence the effective thermal conductivity of any nanofluid.

Fig. 2.2. Parameters influencing nanofluids effective thermal conductivity.

Factors to be considered when selecting nanomaterials on preparing nanofluids for heat transfer applications are (i) chemical stability (ii) thermophysical properties (iii) toxicity (iv) availability (v) compatibility with the basefluid and (vi) cost. The most commonly used nanoparticles for nanofluids formulation are aluminium (Al), copper (Cu), silver (Ag), iron (Fe), titanium (Ti), silicon (Si), zinc (Zn), magnesium (Mg), carbon nanotubes (CNTs), graphene, graphene oxide, and diamond. Commonly used basefluids for nanofluid formulation are water, ethylene glycol (EG), EG – H_2O mixtures, and oils [15].

Several researchers have reported scale formation, also known as 'fouling effect', on the surfaces when using nanofluids in applications at elevated temperature such as the inside of the annulus of heat exchangers [16-22]. This fouling effect acts similarly to surface nanocoating due to its nature of formation which is based on nanoparticles and can be effective in reducing the pressure losses caused by the high viscosity of nanofluids compared to their basefluid. This happens since the layer formed tends to smoothen the surface as illustrated in Fig. 2.3.a and 2.3.b.

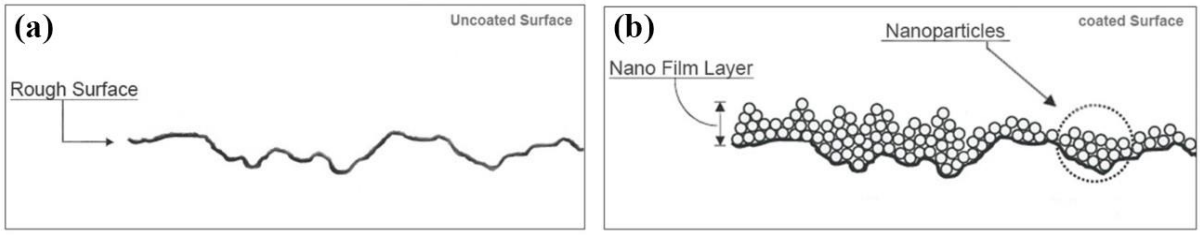

Fig. 2.3. (a) Rough surface, and (b) Nano coated surface or nano fouled surface [23].

Kang et al. demonstrated in their work how coating a riser surface with nanoparticles reduced the pumping power and improved the system efficiency by 25% [24]. This is because coating the riser surface has affected the contact angle between the fluid and the surface, making it more hydrophobic to the liquid in contact to it. Fig. 2.4 demonstrates the relation between the surface contact angle and fluid. Ali et al. [23] also confirmed the changes in surface wettability behaviour caused from nanocoating, where they deposited Al particles on the surface of an Al substrate then examined the film thickness, fluid pH value, and fluid temperature effects on the fluid – surface contact angle. Their findings showed that water of pH values above and below 7 tend to develop higher contact angles as the deposited layer thickness and fluid temperature increased, in contrast to water of neutral pH which showed the opposite behaviour.

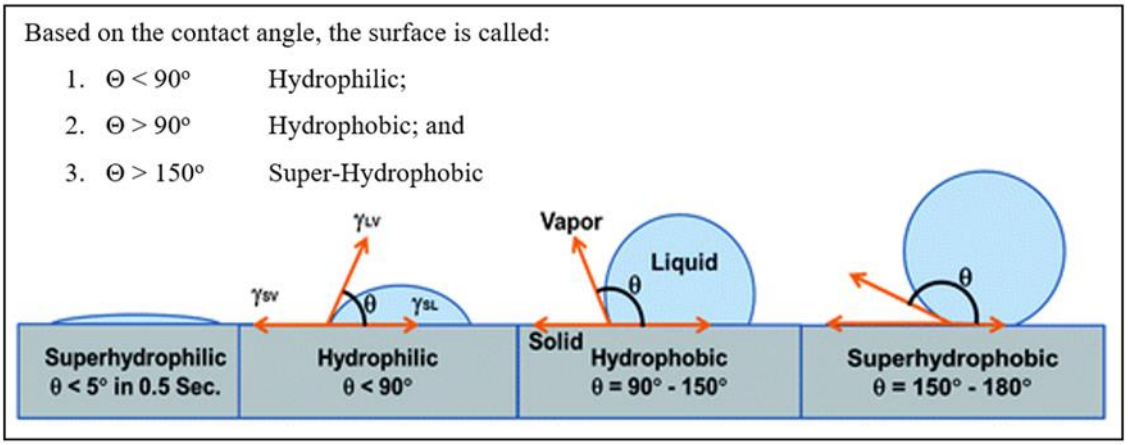

Fig. 2.4. Relation between surface contact angle and fluids [24,25].

Nanofluids fouling effect can also increase or decrease the nucleation boiling heat transfer depending on the surface – liquid contact angle as demonstrated by Phan et al., where they showed in their work that the highest heat transfer coefficient was obtained at a contact angle close to either 90° or 0° [26].

Besides to using nanofluid as a HTF in heat transfer applications, which was the main reason behind the development of such category of fluid, it is also used in, e.g. sunscreen products [27], medicine [28,29], reducing buildings pollution [30], magnetic sealing [31], microbial fuel cells [32], antibacterial activity, and many other applications [33].

Data obtained from the Scopus database from 1995 to 2018, showed an exponential increase in the number of documents with the word “nanofluids” as part of the title as seen in Fig. 2.5, except for the year 2018 which is most likely to change with the upcoming data to the website [34]. Most of the documents reported are in the form of journal papers as shown in Fig. 2.6.

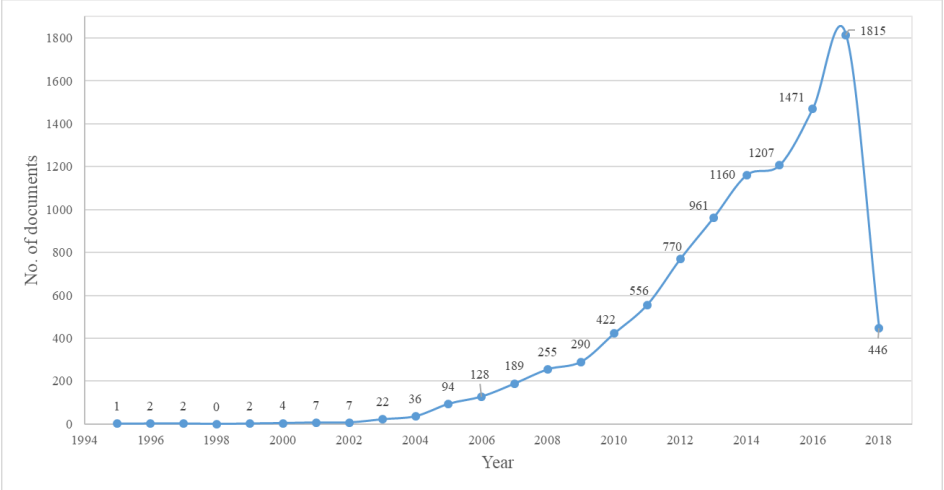

Fig. 2.5. Number of documents with the word nanofluids in the title.

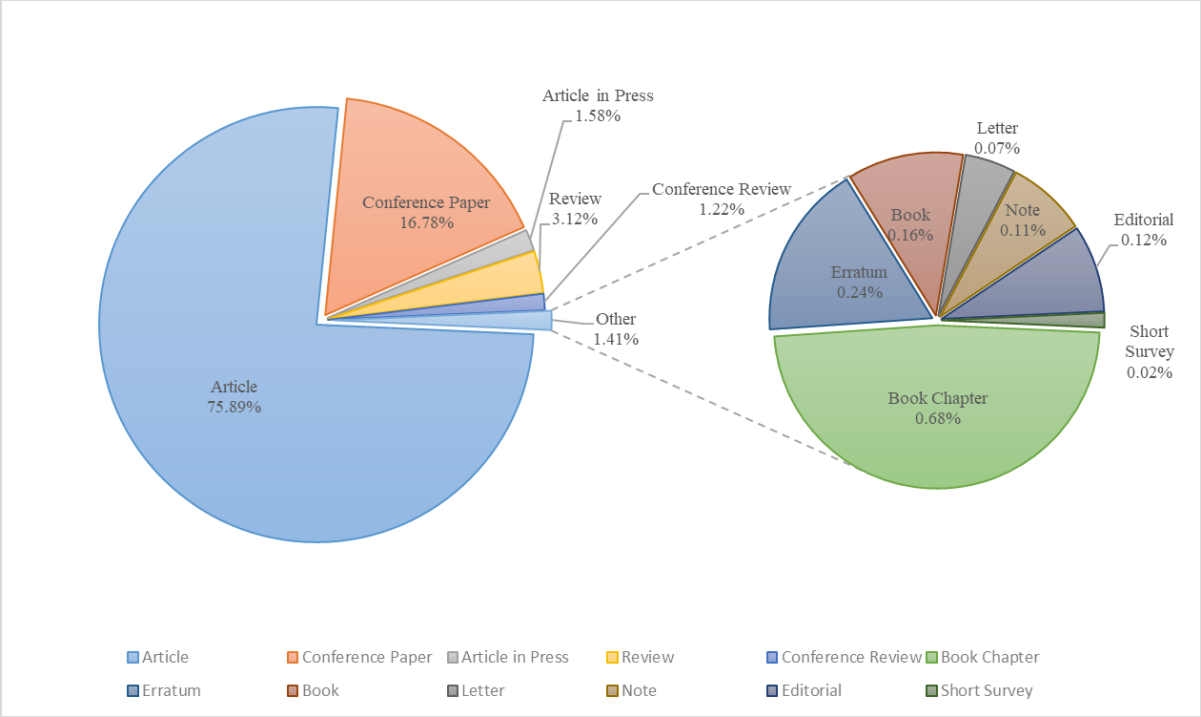

Fig. 2.6. Percentage of available document types.

2. Types of Nanofluids

Nanofluid, which is a term used to describe fluids containing dispersed particles of nano scale, can be formed from nanoparticles of single element (e.g. Cu, Fe, and Ag), single element oxide (e.g. CuO, Cu_2O, Al_2O_3, and TiO_2,), alloys (e.g. Cu-Zn, Fe-Ni, and Ag-Cu), multi element oxides (e.g. $CuZnFe_4O_4$, $NiFe_2O_4$, and $ZnFe_2O_4$), metal carbides (e.g. SiC, B_4C, and ZrC), metal nitrides (e.g. SiN, TiN, and AlN), and carbon materials (e.g. graphite, carbon nanotubes, and diamond) suspended in water, ethanol, EG, oil, and refrigerants, … etc. [35-37]. They can be classified into two main categories: single material nanofluids and hybrid nanofluids.

2.1 Single Material Nanofluids

This category of nanofluid was first proposed by Choi, in 1995, and is considered as the conventional form of nanofluids used, where a single type of nanoparticles are used to produce the suspension via different preparation methods [5]. It was reported by many authors that nanofluids of such category are superior in performance, due to having much favourable thermophysical properties, than their basefluid [38-42].

2.2 Hybrid Nanofluids

Hybrid nanofluids are an advanced category of nanofluids which are made of a combination of more than one type of nanoparticles suspended in a basefluid. This type of fluids were first studied experimentally by Jana et al., in 2007, in order to enhance the fluid thermal conductivity beyond that of a conventional single material type nanofluid [43]. In their study, Cu nanoparticles, CNTs, and Au nanoparticles dispersed in water, as well as their hybrids (CNT–Cu/H_2O and CNT – Au/H_2O) were examined. The results showed that the thermal conductivity of Cu/H_2O nanofluid was the highest among the tested samples and increased linearly with the rise of particle concentration. Nevertheless, the stability of the CNT– Cu/H_2O nanofluid achieved longer settling time than the other types of nanofluids. This enables the fluid to conserve its thermal conductivity much longer before degrading.

3. Preparation of Nanofluids

Uniformity of the particle dispersion depends mainly on the preparation method used and can have a significant effect on the thermophysical properties of the nanofluid. Meaning that, if two similar nanofluids were to be prepared using different preparation methods, their thermophysical properties and tendency to agglomeration are most likely to vary from each other. This is because nanofluids are not simply formed from a solid-liquid mixture, but requires special conditions to be present in the suspension such as homogeneity, physical and chemical stability, durability, dispersibility, … etc. There are mainly two techniques used to fabricate nanofluids, namely, the bottom-up approach known as the one-step method, and the top-down approach identified as the two-step method [44].

3.1 Single-Step Approach

The single-step approach relies on combining the production and dispersion processes of nanoparticles into the basefluid via a single step. There are some differences in this procedure. One of the commonly used method for synthesises nanofluids, known as the direct evaporation one-step approach, depends on solidifying nanoparticles that are originally in gaseous phase inside the basefluid its self. The method was developed by Akoh et al. [45] and was named the vacuum evaporation onto a running oil substrate (VEROS) method. The initial idea of this method was to produce nanoparticles, but was found to be extremely difficult to obtain a dry form of nanoparticles from the produced fluid mixture. Wagener et al. [46] proposed a modified VEROS process, where they used high pressure magnetron sputtering to synthesis dispersions containing Fe, and Ag nanoparticles. Eastman et al. [47] also developed a modified VEROS

process, where they directly condensed Cu vapor with a flowing low-vapor-pressure EG to fabricate their Cu/EG nanofluid. Zhu et al. [48] employed a one-step approach, through chemical reaction, to obtain Cu nanofluid. In their work $NaH_2PO_2.H_2O$ with $CuSO_4.5H_2O$ in EG were irradiated to chemically react into producing the nanofluid. In addition, Tran and Soong [49] used a laser ablation one-step method to synthesis Al_2O_3 nanofluid. Other one-step approach also exists [50,51], with all being favourable in minimizing the agglomeration of nanoparticles in the basefluid. However, the downside of using the one-step approach is the presence of contaminations that are difficult to dispose of [44]. Fig. 2.7 shows a sample of the one-step approach used to prepare nanofluids by vapour deposition.

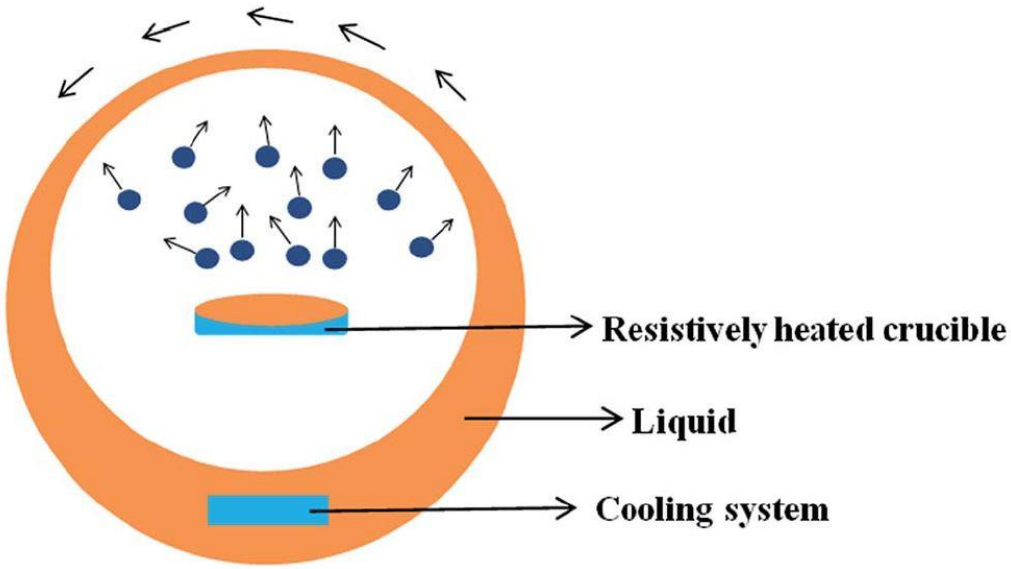

Fig. 2.7. Preparation of nanofluid using one-step vapour deposition method [52].

3.2 Two-Step Approach

In this approach, nanoparticles are initially produced or purchased in the form of dry powder and then dispersed in the basefluid. The commonly employed equipment's for dispersing nanoparticles in the basefluid are magnetic stirrers, ultrasonic bath, homogenizers, high-shear mixers, and bead mills. Unlike the one-step approach, the two-step approach is more commonly used to fabricate nanofluids due to having a lower processing cost and a wide availability of commercially supplied nanoparticles by several companies. Fig. 2.8 demonstrates an example of the schematic procedure of the two-step approach used for synthesising nanofluid.

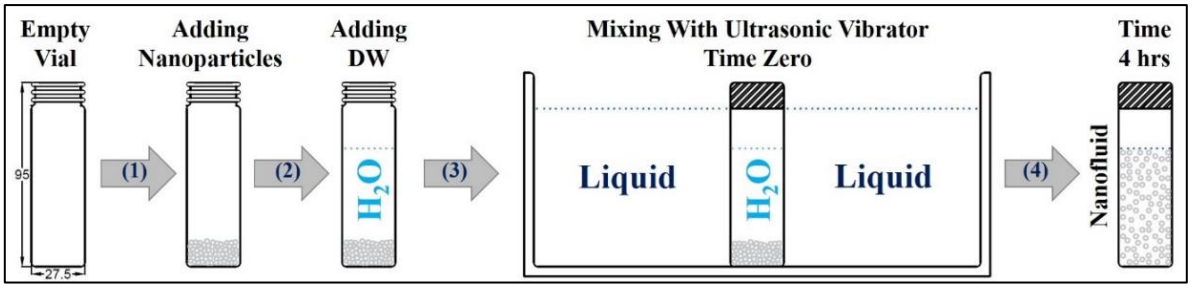

Fig. 2.8. Schematic procedure of the two-step nanofluids preparation.

Eastman et al. [47], Wang et al. [53], and Lee et al. [54] adopted this approach to form their Al_2O_3 nanofluids. Murshed et al. [55] synthesised TiO_2/H_2O nanofluid via the same route. Xuan et al. [56] used as-received Cu nanoparticles to produce transformer oil based and water based nanofluids. Single-walled and multi-walled carbon nanotubes were also reported to be used with or without adding surfactants for preparing nanofluids using the two-step method [57-61].

Some researchers claim that the two-step process is preferable for forming nanofluids containing oxide nanoparticles, while it is less effective toward nanoparticles of metallic origin [62]. The main disadvantage of the two-step approach is the large aggregation of particles that accompanies the process compared to the one-step method. Despite of such disadvantages, this process is still the most popular route for producing nanofluids of large or small quantities and can be used to synthesis almost any kind of nanofluids [52].

4. Stability of Nanofluids

Part of the challenges that faces commercialising nanofluids are their poor stability due to the interaction between the particles themselves and between the particles with the surrounding liquid [63]. This kind of behaviour can be linked to two opposing forces: 1- the well-known Van der Waals attractive forces on the particles surface which causes the particles to be attracted to each other into forming clusters or agglomerations of particles then separate from the basefluid and settle at the bottom due to gravitational force, and 2- the electrical double layer repulsive force which tends to separate the particles from each other via steric and electrostatic repulsion mechanisms [64-66]. Fig. 2.9 shows the steric and electrostatic repulsion mechanisms. Stability is a very important element in commercialising nanofluids as it extends the shelf-life of the product while conserving its thermophysical properties. To obtain a stable nanofluid the electrical double layer repulsive force should surpass the Van der Waals attractive forces.

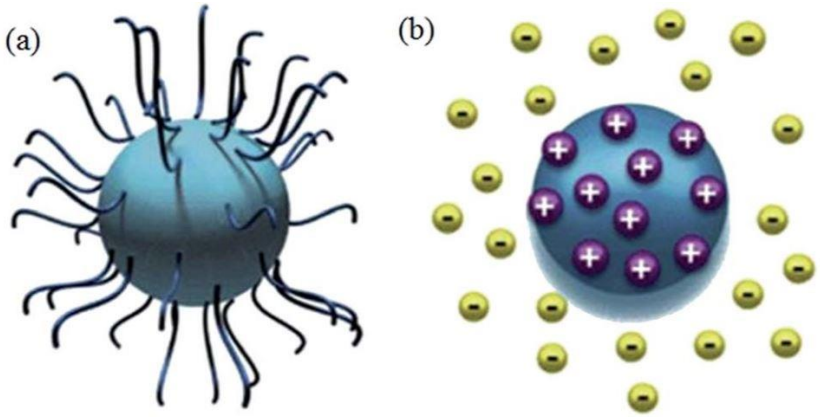

Fig. 2.9. Repulsion mechanisms: (a) steric repulsive, and (b) electrostatic repulsion [67].

4.1 Stability Evaluation Methods

As previously mentioned, stability of nanofluids has a vital role in extending its shelf-life and preserving the thermophysical properties of the fluid. Different evaluation methods for the stability of nanofluids were discussed by different researchers [68,69]. These techniques are discussed below.

4.1.1 Zeta potential analysis. The zeta potential analysis evaluates the stability of nanofluids through the observation of electrophoretic behaviour of the fluid [70]. This is because the free charges in the basefluid get attracted to the opposite charges on the dispersed particles surface, causing the development of a layer of charged ions known as the stern layer. There is an additional layer that surrounds the formed stern layer, defined as the diffuse layer, which has its individual charges and is more diffusive. The zeta potential can be defined as the potential difference between the basefluid and the stern layer in contact to the dispersed particles as shown in Fig. 2.10, and is measured in millivolts.

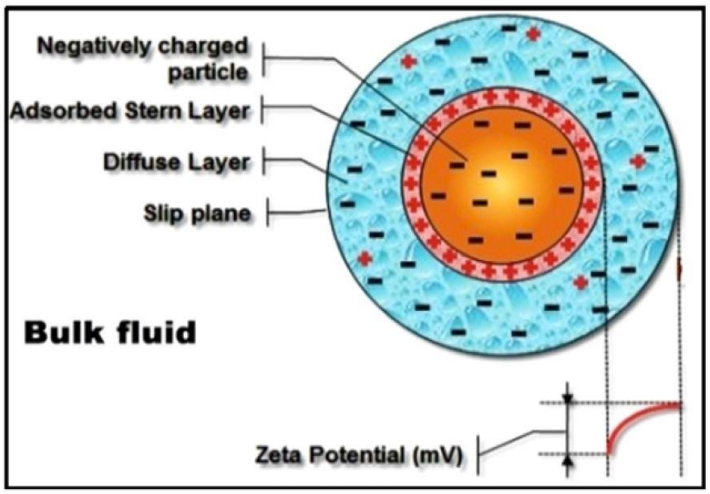

Fig. 2.10. Zeta potential between the slip plane and stern layer of a nanoparticle [71].

In any nanofluid, the zeta potential can be ranged from positive, at low pH values, to negative, at high pH values. In terms of nanofluid stability, zeta potential value > ±60 mV has excellent stability, ± (40 to 60) mV has good stability, ± (30 to 40) mV is considered stable, and < ±30 mV is highly agglomerative [68]. Measurement of the zeta potential value in a nanofluid can be performed using a zeta sizer nano (ZSN) device [72].

Kim et al. [73] fabricated Au/water nanofluids, of particle size ranging from 7.1 to 12.11 nm, without the addition of any dispersants and found out that the suspension remained outstandingly stable for up to 1 month. The stability of the nanofluids was characterised using the zeta potential analysis technique which showed a negative zeta potential values ranging from -32.1 ± 0.95 (0.018 vol%) to -38.5 ± 1.84 (0.0025 vol%). Wang et al. [74] investigated the effect of different pH values and the variation of sodium dodecyl benzene sulfonate (SDBS) concentration on Al_2O_3/H_2O and Cu/H_2O nanofluids stability. Nanoparticles of 0.05 wt% were employed in their zeta potential measurements of the two water based nanofluids. Their results indicated that in the region of 2.0 < pH < 8.0, the zeta potential value of alumina nanofluid was negatively higher than that of copper nanofluid sample at the same pH value, but in the region of pH > 8.0, Cu/H_2O nanofluid had shown better dispersion as the zeta potential value was higher than the Al_2O_3/H_2O nanofluid at the same pH level. The maximum zeta potential values obtained were -40.1 mV for Al_2O_3/H_2O, and -43.8 mV for Cu/H_2O. It was also reported that the addition of SDBS has improved the nanofluids dispersion, where the highest zeta potential value for alumina nanofluid, of pH = 8.0, was at SDBS = 0.1 wt% and the copper nanofluid, of pH = 9.5, was at SDBS = 0.07 wt%. Mondragon et al. [75] examined the increase of silica nanoparticles mass fraction on the stability of silica-water nanofluids of different pH values. They concluded that raising the nanoparticles from 2% to 20% mass fraction have led to a reduction in the zeta potential value from –48.63 mV to -16 mV both at a pH of 10, with a minimum achievable stability of 48 h for the 20% mass fraction. Researchers have reported the value of zeta potential of various types of nanofluids of water base, at different pH values and without the addition of any type of surfactant, as demonstrated in Fig. 2.11.

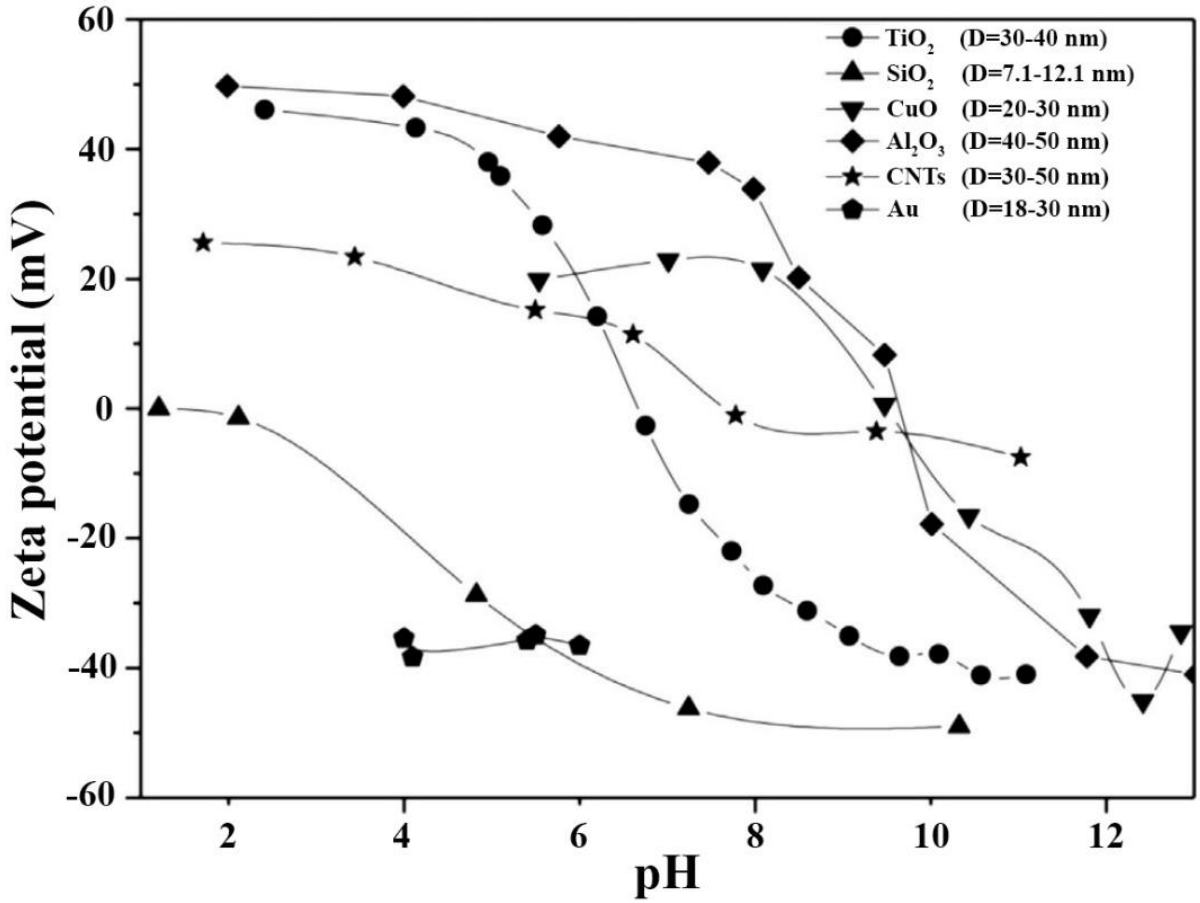

Fig. 2.11. Zeta potential value as a function of pH for different nanoparticles dispersed in water [73,75-79].

4.1.2 Sedimentation photograph capturing method. This method is considered to be one of the simplest approaches to measure the stability of nanofluids [80,81]. In this approach, the volume of the agglomerated nanoparticles in a nanofluid is monitored under an external force. This is done by placing a sample of the prepared nanofluid in a transparent glass vial then the formation of sediments are observed via capturing photographs of the vial at equal intervals of time using a camera [82]. The captured images are then compared to each other to analyse the stability of the nanofluid. Thus, the characterised nanofluid is considered to be stable when the particles size and its dispersity remains constant with time (i.e. no sedimentation occur).

Three behaviour of sedimentation can be observed in any unstable nanofluid: 1- dispersed sedimentation, where the sediment height is gradually increased from the bottom as the solution clarifies; 2- flocculated sedimentation, where the sediment height reduces with respect of time; and 3- mixed sedimentation, where both previous phenomena occur simultaneously in a nanofluid [83]. Fig. 2.12 illustrates the three sedimentation behaviours.

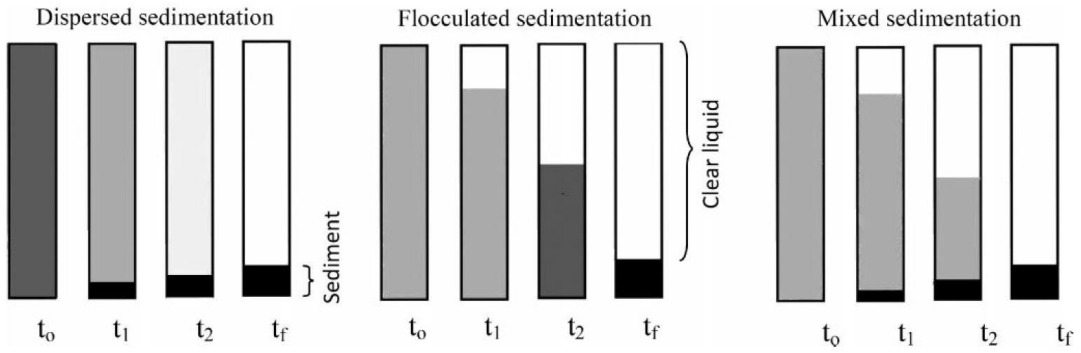

Fig. 2.12. Types of sedimentation behaviours in nanofluids, where t indicates time and $t_o<t_1<t_2<t_f$ [84].

Wang et al. [85] investigated the pH value influence on alumina-water and copper-water nanofluids stability, at similar wt%. Commercial Al_2O_3, of 15 – 50 nm particle size, and Cu, of 25 – 60 nm particle size, nanoparticle were used at a wt% between 0.01% and 0.9% in their two-step fabrication process. Sedimentation photograph capturing method was adopted ,for a period of 7 days, to determine the samples stability. Their results showed that the highest nanoparticles dispersion can be obtained at a pH of 8.0 and 9.5, for Al_2O_3/H_2O and Cu/ H_2O nanofluids, respectively. Angayarkanni and Philip [86] have studied the stability of γ-Al_2O_3 (13 nm) and α-Al_2O_3 (24.4 nm) water based nanofluids at a vol% ranging from 0.5 vol% to 6.0 vol%. Four time intervals were captured to analyse the stability of their nanofluids, specifically, at time 0, 3, 30, and 172 h. From analysing the images, they noticed that up to 3 h there were minimum phase separation for both types of nanofluids, and at time > 3 h, the α-Al_2O_3 particles started settling, with a complete phase separation been reached after 172 h. On the other hand, γ-Al_2O_3 nanofluids have maintained their stability throughout the time period. Witharana and Hodges [87] also used the same approach as part of their investigation of Al_2O_3/deionised water (DIW) nanofluid, of spherical shape and particles size in the range of 10 – 100 nm, aggregation and settling behavior. For the suspensions preparation, they used 0.5 wt% of alumina nanopowder then dispersed it with the basefluid for 4 h using an ultrasound device. The pH of the produced suspensions were afterward adjusted to a pH of 6.3 and pH of 7.8. Their results have illustrated that the as-prepared nanofluid of pH 6.3 was stable for more than 30 min, and the nanofluid of pH 7.8 was rapidly settling (i.e. highly unstable). They also concluded, from their findings, that within the unstable nanofluid there exist two main region, which reflects the phase separation speed. The first region is called the rapid settling region (up to 2 min), where the settling speed was ~ 46 mm/min, and the second is called the slow settling region (beyond

2 min), where the settling was at 4 mm/min. Fig. 2.13. demonstrates the unstable nanofluid phase separation speed regions. Ilyas et al. [88] tested the stability of as-received alumina nanoparticles, of 40, 50, and 100 nm average diameter, dispersed in water-ethanol (0 – 100 wt%) using the same method. They divided their samples between a low particles concentration group (nanoparticles: 0.1, 0.3, and 0.5 wt%, and ethanol: 0 – 50 wt%), and a high particles concentration group (nanoparticles: 1.0, 3.0, and 5.0 wt%, and ethanol: 60 – 100 wt%). Observing the sediment formation, with and without sonication, they found out that the low concentration samples have followed a dispersed sedimentation mechanism, with complete settling after 16 h. On the contrary, the high concentration group showed a flocculated sedimentation behaviour where nanofluids fully settled after 16 h, with an exception to the 100 wt% of ethanol samples, where the settling exhibited a mixed sedimentation behavior.

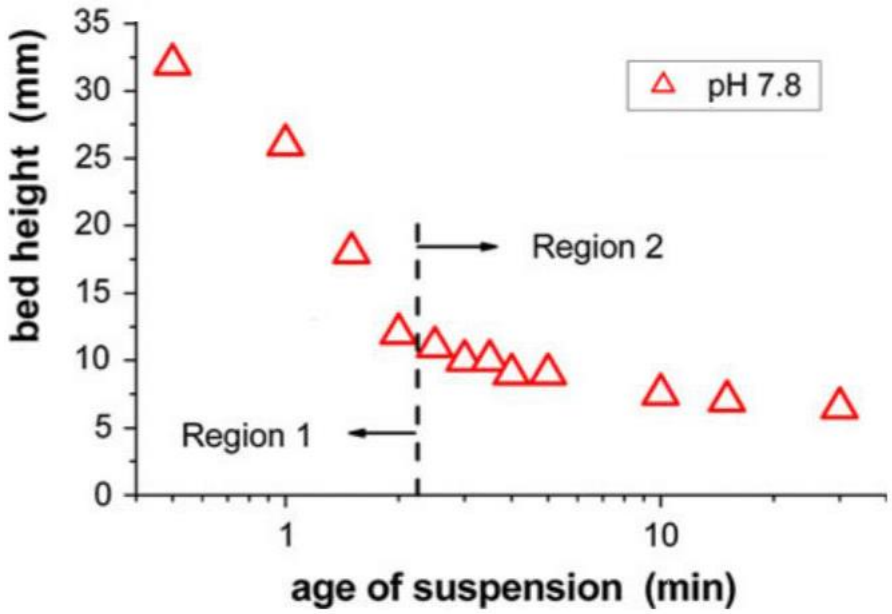

Fig. 2.13. Instable Al_2O_3 nanofluid phase separation speed regions [87].

All of the aforementioned researchers have confirmed that the stability of nanofluid can be indicated using the sedimentation photograph capturing method. Despite the fact that this approach represents a high-performance analysis of nanofluid stability with low cost, very few papers were published using this method [89]. One of the reasons that can be linked to the limited adaptation of such stability evaluation approach is its requirement of a long period of observation which is very time consuming [71].

4.1.3 Centrifugation method. Nanofluid centrifugation is a much faster method for determining the stability of the prepared fluid compared to the sedimentation photograph capturing

approach. It has been employed in a variety of stability studies, in which a visual examination of the nanofluid sedimentation is performed using a dispersion analyser centrifuge.

Singh et al. [90] confirmed the stability of the as-prepared silver/ethanol nanofluids, of 30 – 60 nm particle size and 0.0112 – 0.0114 vol%, with added polyvinylpyrrolidone surfactant and centrifuging the samples for 10 h at 3000 rpm. The outcome of their experiment showed excellent stability with no signs of sedimentation. Li [91] also evaluated the instability of an aqueous polyaniline colloids via manipulating its pH value and employing the same stability technique. He found out that the electrostatic repulsive force surrounded by the nanofibers helped in providing the longest stability to the colloids, with an optimum stability reached at a pH value of 2.6. Mehrali et al. [92] observed the instability via centrifuging their graphene/distilled water (DW) suspension, of 2 μm diameter and 2 nm thickness, from 5 to 20 min at 6000 rpm. Four mass concentrations (0.025, 0.05, 0.075, and 0.1 wt%) were used in their research and all have shown good stability with the present of few sedimentation at the bottom of the test tubes at the end of each centrifugation process.

4.1.4 Spectral analysis method. This method was firstly proposed, in 2003, by Jiang et al. [93] and can be implemented only if the dispersed nanoparticles have an absorption to wavelength between 190 to 1100 nm [67]. The nanoparticle size distribution in nanofluid is characterised via the absorbed spectrum due to the optical properties of the particles, which depends on their morphology (i.e. shape and size). In general, the absorption intensity and the concentration of nanoparticles in a nanofluid cohabit a linear relationship [67]. A UV-vis spectral analyser may be used in such process to determine the variation in sedimentation time with the supernatant particle concentration via measuring the absorption of the nanofluid. The main advantage of this method is its capability of presenting a quantitative concentration from analysing the nanofluid. Hwang et al. [94] estimated the stability of multi-walled carbon nanotube (MWCNTs) dispersed in paraffin oil nanofluids at different sedimentation time for 800 h using this technique. The MWCNTs used into fabricating the nanofluids had an average length of 10 – 50 μm and average diameter of 10 – 30 nm. Their results showed that the MWCNTs nanofluids had a low spectrum absorption throughout their wavelength (between 360 to 700 nm), with the highest spectrum absorption being at a wavelength of 397 nm, revealing the poor stability and large agglomeration of their nanofluids. Chang et al. [95] examined the uniformity distribution of TiO_2/DW, of 40.7 nm average particles size and nanofluids of pH 7.5, via a UV-Vis absorption spectrum analysis. According to their results, the nanofluids wavelength peaked with absorbency > 1 between 280 to 400 nm, which demonstrated high stability. Some of the

nanofluids absorption wavelength peaks reported by different researchers, measured by UV-Vis method, can be seen in Table 2.1.

Table 2.1. Examples of nanofluids absorption wavelength peaks reported using an UV-Vis spectral analyser.

Investigators	**Nanoparticle**	**Basefluid**	**Peak wavelength (nm)**
Liu et al. [96]	Aligned CNTs	DW	210
Jiang et al. [93]	CNTs	DW	253
Chang et al. [97]	Cu	DW	270
Chang et al. [97]	CuO	DW	268
Sato et al. [98]	Ag	DW	410
Hwang et al. [94]	Fullerene	Paraffin oil	397

4.1.5 3ω-method. Evaluation of the thermal conductivity changes in nanofluids, caused by the sedimentation of nanoparticles, was also proposed as a stability measuring approach known as the 3ω-method [71]. Three articles were found using this method [99-101]. Oh et al. [99] work consisted of examining the stability of the as-prepared Al_2O_3/DIW and Al_2O_3/EG nanofluids, where the nanoparticles were of 45 nm diameter and 0 – 4 vol%. The nanofluids effective thermal conductivity was measured for one hour, which showed an increase in its value with time. This was believed to be caused from the aggregation of the nanoparticles within the basefluids. On the other hand, Martínez et al. [100] investigated the same effect on TiO_2/H_2O nanofluids, that were constructed at 5^{o}C and 15^{o}C, using 5 wt% as-received TiO_2 of 6 nm average particles size. It was found that nanofluids fabricated at 5^{o}C lost its stability after 5.55 min, but had maintained its form for 7.53 min when applying a 1000 kPa inert pressure to the samples. Moreover, the 15^{o}C samples had achieved a 7.18 min and 6.77 min stability, with and without added pressure respectively. Fig. 2.14 shows the experimental configuration of the 3ω-method.

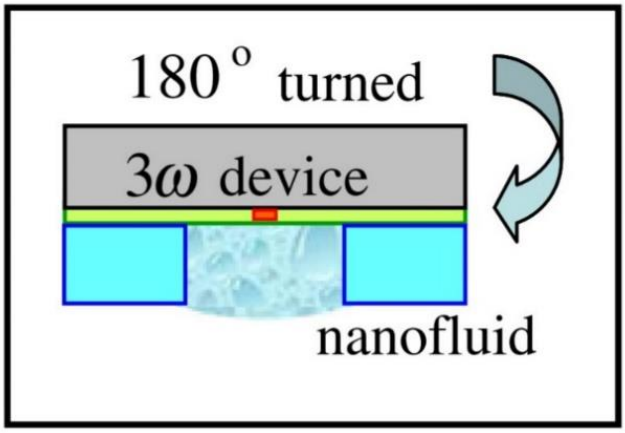

Fig. 2.14. Experimental configuration of the 3ω-method used by Oh et al. [99].

4.1.6 Electron microscopy methods. Particles size distribution can be measured to determine the nanofluid stability using a transmission electron microscopy (TEM) or scanning electron microscopy (SEM) devices. These very high-resolution microscopes tend to capture the digital image, known as the electron micrograph, of approximately 0.1 nm in size [52,71]. If clusters of nanoparticles are found within the obtained images then sedimentation mechanism is most likely to occur (i.e. the nanofluid is considered unstable).

The usual practice reported for inspecting the sample stability using a TEM device is by placing a drop of the as-prepared nanofluid on a carbon coated copper grid then monitoring the distribution of the nanoparticles on top of the copper grid when the basefluid is completely evaporated [52]. Total evaporation of the basefluid always results in aggregation of the nanoparticles. For such reason, the TEM characterisation approach is only applicable for nanofluids of low particles concentration. On the other hand, SEM inspection of the sample is performed by placing a drop of the nanofluid on a sticky tape, which is fixed on top of the specimen holder, then heated in a vacuum oven and dried naturally with air. Finally, the dried sample is placed in the SEM vacuumed chamber to capture the particles images [63]. Fig. 2.15.a and 2.15.b demonstrates the CuO nanoparticles images taken by TEM and SEM, respectively.

Das et al. [102] used TEM images to determine the stability of 99.7% pure alumina (50 nm average particles diameter) dispersed in DW, with and without surfactant, at 0.1 – 2.0 vol%. Sodium dodecyl sulphate (SDS), cetyl trimethyl ammonium bromide (CTAB), and SDBS surfactants were used separately in the fabrication process to form (Al_2O_3 – SDS – DW), (Al_2O_3 – CTAB – DW), and (Al_2O_3 – SDBS – DW) nanofluids, which were compared to pure Al_2O_3/DW samples. In all the examined cases, the nanofluids containing surfactant have illustrated less agglomeration than the pure Al_2O_3/DW nanofluids, with the highest stability

been achieved from the SDBS surfactant of 2:1 particle to surfactant mass ratio. Kim et al. [103] studied the dispersion of one-step fabricated Cu/ethanol, Ni/ethanol, Cu/EG, and Ni/EG nanofluids, of spherical shape and average particles size < 100 nm, by analysing their TEM images. The high magnified images revealed that EG, as a basefluid, had better dispersibility effect on the nanoparticle than ethanol, with Cu/EG nanofluid showing finer particle size and better dispersibility behaviour than the other three cases. SEM technique was adopted by Rubalya et al. [104] to determine the 0.03 vol% dispersed ZnO (69 nm), and ZnZrO (23.9 nm) nanoparticles in rice bran oil with/without tert-Butylhydroquinone (TBHQ) antioxidant. Their results showed that ZnO particles were homogeneously distributed, with or without TBHQ, in the sample and that the ZnZrO nanofluid had noticeable particle agglomerations.

In addition to the TEM and SEM devices used to characterise the nanofluids stability, cryogenic electron microscopy (Cryo-EM) can also analyse the stability of nanofluids, if the microstructure of the nanofluid is unchangeable throughout the examination process [105].

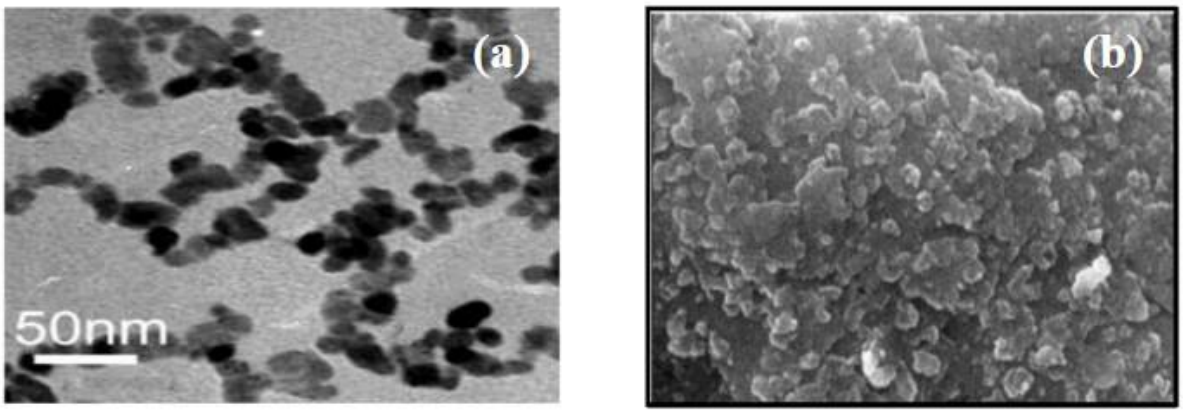

Fig. 2.15. Electron micrograph of CuO nanoparticles using: (a) TEM [106], and (b) SEM [107].

4.2 Stability Enhancement Procedures

Several literatures have reported diverse ways of improving the stability of nanofluids, which are discussed in the following section:

4.2.1 Addition of surfactants. Adding surfactants, also referred to as dispersant, is an effective stability enhancement method that prevents the agglomeration of nanoparticles within the nanofluid [108]. It is considered as a simple and economical chemical method, where it reduces the surface tension of the basefluid and improves the immersion of nanoparticles. This is because surfactants consist of hydrophobic tail portion (e.g. long-chain hydrocarbons), and

hydrophilic polar head group that tends to increase the hydrophilic behaviour between the basefluid and the nanoparticles.

Based on the head composition, dispersant can be divided into four classes: 1- ionic surfactants with head groups of negative charge (e.g. alkyl sulfates, long-chain fatty acids, phosphates, sulfosuccinates, and sulfonates), 2- non-ionic surfactants with neutral head groups (e.g. alcohols, polyethylene oxide, and other polar groups), 3- cationic surfactants with head groups of positive charge (e.g. long-chain quaternary ammonium compounds and long-chain amines), and 4- amphoteric surfactants of zwitterionic head groups (charge is a pH depended) [67].
Commonly used surfactants are listed in Table 2.2. Selecting a suitable surfactant is determined by the basefluid used in preparing the nanofluids. In general, if the basefluid is a polar solvent, then a water-soluble surfactant should be used; otherwise, an oil-soluble is used instead. The solubility of non-ionic dispersant can be estimated through the hydrophilic/lipophilic balance (HLB) value. The higher the HLB value, the more water-soluble the surfactant is, while the lower the HLB value, the more oil-soluble the surfactant is considered. HLB values can be found in many handbooks [67].

Table 2.2. Commonly used surfactants and their structure formulas.

Surfactant	Structure formula
Polyvinylpyrrolidone (PVP) [109]	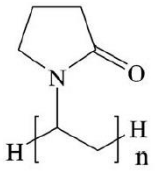
Sodium dodecyl sulphate [110]	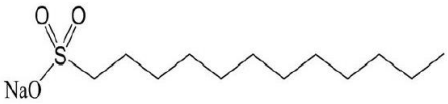
Oleic acid (OA) [111]	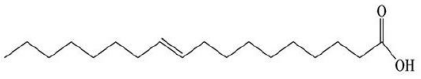
Hexadecyl trimethyl ammonium bromide (HCTAB) [112]	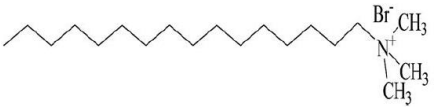
Poly (acrylic acid sodium salt) [52]	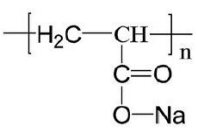

Sodium dodecyl benzene sulfonate [52]	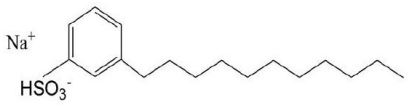
Dodecyltrimethylammonium bromide (DTAB) [113]	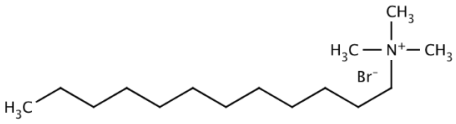
Gum Arabic [114]	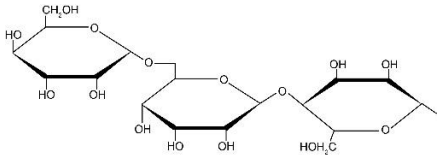
Sodium octanoate (SOCT) [63]	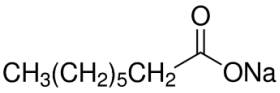

The disadvantages of using dispersant as a nanofluid stabilizer is its sensitivity to hot temperature. This is because the rise in temperature causes the bounds between the nanoparticles and the surfactant to be damaged and in some cases, it can chemically react into producing foams [115]. Additionally, excessive amount of surfactant affects the thermophysical properties of the nanofluid, where it increases the viscosity of the nanofluid and reduces its thermal conductivity [52,116].

Timofeeva et al. [117] dispersed 15 nm silicon dioxide nanoparticles in synthetic oil, therminol 66 (TH66), to improve the basefluid heat transfer efficiency. Benzethonium chloride (BZC), benzalkonium chloride (BAC), and CTAB were used as surfactants, at 5 wt%, to examine their influence on the nanoparticles dispersion behaviour. The SiO_2 nanopowder, of 1 vol%, and TH66 basefluid were sonicated with/without surfactant for 50 min to prepare the nanofluids. Visual appearance of the samples, for 24 h, indicated that the surfactants had improved the stability of the nanofluids, with BAC showing the highest dispersion condition. However, pure SiO_2/TH66 nanofluid had illustrated large particles agglomeration which was linked to the strong attraction force between the nanoparticles. The findings were also confirmed through SEM and spectral analysis. Priya et al. [118] fabricated 40 – 60 nm particle size CuO with H_2O and tiron (surfactant) nanofluids via 6 h sonication. It was reported that the ideal CuO:tiron ratio that could ensure colloidal stability corresponded to 2.5:1. This was also confirmed from the zeta potential measurements, where the nanofluids were found to possess an absolute value of 30 mV, which was sufficient to preserve the stability of the colloidal. Furthermore, the

authors have stated that the stability of their nanofluids were also confirmed through visual observation but gave no data on the manner. Byrne et al. [119] prepared CuO/DW nanofluids with and without CTAB. Three concentrations of the CuO nanopowder were used, 0.005 vol%, 0.01 vol%, and 0.1 vol%, with and without surfactant, of 1:1 vol% ratio, to produce the suspensions. Dynamic light scattering (DLS) measurements indicated an increase in agglomeration with the rise in particles concentration, where the 0.1 vol% sample containing no surfactant showed a rapid decrease in particle size from about 3000 nm at time zero to 300 nm after 4 h. This reduction in particle size was explained by the researchers to be caused from the settling of heavier agglomerates of particles, leaving the smaller particles freely detected. On the other hand, the samples that contained surfactant had an average particle size of 200 nm with no variation for a period of 7 days.

4.2.2 Surface modification techniques. One of the methods used to achieve long term stability of nanofluids, without the need of surfactants, is by modifying the nanoparticles surface via functionalization. This is done by introducing functionalized nanoparticles into the basefluid in order to obtain a self-stabilized nanofluid. Usually, suitable functional organic groups are selected as they tend to attach to the atoms surface, enabling the nanoparticles to self-organize and avoid agglomeration [120].

There are two approaches where functional groups can be introduced. The first method is by introducing all the functional ligand in one step, which requires bifunctional organic compounds. A single functionality (X) is employed to be attached to the nanoparticle surface and an additional group (Z) is where the nanoparticles are functionalized. The second method, relies on the reaction between the bifunctional compounds X-Y, where group Y acts as a coupling location and can convert afterwards to a final functionality Z [120]. Fig. 2.16 Shows the two functionalize nanoparticles approaches.

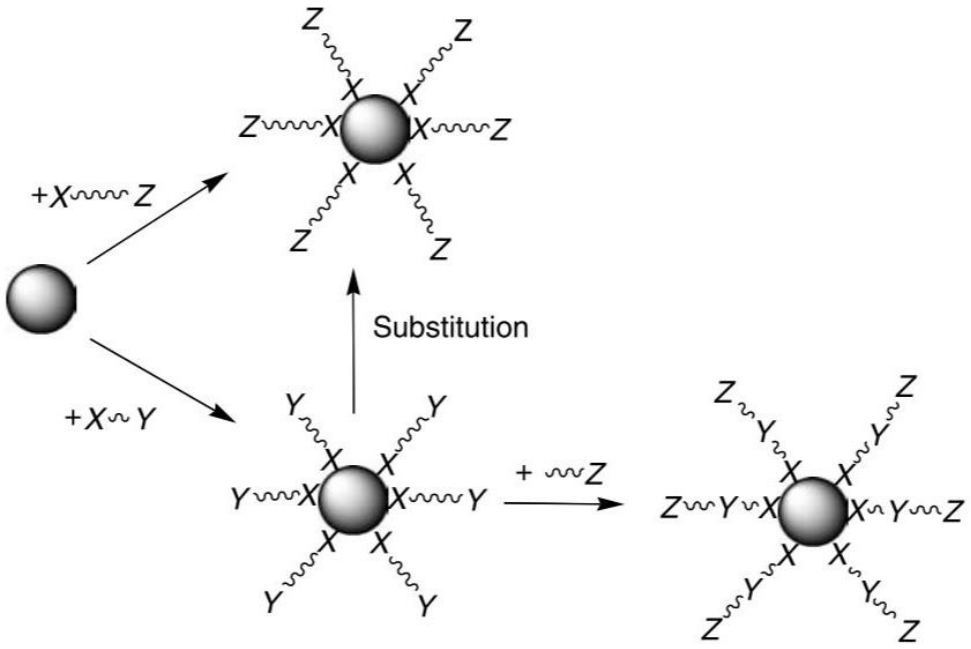

Fig. 2.16. The two functionalize nanoparticles approaches. Method 1 (top): Z functionality with the ligands react directly with the nanoparticle; method 2 (bottom): Y functionality with the ligand reacts directly with the nanoparticle and is then converted in another functionality Z [120].

Kayhani et al. [121] functionalized spherical TiO_2 nanoparticles, of 15 nm particles size, by chemical treatment to achieve stabilized TiO_2/DW nanofluids. Titanium dioxide powder was mixed with 1,1,1,3,3,3, hexamethyldisilazane (C6H19NSi2), at a mass fraction ratio of 2:1, then sonicated for 1 h under 30^{o}C to obtain soaked nanoparticles. Using a rotary evaporation device, the soaked nanoparticles were dried then dispersed by ultrasonic vibration, for 3 – 5 h, with DW. The fabricated nanofluids were stable for several days without any visible signs of agglomerations. This stability behaviour was linked to the hydrophilic ammonium groups placed on the TiO_2 nanoparticles surface. Yang and Liu [122] were able to maintain the dispersion of SiO_2/DIW nanofluids, of 30 nm size and 10% mass concentration, for 12 months by functionalizing the nanoparticles with silanes of (3-glycidoxylproyl) trimethyoxysilane. The term 'functionalized nanofluid' was also proposed to describe any nanofluid that uses functionalizing in its fabrication process. Chen et al. [115] compared the stability of presitine CNTs (PCNTs) and chemically treated CNTs (TCNTs) dispersed in DW, EG, and glycerol. The average length and diameter of the CNTs used were about 30 µm and 15 nm, respectively. Potassium hydroxide was used, via a mechanochemical reactor, to introduce hydrophilic functional groups to the CNTs surface, and hence produce TCNTs. Through TEM images and visual evaluation, it was revealed that the PCNTs nanofluids were rapidly aggregating and

completely sedimented after 5 min from preparing the nanofluids of 0.1 vol% PCNT. On the other hand, the TCNTs nanofluids, of similar vol%, maintained a long-term stability (many months) with no visible precipitation at the bottom of the test vial. It is worth mentioning that surface modification technique via functionalization is not a special method used only for nanofluid, but can also be employed in other applications (e.g. functionalizing graphene oxide bonded to a graphene – based film to improve thermal management) [123].

4.2.3 Ultrasonic agitation. Sonication, which is a physical method that depends on employing ultrasonic waves through the fluid, can be used to enhance the stability of the nanofluid by rupturing the nanoparticles attractional force within the sediments [124]. There are two types of ultrasonicators available, the probe type and the bath type. Both types can be seen in Fig. 2.17.

Many researchers have used ultrasonication in preparing and stabilizing their nanofluids. It was also reported that the probe type sonicator gave a better improvement to the nanofluid than the bath type [63]. Chung et al. [125] demonstrated this through their research work, where they examined the as-prepared ZnO/H_2O nanofluid, of 20 nm average particle size, in terms of rate of sedimentation, rate of size reduction, and minimum size achieved. They found out that the probe type sonicator was more effective than the bath type sonicator, where the particles within the nanofluid were of 50 – 300 nm in size. Petzold et al. [126] investigated the distribution of 1.0 g of fumed silica (aerosol) particles, of 7 – 40 nm size, dispersed in 100 ml of water samples. Particles scattering, within the basefluid, was performed using a magnetic stirrer, high intensity ultrasonic probe, and an ultraturrax, each for 10 min. The zeta sizer analysis results have shown that, unlike the magnetic stirrer and ultraturrax samples, the nanofluids prepared using ultrasonic probe had an uniform particles dispersion along the 30 min examination period.

Although sonication technique is widely used, particularly in the nanofluid two-step preparation method, the optimum sonication time, wave, and pulse mode is still unknown. It was also pointed out that increasing sonication time does not necessarily improves the reduction in particle size, as it can largen rather than reduce the particle size as illustrated by Kole and Dey [127]. In their work, ZnO/EG nanofluid, of 1.0 vol%, showed a rapid decrease in particles size (from 459 nm to 91 nm) between 40 – 60 h of sonication, then an increase in size that reached to 220 nm after 100 h.

Fig. 2.17. Probe type and bath type ultrasonicators [128,129].

4.2.4 pH control of nanofluids. Manipulating the pH value of nanofluids changes the nanoparticles surface and can strongly improve the stability of the dispersed nanoparticles [130,131]. This is because the stability of a nanofluid is directly related to its electro-kinetic properties. Therefore, the zeta potential can be increased/decreased by changing the pH value of the nanofluid and as mentioned previously, zeta potential values of nanofluids above +30 mV or below -30 mV are considered to be more stable because of the high repulsive force generated between the charged nanoparticles. The pH value of a nanofluid can be increased or decreased by adding an appropriate non-reactive alkaline or acidic solution, respectively [132].

Many studies were carried out to demonstrate the effect of pH level on the stability of nanofluids [133-138]. Witharana et al. [87] examined the settling and aggregation behaviour of alumina (Al_2O_3)/H_2O nanofluid of 0.5 wt%, 46 nm particle size, and of spherical particle shape at pH values of 6.3 and 7.8. They discovered that the suspensions were stable at a pH value of 6.3 for more than 30 min compared with the pH value of 7.8 which had endured a complete particle separation and settlement after 30 min. Manjula et al. [139] studied in their work the effect of added surfactants and pH level on the dispersion behaviour of water based alumina nanofluid through its sedimentations. Their results showed that adding surfactant and optimizing the pH level maximized the stability of the nanosuspension. Zhu et al. [140] investigated the influence of different concentrations of SDBS and pH values on the behaviour of Al_2O_3/H_2O suspension. They found out that the effective thermal conductivity and stability of their nanofluid were significantly dependent on the SDBS concentration and pH value of the fluid, where the effective thermal conductivity was increased by 10.1% at a pH value of 8 and particle concentration of 0.15 wt%.

Modak et al. [38] experimentally investigated the heat transfer characteristics of copper oxide (CuO)/H_2O nanosuspension impingement on a hot surface. During the preparational phase of

the nanofluid, they found out that the optimum stability for the 0.15% and 0.60% volume concentration dispersion, at stationary condition, can be achieved for a period of 60 h at a pH value of 10.1 with a 0.2 wt % added SDS surfactant. Lee et al. [141] evaluated the thermal conductivity and stability of CuO nanoparticles, of 25 nm mean diameter, dispersed in DIW. Their particle size measurements revealed that the formed agglomeration of particles sized from 160 nm to 280 nm at a pH range of 3 to 11. They concluded that the stability of the suspension was influenced by the hydrodynamic size of the embedded particles and the pH value. It was also reported that the effective thermal conductivity enhanced by about 11% over that of the basefluid at a pH value of 11. Chang et al. [142] studied the sterical and electrostatic stability of a high suspension self-prepared CuO nanofluid, of an average particle size of 60 nm and 0.01 wt% nanoparticle concentration, without the addition of any dispersant. The suspensions were prepared using a vacuum arc spray nanofluid synthesis system (ASNSS) combined with an ultrasonic vibrator. The prepared nanofluids pH were adjusted to a range of values between 4 to 13 by adding NaOH or HCl to the solutions. Different lengths of settling time, average particle size, and zeta potential of the nanofluids were observed for 7, 30, 90, and 180 days. They concluded that their nanofluid can maintain its stability for more than 6 months once achieved a zeta potential value above 30 mV. Song [143] explored the possibility of stabilizing stainless steel (SS) 316L, of 70 nm particle size, dispersed in water with SDS and SDBS surfactants. The pH values used in their experiment were 8.0, 9.0, 10.0, 11.0, and 12.6. They used five methods to determine the stability and durability of their prepared nanofluids, namely: 1- transmission electron microscope observation, 2- sedimentation observation, 3- zeta potential measurement, 4- particle size distribution measurement, and 5- absorbance measurement. The results of the long-term stability showed that the prepared nanofluids of pH 11 lasted for 10 days, pH 10 lasted for 3 days, and those of lower pH value completely settled in less than a day. As for the sample of pH 12.6, it experienced an excess amount of OH^- ions which caused the electrostatic stability of the fluid to be disrupted and settle rapidly.

Our review of the available literature quoted above shows that the pH value of nanofluids has a strong effect on their stability and that the optimum pH value varies between samples. It also reviled that the pH value is influenced by the nanofluid temperature.

Table 2.3 summarises some of the available studies, on water base nanofluids stability measurements and dispersion improvement, conducted by different researchers. The type of nanofluids, parameters used, characterisation technique, and main findings are also shown.

Table 2.3. Summary of available studies on water base nanofluids stability measurements and dispersion improvement.

Researchers	Basefluids	Particles material	Parameters	Surfactant	pH control	Stability evaluation methods	Observations
Li et al. [81]	Water	Cu	ϕ = 0.0005 – 0.5 wt% D = 25 nm	SDBS, and CTAB	–	Sedimentation photographs, and zeta size analyser	Nanofluids with CTAB lasted for 1 week without sedimentation.
Kim et al. [73]	Water	Au	ϕ = (0.6 x 10^{-4}) – (2.6 x 10^{-4}) vol% D = 7.1 – 12.1 nm	–	–	Zeta potential analyser	Good particle dispersion for 1 month.
Paul et al. [144]	Water	Au	ϕ = (0.6 x 10^{-4}) – (2.6 x 10^{-4}) vol% D = 21 nm	–	–	TEM, SEM, and DLS	No agglomeration or sedimentation even after 48 h.
Qu et al. [145]	Water	Al_2O_3	ϕ = 0.1 – 1.2 wt% D = 43 nm	–	4.9	SEM	Nanoparticles suspended stably for 3 days.
Anoop et al. [146]	Water	Al_2O_3	ϕ = 1 – 6 wt% D = 45 and 150 nm	–	6.5 (1 wt%) 6.0 (2 wt%) 5.5 (4 wt%) 5.0 (6 wt%)	TEM	Several weeks of stability was achieved.
Rohini Priya et al. [118]	Water	CuO	$\phi \leq$ 0.016 vol% 10:1 Length to thickness ratio	Tiron	–	Zeta potential analysis, and visual observation	Stability was maintained throughout the experiment.
Chang et al. [147]	Water	CuO	ϕ = 0.01 – 0.4 vol% D = 20 – 30 nm	Sodium hexametaphosphate (NaHMP)	6.64 – 6.70 (with surfactant), and > 9.5 (without surfactant)	Zeta potential analysis	CuO content > 0.04 vol% showed very high instability and particles tended to settle within minutes.
Liu et al. [148]	Water	CuO	ϕ = 0.5, and 1 wt% D = 30 nm	–	–	TEM	The uniformity and stability of the suspensions were poor after a couple of days.
Yang and Liu [122]	Water	SiO_2	ϕ = 0.5 – 2.5 wt% D = 30 nm	Trimethyoxysilane	–	SEM	Functionalized nanofluids kept good dispersion for 12 months; Pure nanofluid

Researchers	Basefluids	Particles material	Parameters	Surfactant	pH control	Stability evaluation methods	Observations
							developed sedimentation after several days.
Qu and Wu [149]	Water	SiO_2; Al_2O_3	ϕ = 0.1 – 0.6 wt% D = 30 nm; ϕ = 0.1 – 1.2 wt% D = 56 nm	–	9.7; 4.9	TEM	Both types of nanofluids maintained their stability for several days, but the alumina nanofluid had better particles dispersion.
Suganthi and Rajan [150]	Water	ZnO	ϕ = 0.25 – 2.0 vol% D = 30 – 45 nm	NaHMP	–	Zeta potential analysis, and SEM	All samples showed good stability, with highest stability at 2 vol%; Sonication for 3 h reduced the aggregated size leading to a better improvement.
Duangthongsuk and Wongwises [151]	Water	TiO_2	ϕ = 0.2 – 2.0 vol% D = 21 nm	CTAB	–	TEM	Few agglomerations were observed after 3 h from sonication.
Hari et al. [152]	DIW	Ag	Basefluid = 20 ml $AgNo_3$ = 0.25 mM Tri-sodium = 0.25 mM Size = 21 nm	CTAB	–	UV-vis spectroscopy	The suspensions were stable for one week.
Kole and T.K. Dey [153]	DIW	Cu	ϕ = 0.0005 – 0.5 wt% D = 40 nm	–	–	DLS, and TEM	No visible signs of sedimentation for more than 15 days.
Kathiravan et al. [154]	DIW	Cu	ϕ = 0.25, 0.5, and 1.0 wt% D = 10 nm	SDS	–	TEM	Nanofluid maintained particles dispersion for more than 10 h.
Yousefi et al. [155]	DIW	MWCN Ts	ϕ = 0.2 wt% D = 10 – 30 nm	Triton X-100	7.4	TEM	Colloid was stable for 10 days; optimum sonication time was found to be 30 min.
Garg et al. [156]	DIW	MWCN Ts	ϕ = 1.0 wt% D = 10 – 20 nm H = 0.5 – 40 μm	Gum arabic	–	TEM	Over 1 month suspension stability achieved with no visible sedimentation or settling.

Researchers	Basefluids	Particles material	Parameters	Surfactant	pH control	Stability evaluation methods	Observations
Ding et al. [157]	DIW	MWCNTs	ϕ = 0 – 1.0 vol% D = 5 – 10 nm H = 10 – 30 µm	Gum arabic	2, 6, 10.5, and 11	SEM	Nanofluids showed good stability for months.
Abareshi et al. [158]	DIW	Fe_3O_4	ϕ = 0.025 – 3.0 vol% Size = 15 – 22 nm	Tetramethyl ammonium hydroxide	12.8	Zeta potential analysis	Suspensions showed good dispersion and stability.
Phuoc et al. [159]	DIW	Ag	ϕ = 0.01 vol% D = 20 – 30 nm	–	–	TEM	Nanofluids were stable for several months.
Parametthanuwat et al. [160]	DIW	Ag	ϕ = 0.5% w/v D < 100 nm	–	–	–	Samples stability lasted for 48 h.
Yousefi et al. [161]	DIW	Al_2O_3	ϕ = 0.2, and 0.4 wt% D = 15 nm	Triton X-100	–	visual observation	Suspension stability lasted for about 3 days.
Hung et al. [162]	DIW	Al_2O_3	ϕ = 0.5, 1.0, and 3.0 wt% D = 20 nm	Chitosan	–	UV-vis spectroscopy	Nanofluid of 3.0 wt% showed a difference of 5% in its stability, compared to the 0.5 wt% sample.
Heyhat et al. [163]	DIW	γ- Al_2O_3	ϕ = 1.0 – 2.0 vol% D = 40 nm	–	–	SEM, and Zeta potential analysis	Suspensions were stable due to having a zeta potential value of 30 mV.

- Note: Particles concentration, diameter, height, and weight by volume are represented as ϕ, D, H, and w/v, respectively.

5. Nanofluids Thermophysical Properties

Nanofluids are considered superior to their basefluid, because a new type of fluid has been formed with a completely different thermophysical properties such as density, specific heat capacity, thermal conductivity, convective heat transfer, thermal diffusivity, and viscosity [14]. The word 'Effective' is commonly used to describe the thermophysical properties of nanofluids (e.g. effective viscosity, and effective density, … etc.). This is done to differ between the thermophysical properties of the basefluid and the fabricated nanofluid. Fig. 2.18 demonstrates the thermophysical properties of nanofluids which are discussed in more detail below.

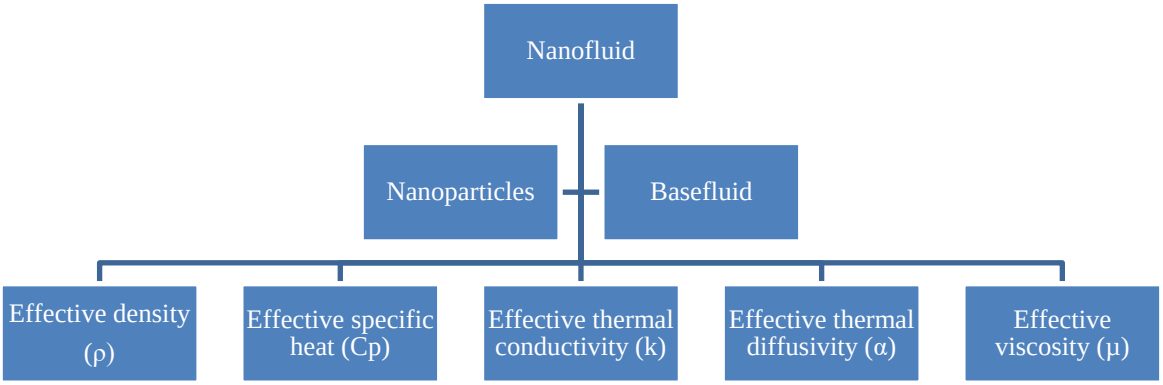

Fig.2.18. Nanofluid thermophysical properties.

5.1 Effective Density

The effective density of a nanofluid can be theoretically calculated through its basefluid density (ρ_{bf}), and nanoparticle density (ρ_{np}) as it is assumed to be a mixed property of both, basefluid and nanoparticles [14]. To determine the nanofluid effective density (ρ_{nf}), the mixing theory (Eq. 1 and 2) is employed [164].

$$\int_V = \frac{V_{np}}{V_{np} + V_{bf}} \approx \frac{V_{np}}{V_{bf}} \quad (1)$$

$$\rho_{nf} = \int_V . \rho_{np} + (1 - \int_V) . \rho_{bf} \quad (2)$$

Where V_{np}, V_{bf}, and $\int_V$ are the nanoparticles volume, basefluid volume, and particle volumetric fraction, respectively.

The only constrain to the aforementioned Eq. 2 is that it is generally limited to a low $\int_V$ as illustrated in Vajjha et al. [165] research findings, where they compared between the theoretical and experimental effective density of alumina, antimony-tin oxide, and zinc oxide nanoparticles dispersed in 60:40 EG/H_2O basefluid at a temperature range of 0°C to 50°C. A

digital density meter and a circulating fluid temperature bath were used to experimental measure effective density of the 1, 2, 4, 6, 8, and 10 vol% alumina nanofluids; 1, 2, 4, and 5.88 vol% antimony-tin oxide nanofluids; and 1, 2, 3, 4, 5, 6, and 7 vol% zinc oxide nanofluids. The range of deviation percentage between the measurements and Eq. 2 were found to be: -0.7897 – 1.1854 (alumina nanofluids), 0.1116 – 1.2073 (antimony-tin oxide nanofluids), and -7.0736 – -1.3591 (zinc oxide nanofluids). From the previous comparison, it can be concluded that Eq. 2 has a good prediction of effective density for some types of nanofluids with different particle concentrations, but is more accurately used toward nanofluids of low vol%.

There were few attempts undertaken to measure the density of nanofluids experimentally, as the majority of researchers tend to use the mixing theory in order to predict its value [121,166-202]. Sommers and Yerkes [203] measured the effective density of alumina/propanol nanofluid, of 10 ± 5 nm average particles size and $0 – 4$ wt% concentration, at room temperature using two ways: 1- hydrometer, and 2- weighting a sample, of known volume, with a high precision balance (± 0.001 g). The two measuring methods, at nanoparticles concentrations ≤ 4 wt%, were found to be 98.2% agreeable to each other. Ho et al. [204] used a density meter, of 5 ± 10^{-5} g/cm^3 accuracy, to measure the effective density of alumina nanofluids at a temperature range between 10^{o}C to 40^{o}C with 0, 0.1, 0.3, 1.0, 2.0, 3.0, and 4 vol% nanofluids samples. It was reported that the experimental results compiled well with Eq. 2 and that the density of alumina particles were less sensitive to the temperature variation in comparison with the basefluid. Eggers and Kabelac [14] measured the effective density of Ag/H2O and Ti/H2O nanofluids, by a pycnometer, and used Eq. 2 to compared its outcomes with their measurements and other published experimental data as seen in Fig. 2.19. The dashed line in the figure represent a perfect fit to Eq. 2 and the two parallel lines shows a ±1% deviation to its value. It can be concluded that the mixing theory complied very well with the published data, indicating a reliable prediction to the effective density value within the margin of error.

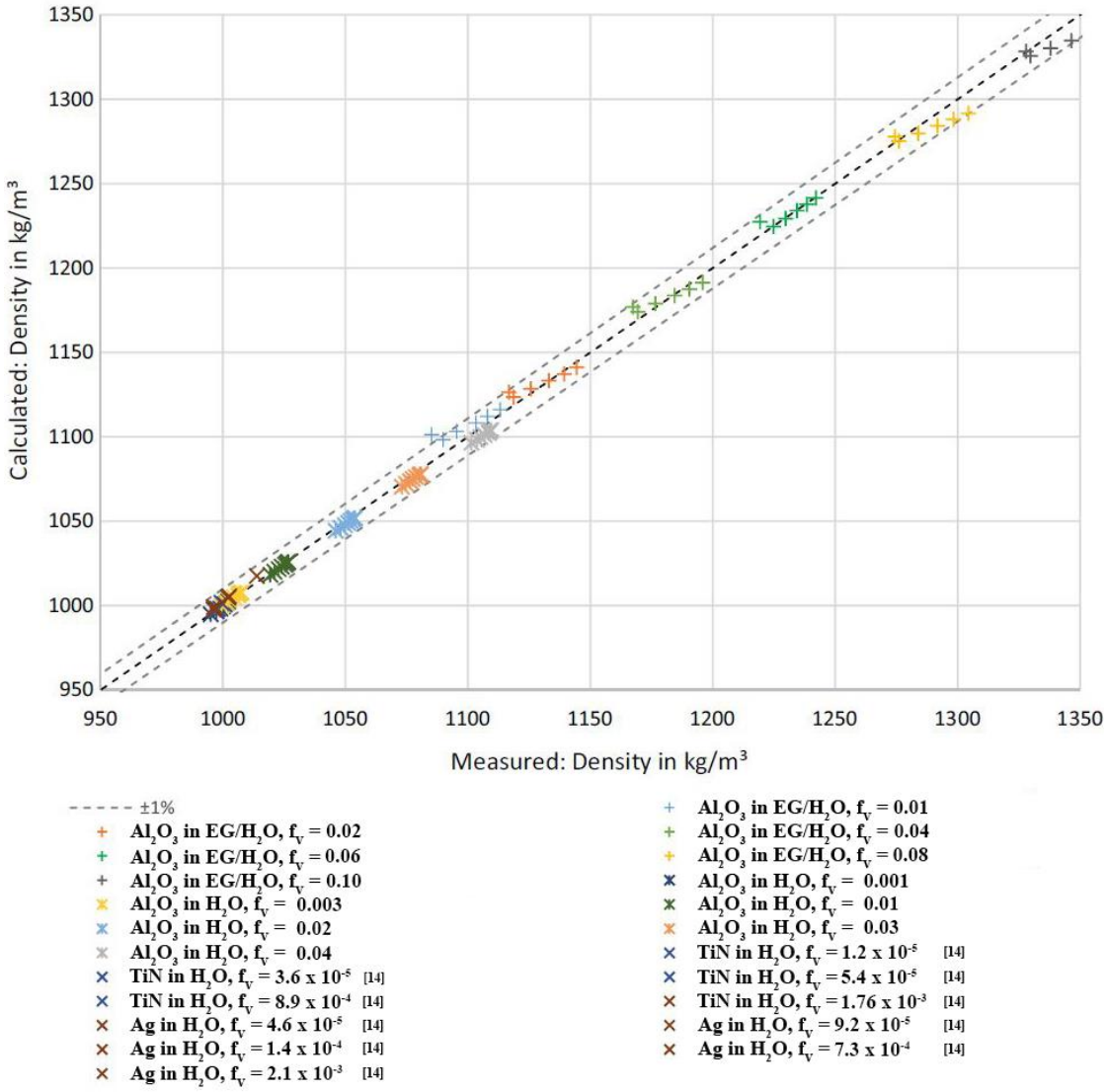

Fig. 2.19. Comparison between theoretically calculated effective density (Eq. 2) and measured data [14].

There are limited number of correlations available, for the effective density of nanofluid, that takes into account the particle size and shape, nanofluid temperature, added surfactant, and the nanolayer between the particles and the basefluid effect [205,206] . Hence more work is needed in this area to insure a much accurate prediction of the effective density at higher particles concentrations.

5.2 Effective Specific Heat

The effective specific heat of a nanofluid ($C_{p_{nf}}$) is the amount of heat needed to increase the temperature of one gram of nanofluid by one degree Celsius. It is a very important property that effects the heat transfer rate of a nanofluid. There are two main effective specific heat

models that were suggested to calculate the effective specific heat of nanofluids. The first model was proposed by Pak and Cho [164], based on the volume concentration of nanoparticles and the liquid – particle mixture formula.

$$C_{p_{nf}} = \int_V . (C_p)_{np} + (1 - \int_V) . (C_p)_{bf} \quad (3)$$

The second model, is the commonly accepted correlation, which was presented by Xuan and Roetzel [207].

$$C_{p_{nf}} = \frac{(1-\int_V) . (\rho C_p)_{bf} + \int_V . (\rho C_p)_{np}}{\int_V . \rho_{np} + (1-\int_V) . \rho_{bf}} \quad (4)$$

Where $C_{p_{bf}}$ and $C_{p_{np}}$ are the specific heat capacity of the basefluid and the specific heat capacity of the nanoparticles, correspondingly.

Zhou an Ni [208] experimentally investigated the effective specific heat of Al_2O_3/DIW suspension, of 45 nm average particles diameter and 0 – 21.7 vol%, at a temperature range between 25°C and 40°C. It was found that the prediction of Eq. 4 collapsed well with the experimental data obtained from the differential scanning calorimeter (DSC), and that Eq. 3 had shifted largely from these data. For example, at 21.7 vol%, the effective specific heat was 1.3% and 3.8% higher when using Eq. 4 and Eq. 3, respectively, than the measured values. Teng and Hung [209] examined the deviation between the experimental and calculated effective specific heat of 20 nm Al_2O_3 nanoparticle dispersed in H_2O. The nanofluids were fabricated at 0.5, 1.0, and 1.5 wt% of nanoparticles and 0.2 wt% added chitosan as surfactant using the single-step approach. A DSC device was used, at a temperature range of 25°C to 65°C, to measure the effective specific heat of the samples then compare them to the calculated results from Eq. 3 and Eq. 4. It was found that the theoretical calculation using Eq. 3 was able to predict the effective specific heat of the 0.5 wt% samples but had a large overestimation in its value with the 1.0 wt% and 1.5 wt% nanofluids, which suggest that Eq. 3 is more suitable to be employed toward suspensions of low concentrations. Moreover, Eq. 4 had underestimated the effective specific heat value of the 0.5 wt% suspension and over predicted it with the 1.0 wt% and 1.5 wt% samples. The reported deviations between the experimental data and the two equations were in the range of -0.07% to 5.88% and -0.35% to 4.94% for Eq. 3 and Eq. 4, respectively. Kulkarni et al. [210] used a self-designed specific heat measuring device to obtain the effective specific heat of 45 nm alumina particles dispersed as 2, 4, and 6 vol% into an equal quantity of EG/DIW mixture. Comparing Eq. 3 and 4 to their experimental data, obtained at a temperature range of 25°C to 70°C, they discovered that both equations have failed to

predict the effective specific heat, with Eq. 4 having less deviation to the measured data than Eq. 3. In addition, it was concluded that: 1- the effective specific heat of the dispersion decreases as the concentration of nanoparticles increase, and 2- the effective specific heat of nanofluids increases with the rise in temperature. Eggers and Kabelac [14] evaluated Eq. 4 performance with their DSC measured effective specific heat of TiN/H_2O and Ag/H_2O nanofluids and other published data. Fig. 2.20 illustrates the theoretical and experimental comparison, where the dashed line shows a perfect fit to Eq. 4 and the two parallel lines indicates a ±5% deviation from it. One can conclude from Fig . 2.20 that the model can predict the effective specific heat value of nanofluids well within the ±5% margin.

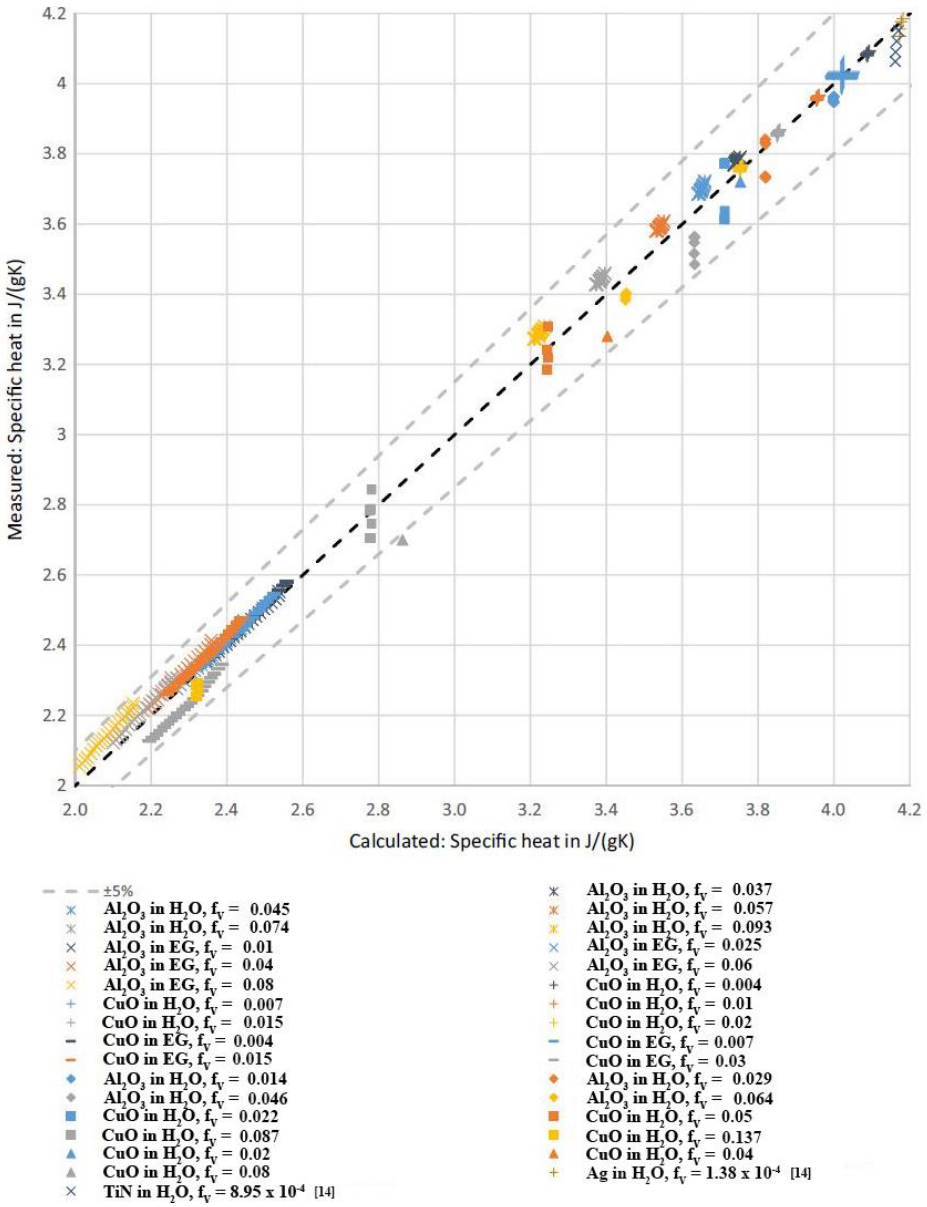

Fig. 2.20. Comparison between theoretically calculated effective specific heat (Eq. 4) and measured data [14].

From the previous studies, it can be noticed that there are few published work on effective specific heat of nanofluids, hence more work is needed to narrow the gap of knowledge in this area. In addition, nanoparticles size and concentration, nanofluid temperature, and basefluid type have shown to strongly influence the effective specific heat of nanofluids which was also pointed out by Sekhar and Sharma [211]. Other effective specific heat models that contains correction factors to compensates for the over/underestimation of the results or were designed for certain testing conditions can be found in the following literatures [211-217].

5.3 Effective Thermal Conductivity

One of the main driving force behind the concept of nanofluids is the enhancement of the thermal conductivity compared to conventional fluids, which has a positive effect on the fluid convective heat transfer. Adding nanoparticles to a conventional fluid improves its thermal conductivity, if the added nanoparticles had a higher thermal conductivity than its basefluid. Some of the most common nanoparticles and basefluids thermal conductivities are shown in Table 2.4 and 2.5, respectively.

Table 2.4. Commonly used nanoparticles thermal conductivities [42].

Material	**Thermal conductivity (W/mK)**
Al_2O_3	40
CuO	76.5
Fe_2O_3	6
MgO	54.9
SiO_2	1.34 – 1.38
TiO_2	8.4
ZnO	29
Ag	429
Al	238 – 273
Au	310
Cu	401
Fe	75 – 80
MWCNTs	2000 – 3000

Table 2.5. Commonly used basefluids thermal conductivities [42].

Fluid	Thermal conductivity (W/mK)
EG	0.257
Ethylene Oxide	0.139 – 0.146
Ethanol	0.161 – 0.171
Glycerol	0.285
Kerosene	0.145 – 0.168
Toluene	0.133
Water	0.608

This increase in effective thermal conductivity can be linked to different factors such as the Brownian motion (Fig. 2.21.a) which is the core mechanism controlling the thermal behaviour of fluid – nanoparticles dispersion. Another reason is the liquid molecules surrounding the nanoparticles into forming layered structures, known as the nanolayer (Fig. 2.21.b). These layered structures are considered as a thermal bridge between the bulk liquid and the nanoparticles, and hence increases the thermal conductivity of the nanofluid [58]. In addition, the heat in the crystalline solids is carried by phonons that are formed randomly, propagate in random direction, and are scattered via defects or by colliding each other [218-220]. Moreover, clustering of particles was found to influence the effective thermal conductivity [220]. This is due to the creation of localized particle-rich zones, caused from particles agglomerations settling, which have less thermal resistance to heat flow. It was also reported that thermophoresis (also called thermodiffusion, thermomigration, the Ludwig-Soret effect, or the Sort effect), which is a phenomenon exhibited in a mixture of particles that tends to response differently to the force of a temperature gradient, can influence the effective thermal conductivity of nanofluids at high temperatures, but such theory was never proven by any of the published literature up to today [221,222].

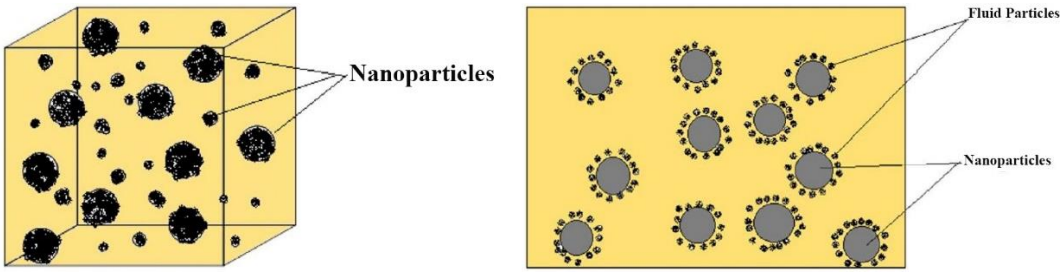

Fig. 2.21. (a) Nanoparticles Brownian motion, and (b) Nanofluid structure containing bulk fluid, nanoparticles, and nanolayers at the liquid/solid interface [36].

Many experimental and theoretical work have been carried out to investigate the changes in nanofluids thermal conductivity. Maxwell model (Eq. 5), which was developed in 1881, was the first correlation used to predict the effective thermal conductivity (K_{nf}) of solid – liquid dispersion, using the thermal conductivities of both nanoparticles (K_{np}) and basefluid (K_{bf}) [223].

$$K_{nf} = K_{bf} \cdot \frac{K_{np}+2 \cdot K_{bf}+ 2 \cdot (K_{np}- K_{bf}) \cdot \int_V}{K_{np}+2 \cdot K_{bf}- (K_{np}- K_{bf}) \cdot \int_V} \quad (5)$$

The model considers the two phases (solid and liquid) of the nanofluid and satisfactorily predicts the effective thermal conductivity of nanofluids when the added particles are of spherical shape, low vol%, and the suspension is at ambient conditions. Bruggeman [224] afterwards proposed, in 1935, an implicit model (Eq. 6) of the effective thermal conductivity which can analyse the interactions between randomly distributed particles.

$$\left[\left(\frac{K_{np}- K_{nf}}{K_{np}+2K_{nf}}\right) \cdot \int_V + (1 - \int_V)\left(\frac{K_{bf}-2K_{nf}}{K_{bf}+2K_{nf}}\right)\right] = 0 \quad (6)$$

Bruggeman model can be applied to suspensions fabricated from particles of spherical shape at any concentration, where for low vol%, Eq. 6 gave almost the same results as Eq. 5.
Eq. 5 was modified several times in an attempt to improve the accuracy of the predicted results by taking into consideration different effects such as: the Brownian motion, surface charge, liquid – particle interface layer, particle clustering, and ballistic phonon transport. However, factors such as: convection induced by electrophoresis, particle driven natural convection, thermophoresis, and others are still not considered but needs to be encountered for better estimation of the effective thermal conductivity. Examples of some of the developed correlations with their remarks can be seen in Table 2.6 and additional models can be found at the following published literatures [222,225-243].

Table 2.6. Examples of different effective thermal conductivity correlations available in literatures.

Researchers	Model	Remarks
Hamilton and Crosser [244]	$\left[\frac{K_{nf}}{K_{bf}}\right] = \left[\frac{K_{np} + (n-1)\,.\,K_{bf} - (n-1).\left(K_{bf} - K_{np}\right).\mathrm{f_V}}{K_{np} + (n-1).K_{bf} + \mathrm{f_V}\,.\left(K_{bf} - K_{np}\right)}\right]$	Modified Maxwell model that determine the effective thermal conductivity of nonspherical particles using a shape factor (n), where n = 3/ψ and ψ = 0.5 (cylindrical particles) or ψ = 1.0 (spherical particles). The model is shown to take into account the particle shape, particle distribution, particle shell structure, high volume fraction, and interface contact resistance. At $\mathrm{f_V} < 0.3$ and $K_{np} > K_{bf}$ by a factor of 100, the model has shown good agreement with the experimental data.
Wasp et al. [245]	$\left[\frac{K_{nf}}{K_{bf}}\right] = \left[\frac{K_{np} + 2K_{bf} - 2\mathrm{f_V}\,.\left(K_{bf} - K_{np}\right)}{K_{np} + 2K_{bf} + \mathrm{f_V}\,.\left(K_{bf} - K_{np}\right)}\right]$	Spherical case of the Hamilton and Crosser model (i.e. ψ = 1.0) with the interfacial layer thickness results having a higher thermal conductivity than the basefluid and a larger effective volume concentration of the particle – liquid layered structure which tends to improve the thermal conductivity prediction.
Yu and Choi [246]	$\left[\frac{K_{nf}}{K_{bf}}\right] = \left[\frac{K_{np} + 2K_{bf} + 2\mathrm{f_V}\,.\left(K_{np} - K_{bf}\right).(1+\beta)^3}{K_{np} + 2K_{bf} - \mathrm{f_V}\,.\left(K_{np} - K_{bf}\right).(1+\beta)^3}\right]$	Another modified Maxwell model where all volume fraction, and the combination of nanolayer and nanoparticles thermal conductivity are taken into account. The thermal conductivity of the nanolayer (K_{layer}), needs to be less than $10K_{bf}$ to obtain a good prediction. The β used in the equation represent the ratio of the nanolayer thickness to the nanoparticle diameter,
Xuan et al. [247]	$\left[\frac{K_{nf}}{K_{bf}}\right] = \left[\frac{K_{np} + 2K_{bf} + 2\mathrm{f_V}\,.\left(K_{np} - K_{bf}\right)}{K_{np} + 2K_{bf} - 2\mathrm{f_V}\,.\left(K_{np} - K_{bf}\right)}\right] + \frac{\mathrm{f_V}}{2K_{bf}}\,\rho_{np}C_{pnp}\sqrt{\frac{TK_B}{3\pi\mu_{bf}r_c}}$	Modified Maxwell model that takes into consideration the Brownian motion effect and the aggregation structure of nanoparticles clusters. The model was found to yield incorrect units in the Brownian motion as described by different researchers [58,248] . The temperature of the fluid, density of the nanoparticles, specific heat of the nanoparticles, Boltzmann constant, viscosity of the basefluid, and the mean radius of the cluster are represented as T, ρ_{np}, C_{pnp}, K_B, μ_{bf}, and r_c, respectively in the model.

Researchers	Model	Remarks
Koo and Kleinstreuer [249]	$\left[\frac{K_{nf}}{K_{bf}}\right] = \left[\frac{K_{np} + 2K_{bf} + 2\mathrm{f_V} \cdot (K_{np} - K_{bf})}{K_{np} + 2K_{bf} - 2\mathrm{f_V} \cdot (K_{np} - K_{bf})}\right] + \frac{(5 \times 10^4)\mathrm{f_V}}{K_{bf}} \theta \rho_{bf} C_{pbf} f(T, \mathrm{f_V}) \sqrt{\frac{TK_B}{\rho_{np} d_{np}}}$	This model considers the kinetic energy of the nanoparticles that is produced from the Brownian movement in addition to the effects of particle vol%, particle size, basefluid properties, and temperature dependence. The thermal conductivity due to both Brownian motion ($K_{Brownian}$) and static dilute dispersion (K_{static}) where combined ($K_{nf} = K_{Brownian} + K_{static}$). The diameter of the nanoparticle, density of the basefluid, specific heat of the basefluid, hydrodynamic interaction between particles affected fluid, and augmented temperature dependence via particle interactions are shown as d_{np}, ρ_{bf}, C_{pbf}, θ, and f, respectively. Using experimental data of Das et al. [250] for CuO nanofluids, an empirical equation was established as $f(T, \mathrm{f_V}) = (-6.04\mathrm{f_V} + 0.4705)T + (1722.3\mathrm{f_V} - 134.63)$. The $f(T, \mathrm{f_V})$ equation is valid in the range of 27°C < T < 52°C and 0.01 < $\mathrm{f_V}$ < 0.04.
Xue and Xu [251]	$\left(1 - \frac{\mathrm{f_V}}{\alpha}\right)\left[\frac{K_{nf} - K_{bf}}{2K_{nf} + K_{bf}}\right] + \frac{\mathrm{f_V}}{\alpha}\left[\frac{(K_{nf} - K_i)(2K_i + K_{np}) - \alpha(K_{np} - K_i)(2K_i + K_{nf})}{(2K_{nf} - K_i)(2K_i + K_{np}) + 2\alpha(K_{np} - K_i)(K_i - K_{nf})}\right] = 0$	An implicit model that assumes the existing of nanoparticles shells which covers the solid particle and interact with the surrounding basefluid. The model was developed based on the data of effective thermal conductivity of CuO/H2O and CuO/EG, where $\alpha = \left[\frac{d_{np}}{d_{np} + 2t_1}\right]$, and both K_i and t_1 represent the thermal conductivity and thickness of the interfacial shell, respectively.
Prasher et al. [252]	$\left[\frac{K_{nf}}{K_{bf}}\right] = \left(1 + 4 \times 10^4 \mathrm{f_V} Re_B^m Pr_{bf}^{0.33}\right) + \left(\frac{\left[K_{np}(1 + 2\alpha_B) + 2K_m\right] + 2\mathrm{f_V}\left[K_{np}(1 - \alpha_B) - K_m\right]}{\left[K_{np}(1 + 2\alpha_B) + 2K_m\right] - \mathrm{f_V}\left[K_{np}(1 - \alpha_B) - K_m\right]}\right)$	This model uses the effect of Brownian motion as a correction factor to the Maxwell correlation to predict the enhancement in thermal conductivity caused from the nanoparticles local convection mechanism. Where the $Re_B = \frac{1}{\vartheta}\sqrt{\frac{18TK_B}{\pi \rho_{np} d_{np}}}$ is the Brownian – Reynolds number, $K_m = K_{bf}(1 + 0.25 Re_B Pr)$

Researchers	Model	Remarks
Jang and Choi [253]	$\left[\frac{K_{nf}}{K_{bf}}\right] = (1 - \mathrm{f_V}) + \beta \mathrm{f_V} \frac{K_{np}}{K_{bf}} + (18 \times 10^6) \frac{d_{bf}}{d_{np}} Re_{d_{nano}}^2 \mathrm{f_V} Pr_{bf}$	is the matrix conductivity, $\alpha_B = \frac{2R_b K_m}{d_{np}}$ is the nanoparticle Biot number, R_b is the interfacial thermal resistance between nanoparticle and the surrounding fluid, Pr is the Prandtl number, and m = 2.5% ± 15% for H_2O based nanofluid. This model takes into account the relation between the kinetic theory and Nusselt number for flow past a sphere. The symbol β in the equation is a constant associated to the Kapitza resistance (0.01) per unit area, $Re_{d_{nano}} = \frac{d_{np} C_{RM}}{\vartheta}$, and $C_{RM} = \frac{TK_B}{3\pi\mu_b d_{np} l_{bf}}$. For water at 27°C, $d_{bf} = 0.384$ nm and $l_{bf} = 0.738$ nm.

Experimental measurements of nanofluids effective thermal conductivity were performed by several researchers using transient hot-wire method (low cost and easy to use, where the measurements are based on the Fourier's law and the effective thermal conductivity reported to be of 5% uncertainty) [254-256], 3ω method (uses frequency dependence of temperature oscillation to measure the thermal conductivity) [99,257,258], temperature oscillation method (based on the oscillation method and requires the measurement of the temperature response of the sample) [250,259], thermal constants analyser (easy to perform, very fast, and can measure thermal conductivity in the range of 0.02 – 200 W/m.K) [260], steady-state parallel-plate technique (uses the one – dimensional heat conduction equation in its calculation), micro-hot strip method (significantly low measurement time and much accurate than the hot-wire method), and optical beam deflection technique (self-built device which requires long measurement time and can only predict the thermal conductivity at ~ 100 vol% accurately) [53,261,262]. Among all the aforementioned techniques, the thermal constant analyser has been the most favourable method used by many researchers.

5.4 Thermal Diffusivity

Very few published papers have considered the effective thermal diffusivity of nanofluids (α_{nf}) [14], which can be theoretically calculated using Eq. 7.

$$\alpha_{nf} = \frac{K_{nf}}{\rho_{nf} \cdot C_{p_{nf}}} \tag{7}$$

Experimental measurement of the effective thermal diffusivity can be achieved using the transient hot disk system, which is a robust and rapid thermal characterisation system [263], Laser Flash method [264], a temperature controlled photoacoustic device developed by Agresti et al. [265], thermal-wave cavity technique, hot-wire method, and temperature oscillation method [266-268]. The thermal lens method is a sensitive technique used to measure the absolute thermal diffusivity value of liquids. This method is favourable due to its ultra-high sensitivity, small volume of sample requirement, and its dependence on solvent thermos-optical properties [269,270]. Murshed et al. [271] reported the enhancement in effective thermal diffusivity of nanofluids experimentally and found that they exceeded those calculated by Eq. 7. It should be pointed out that they used measured values in calculating the effective thermal diffusivity. Zhang et al. [272] have reported a 5% error in the effective thermal diffusivity measurement using the hot-wire technique. Agresti et al. [265] pointed in his article

that measuring techniques such as the laser flash and hot disk methods are more suitable for solids and powders, and that the implementation of these two techniques are very complicated in comparison to the photoacustic approach. To the best of our knowledge and from reviewing many literature, there exist only one effective thermal diffusivity theoretical model (Eq. 7), which is currently been used. This gap of knowledge needs to be encountered for in order to gain better prediction of the theoretical values with the experimental results.

5.5 Effective Viscosity

Nanofluid viscosity is a measure of the tendency of the suspension to resist the flow. It can also be defined as the ratio of the shear stress to the shear rate. The benefit associated with nanofluids heat enhancement is counteracted by the rise in effective viscosity caused from the added nanoparticles in the basefluid. This increase in viscosity leads to higher pressure losses, and hence elevates the pumping power demands. The main parameters that influences the effective viscosity are the basefluid viscosity, nanoparticles concentration, particle shape, particle diameter, particles type, temperature, pressure, pH value, and shear rate [14]. Phenomenological hydrodynamic equations were the first attempts used, by Einstein, to calculate the effective viscosity of suspensions of spherical solids [273,274]. Driven from the basefluid viscosity (μ_{bf}) and the f_V, the Einstein effective viscosity (μ_{nf}) equation is given as:

$$\mu_{nf} = \mu_{bf} . (1 + 2.5 f_V) \quad (8)$$

The viscosity of μ_{nf} is always greater than μ_{bf} and depends only on the f_V of the particles dispersed. Comparison between Eq. 8 and experimental data has shown that the equation can be used to predict the effective viscosity of nanofluids with vol% $\leq 10^{-2}$. At a particle concentration of 10 – 15 vol%, the interaction between the particles becomes more influential. For such reason, Eq. 8 had been modified continuously in an attempt to develop a much accurate effective viscosity correlation. The effective viscosity was also modified to represent a linear relation [275] as seen in Eq. 9, where α is a coefficient that varies, based on the nanofluid, from 4.3 to 22.

$$\mu_{nf} = \mu_{bf} . (1 + \alpha f_V) \quad (9)$$

The results of Eq. 9 where found to be several times higher than the ones predicted by Eq. 8. Many other correlations where then developed to determine the effective viscosity of nanofluids, which can be found published [276,277]. Unlike the effective density and the effective specific heat correlations, which are widely accepted by researchers, effective viscosity is considered to be one of the intensely discussed field of research [36]. This is because several parameters affect the nanofluid effective viscosity such as particle size, particle shape, particle concentration, basefluid type, nanofluid temperature, … etc. The effect of the particle size was first found by molecular dynamic simulation [278]. It was discovered that nanofluids, of particle size 1 – 2 nm, had a reduction in its effective viscosity with the increase in nanoparticle size, which was also confirmed experimentally by Namburu et al. [279].

Up-to-today, The Einstein equation can be assumed to be the only available universal correlation that can predict the effective viscosity of nanofluids of low concentration [275]. In addition, the best available model, based on a committee machine intelligent system (CMIS), is the one developed by Hemmati-Sarapardeh et al. [277], which had approximately 4% relative error. Instruments used to determine the effective viscosity of nanofluids are capillary viscometer, piston type rheometer, and rotational rheometer.

6. Challenges of Nanofluids and Future Direction

Nanofluids have shown to be superior, as a HTF, to conventional known fluids available in the market. In order to commercialise such type of advanced fluids, some factors are required to be improved and better understood by researchers. Examples of these factors are listed below [14,35,36,44,63,205]:

- Experimental investigations of nanofluids needs to be optimised with respect to stability, preparation technique, temperature, particle size, particle shape, and particles type.
- Finding the right ratio of nanoparticles to basefluid to obtain the highest effective thermal conductivity as well as the lowest possible effective viscosity from the fabricated nanofluid. This is important to meet the applications of heat transfer and overcome the pressure drop in the system.
- Additional research inputs are needed to develop much precise correlations, which can predict the changes in nanofluids pH value caused by temperature, particle

concentration, type of basefluid, … etc, since it affects the stability and thermophysical properties of nanofluids.

- Several studies have considered the fouling effect of nanofluids in a thermal aspect but, to the best of our knowledge, have ignored its influence on the dynamics of the fluid. Although, if fully deposited on the inner pipe surface, it can provide similar wettability properties as nanocoating's.

The aforementioned challenges need to be focused on and tackled by researches so that commercialisation of nanofluids can be possible.

7. Conclusion

The types of nanofluids, preparation approaches, fluid stability, and stability enhancement has been reviewed. The article also extends to the thermophysical properties of nanofluids, covering both the theoretical and experimental aspects. According to literature, several studies have discussed the potential of enhancing heat transfer using nanofluids, and how the stability of a nanofluid affects its thermophysical properties. It was also pointed out, that the stability of a nanofluid gets effected by a range of factors, such as preparation technique, pH value, nanoparticle concentration, particles type, particle shape, particle size, and fluid temperature.

To the best of our knowledge, in all the literature related to using nanofluids, it has not been reported any existing work related to controlling the temperature of the fluid while fabricating the nanofluid using an ultrasonicator. This preparation approach is very important as it can result in a completely different pH values, settling behavior, particles agglomeration, and thermophysical properties. Additionally, using an ultrasonic device, for fabricating nanofluids, will increase the temperature of the fluid gradually; but is strongly affected by the ambient temperature where the sample is prepared. Meaning that various locations or different weather conditions will most likely result in producing a diverse nanofluid.

In addition, one can conclude from the literature that the major drawback of using such type of fluids is the rise in pressure losses in piping systems caused from the increase in viscosity of nanofluids. This increase in viscosity leads to a higher shear stress between the fluid and the surrounding surface. Moreover, the nanoparticles hosted by the fluid are most likely to deposit on the inner surface of the pipe when used in elevated temperature applications, causing what is known as the fouling effect. The deposited layer or foul would act similarly as inner pipe

coating with nanoparticles (i.e. nanocoating) since the foul is formed from nanoparticles that were hosted by the carrier fluid itself. It was reported, by a number of authors, that nanocoating has the advantage of reducing the surface roughness which strongly influences the shear stress between the surface and the fluid [280]. Therefore, examining the wettability effect of nanoparticles of similar material type to the inner pipes can be very promising in encountering the pressure losses problem, while maintaining the thermal performance of the system.

References

1. Coco-Enríquez, L.; Muñoz-Antón, J.; Martínez-Val, J.M. New text comparison between co 2 and other supercritical working fluids (ethane, xe, ch 4 and n 2) in line-focusing solar power plants coupled to supercritical brayton power cycles. *Int J Hydrogen Energy* **2017**, *42*, 17611-17631.

2. Memon, A.G.; Memon, R.A. Thermodynamic analysis of a trigeneration system proposed for residential application. *Energy Conversion and Management* **2017**, *145*, 182-203.

3. Yue, C.; Han, D.; Pu, W.H.; He, W.F. Parametric analysis of a vehicle power and cooling/heating cogeneration system. *Energy* **2016**, *115*, 800-810.

4. Uebel, K.; Rossger, P.; Prufert, U.; Richter, A.; Meyer, B. A new co conversion quench reactor design. *Fuel Process Technol* **2016**, *148*, 198-208.

5. Choi, S.U.S.; Eastman, J.A. *Enhancing thermal conductivity of fluids with nanoparticles.* ; Argonne National Lab., IL (United States): 1995; p Medium: ED; Size: 8 p.

6. Hashemian, M.; Jafarmadar, S.; Nasiri, J.; Dizaji, H.S. Enhancement of heat transfer rate with structural modification of double pipe heat exchanger by changing cylindrical form of tubes into conical form. *Appl Therm Eng* **2017**, *118*, 408-417.

7. Maxwell, J.C. *A treatise on electricity and magnetism*. 2 ed.; Clarendon Press: 1881; Vol. 1.

8. Choi, S.U.S.; Cho, Y.I.; Kasza, K.E. Degradation effects of dilute polymer-solutions on turbulent friction and heat-transfer behavior. *J. Non-Newton. Fluid Mech.* **1992**, *41*, 289-307.

9. Choi, U.; France, D.M.; Knodel, B.D. *Impact of advanced fluids on costs of district cooling systems*; Argonne National Lab., IL (United States): 1992.

10. Choi, U.; Tran, T. Experimental studies of the effects of non-newtonian surfactant solutions on the performance of a shell-and-tube heat exchanger. In *Recent developments in non-newtonian flows and industrial applications*, The American Society of Mechanical Engineers New York, FED: 1991; Vol. 124, pp 47-52.

11. Liu, K.; Choi, U.; Kasza, K.E. *Measurements of pressure drop and heat transfer in turbulent pipe flows of particulate slurries*; Argonne National Lab., IL (USA): 1988.

12. Xuan, Y.; Li, Q. Heat transfer enhancement of nanofluids. *International Journal of Heat and Fluid Flow* **2000**, *21*, 58-64.

13. Wen, D.S.; Lin, G.P.; Vafaei, S.; Zhang, K. Review of nanofluids for heat transfer applications. *Particuology* **2009**, *7*, 141-150.

14. Eggers, J.R.; Kabelac, S. Nanofluids revisited. *Appl Therm Eng* **2016**, *106*, 1114-1126.

15. Suganthi, K.S.; Rajan, K.S. Metal oxide nanofluids: Review of formulation, thermo-physical properties, mechanisms, and heat transfer performance. *Renewable & Sustainable Energy Reviews* **2017**, *76*, 226-255.

16. Sarafraz, M.M.; Nikkhah, V.; Nakhjavani, M.; Arya, A. Fouling formation and thermal performance of aqueous carbon nanotube nanofluid in a heat sink with rectangular parallel microchannel. *Appl Therm Eng* **2017**, *123*, 29-39.

17. Sarafraz, M.M.; Hormozi, F.; Peyghambarzadeh, S.M. Role of nanofluid fouling on thermal performance of a thermosyphon: Are nanofluids reliable working fluid? *Appl Therm Eng* **2015**, *82*, 212-224.

18. Sarafraz, M.M.; Hormozi, F. Convective boiling and particulate fouling of stabilized cuo-ethylene glycol nanofluids inside the annular heat exchanger. *Int. Commun. Heat Mass Transf.* **2014**, *53*, 116-123.

19. Nikkhah, V.; Sarafraz, M.M.; Hormozi, F.; Peyghambarzadeh, S.M. Particulate fouling of cuo–water nanofluid at isothermal diffusive condition inside the conventional heat exchanger-experimental and modeling. *Exp. Therm. Fluid Sci.* **2015**, *60*, 83-95.

20. Sarafraz, M.M.; Nikkhah, V.; Madani, S.A.; Jafarian, M.; Hormozi, F. Low-frequency vibration for fouling mitigation and intensification of thermal performance of a plate heat exchanger working with cuo/water nanofluid. *Appl Therm Eng* **2017**, *121*, 388-399.

21. Teng, K.H.; Amiri, A.; Kazi, S.N.; Bakar, M.A.; Chew, B.T.; Al-Shamma'a, A.; Shaw, A. Retardation of heat exchanger surfaces mineral fouling by water-based diethylenetriamine pentaacetate-treated cnt nanofluids. *Appl Therm Eng* **2017**, *110*, 495-503.

22. Kouloulias, K.; Sergis, A.; Hardalupas, Y. Sedimentation in nanofluids during a natural convection experiment. *Int. J. Heat Mass Transf.* **2016**, *101*, 1193-1203.

23. Ali, N.; Teixeira, J.A.; Addali, A.; Al-Zubi, F.; Shaban, E.; Behbehani, I. The effect of aluminium nanocoating and water ph value on the wettability behavior of an aluminium surface. *Applied Surface Science* **2018**, *443*, 24-30.

24. Kang, M.; Lee, J.W.; Kang, Y.T. Reduction of liquid pumping power by nanoscale surface coating. *International Journal of Refrigeration-Revue Internationale Du Froid* **2016**, *71*, 8-17.

25. Ganesan, P.; Vanaki, S.M.; Thoo, K.K.; Chin, W.M. Air-side heat transfer characteristics of hydrophobic and super-hydrophobic fin surfaces in heat exchangers: A review. *Int. Commun. Heat Mass Transf.* **2016**, *74*, 27-35.

26. Phan, H.T.; Caney, N.; Marty, P.; Colasson, S.; Gavillet, J. Surface wettability control by nanocoating: The effects on pool boiling heat transfer and nucleation mechanism. *Int. J. Heat Mass Transf.* **2009**, *52*, 5459-5471.

27. Burnett, M.E.; Wang, S.Q. Current sunscreen controversies: A critical review. *Photodermatol Photoimmunol Photomed* **2011**, *27*, 58-67.

28. Lapotko, D. Corrigendum. *Nanomedicine (Lond)* **2016**, *11*, 566.

29. Maier-Hauff, K.; Rothe, R.; Scholz, R.; Gneveckow, U.; Wust, P.; Thiesen, B.; Feussner, A.; von Deimling, A.; Waldoefner, N.; Felix, R., *et al.* Intracranial thermotherapy using magnetic nanoparticles combined with external beam radiotherapy: Results of a feasibility study on patients with glioblastoma multiforme. *J Neurooncol* **2007**, *81*, 53-60.

30. Kulkarni, D.P.; Das, D.K.; Vajjha, R.S. Application of nanofluids in heating buildings and reducing pollution. *Appl. Energy* **2009**, *86*, 2566-2573.

31. Vekas, L.; Bica, D.; Avdeev, M.V. Magnetic nanoparticles and concentrated magnetic nanofluids: Synthesis, properties and some applications. *China Particuology* **2007**, *5*, 43-49.

32. Sharma, T.; Reddy, A.L.M.; Chandra, T.S.; Ramaprabhu, S. Development of carbon nanotubes and nanofluids based microbial fuel cell. *Int J Hydrogen Energy* **2008**, *33*, 6749-6754.

33. Taylor, R.; Coulombe, S.; Otanicar, T.; Phelan, P.; Gunawan, A.; Lv, W.; Rosengarten, G.; Prasher, R.; Tyagi, H. Small particles, big impacts: A review of the diverse applications of nanofluids. *J. Appl. Phys.* **2013**, *113*.

34. Scopus-Database. Nanofluids analyze search results from 2015 to 2018. https://www.scopus.com/term/analyzer.uri?sid=15ed1428e49c63d726c572eb1400c1e1&origin=resultslist&src=s&s=TITLE-ABS-KEY%28nanofluids%29&sort=plf-f&sdt=b&sot=b&sl=25&count=9862&analyzeResults=Analyze+results&txGid=c899ff1cd6b4f5e63c42b0db4fed8fb8 (6th of March),

35. Gupta, N.K.; Tiwari, A.K.; Ghosh, S.K. Heat transfer mechanisms in heat pipes using nanofluids – a review. *Exp. Therm. Fluid Sci.* **2018**, *90*, 84-100.

36. Gupta, M.; Singh, V.; Kumar, R.; Said, Z. A review on thermophysical properties of nanofluids and heat transfer applications. *Renewable & Sustainable Energy Reviews* **2017**, *74*, 638-670.

37. Sundar, L.S.; Sharma, K.V.; Singh, M.K.; Sousa, A.C.M. Hybrid nanofluids preparation, thermal properties, heat transfer and friction factor – a review. *Renewable Sustainable Energy Rev* **2017**, *68*, 185-198.

38. Modak, M.; Chougule, S.S.; Sahu, S.K. An experimental investigation on heat transfer characteristics of hot surface by using cuo-water nanofluids in circular jet impingement cooling. *Journal of Heat Transfer-Transactions of the Asme* **2018**, *140*.

39. Yang, L.; Du, K. A comprehensive review on heat transfer characteristics of tio2 nanofluids. *Int. J. Heat Mass Transf.* **2017**, *108*, 11-31.

40. Azmi, W.H.; Sharif, M.Z.; Yusof, T.M.; Mamat, R.; Redhwan, A.A.M. Potential of nanorefrigerant and nanolubricant on energy saving in refrigeration system – a review. *Renewable Sustainable Energy Rev* **2017**, *69*, 415-428.

41. Reddy, K.S.; Kamnapure, N.R.; Srivastava, S. Nanofluid and nanocomposite applications in solar energy conversion systems for performance enhancement: A review. *Int. J. Low Carbon Technol.* **2017**, *12*, 1-23.

42. Tawfik, M.M. Experimental studies of nanofluid thermal conductivity enhancement and applications: A review. *Renewable Sustainable Energy Rev* **2017**, *75*, 1239-1253.

43. Jana, S.; Salehi-Khojin, A.; Zhong, W.H. Enhancement of fluid thermal conductivity by the addition of single and hybrid nano-additives. *Thermochim Acta* **2007**, *462*, 45-55.

44. Chamsa-Ard, W.; Brundavanam, S.; Fung, C.C.; Fawcett, D.; Poinern, G. Nanofluid types, their synthesis, properties and incorporation in direct solar thermal collectors: A review. *Nanomaterials (Basel)* **2017**, *7*.

45. Akoh, H.; Tsukasaki, Y.; Yatsuya, S.; Tasaki, A. Magnetic-properties of ferromagnetic ultrafine particles prepared by vacuum evaporation on running oil substrate. *J. Cryst. Growth* **1978**, *45*, 495-500.

46. Wagener, M.; Murty, B.S.; Guenther, B. In *Preparation of metal nanosuspensions by high-pressure dc-sputtering on running liquids*, Proceedings of the 1996 MRS Fall Symposium, Pittsburgh, PA, United States

Boston, MA, USA, 1997; George, E.P.; Gotthardt, R.; Otsuka, K.; Trolier-McKinstry, S.; Wun-Fogle, M., Eds. Materials Research Society: Pittsburgh, PA, United States

Boston, MA, USA, pp 149-154.

47. Eastman, J.A.; Choi, U.S.; Li, S.; Thompson, L.J.; Lee, S. In *Enhanced thermal conductivity through the development of nanofluids*, Proceedings of the 1996 MRS Fall Symposium, Pittsburgh, PA, United States

Boston, MA, USA, 1997; George, E.P.; Gotthardt, R.; Otsuka, K.; Trolier-McKinstry, S.; Wun-Fogle, M., Eds. Materials Research Society: Pittsburgh, PA, United States

Boston, MA, USA, pp 3-11.

48. Zhu, H.T.; Lin, Y.S.; Yin, Y.S. A novel one-step chemical method for preparation of copper nanofluids. *J Colloid Interface Sci* **2004**, *277*, 100-103.

49. Tran, P.X.; Soong, Y. In *Preparation of nanofluids using laser ablation in liquid technique*, United States, 2007-06-01, 2007; Not published - presentation only: United States, Sponsor Org.: USDOE - Office of Fossil Energy (FE).

50. Lo, C.H.; Tsung, T.T.; Chen, L.C. Shape-controlled synthesis of cu-based nanofluid using submerged arc nanoparticle synthesis system (sanss). *J. Cryst. Growth* **2005**, *277*, 636-642.

51. Lo, C.H.; Tsung, T.T.; Chen, L.C. Ni nano-magnetic fluid prepared by submerged arc nano synthesis system (sanss). *Jsme International Journal Series B-Fluids and Thermal Engineering* **2005**, *48*, 750-755.

52. Kong, L.H.; Sun, J.L.; Bao, Y.Y. Preparation, characterization and tribological mechanism of nanofluids. *RSC Adv.* **2017**, *7*, 12599-12609.

53. Wang, X.W.; Xu, X.F.; Choi, S.U.S. Thermal conductivity of nanoparticle-fluid mixture. *J Thermophys Heat Transfer* **1999**, *13*, 474-480.

54. Lee, S.; Choi, S.U.S.; Li, S.; Eastman, J.A. Measuring thermal conductivity of fluids containing oxide nanoparticles. *Journal of Heat Transfer-Transactions of the Asme* **1999**, *121*, 280-289.

55. Murshed, S.M.S.; Leong, K.C.; Yang, C. Enhanced thermal conductivity of tio2 - water based nanofluids. *Int. J. Therm. Sci.* **2005**, *44*, 367-373.

56. Xuan, Y.M.; Li, Q. Heat transfer enhancement of nanofluids. *International Journal of Heat and Fluid Flow* **2000**, *21*, 58-64.

57. Yu, Q.S.; Kim, Y.J.; Ma, H.B. Nanofluids with plasma treated diamond nanoparticles. *Appl. Phys. Lett.* **2008**, *92*.

58. Keblinski, P.; Eastman, J.A.; Cahill, D.G. Nanofluids for thermal transport. *Materials Today* **2005**, *8*, 36-44.

59. Liu, M.S.; Lin, M.C.C.; Huang, I.T.; Wang, C.C. Enhancement of thermal conductivity with carbon nanotube for nanofluids. *Int. Commun. Heat Mass Transf.* **2005**, *32*, 1202-1210.

60. Boncel, S.; Zniszczoł, A.; Pawlyta, M.; Labisz, K.; Dzido, G. Heat transfer nanofluid based on curly ultra-long multi-wall carbon nanotubes. *Heat and Mass Transfer* **2017**, *54*, 333-339.

61. Arya, A.; Sarafraz, M.M.; Shahmiri, S.; Madani, S.A.H.; Nikkhah, V.; Nakhjavani, S.M. Thermal performance analysis of a flat heat pipe working with carbon nanotube-water nanofluid for cooling of a high heat flux heater. *Heat and Mass Transfer* **2017**, 1-13.

62. Eastman, J.A.; Choi, S.U.S.; Li, S.; Yu, W.; Thompson, L.J. Anomalously increased effective thermal conductivities of ethylene glycol-based nanofluids containing copper nanoparticles. *Appl. Phys. Lett.* **2001**, *78*, 718-720.

63. Dey, D.; Kumar, P.; Samantaray, S. A review of nanofluid preparation, stability, and thermo-physical properties. *Heat Transfer-Asian Research* **2017**, *46*, 1413-1442.

64. Bushehri, M.K.; Mohebbi, A.; Rafsanjani, H.H. Prediction of thermal conductivity and viscosity of nanofluids by molecular dynamics simulation. *J. Eng. Thermophys.* **2016**, *25*, 389-400.

65. Hong, J.; Kim, D. Effects of aggregation on the thermal conductivity of alumina/water nanofluids. *Thermochim Acta* **2012**, *542*, 28-32.

66. Arthur, O.; Karim, M.A. An investigation into the thermophysical and rheological properties of nanofluids for solar thermal applications. *Renewable & Sustainable Energy Reviews* **2016**, *55*, 739-755.

67. Yu, W.; Xie, H.Q. A review on nanofluids: Preparation, stability mechanisms, and applications. *J. Nanomater.* **2012**, *2012*.

68. Setia, H.; Gupta, R.; Wanchoo, R.K. Stability of nanofluids. In *Materials Science Forum*, Trans Tech Publications Ltd: 2013; Vol. 757, pp 139-149.

69. Wu, J.M.; Zhao, J.Y. A review of nanofluid heat transfer and critical heat flux enhancement-research gap to engineering application. *Prog. Nucl. Energy* **2013**, *66*, 13-24.

70. Ghadimi, A.; Saidur, R.; Metselaar, H.S.C. A review of nanofluid stability properties and characterization in stationary conditions. *Int. J. Heat Mass Transf.* **2011**, *54*, 4051-4068.

71. Mukherjee, S.; Paria, S. Preparation and stability of nanofluids-a review. *IOSR Journal of Mechanical and civil engineering* **2013**, *9*, 63-69.

72. Chang, H.; Jwo, C.S.; Fan, P.S.; Pai, S.H. Process optimization and material properties for nanofluid manufacturing. *Int J Adv Manuf Technol* **2007**, *34*, 300-306.

73. Kim, H.J.; Bang, I.C.; Onoe, J. Characteristic stability of bare au-water nanofluids fabricated by pulsed laser ablation in liquids. *Opt Lasers Eng* **2009**, *47*, 532-538.

74. Wang, X.J.; Zhu, D.S.; Yang, S. Investigation of ph and sdbs on enhancement of thermal conductivity in nanofluids. *Chem. Phys. Lett.* **2009**, *470*, 107-111.

75. Mondragon, R.; Julia, J.E.; Barba, A.; Jarque, J.C. Characterization of silica–water nanofluids dispersed with an ultrasound probe: A study of their physical properties and stability. *Powder Technol.* **2012**, *224*, 138-146.

76. Chang, M.H.; Liu, H.S.; Tai, C.Y. Preparation of copper oxide nanoparticles and its application in nanofluid. *Powder Technol.* **2011**, *207*, 378-386.

77. Wen, D.S.; Ding, Y.L. Formulation of nanofluids for natural convective heat transfer applications. *International Journal of Heat and Fluid Flow* **2005**, *26*, 855-864.

78. Pastoriza-Gallego, M.J.; Casanova, C.; Páramo, R.; Barbés, B.; Legido, J.L.; Piñeiro, M.M. A study on stability and thermophysical properties (density and viscosity) of al2o3 in water nanofluid. *J. Appl. Phys.* **2009**, *106*.

79. Chen, L.F.; Xie, H.Q. Properties of carbon nanotube nanofluids stabilized by cationic gemini surfactant. *Thermochim Acta* **2010**, *506*, 62-66.

80. Wei, X.H.; Wang, L.Q. Synthesis and thermal conductivity of microfluidic copper nanofluids. *Particuology* **2010**, *8*, 262-271.

81. Li, X.; Zhu, D.; Wang, X. Evaluation on dispersion behavior of the aqueous copper nano-suspensions. *J Colloid Interface Sci* **2007**, *310*, 456-463.

82. Wei, X.H.; Zhu, H.T.; Kong, T.T.; Wang, L.Q. Synthesis and thermal conductivity of cu2o nanofluids. *Int. J. Heat Mass Transf.* **2009**, *52*, 4371-4374.

83. Ilyas, S.U.; Pendyala, R.; Marneni, N. Preparation, sedimentation, and agglomeration of nanofluids. *Chemical Engineering & Technology* **2014**, *37*, 2011-2021.

84. Ilyas, S.U.; Pendyala, R.; Marneni, N. Settling characteristics of alumina nanoparticles in ethanol-water mixtures. In *2013 2nd International Conference on Advanced Materials Design and Mechanics, ICAMDM 2013*, Kuala Lumpur, 2013; Vol. 372, pp 143-148.

85. Wang, X.J.; Li, X.F. Influence of ph on nanofluids' viscosity and thermal conductivity. *Chinese Physics Letters* **2009**, *26*, 056601.

86. Angayarkanni, S.A.; Philip, J. Effect of nanoparticles aggregation on thermal and electrical conductivities of nanofluids. *Journal of Nanofluids* **2014**, *3*, 17-25.

87. Witharana, S.; Hodges, C.; Xu, D.; Lai, X.J.; Ding, Y.L. Aggregation and settling in aqueous polydisperse alumina nanoparticle suspensions. *J. Nanopart. Res.* **2012**, *14*.

88. Ilyas, S.U.; Pendyala, R.; Marneni, N. In *Stability and agglomeration of alumina nanoparticles in ethanol-water mixtures*, 4th International Conference on Process Engineering and Advanced Materials, ICPEAM 2016, 2016; Bustam, M.A.; Keong, L.K.; Man, Z.; Hassankiadeh, A.A.; Fong, Y.Y., Eds. Elsevier Ltd: pp 290-297.

89. Lemes, M.A.; Rabelo, D.; de Oliveira, A.E. A novel method to evaluate nanofluid stability using multivariate image analysis. *Anal. Methods* **2017**, *9*, 5826-5833.

90. Singh, A.K.; Raykar, V.S. Microwave synthesis of silver nanofluids with polyvinylpyrrolidone (pvp) and their transport properties. *Colloid and Polymer Science* **2008**, *286*, 1667-1673.

91. Li, D.; Kaner, R.B. Processable stabilizer-free polyaniline nanofiber aqueous colloids. *Chem Commun (Camb)* **2005**, 3286-3288.

92. Mehrali, M.; Sadeghinezhad, E.; Rosen, M.A.; Akhiani, A.R.; Latibari, S.T.; Mehrali, M.; Metselaar, H.S.C. Heat transfer and entropy generation for laminar forced convection flow of graphene nanoplatelets nanofluids in a horizontal tube. *Int. Commun. Heat Mass Transf.* **2015**, *66*, 23-31.

93. Jiang, L.; Gao, L.; Sun, J. Production of aqueous colloidal dispersions of carbon nanotubes. *J Colloid Interface Sci* **2003**, *260*, 89-94.

94. Hwang, Y.; Lee, J.K.; Lee, C.H.; Jung, Y.M.; Cheong, S.I.; Lee, C.G.; Ku, B.C.; Jang, S.P. Stability and thermal conductivity characteristics of nanofluids. *Thermochim Acta* **2007**, *455*, 70-74.

95. Souza, D.G.; Bellaver, B.; Raupp, G.S.; Souza, D.O.; Quincozes-Santos, A. Astrocytes from adult wistar rats aged in vitro show changes in glial functions. *Neurochem Int* **2015**, *90*, 93-97.

96. Liu, Z.Q.; Ma, J.; Cui, Y.H. Carbon nanotube supported platinum catalysts for the ozonation of oxalic acid in aqueous solutions. *Carbon* **2008**, *46*, 890-897.

97. Chang, H.; Wu, Y.; Chen, X.; Kao, M. Fabrication of cu based nanofluid with superior dispersion. *National Taipei University of Technology Journal* **2000**, *5*, 201-208.

98. Sato, M.; Abe, Y.; Urita, Y.; Di Paola, R.; Cecere, A.; Savino, R. Thermal performance of self-rewetting fluid heat pipe containing dilute solutions of polymer-capped silver nanoparticles synthesized by microwave-polyol process. *International Journal of Transport Phenomena* **2011**, *12*, 339-345.

99. Oh, D.-W.; Jain, A.; Eaton, J.K.; Goodson, K.E.; Lee, J.S. Thermal conductivity measurement and sedimentation detection of aluminum oxide nanofluids by using the 3ω method. *International Journal of Heat and Fluid Flow* **2008**, *29*, 1456-1461.

100. Martínez, V.A.; Vasco, D.A.; García–Herrera, C.M. Transient measurement of the thermal conductivity as a tool for the evaluation of the stability of nanofluids subjected to a pressure treatment. *Int. Commun. Heat Mass Transf.* **2018**, *91*, 234-238.

101. Karthikeyan, N.R.; Philip, J.; Raj, B. Effect of clustering on the thermal conductivity of nanofluids. *Materials Chemistry and Physics* **2008**, *109*, 50-55.

102. Das, P.K.; Islam, N.; Santra, A.K.; Ganguly, R. Experimental investigation of thermophysical properties of al 2 o 3 –water nanofluid: Role of surfactants. *Journal of Molecular Liquids* **2017**, *237*, 304-312.

103. Kim, H.S.; Yilmaz, F.; Dharmaiah, P.; Lee, D.J.; Lee, T.H.; Hong, S.J. Characterization of cu and ni nano-fluids synthesized by pulsed wire evaporation method. *Archives of Metallurgy and Materials* **2017**, *62*, 999-1004.

104. Rubalya Valantina, S.; Arockia Jayalatha, K.; Phebee Angeline, D.R.; Uma, S.; Ashvanth, B. Synthesis and characterisation of electro-rheological property of novel eco-friendly rice bran oil and nanofluid. *Journal of Molecular Liquids* **2018**, *256*, 256-266.

105. Wu, D.X.; Zhu, H.T.; Wang, L.Q.; Liu, L.M. Critical issues in nanofluids preparation, characterization and thermal conductivity. *Curr. Nanosci.* **2009**, *5*, 103-112.

106. Nallusamy, S. Thermal conductivity analysis and characterization of copper oxide nanofluids through different techniques. *J. Nano. Res.* **2016**, *40*, 105-112.

107. Razi, P.; Akhavan-Behabadi, M.A.; Saeedinia, M. Pressure drop and thermal characteristics of cuo-base oil nanofluid laminar flow in flattened tubes under constant heat flux. *Int. Commun. Heat Mass Transf.* **2011**, *38*, 964-971.

108. Tiara, A.M.; Chakraborty, S.; Sarkar, I.; Ashok, A.; Pal, S.K.; Chakraborty, S. Heat transfer enhancement using surfactant based alumina nanofluid jet from a hot steel plate. *Exp. Therm. Fluid Sci.* **2017**, *89*, 295-303.

109. Pantzali, M.N.; Mouza, A.A.; Paras, S.V. Investigating the efficacy of nanofluids as coolants in plate heat exchangers (phe). *Chem. Eng. Sci.* **2009**, *64*, 3290-3300.

110. Chandrasekar, M.; Suresh, S.; Bose, A.C. Experimental investigations and theoretical determination of thermal conductivity and viscosity of al2o3/water nanofluid. *Exp. Therm. Fluid Sci.* **2010**, *34*, 210-216.

111. Hwang, Y.; Lee, J.K.; Lee, J.K.; Jeong, Y.M.; Cheong, S.I.; Ahn, Y.C.; Kim, S.H. Production and dispersion stability of nanoparticles in nanofluids. *Powder Technol.* **2008**, *186*, 145-153.

112. Yu, W.; Xie, H.Q.; Chen, L.F.; Li, Y. Enhancement of thermal conductivity of kerosene-based fe3o4 nanofluids prepared via phase-transfer method. *Colloids and Surfaces a-Physicochemical and Engineering Aspects* **2010**, *355*, 109-113.

113. Li, X.F.; Zhu, D.S.; Wang, X.J.; Wang, N.; Gao, J.W.; Li, H. Thermal conductivity enhancement dependent ph and chemical surfactant for cu-h2o nanofluids. *Thermochim Acta* **2008**, *469*, 98-103.

114. Madni, I.; Hwang, C.Y.; Park, S.D.; Choa, Y.H.; Kim, H.T. Mixed surfactant system for stable suspension of multiwalled carbon nanotubes. *Colloids and Surfaces a-Physicochemical and Engineering Aspects* **2010**, *358*, 101-107.

115. Chen, L.F.; Xie, H.Q.; Li, Y.; Yu, W. Nanofluids containing carbon nanotubes treated by mechanochemical reaction. *Thermochim Acta* **2008**, *477*, 21-24.

116. Mingzheng, Z.; Guodong, X.; Jian, L.; Lei, C.; Lijun, Z. Analysis of factors influencing thermal conductivity and viscosity in different kinds of surfactant solutions. *Exp. Therm. Fluid Sci.* **2012**, *36*, 22-29.

117. Timofeeva, E.V.; Moravek, M.R.; Singh, D. Improving the heat transfer efficiency of synthetic oil with silica nanoparticles. *J. Colloid Interface Sci.* **2011**, *364*, 71-79.

118. Rohini Priya, K.; Suganthi, K.S.; Rajan, K.S. Transport properties of ultra-low concentration cuo–water nanofluids containing non-spherical nanoparticles. *Int. J. Heat Mass Transf.* **2012**, *55*, 4734-4743.

119. Byrne, M.D.; Hart, R.A.; da Silva, A.K. Experimental thermal–hydraulic evaluation of cuo nanofluids in microchannels at various concentrations with and without suspension enhancers. *Int. J. Heat Mass Transf.* **2012**, *55*, 2684-2691.

120. Neouze, M.A.; Schubert, U. Surface modification and functionalization of metal and metal oxide nanoparticles by organic ligands. *Monatsh. Chem.* **2008**, *139*, 183-195.

121. Kayhani, M.H.; Soltanzadeh, H.; Heyhat, M.M.; Nazari, M.; Kowsary, F. Experimental study of convective heat transfer and pressure drop of tio2/water nanofluid. *Int. Commun. Heat Mass Transf.* **2012**, *39*, 456-462.

122. Yang, X.-F.; Liu, Z.-H. Pool boiling heat transfer of functionalized nanofluid under sub-atmospheric pressures. *Int. J. Therm. Sci.* **2011**, *50*, 2402-2412.

123. Han, H.; Zhang, Y.; Wang, N.; Samani, M.K.; Ni, Y.; Mijbil, Z.Y.; Edwards, M.; Xiong, S.; Sääskilahti, K.; Murugesan, M., *et al*. Functionalization mediates heat transport in graphene nanoflakes. *Nature Communications* **2016**, *7*.

124. Mahbubul, I.M.; Elcioglu, E.B.; Saidur, R.; Amalina, M.A. Optimization of ultrasonication period for better dispersion and stability of tio2-water nanofluid. *Ultrason Sonochem* **2017**, *37*, 360-367.

125. Chung, S.J.; Leonard, J.P.; Nettleship, I.; Lee, J.K.; Soong, Y.; Martello, D.V.; Chyu, M.K. Characterization of zno nanoparticle suspension in water: Effectiveness of ultrasonic dispersion. *Powder Technol.* **2009**, *194*, 75-80.

126. Petzold, G.; Rojas-Reyna, R.; Mende, M.; Schwarz, S. Application relevant characterization of aqueous silica nanodispersions. *J. Dispersion Sci. Technol.* **2009**, *30*, 1216-1222.

127. Kole, M.; Dey, T.K. Effect of prolonged ultrasonication on the thermal conductivity of zno-ethylene glycol nanofluids. *Thermochim Acta* **2012**, *535*, 58-65.

128. Q500 sonicator - qsonica. http://www.sonicator.com/11-q500-sonicator.html (21 November),

129. Digital bench-top ultrasonic cleaners | soniclean | so easy - so fast - so clean. http://www.soniclean.com.au/products/digital-bench-top-cleaner (21 November),

130. Peng, X.F.; Yu, X.L.; Xia, L.F.; Zhong, X. Influence factors on suspension stability of nanofluids. *Zhejiang Daxue Xuebao (Gongxue Ban)* **2007**, *41*, 577-580.

131. Choudhary, R.; Khurana, D.; Kumar, A.; Subudhi, S. Stability analysis of al2o3/water nanofluids. *J. Exp. Nanosci.* **2017**, *12*, 140-151.

132. Azizian, R.; Doroodchi, E.; Moghtaderi, B. Influence of controlled aggregation on thermal conductivity of nanofluids. *Journal of Heat Transfer-Transactions of the Asme* **2016**, *138*.

133. Askari, S.; Koolivand, H.; Pourkhalil, M.; Lotfi, R.; Rashidi, A. Investigation of fe3o4/graphene nanohybrid heat transfer properties: Experimental approach. *Int. Commun. Heat Mass Transf.* **2017**, *87*, 30-39.

134. Mohammadi, M.; Dadvar, M.; Dabir, B. Tio2/sio2 nanofluids as novel inhibitors for the stability of asphaltene particles in crude oil: Mechanistic understanding, screening, modeling, and optimization. *Journal of Molecular Liquids* **2017**, *238*, 326-340.

135. Leong, K.Y.; Najwa, Z.A.; Ahmad, K.Z.K.; Ong, H.C. Investigation on stability and optical properties of titanium dioxide and aluminum oxide water-based nanofluids. *Int J Thermophys* **2017**, *38*.

136. Kumar, P.C.M.; Muruganandam, M. Stability analysis of heat transfer mwcnt with different base fluids. *J. Appl. Fluid Mech.* **2017**, *10*, 51-59.

137. Menbari, A.; Alemrajabi, A.A.; Ghayeb, Y. Investigation on the stability, viscosity and extinction coefficient of cuo-al2o3/water binary mixture nanofluid. *Exp. Therm. Fluid Sci.* **2016**, *74*, 122-129.

138. Witharana, S.; Palabiyik, I.; Musina, Z.; Ding, Y.L. Stability of glycol nanofluids - the theory and experiment. *Powder Technol.* **2013**, *239*, 72-77.

139. Manjula, S.; Kumar, S.M.; Raichur, A.M.; Madhu, G.M.; Suresh, R.; Raj, M.A.L.A. A sedimentation study to optimize the dispersion of alumina nanoparticles in water. *Cerâmica* **2005**, *51*, 121-127.

140. Zhu, D.S.; Li, X.F.; Wang, N.; Wang, X.J.; Gao, J.W.; Li, H. Dispersion behavior and thermal conductivity characteristics of al2o3-h2o nanofluids. *Curr. Appl. Phys.* **2009**, *9*, 131-139.

141. Lee, D.; Kim, J.W.; Kim, B.G. A new parameter to control heat transport in nanofluids: Surface charge state of the particle in suspension. *J Phys Chem B* **2006**, *110*, 4323-4328.

142. Chang, H.; Chen, X.Q.; Jwo, C.S.; Chen, S.L. Electrostatic and sterical stabilization of cuo nanofluid prepared by vacuum arc spray nanofluid synthesis system (asnss). *Mater. Trans.* **2009**, *50*, 2098-2103.

143. Song, Y.Y.; Bhadeshia, H.K.D.H.; Suh, D.W. Stability of stainless-steel nanoparticle and water mixtures. *Powder Technol.* **2015**, *272*, 34-44.

144. Paul, G.; Sarkar, S.; Pal, T.; Das, P.K.; Manna, I. Concentration and size dependence of nano-silver dispersed water based nanofluids. *J. Colloid Interface Sci.* **2012**, *371*, 20-27.

145. Qu, J.; Wu, H.-y.; Cheng, P. Thermal performance of an oscillating heat pipe with al2o3–water nanofluids. *Int. Commun. Heat Mass Transf.* **2010**, *37*, 111-115.

146. Anoop, K.B.; Sundararajan, T.; Das, S.K. Effect of particle size on the convective heat transfer in nanofluid in the developing region. *Int. J. Heat Mass Transf.* **2009**, *52*, 2189-2195.

147. Chang, M.-H.; Liu, H.-S.; Tai, C.Y. Preparation of copper oxide nanoparticles and its application in nanofluid. *Powder Technol.* **2011**, *207*, 378-386.

148. Liu, Z.-h.; Xiong, J.-g.; Bao, R. Boiling heat transfer characteristics of nanofluids in a flat heat pipe evaporator with micro-grooved heating surface. *International Journal of Multiphase Flow* **2007**, *33*, 1284-1295.

149. Qu, J.; Wu, H. Thermal performance comparison of oscillating heat pipes with sio2/water and al2o3/water nanofluids. *Int. J. Therm. Sci.* **2011**, *50*, 1954-1962.

150. Suganthi, K.S.; Rajan, K.S. Temperature induced changes in zno–water nanofluid: Zeta potential, size distribution and viscosity profiles. *Int. J. Heat Mass Transf.* **2012**, *55*, 7969-7980.

151. Duangthongsuk, W.; Wongwises, S. An experimental study on the heat transfer performance and pressure drop of tio2-water nanofluids flowing under a turbulent flow regime. *Int. J. Heat Mass Transf.* **2010**, *53*, 334-344.

152. Hari, M.; Joseph, S.A.; Mathew, S.; Nithyaja, B.; Nampoori, V.P.N.; Radhakrishnan, P. Thermal diffusivity of nanofluids composed of rod-shaped silver nanoparticles. *Int. J. Therm. Sci.* **2013**, *64*, 188-194.

153. Kole, M.; Dey, T.K. Thermal performance of screen mesh wick heat pipes using water-based copper nanofluids. *Appl Therm Eng* **2013**, *50*, 763-770.

154. Kathiravan, R.; Kumar, R.; Gupta, A.; Chandra, R. Preparation and pool boiling characteristics of copper nanofluids over a flat plate heater. *Int. J. Heat Mass Transf.* **2010**, *53*, 1673-1681.

155. Yousefi, T.; Shojaeizadeh, E.; Veysi, F.; Zinadini, S. An experimental investigation on the effect of ph variation of mwcnt–h2o nanofluid on the efficiency of a flat-plate solar collector. *Solar Energy* **2012**, *86*, 771-779.

156. Garg, P.; Alvarado, J.L.; Marsh, C.; Carlson, T.A.; Kessler, D.A.; Annamalai, K. An experimental study on the effect of ultrasonication on viscosity and heat transfer performance of multi-wall carbon nanotube-based aqueous nanofluids. *Int. J. Heat Mass Transf.* **2009**, *52*, 5090-5101.

157. Ding, Y.; Alias, H.; Wen, D.; Williams, R.A. Heat transfer of aqueous suspensions of carbon nanotubes (cnt nanofluids). *Int. J. Heat Mass Transf.* **2006**, *49*, 240-250.

158. Abareshi, M.; Goharshadi, E.K.; Mojtaba Zebarjad, S.; Khandan Fadafan, H.; Youssefi, A. Fabrication, characterization and measurement of thermal conductivity of fe3o4 nanofluids. *Journal of Magnetism and Magnetic Materials* **2010**, *322*, 3895-3901.

159. Phuoc, T.X.; Soong, Y.; Chyu, M.K. Synthesis of ag-deionized water nanofluids using multi-beam laser ablation in liquids. *Opt Lasers Eng* **2007**, *45*, 1099-1106.

160. Parametthanuwat, T.; Rittidech, S.; Pattiya, A. A correlation to predict heat-transfer rates of a two-phase closed thermosyphon (tpct) using silver nanofluid at normal operating conditions. *Int. J. Heat Mass Transf.* **2010**, *53*, 4960-4965.

161. Yousefi, T.; Veysi, F.; Shojaeizadeh, E.; Zinadini, S. An experimental investigation on the effect of al2o3–h2o nanofluid on the efficiency of flat-plate solar collectors. *Renewable Energy* **2012**, *39*, 293-298.

162. Hung, Y.-H.; Teng, T.-P.; Lin, B.-G. Evaluation of the thermal performance of a heat pipe using alumina nanofluids. *Exp. Therm. Fluid Sci.* **2013**, *44*, 504-511.

163. Heyhat, M.M.; Kowsary, F.; Rashidi, A.M.; Momenpour, M.H.; Amrollahi, A. Experimental investigation of laminar convective heat transfer and pressure drop of water-based al2o3 nanofluids in fully developed flow regime. *Exp. Therm. Fluid Sci.* **2013**, *44*, 483-489.

164. Pak, B.C.; Cho, Y.I. Hydrodynamic and heat transfer study of dispersed fluids with submicron metallic oxide particles. *Exp. Heat Transf.* **1998**, *11*, 151-170.

165. Vajjha, R.S.; Das, D.K.; Mahagaonkar, B.M. Density measurement of different nanofluids and their comparison with theory. *Petrol Sci Technol* **2009**, *27*, 612-624.

166. Behroyan, I.; Vanaki, S.M.; Ganesan, P.; Saidur, R. A comprehensive comparison of various cfd models for convective heat transfer of al2o3 nanofluid inside a heated tube. *Int. Commun. Heat Mass Transf.* **2016**, *70*, 27-37.

167. Vanaki, S.M.; Mohammed, H.A. Numerical study of nanofluid forced convection flow in channels using different shaped transverse ribs. *Int. Commun. Heat Mass Transf.* **2015**, *67*, 176-188.

168. Selimefendigil, F.; Öztop, H.F.; Abu-Hamdeh, N. Mixed convection due to rotating cylinder in an internally heated and flexible walled cavity filled with sio2–water nanofluids: Effect of nanoparticle shape. *Int. Commun. Heat Mass Transf.* **2016**, *71*, 9-19.

169. Yang, Y.-T.; Tang, H.-W.; Zeng, B.-Y.; Wu, C.-H. Numerical simulation and optimization of turbulent nanofluids in a three-dimensional rectangular rib-grooved channel. *Int. Commun. Heat Mass Transf.* **2015**, *66*, 71-79.

170. Sun, B.; Lei, W.; Yang, D. Flow and convective heat transfer characteristics of fe2o3–water nanofluids inside copper tubes. *Int. Commun. Heat Mass Transf.* **2015**, *64*, 21-28.

171. Salman, B.H.; Mohammed, H.A.; Kherbeet, A.S. Numerical and experimental investigation of heat transfer enhancement in a microtube using nanofluids. *Int. Commun. Heat Mass Transf.* **2014**, *59*, 88-100.

172. Meng, X.; Li, Y. Numerical study of natural convection in a horizontal cylinder filled with water-based alumina nanofluid. *Nanoscale Research Letters* **2015**, *10*, 142.

173. Mohammadpourfard, M.; Aminfar, H.; Karimi, M. Numerical investigation of non-uniform transverse magnetic field effects on the swirling flow boiling of magnetic nanofluid in annuli. *Int. Commun. Heat Mass Transf.* **2016**, *75*, 240-252.

174. Akdag, U.; Akcay, S.; Demiral, D. Heat transfer enhancement with laminar pulsating nanofluid flow in a wavy channel. *Int. Commun. Heat Mass Transf.* **2014**, *59*, 17-23.

175. Yacob, N.A.; Ishak, A.; Pop, I.; Vajravelu, K. Boundary layer flow past a stretching/shrinking surface beneath an external uniform shear flow with a convective surface boundary condition in a nanofluid. *Nanoscale Research Letters* **2011**, *6*, 314.

176. Moraveji, M.K.; Ardehali, R.M. Cfd modeling (comparing single and two-phase approaches) on thermal performance of al2o3/water nanofluid in mini-channel heat sink. *Int. Commun. Heat Mass Transf.* **2013**, *44*, 157-164.

177. Xu, H.; Fan, T.; Pop, I. Analysis of mixed convection flow of a nanofluid in a vertical channel with the buongiorno mathematical model. *Int. Commun. Heat Mass Transf.* **2013**, *44*, 15-22.

178. Parsazadeh, M.; Mohammed, H.A.; Fathinia, F. Influence of nanofluid on turbulent forced convective flow in a channel with detached rib-arrays. *Int. Commun. Heat Mass Transf.* **2013**, *46*, 97-105.

179. Sheikholeslami, M.; Gorji-Bandpay, M.; Ganji, D.D. Magnetic field effects on natural convection around a horizontal circular cylinder inside a square enclosure filled with nanofluid. *Int. Commun. Heat Mass Transf.* **2012**, *39*, 978-986.

180. Rashad, A.M.; Rashidi, M.M.; Lorenzini, G.; Ahmed, S.E.; Aly, A.M. Magnetic field and internal heat generation effects on the free convection in a rectangular cavity filled with a porous medium saturated with cu–water nanofluid. *Int. J. Heat Mass Transf.* **2017**, *104*, 878-889.

181. Leong, K.Y.; Saidur, R.; Khairulmaini, M.; Michael, Z.; Kamyar, A. Heat transfer and entropy analysis of three different types of heat exchangers operated with nanofluids. *Int. Commun. Heat Mass Transf.* **2012**, *39*, 838-843.

182. Shahi, M.; Mahmoudi, A.H.; Talebi, F. Numerical simulation of steady natural convection heat transfer in a 3-dimensional single-ended tube subjected to a nanofluid. *Int. Commun. Heat Mass Transf.* **2010**, *37*, 1535-1545.

183. Ghaffari, O.; Behzadmehr, A.; Ajam, H. Turbulent mixed convection of a nanofluid in a horizontal curved tube using a two-phase approach. *Int. Commun. Heat Mass Transf.* **2010**, *37*, 1551-1558.

184. Manca, O.; Mesolella, P.; Nardini, S.; Ricci, D. Numerical study of a confined slot impinging jet with nanofluids. *Nanoscale Research Letters* **2011**, *6*, 188.

185. Rostamani, M.; Hosseinizadeh, S.F.; Gorji, M.; Khodadadi, J.M. Numerical study of turbulent forced convection flow of nanofluids in a long horizontal duct considering variable properties. *Int. Commun. Heat Mass Transf.* **2010**, *37*, 1426-1431.

186. Büyük Öğüt, E. Natural convection of water-based nanofluids in an inclined enclosure with a heat source. *Int. J. Therm. Sci.* **2009**, *48*, 2063-2073.

187. Kumar, S.; Prasad, S.K.; Banerjee, J. Analysis of flow and thermal field in nanofluid using a single phase thermal dispersion model. *Applied Mathematical Modelling* **2010**, *34*, 573-592.

188. Alloui, Z.; Guiet, J.; Vasseur, P.; Reggio, M. Natural convection of nanofluids in a shallow rectangular enclosure heated from the side. *The Canadian Journal of Chemical Engineering* **2012**, *90*, 69-78.

189. Ryzhkov, I.I.; Minakov, A.V. The effect of nanoparticle diffusion and thermophoresis on convective heat transfer of nanofluid in a circular tube. *Int. J. Heat Mass Transf.* **2014**, *77*, 956-969.

190. Minea, A.A. Uncertainties in modeling thermal conductivity of laminar forced convection heat transfer with water alumina nanofluids. *Int. J. Heat Mass Transf.* **2014**, *68*, 78-84.

191. Sadeghi, O.; Mohammed, H.A.; Bakhtiari-Nejad, M.; Wahid, M.A. Heat transfer and nanofluid flow characteristics through a circular tube fitted with helical tape inserts. *Int. Commun. Heat Mass Transf.* **2016**, *71*, 234-244.

192. Azimi, S.S.; Kalbasi, M. Numerical study of dynamic thermal conductivity of nanofluid in the forced convective heat transfer. *Applied Mathematical Modelling* **2014**, *38*, 1373-1384.

193. Inakov, A.; Lobasov, A.; Guzei, D.; Pryazhnikov, M.; Ya Rudyak, V. The experimental and theoretical study of laminar forced convection of nanofluids in the round channel. *Appl. Therm. Eng.* **2014**, 1-9.

194. Togun, H.; Abu-Mulaweh, H.I.; Kazi, S.N.; Badarudin, A. Numerical simulation of heat transfer and separation al2o3/nanofluid flow in concentric annular pipe. *Int. Commun. Heat Mass Transf.* **2016**, *71*, 108-117.

195. Cianfrini, C.; Corcione, M.; Habib, E.; Quintino, A. Buoyancy-induced convection in al2o3/water nanofluids from an enclosed heater. *European Journal of Mechanics - B/Fluids* **2014**, *48*, 123-134.

196. Hemmat Esfe, M.; Saedodin, S.; Mahmoodi, M. Experimental studies on the convective heat transfer performance and thermophysical properties of mgo–water nanofluid under turbulent flow. *Exp. Therm. Fluid Sci.* **2014**, *52*, 68-78.

197. Ghodsinezhad, H.; Sharifpur, M.; Meyer, J.P. Experimental investigation on cavity flow natural convection of al2o3–water nanofluids. *Int. Commun. Heat Mass Transf.* **2016**, *76*, 316-324.

198. Chen, W.-C.; Cheng, W.-T. Numerical simulation on forced convective heat transfer of titanium dioxide/water nanofluid in the cooling stave of blast furnace. *Int. Commun. Heat Mass Transf.* **2016**, *71*, 208-215.

199. Maddah, H.; Alizadeh, M.; Ghasemi, N.; Wan Alwi, S.R. Experimental study of al2o3/water nanofluid turbulent heat transfer enhancement in the horizontal double pipes fitted with modified twisted tapes. *Int. J. Heat Mass Transf.* **2014**, *78*, 1042-1054.

200. Abed, A.M.; Alghoul, M.A.; Sopian, K.; Mohammed, H.A.; Majdi, H.s.; Al-Shamani, A.N. Design characteristics of corrugated trapezoidal plate heat exchangers using nanofluids. *Chemical Engineering and Processing: Process Intensification* **2015**, *87*, 88-103.

201. Huminic, G.; Huminic, A. Heat transfer and entropy generation analyses of nanofluids in helically coiled tube-in-tube heat exchangers. *Int. Commun. Heat Mass Transf.* **2016**, *71*, 118-125.

202. Al-Shamani, A.N.; Sopian, K.; Mohammed, H.A.; Mat, S.; Ruslan, M.H.; Abed, A.M. Enhancement heat transfer characteristics in the channel with trapezoidal rib–groove using nanofluids. *Case Studies in Thermal Engineering* **2015**, *5*, 48-58.

203. Sommers, A.D.; Yerkes, K.L. Experimental investigation into the convective heat transfer and system-level effects of al2o3-propanol nanofluid. *J. Nanopart. Res.* **2010**, *12*, 1003-1014.

204. Ho, C.J.; Liu, W.K.; Chang, Y.S.; Lin, C.C. Natural convection heat transfer of alumina-water nanofluid in vertical square enclosures: An experimental study. *Int. J. Therm. Sci.* **2010**, *49*, 1345-1353.

205. Devendiran, D.K.; Amirtham, V.A. A review on preparation, characterization, properties and applications of nanofluids. *Renewable & Sustainable Energy Reviews* **2016**, *60*, 21-40.

206. Sharifpur, M.; Yousefi, S.; Meyer, J.P. A new model for density of nanofluids including nanolayer. *Int. Commun. Heat Mass Transf.* **2016**, *78*, 168-174.

207. Xuan, Y.M.; Roetzel, W. Conceptions for heat transfer correlation of nanofluids. *Int. J. Heat Mass Transf.* **2000**, *43*, 3701-3707.

208. Zhou, S.-Q.; Ni, R. Measurement of the specific heat capacity of water-based al2o3 nanofluid. *Appl. Phys. Lett.* **2008**, *92*, 093123.

209. Teng, T.P.; Hung, Y.H. Estimation and experimental study of the density and specific heat for alumina nanofluid. *J. Exp. Nanosci.* **2014**, *9*, 707-718.

210. Kulkarni, D.P.; Vajjha, R.S.; Das, D.K.; Oliva, D. Application of aluminum oxide nanofluids in diesel electric generator as jacket water coolant. *Appl Therm Eng* **2008**, *28*, 1774-1781.

211. Sekhar, Y.R.; Sharma, K.V. Study of viscosity and specific heat capacity characteristics of water-based al2o3 nanofluids at low particle concentrations. *J. Exp. Nanosci.* **2015**, *10*, 86-102.

212. Ghazvini, M.; Akhavan-Behabadi, M.A.; Rasouli, E.; Raisee, M. Heat transfer properties of nanodiamond-engine oil nanofluid in laminar flow. *Heat Transfer Eng* **2012**, *33*, 525-532.

213. Vajjha, R.S.; Das, D.K. A review and analysis on influence of temperature and concentration of nanofluids on thermophysical properties, heat transfer and pumping power. *Int. J. Heat Mass Transf.* **2012**, *55*, 4063-4078.

214. Zhou, L.P.; Wang, B.X.; Peng, X.F.; Du, X.Z.; Yang, Y.P. On the specific heat capacity of cuo nanofluid. *Adv. Mech. Eng.* **2010**, *2010*.

215. Shin, D.; Banerjee, D. Enhancement of specific heat capacity of high-temperature silica-nanofluids synthesized in alkali chloride salt eutectics for solar thermal-energy storage applications. *Int. J. Heat Mass Transf.* **2011**, *54*, 1064-1070.

216. Shin, D.; Banerjee, D. Specific heat of nanofluids synthesized by dispersing alumina nanoparticles in alkali salt eutectic. *Int. J. Heat Mass Transf.* **2014**, *74*, 210-214.

217. Fakoor Pakdaman, M.; Akhavan-Behabadi, M.A.; Razi, P. An experimental investigation on thermo-physical properties and overall performance of mwcnt/heat transfer oil nanofluid flow inside vertical helically coiled tubes. *Exp. Therm. Fluid Sci.* **2012**, *40*, 103-111.

218. Volz, S.; Ordonez-Miranda, J.; Shchepetov, A.; Prunnila, M.; Ahopelto, J.; Pezeril, T.; Vaudel, G.; Gusev, V.; Ruello, P.; Weig, E.M., *et al.* Nanophononics: State of the art and perspectives. *European Physical Journal B* **2016**, *89*.

219. Han, H.; Feng, L.; Xiong, S.; Shiga, T.; Shiomi, J.; Volz, S.; Kosevich, Y.A. Effects of phonon interference through long range interatomic bonds on thermal interface conductance. *Low Temperature Physics* **2016**, *42*, 711-716.

220. Keblinski, P.; Phillpot, S.R.; Choi, S.U.S.; Eastman, J.A. Mechanisms of heat flow in suspensions of nano-sized particles (nanofluids). *Int. J. Heat Mass Transf.* **2002**, *45*, 855-863.

221. Koo, J.; Kleinstreuer, C. Impact analysis of nanoparticle motion mechanisms on the thermal conductivity of nanofluids. *Int. Commun. Heat Mass Transf.* **2005**, *32*, 1111-1118.

222. Buongiorno, J. Convective transport in nanofluids. *ASME J Heat Transfer* **2006**, *128*.

223. Nan, C.W.; Birringer, R.; Clarke, D.R.; Gleiter, H. Effective thermal conductivity of particulate composites with interfacial thermal resistance. *J. Appl. Phys.* **1997**, *81*, 6692-6699.

224. Bruggeman, D.A.G. Dielectric constant and conductivity of mixtures of isotropic materials. *Ann. Phys. (Leipzig)* **1935**, *24*, 636-679.

225. Kumar, D.H.; Patel, H.E.; Kumar, V.R.R.; Sundararajan, T.; Pradeep, T.; Das, S.K. Model for heat conduction in nanofluids. *Phys. Rev. Lett.* **2004**, *93*, 144301.

226. Leong, K.C.; Yang, C.; Murshed, S.M.S. A model for the thermal conductivity of nanofluids – the effect of interfacial layer. *J. Nanopart. Res.* **2006**, *8*, 245-254.

227. Xie, H.; Fujii, M.; Zhang, X. Effect of interfacial nanolayer on the effective thermal conductivity of nanoparticle-fluid mixture. *Int. J. Heat Mass Transf.* **2005**, *48*, 2926-2932.

228. Yamada, E.; Ota, T. Effective thermal conductivity of dispersed materials. *Wärme - und Stoffübertragung* **1980**, *13*, 27-37.

229. Hasselman, D.P.H.; Johnson, L.F. Effective thermal conductivity of composites with interfacial thermal barrier resistance. *Journal of Composite Materials* **1987**, *21*, 508-515.

230. Wang, B.-X.; Zhou, L.-P.; Peng, X.-F. A fractal model for predicting the effective thermal conductivity of liquid with suspension of nanoparticles. *Int. J. Heat Mass Transf.* **2003**, *46*, 2665-2672.

231. Davis, R.H. The effective thermal conductivity of a composite material with spherical inclusions. *Int J Thermophys* **1986**, *7*, 609-620.

232. Jie, X.; Boming, Y.; Mingqing, Z.; Peng, X. A new model for heat conduction of nanofluids based on fractal distributions of nanoparticles. *J Phys D* **2006**, *39*, 4486.

233. Evans, W.; Fish, J.; Keblinski, P. Role of brownian motion hydrodynamics on nanofluid thermal conductivity. *Appl. Phys. Lett.* **2006**, *88*, 093116.

234. Vladkov, M.; Barrat, J.-L. Modeling transient absorption and thermal conductivity in a simple nanofluid. *Nano Letters* **2006**, *6*, 1224-1228.

235. Shima, P.D.; Philip, J.; Raj, B. Role of microconvection induced by brownian motion of nanoparticles in the enhanced thermal conductivity of stable nanofluids. *Appl. Phys. Lett.* **2009**, *94*, 223101.

236. Murshed, S.M.S.; Leong, K.C.; Yang, C. A combined model for the effective thermal conductivity of nanofluids. *Appl Therm Eng* **2009**, *29*, 2477-2483.

237. Chon, C.H.; Kihm, K.D.; Lee, S.P.; Choi, S.U.S. Empirical correlation finding the role of temperature and particle size for nanofluid (al2o3) thermal conductivity enhancement. *Appl. Phys. Lett.* **2005**, *87*, 153107.

238. Patel, H.E.; Sundararajan, T.; Pradeep, T.; Dasgupta, A.; Dasgupta, N.; Das, S.K. A micro-convection model for thermal conductivity of nanofluids. *Pramana* **2005**, *65*, 863-869.

239. Maïga, S.E.B.; Nguyen, C.T.; Galanis, N.; Roy, G. Heat transfer behaviours of nanofluids in a uniformly heated tube. *Superlattices and Microstructures* **2004**, *35*, 543-557.

240. Timofeeva, E.V.; Gavrilov, A.N.; McCloskey, J.M.; Tolmachev, Y.V.; Sprunt, S.; Lopatina, L.M.; Selinger, J.V. Thermal conductivity and particle agglomeration in alumina nanofluids: Experiment and theory. *Physical Review E* **2007**, *76*, 061203.

241. Azmi, W.H.; Sharma, K.V.; Rizalman, M.; Alias, A.B.S.; Izan Izwan, M. Correlations for thermal conductivity and viscosity of water based nanofluids. *IOP Conference Series: Materials Science and Engineering* **2012**, *36*, 012029.

242. Li, C.H.; Peterson, G.P. Experimental investigation of temperature and volume fraction variations on the effective thermal conductivity of nanoparticle suspensions (nanofluids). *J. Appl. Phys.* **2006**, *99*, 084314.

243. Corcione, M. Empirical correlating equations for predicting the effective thermal conductivity and dynamic viscosity of nanofluids. *Energy Conversion and Management* **2011**, *52*, 789-793.

244. Hamilton, R.L.; Crosser, O.K. Thermal conductivity of heterogeneous two-component systems. *Industrial & Engineering Chemistry Fundamentals* **1962**, *1*, 187-191.

245. Wasp, E.J.; Kenny, J.P.; Gandhi, R.L. *Solid--liquid flow: Slurry pipeline transportation. [pumps, valves, mechanical equipment, economics]*. 1977; Vol. 1:4.

246. Yu, W.; Choi, S.U.S. The role of interfacial layers in the enhanced thermal conductivity of nanofluids: A renovated maxwell model. *J. Nanopart. Res.* **2003**, *5*, 167-171.

247. Xuan, Y.; Li, Q.; Hu, W. Aggregation structure and thermal conductivity of nanofluids. *AIChE Journal* **2003**, *49*, 1038-1043.

248. Vajjha, R.S.; Das, D.K. Experimental determination of thermal conductivity of three nanofluids and development of new correlations. *Int. J. Heat Mass Transf.* **2009**, *52*, 4675-4682.

249. Koo, J.; Kleinstreuer, C. A new thermal conductivity model for nanofluids. *J. Nanopart. Res.* **2004**, *6*, 577-588.

250. Das, S.K.; Putra, N.; Thiesen, P.; Roetzel, W. Temperature dependence of thermal conductivity enhancement for nanofluids. *Journal of Heat Transfer-Transactions of the Asme* **2003**, *125*, 567-574.

251. Xue, Q.; Xu, W.-M. A model of thermal conductivity of nanofluids with interfacial shells. *Materials Chemistry and Physics* **2005**, *90*, 298-301.

252. Prasher, R.; Bhattacharya, P.; Phelan, P.E. Brownian-motion-based convective-conductive model for the effective thermal conductivity of nanofluids. *J. Heat Transf.* **2005**, *128*, 588-595.

253. Jang, S.P.; Choi, S.U.S. Role of brownian motion in the enhanced thermal conductivity of nanofluids. *Appl. Phys. Lett.* **2004**, *84*, 4316-4318.

254. Xie, H.; Wang, J.; Xi, T.; Liu, Y. Thermal conductivity of suspensions containing nanosized sic particles. *Int J Thermophys* **2002**, *23*, 571-580.

255. Assael, M.J.; Metaxa, I.N.; Arvanitidis, J.; Christofilos, D.; Lioutas, C. Thermal conductivity enhancement in aqueous suspensions of carbon multi-walled and double-walled nanotubes in the presence of two different dispersants. *Int J Thermophys* **2005**, *26*, 647-664.

256. Teng, T.P.; Hung, Y.H.; Teng, T.C.; Mo, H.E.; Hsu, H.G. The effect of alumina/water nanofluid particle size on thermal conductivity. *Appl Therm Eng* **2010**, *30*, 2213-2218.

257. Choi, T.Y.; Maneshian, M.H.; Kang, B.; Chang, W.S.; Han, C.S.; Poulikakos, D. Measurement of the thermal conductivity of a water-based single-wall carbon nanotube colloidal suspension with a modified 3- omega method. *Nanotechnology* **2009**, *20*, 315706.

258. Paul, G.; Chopkar, M.; Manna, I.; Das, P.K. Techniques for measuring the thermal conductivity of nanofluids: A review. *Renewable & Sustainable Energy Reviews* **2010**, *14*, 1913-1924.

259. Czarnetzki, W.; Roetzel, W. Temperature oscillation techniques for simultaneous measurement of thermal-diffusivity and conductivity. *Int J Thermophys* **1995**, *16*, 413-422.

260. Jiang, W.; Ding, G.; Peng, H. Measurement and model on thermal conductivities of carbon nanotube nanorefrigerants. *Int. J. Therm. Sci.* **2009**, *48*, 1108-1115.

261. Murshed, S.M.S.; Leong, K.C.; Yang, C. In *Thermal conductivity of nanoparticle suspensions (nanofluids)*, 2006 IEEE Conference on Emerging Technologies - Nanoelectronics, Singapore, 2006; Singapore, pp 155-158.

262. Ju, Y.S.; Kim, J.; Hung, M.T. Experimental study of heat conduction in aqueous suspensions of aluminum oxide nanoparticles. *Journal of Heat Transfer-Transactions of the Asme* **2008**, *130*.

263. Warzoha, R.J.; Fleischer, A.S. Determining the thermal conductivity of liquids using the transient hot disk method. Part i: Establishing transient thermal-fluid constraints. *Int. J. Heat Mass Transf.* **2014**, *71*, 779-789.

264. Agresti, F.; Barison, S.; Battiston, S.; Pagura, C.; Colla, L.; Fedele, L.; Fabrizio, M. In *Influence of molecular weight of pvp on aggregation and thermal diffusivity of silver-based nanofluids*, Nanotechnology 2013: Electronics, Devices, Fabrication, MEMS, Fluidics and Computational - 2013 NSTI Nanotechnology Conference and Expo, NSTI-Nanotech 2013, Washington, DC, 2013; Washington, DC, pp 366-369.

265. Agresti, F.; Ferrario, A.; Boldrini, S.; Miozzo, A.; Montagner, F.; Barison, S.; Pagura, C.; Fabrizio, M. Temperature controlled photoacoustic device for thermal diffusivity measurements of liquids and nanofluids. *Thermochim Acta* **2015**, *619*, 48-52.

266. Astrath, N.G.C.; Medina, A.N.; Bento, A.C.; Jacinto, C.; Catunda, T.; Lima, S.M.; da Silva, L.M.; Gandra, F.G.; Baesso, M.L. Time resolved thermal lens measurements of the thermo-optical properties of nd2o3-doped low silica calcium aluminosilicate glasses down to 4.3k. *J. Non·Cryst. Solids* **2008**, *354*, 574-579.

267. Jiménez Pérez, J.L.; Gutierrez Fuentes, R.; Sanchez Ramirez, J.F.; Cruz-Orea, A. Study of gold nanoparticles effect on thermal diffusivity of nanofluids based on various solvents by using thermal lens spectroscopy. *The European Physical Journal Special Topics* **2008**, *153*, 159-161.

268. Rodriguez, L.G.; Iza, P.; Paz, J.L. Study of dependence between thermal diffusivity and sample concentration measured by means of frequency-resolved thermal lens experiment. *Journal of Nonlinear Optical Physics & Materials* **2016**, *25*, 1650022.

269. Joseph, S.A.; Hari, M.; Mathew, S.; Sharma, G.; Soumya; Hadiya, V.M.; Radhakrishnan, P.; Nampoori, V.P.N. Thermal diffusivity of rhodamine 6g incorporated in silver nanofluid measured using mode-matched thermal lens technique. *Opt. Commun.* **2010**, *283*, 313-317.

270. Baesso, M.L.; Pereira, J.R.D.; Bento, A.C.; Palangana, A.J.; Mansanares, A.M.; Evangelista, L.R. Thermal lens spectrometry to study complex fluids. *Brazilian Journal of Physics* **1998**, *28*, 00-00.

271. Murshed, S.M.S.; Leong, K.C.; Yang, C. Determination of the effective thermal diffusivity of nanofluids by the double hot-wire technique. *Journal of Physics D-Applied Physics* **2006**, *39*, 5316-5322.

272. Zhang, X.; Gu, H.; Fujii, M. Effective thermal conductivity and thermal diffusivity of nanofluids containing spherical and cylindrical nanoparticles. *Exp. Therm. Fluid Sci.* **2007**, *31*, 593-599.

273. Einstein, A. Investigations on the theory of the brownian movement. *Courier Corporation* **1956**.

274. Einstein, A. Eine neue bestimmung der moleküldimensionen. *Ann Phys Leipzig* **1906**, *324*, 289-306.

275. Rudyak, V.Y.; Minakov, A.V. Thermophysical properties of nanofluids. *The European Physical Journal E* **2018**, *41*, 15.

276. Ilyas, S.U.; Pendyala, R.; Shuib, A.S.; Marneni, N. A review on the viscous and thermal transport properties of nanofluids. In *International Conference on Process Engineering and Advanced Materials, ICPEAM 2012*, Trans Tech Publications Ltd: Kuala Lumpur, 2014; Vol. 917, pp 18-27.

277. Hemmati-Sarapardeh, A.; Varamesh, A.; Husein, M.M.; Karan, K. On the evaluation of the viscosity of nanofluid systems: Modeling and data assessment. *Renewable & Sustainable Energy Reviews* **2018**, *81*, 313-329.

278. Rudyak, V.Y.; Belkin, A.A.; Egorov, V.V. On the effective viscosity of nanosuspensions. *Technical Physics* **2009**, *54*, 1102-1109.

279. Namburu, P.K.; Kulkarni, D.P.; Dandekar, A.; Das, D.K. Experimental investigation of viscosity and specific heat of silicon dioxide nanofluids. *Micro and Nano Letters* **2007**, *2*, 67-71.

280. Vasiliev, L.L.; Grakovich, L.P.; Rabetsky, M.; Vasiliev Jr, L.L. Heat transfer enhancement in heat pipes and thermosyphons using nanotechnologies (nanofluids, nanocoatings, and nanocomposites) as an hp envelope. *Heat Pipe Science and Technology, An International Journal* **2013**, *4*.

Chapter 3

Publication 2: New pH Correlations for Stainless Steel 316L, Aluminium, and Copper(I) Oxide Nanofluids Fabricated at Controlled Sonication Temperatures

(Ali, N.; Teixeira, J.A.; Addali, A. New pH Correlations for Stainless Steel 316L, Alumina, and Copper(I) Oxide Nanofluids Fabricated at Controlled Sonication Temperatures, *J. Nano. Res.*, **2019**, *58*, 125-138. DOI: 10.4028/www.scientific.net/JNanoR.58.125)

New pH Correlations for Stainless Steel 316L, Aluminium, and Copper(I) Oxide Nanofluids Fabricated at Controlled Sonication Temperatures

A B S T R A C T

This research investigates the pH value of stainless steel (SS) 316L/ deionised water (DIW), aluminium (Al)/DIW, and copper(I) oxide (Cu_2O)/DIW nanofluids prepared using a two-step controlled sonication temperature approach of 10°C to 60°C. The nanoparticles volumetric concentration of each family of as-prepared nanofluid ranged from 0.1 to 1.0 vol%, using as-received nanopowders, of 18 – 80 nm average particles size. Furthermore, the pH measuring apparatus and the measurement procedure were validated by determining the pH of commercially supplied calibration fluids, of pH 4, 7, and 10. Following the validation, pH correlations were obtained from the experimental measurements of the 0.1, 0.5, and 1.0 vol% nanofluids in terms of varied sonication bath temperatures and volumetric concentrations. Those correlations were then combined into one robust pH_{nf} correlation and validated using the pH data of the 0.3 and 0.7 vol% nanofluids. The new proposed correlation was found to have a 2.18%, 0.92%, and 0.63%, average deviation from the experimental pH measurements of SS 316L, Al, and Cu_2O nanofluids, respectively, with an overall prediction accuracy of ~ 92%.

Keywords: Aluminium; copper(I) oxide; nanofluids; pH correlation; stainless steel 316L.

1. Introduction

A new class of engineered fluids that rely on the dispersion of metals, metal oxides, allotropes of carbon, or a combination of any of these materials in the form of nanoparticles (NPs) of average diameter less than 100 nm and of low concentration, preferably < 1 vol%, in a non-carcinogenic basefluid (e.g. water, oil, kerosene, glycols, … etc.) were defined by Choi in 1995 as 'Nanofluids' [1-3]. This advance category of fluids have gained the interest of many researchers due to their distinctive properties compared to conventional fluids in the field of

heat transfer enhancement, drug delivery, paint additives, magnetic sealing, ionic liquid synthesis, … etc [4-11]. Although significant research findings on the thermophysical properties of different nanofluids and their applicability are available in the literature, there is still a need for better understanding of the fluid stability behaviour [12, 13]. To be more specific, the interaction between the NPs themselves and between the particles with the surrounding medium is still considered to be an area of exploration and of major concern. In general, nanofluids stability can be subclassified into dispersion stability, and kinetic stability [14]. Dispersion stability takes into account both the Van der Waals attraction force between the particles, and the electrostatic repulsion force caused by the electrical double layers on the particles surface, where clusters formation or agglomerations of particles are more likely to occur in a nanofluid when the attraction force is higher than the particle electrostatic repulsion force [15]. On the other hand, the kinetic stability describes the NPs dynamic Brownian motion in the basefluid, which causes particle sedimentation or phase-separation due to gravitational force [16]. The problem arising from the two aforementioned mechanisms is their negative impact on the long term stability of the suspensions if not appropriately dealt with, and hence can degrade the nanofluid thermophysical properties [17-19]. Basically, there are three main approaches to improve the stability of nanofluids: 1- sonicating the fluid, 2- adding surfactant, and 3- adjusting the pH value to optimize the zeta potential. Sonication, which is a physical method that depends on employing ultrasonic waves through the fluid, can be used to enhance the stability of the solution by rupturing the particles attractional force within the sediments [20]. Furthermore, using a surfactant of organic compounds that has hydrophilic head and hydrophobic tail group, has shown to be useful in increasing the stability of the aqueous solutions [21]. In addition, manipulating the pH value of nanofluids changes the NPs surface and can strongly improve the stability of the dispersed NPs [22, 23]. This is because the zeta potential, which is the potential difference between the layered fluid attached to the particles and the dispersed particles surface, can be increased/decreased by changing the pH value and/or adding surfactant to the nanofluid. In principle, zeta potential values of nanofluids above +30 mV or below -30 mV are considered to be more stable due to the high repulsive force generated between the charged NPs [24-26]. Implementing one or more of the aforementioned techniques can result in obtaining a more homogeneous and better dispersed nanofluid.

Several studies were undertaken to illustrate the influence of the pH value on the nanofluids stability [27-39]. For example, Manjula et al. [40] examined the effect of pH value and

surfactants on the suspension behaviour of alumina (Al_2O_3)/H_2O nanofluid via monitoring the formed sedimentations in the fluid. It was found that optimizing the pH value and adding surfactant to the nanofluid have resulted in maximising the stability of the nanosuspension. Witharana et al. [41] studied the aggregation and settling performance of 0.5 wt% (Al_2O_3)/H_2O nanofluid, of 46 nm particle diameter and water of pH of 6.3 and 7.8. Their results showed that the samples made of pH 6.3 were stable for more than 30 minutes, and that the nanofluids fabricated with a basefluid of pH 7.8 had a complete settling and particles separation after 30 min. Lee et al. [42] examined the stability and effective thermal conductivity of copper oxide (CuO), of 25 nm average particles diameter, suspended in deionized water. Measurements of the formed agglomeration particles size, for the nanofluids of pH 3 to 11, have revealed that the attracted particles were mostly sized between 160 to 280 nm. It was concluded that the stability of the nanofluid was highly influenced by the pH value and the hydrodynamic size of the embedded particles. In addition, at a pH value of 11, the effective thermal conductivity has shown 11% enhancement over that of the basefluid. Song [43] studied the possibility of stabilising stainless steel (SS) 316L/ H_2O nanofluids, of 70 nm average particles size, with added surfactants of sodium dodecyl benzene sulfonate (SDBS) and sodium dodecyl sulfonate (SDS). In their experiment, the nanofluids investigated were adjusted to a pH value of 8.0, 9.0, 10.0, 11.0, and 12.6, before determining their durability and stability. Five approaches were used for their characterisation, namely: 1- absorbance measurement, 2- particle size distribution measurement, 3- sedimentation observation, 4- transmission electron microscope (TEM) observation, 5- zeta potential measurement. The long term stability analysis illustrated that the fabricated suspension of pH 11 maintained for 10 days, pH 10 maintained for 3 days, and those of less pH value have fully settled within one day. On the other hand, the nanofluid of pH 12.6 showed an excess amount of OH^- ions, which resulted in disturbing the electrostatic stability, causing the particles to rapidly settle.

Our review of the available literature quoted above shows that the pH value of nanofluids has a strong effect on its stability, and that the pH value of the suspension is influenced by its temperature and NPs concentration. The effect of a fluid pH was also reported to extend to the level of changing the wettability nature of the surface in contact to it [44, 45]. Given these facts, using an ultrasonic device for preparing nanofluids will lead to an increase in the fluid temperature and hence affect the resulting pH value of the nanofluid. This rise in temperature is limited by the surrounding atmospheric temperature of the site where the nanofluid is been

prepared. This fact needs to be factored in when the commercial production of nanofluids in large scale is considered.

To the best of our knowledge, there is no existing empirical or theoretical relation that links the nanofluid controlled fabrication temperature and concentration to its pH value. Therefore, in this study, the pH value of SS 316L, copper(I) oxide (Cu_2O), and aluminium (Al) NPs dispersed in deionised water (DIW), was measured experimentally at range of controlled sonication bath temperatures and particle concentrations. An empirical correlation was then developed from the measured pH values, controlled fabrication temperatures, and particle concentrations of the prepared nanofluids and validated to help estimate the pH value of similar nanofluids robustly, within the same range of conditions. Such correlation is expected to be beneficial to nanofluids manufacturers and even researchers, where it can aid them in predicting the fluids pH value beforehand, so that a more convenient nanofluid with the desired stability can be achieved.

2. Experimental procedure

2.1 Materials

Portable pH meter calibration fluids of values 4, 7, and 10 were purchased from Metrohm USA Inc. A purity of 99.9% Al NPs and SS 316L NPs, of spherical particles shape and particles size between 40 to 60 nm and 60 to 80 nm, respectively, were purchased from SkySpring Nanomaterials. The chemical composition, as supplied by the manufacture, of the SS 316L NPS is shown in Table 3.1. A 99.86% super fine Cu_2O NPs, of 18 nm average particles size, were supplied by US Research Nanomaterials. A set of 40 mL, 27.5 mm outer diameter and 95 mm height, glass clear vials with screwed top were provided by SIGMA-ALDRICH. Deionised water, produced by an Elga PR030BPM1-US Purelab Prima 30 water purification system, was used as the basefluid for the nanofluids preparation after adjusting its pH value to 7.

Table 3.1. Stainless steel 316L chemical composition, wt% [46].

Elements	**Cr**	**Ni**	**Mo**	**Si**	**Mn**	**S**	**C**	**P**	**Fe**
wt.%	16-18	10-14	2-3	0.75 max	2 max	0.03 max	0.03 max	0.045 max	balance

2.2 Characterization

Characterization tests were performed for the SS 316L, Al, and Cu_2O NPs through a 9 kW Rigaku SmartLab, Japan, X-ray diffraction (XRD) analyser and its software, SmartLab Guidance, using a Cu K_α X-ray source with a diffraction angle of 2θ and an incidence beam step of 0.2° to determine the Bragg's peaks of the phase constitution in the examined sample. The diffraction scanning angle range was from 20° to 80°, with a scanning rate of 1°/min. NPs densities were obtained in order to calculate the nanoparticle volumetric concentrations, which was required for the nanofluids fabrication. This was done by first measuring the samples weight, using an ae-ADAM PW 214 analytical balance of 0.0001 g readability and ±0.0002 g accuracy, then placing them in a HumiPyc trademark Model 1 gas pycnometer – volumetric analyser at an operational temperature of 25°C. The pH values of the DIW and fabricated nanofluids were measured from inside the vials, after placing them on a benchtop, by immersing the Hach PHC20101 Intellical pH measuring electrode connected to a HACH HQ40D portable pH meter, of accuracy ±0.002 pH, vertically to a depth of 5 cm then obtaining the reading for three times and averaging the values. The aforementioned procedure was done after calibrating the pH meter, before each conducted measurement and taking into account the temperature compensation, using the three as-received calibration fluids and the manufacturer instructions [47, 48]. Fig. 3.1 illustrates the experimental set up used for measuring the pH value of the nanofluid samples, which was also adopted for measuring the DIW pH value, at different temperature gradient.

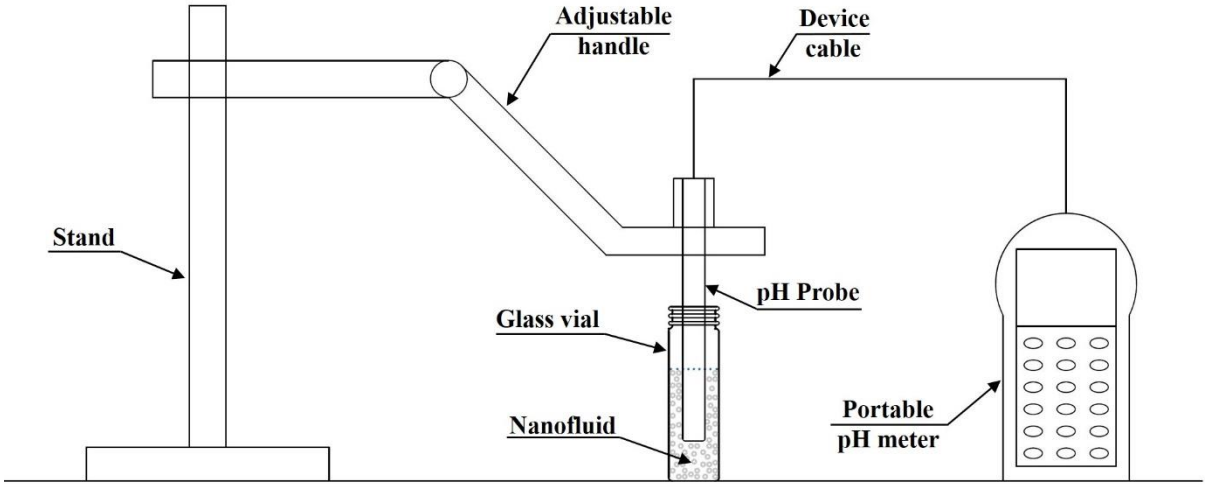

Fig. 3.1. Experimental set up used in measuring pH value of nanofluids samples.

2.3 Nanofluids preparation

Each nanofluid sample was prepared by placing the NPs first inside the vial then injecting 20 mL of DIW, using a disposable syringe, on top of the nanopowder after which the vial was sealed using the provided cap. The volume concentrations (ϕ) of NPs used were 0.1, 0.3, 0.5, 0.7, and 1.0 vol%, for each individual type of material. The vial containing the solution was then placed gently in a Soniclean company benchtop bath type ultrasonic vibrator, running at 100% power (43 kHz pulse) and filled with water to the recommended operating level by the manufacturer, for 4 hours to agitate the mixture. This kind of particles dispersion method is known as the two-step approach, which is a common procedure used for the production of nanofluids by many researchers [16, 33]. The sonicator bath temperature was then controlled, at a margin of ±1°C, for a temperature (T) that ranged from 10°C to 60°C, with an increment of 10°C, by gradually adding hot or cold water inside the ultrasonic bath and extracting the access water from the device via the attached ejection valve. This was done in order to characterise the variation in nanofluids pH (pH_{nf}) value at different points of temperature (e.g. pH value of nanofluid fabricated for 4 hours at fixed sonication bath temperature of 30°C with a margin of ±1°C). It should be pointed out that the lab temperature, where the experiments were performed, was 25°C and that surfactants or dispersing materials/chemicals were not used for the production of the nanofluids to avoid additional parameters effects on the fluid-particles pH value. Fig. 3.2 demonstrates the schematic procedure of the two-step nanofluids preparation.

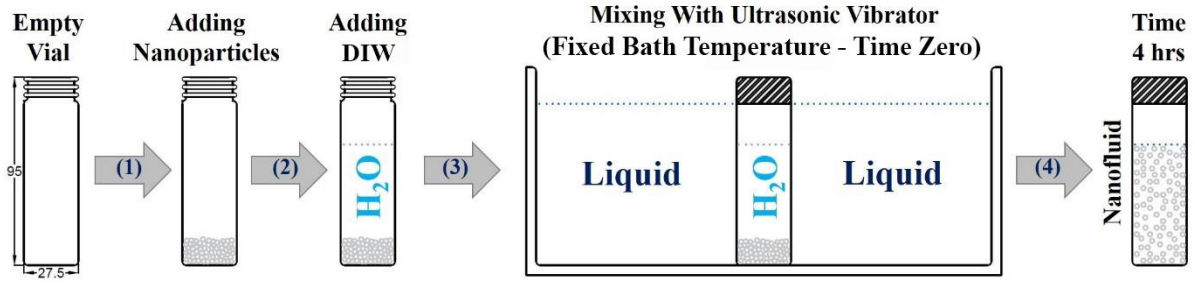

Fig. 3.2. Schematic procedure for the two-step nanofluids preparation.

2.4 Correlations development and validation

The pH value of the basefluid (pH_{bf}) was first measured for three times and averaged, at a temperature range of 10°C to 60°C with an increment of 5°C, as these values reflect the behaviour of the nanofluids with zero nanoparticle concentration. The measurements were then

plotted and fitted with a suitable trendline relation in order to obtain the best fit equation, which is valid in the range of $10°C \leq T \leq 60°C$. Next, the average pH values of each material employed to form the nanofluids, of 0.1, 0.5, and 1.0 vol%, were plotted after measuring them at different controlled production temperature, while fixing a single parameter (i.e. sonication bath temperature or particles concentration). The plotted data were then fitted with a trendline relation to acquire their equations and nondimensionalised using a reference temperature (T_0) and a reference basefluid pH value (pH_{bf0}), which were selected to be 25ºC and 7, respectively. This was done to have the correlations independent of any units using the surrounding temperature condition. Afterwards, the temperature dependant correlation and the particle concentration correlation were combined together and their regression coefficients were taking as unknown variables. An Excel 2016 data analysis tool was used to determine the new correlation regression coefficient variables and the validation of the proposed correlation was performed by comparing it with the 0.3 and 0.7 vol% as-fabricated nanofluids measured pH values.

3. Results and discussion

3.1 X-ray diffraction analysis and nanoparticles density measurement

The XRD pattern of the as-received SS 316L is shown in Fig. 3.3(a). It can be notice that only ferrite (BCC) and austenite (FCC) peaks are shown in the plot which indicates that the microstructure is solely composed of these two phases. The crystallite sizes obtained from the strongest Bragg's peaks of the austenite (111) and ferrite (110) phases are about 47 nm and 44 nm, respectively. Figure 3.3(b) demonstrates the diffraction pattern of the as-received Al NPs. The peaks observed from the analysis shows traces of oxidation in the Al sample, practically at angles 2θ = 20.46°, 40.80°, and 48.82° which are indexed as (020), (041), and (042), subsequently. Crystallite sizes found at the highest peaks of Al (111) and α-Al_2O_3 (042) are about 50 nm and 91 nm, respectively. Figure 3.3(c) of the as-received Cu_2O nanopowder pattern shows the present of Cu and CuO peaks, which is normal, since the Cu_2O NPs are very unstable and when exposed to the outer air the material is likely to oxidize to CuO, or return back to Cu. This kind of behaviour was also stated by the manufacturer [49]. Highest peaks of Cu_2O (111), Cu_2O (200), Cu_2O (220), and Cu (111) showed crystallite sizes of 20 nm, 15 nm, 13 nm, and 75 nm, respectively. It is worth noting that all crystallite sizes (D_{hkl}) were obtained using the Scherrer formula (Eq. 1), which is commonly used by many researchers [50-53].

$$D_{hkl} = \frac{F\lambda}{\beta_{hkl} cos\theta_{hkl}} \quad (1)$$

Where F represents a constant value equal to 0.9, λ illustrates the wavelength of the Cu K_α X-ray radiation source and is equal to 0.15405 nm, β_{hkl} demonstrates the full width at half the maximum of the (hkl) diffraction peak, and θ_{hkl} represents the Bragg angle at (hkl) peak.

Density of the as-received SS 316L, Al, and Cu_2O NPs, based on the volume and mass, are shown in Table 3.2 along with their standard deviation (SD).

Table 3.2. The as-received nanoparticles densities.

Nanoparticle type	**Mass (g)**	**Sample volume (cm^3)**	**Density (g/cm^3)**	**SD $\times 10^{-2}$**
Stainless steel 316L	0.2	0.033	6.02	0.18
Aluminium	0.2	0.621	3.22	0.81
Copper(I) oxide	0.2	0.566	3.53	0.14

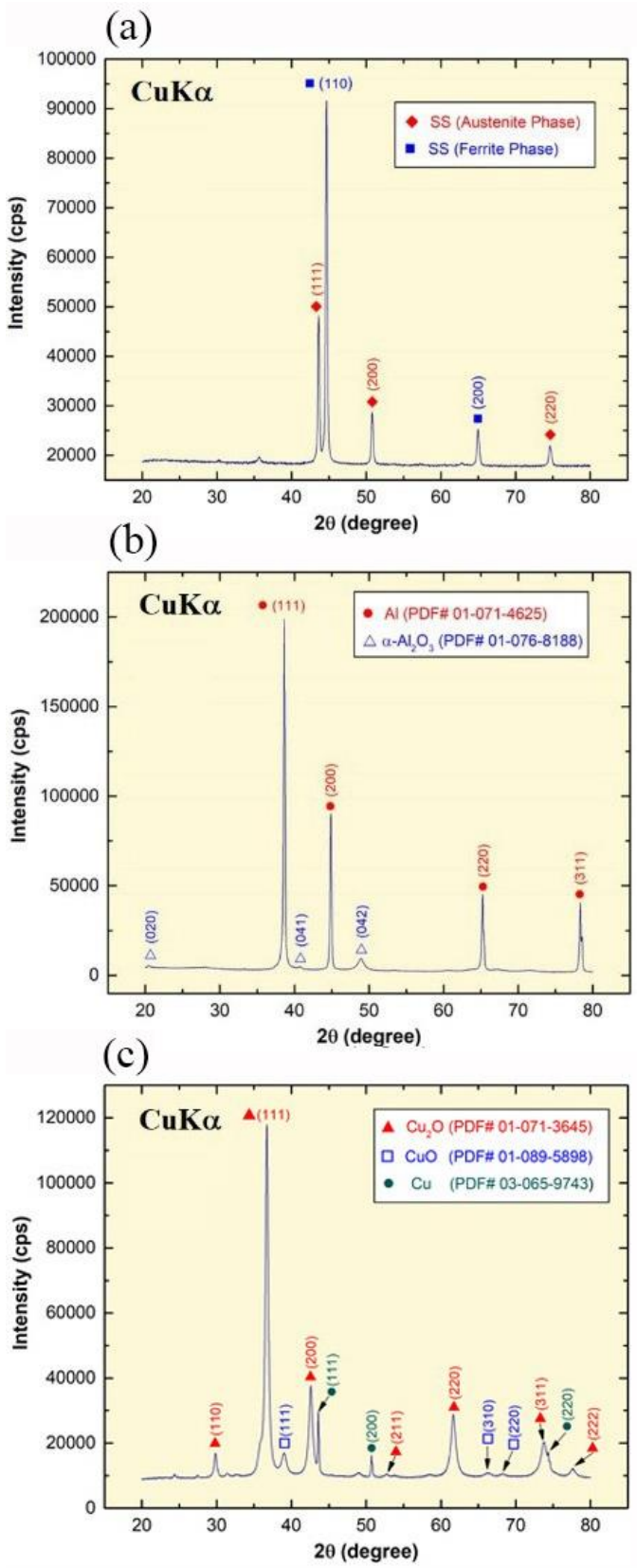

Fig. 3.3. X-ray diffraction patterns of: (a) Stainless steel 316L NPs, (b) Aluminium NPs, and (c) Copper(I) oxide NPs.

These density (ρ) values were employed in the mixing theory (Eq. 2) [54], which is widely used and agreed upon by many researchers [16], to calculate the amount of NPs required for the preparation of the nanofluids of selected vol%, where V_{np}, V_{bf}, and m are the NPs volume, basefluid volume, and mass, respectively.

$$vol\% = \frac{V_{np}}{V_{np} + V_{bf}} = \frac{\left(\frac{m}{\rho}\right)_{np}}{\left(\frac{m}{\rho}\right)_{np} + \left(\frac{m}{\rho}\right)_{bf}} \quad (2)$$

3.2 Basefluid pH variation with temperature

In this study, DIW was used as the basefluid for preparing the different types of nanofluids. Thus, the pH value of DIW was measured first at a temperature range of 10°C to 60°C, in order to reflect the nanofluids pH values when the concentration of NPs is equal to zero. Figure 3.4(a) shows the DIW averaged pH value measurements results at different point of temperature, where a monotonic variation in pH with temperature is observed. The highest variation in the pH measurements, within one temperature point, was ±0.05 at 10°C and 60°C, and the lowest was ±0.02 at 20°C to 35°C. It is important to note that, although the pH value of DIW, of pH 7 at 25°C, is increasing/decreasing with the change in liquid temperature, the fluid is still considered to be neutral, but only at that point of temperature. This is because, theoretically, rising/lowering the temperature of DIW above/below 25°C would result in increasing/decreasing the amount of free hydrogen ions and hydroxide ions equally, thus the variation seen in pH value is due to the change in the ionic product constant of water (K_w) [55]. A 3rd order polynomial relation fits the data well and the equation obtained from it (Eq. 3) is valid in the range of 10°C ≤ T ≤ 60°C.

$$pH_{bf} = a_0 + a_1 T + a_2 T^2 + a_3 T^3; \quad (3)$$

With $R^2 = 0.993$

Where the regression constants a_0, a_1, a_2, and a_3 are equal to 7.56, -0.027, 1.86×10^{-4}, and -3.22×10^{-7}, respectively.

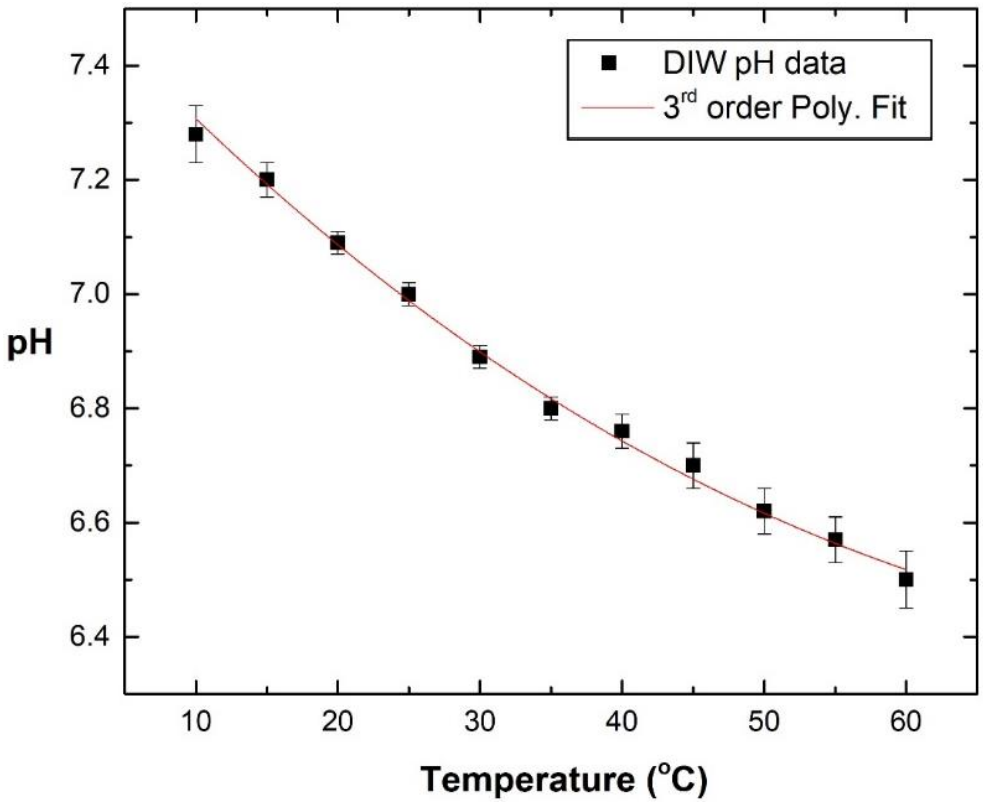

Fig. 3.4. Measured deionised water pH value at a temperature range from 10°C to 60°C.

3.3 Nanofluids pH variation

The pH value of SS 316L/DIW, Al/DIW, and Cu_2O/DIW nanofluids for three concentrations, namely, 0.1, 0.5, and 1.0 vol% is presented in terms of sonication bath temperature variation (Fig. 3.5(a-c)) and change in NPs volume percentage (Fig. 3.6(a-c)). The maximum deviation in the three pH measurements for all three nanofluids, at a single point of temperature, was seen to be ±0.04. Several distinct characteristics of the nanofluids are observed from the plots. Similar to the basefluid behaviour (Fig. 3.4), the nanofluids pH value tends to decrease with the increase in fabrication temperature. For example, Fig. 3.5(a) shows a reduction of 4.40, 4.68, and 7.84% in the measured pH values of the 0.1. 0.5, and 1.0 vol% SS 316L nanofluids at a temperature of 60°C compared with their pH values at 10°C. It is important to note that the mechanism in which the fabrication temperature influences the as-prepared nanofluid pH value is not quite clear. In addition, it was further noticed that the increase in NPs concentration caused the fluid pH value to rise from its initial basefluid state. This kind of outcome is expected, since the added NPs to the basefluid tend to attract the free hydrogen ions within the as-prepared DIW, thus keeping the liquid with higher amount of free hydroxide ions. Hence, the pH_{nf} is predicted to be higher than the pH_{bf} at each preparation temperature.

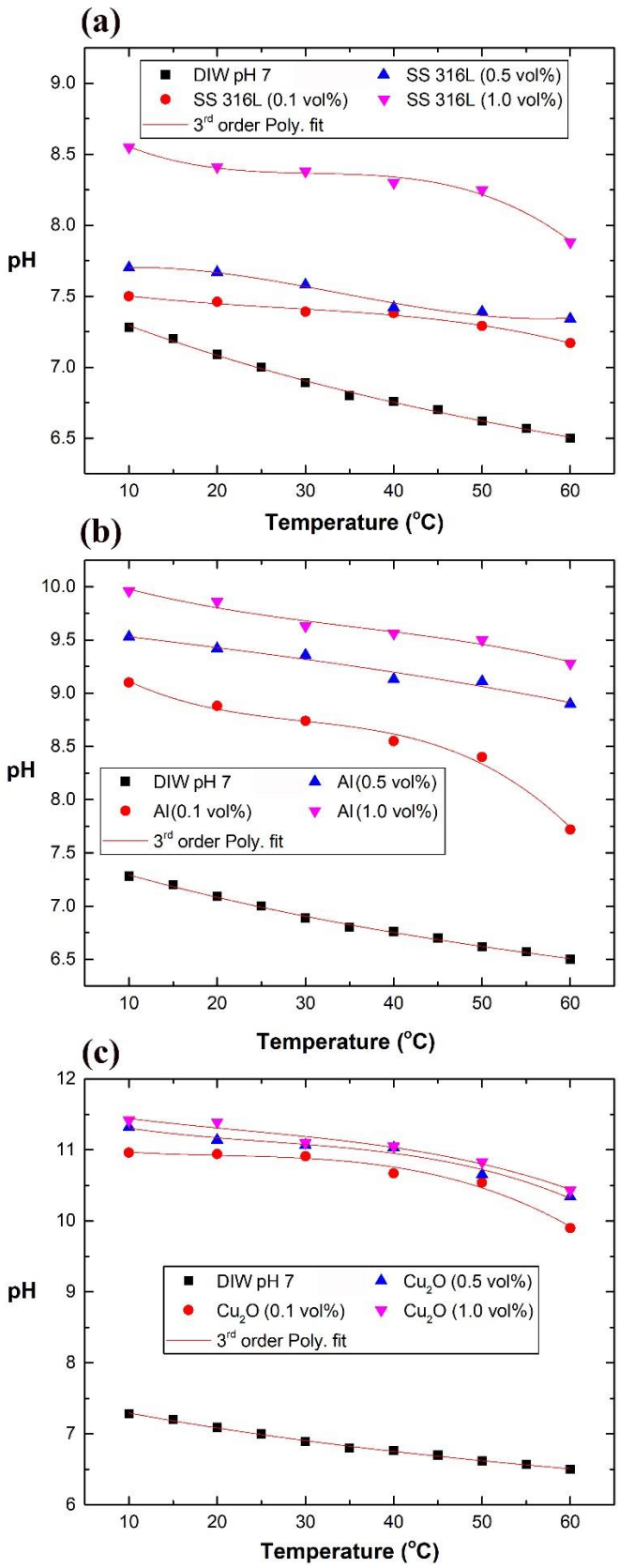

Fig. 3.5. Nanofluids, of 0.1, 0.5, and 1.0 vol%, pH variation with temperature for: (a) SS 316L/DIW, (b) Al/DIW, and (c) Cu_2O/DIW.

Depending on the NPs material used, the nanofluid pH value can either be strongly influenced by the NPs concentration (e.g. SS 316L/DIW and Al/DIW), or fixed fabrication temperature (e.g. Cu_2O/DIW). For further illustration, analysing the NPs volumetric concentration and controlled production temperature effect on the pH value of Al/DIW nanofluids (Fig. 3.5(b) and 3.6(b)) showed that the average change in pH obtained from increasing the concentration alone across the examined temperature range was 11.13%, while increasing the production temperature for each fixed concentration had an average pH variation of 9.53%.

In addition, it can be seen that all three types of nanofluids pH data, at a specific concentration, follows a 3rd order polynomial relation fit which can be expressed by Eq. 4 along with the regression constants shown in Table 3.3.

$$pH_{nf} = b_0 + b_1 \mathrm{T} + b_2 T^2 + b_3 T^3 \quad (4)$$

Furthermore, from the data in Fig. 3.6, at each as-prepared fluid fabrication temperature, the variation in pH value in respect of NPs volume percentage is seen to cohabit a 2nd order polynomial relation, for all three types of nanofluids, which can be expressed as:

$$pH_{nf} = c_0 + c_1 \phi + c_2 \phi^2 \quad (5)$$

With $R^2 = 1$

Equations 4 and 5 are valid in the range of $10°C \leq T \leq 60°C$, and $0.1 \text{ vol\%} \leq \phi \leq 1.0 \text{ vol\%}$ with the regression constants of Eq. 5 (i.e. c_0, c_1, and c_2) are tabulated in Table 3.4.

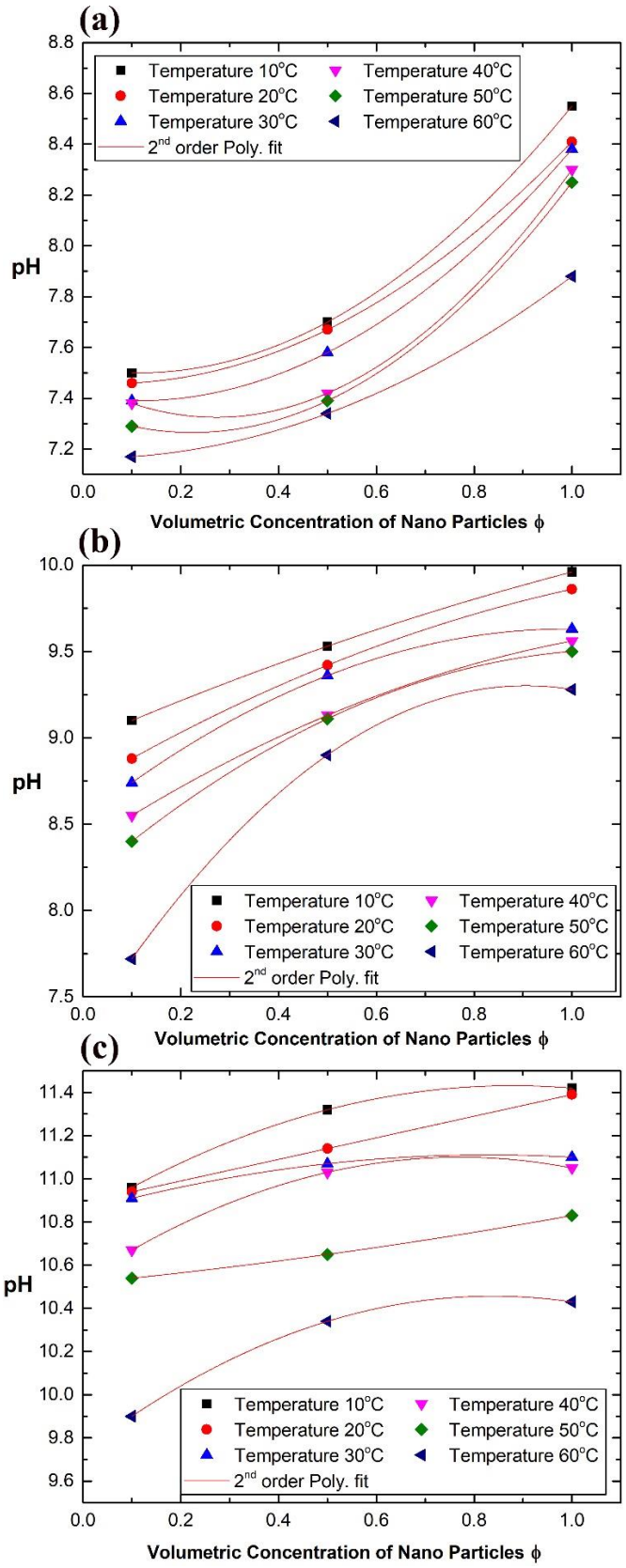

Fig. 3.6. Nanofluids, of 0.1, 0.5, and 1.0 vol%, pH variation with concentration for: (a) SS 316L/DIW, (b) Al/DIW, and (c) Cu_2O/DIW.

Table 3.3. Regression coefficients of Eq. 4 for SS 316L, Al/DIW, and Cu_2O/DIW nanofluids.

Regression constants	**SS 316L/DIW**			**Al/DIW**			**Cu_2O/DIW**		
	0.1 vol%	**0.5 vol%**	**1.0 vol%**	**0.1 vol%**	**0.5 vol%**	**1.0 vol%**	**0.1 vol%**	**0.5 vol%**	**1.0 vol%**
b_0	7.60	7.63	8.93	9.68	9.63	10.24	11.10	11.56	11.64
b_1	-0.013	0.014	-0.052	-0.077	-0.01	-0.032	-0.021	-0.033	-0.024
b_2	3.226×10^{-4}	-7.528×10^{-4}	1.64×10^{-3}	0.0023	-2.381×10^{-6}	5.976×10^{-4}	8.722×10^{-4}	9.361×10^{-4}	5.266×10^{-4}
b_3	-3.889×10^{-6}	7.407×10^{-6}	-1.769×10^{-5}	-2.574×10^{-5}	-5.556×10^{-7}	-5.556×10^{-6}	-1.426×10^{-5}	-1.213×10^{-5}	-7.685×10^{-6}
R^2	0.974	0.959	0.970	0.978	0.921	0.932	0.955	0.950	0.941

Table 3.4. Regression coefficients of Eq. 5 for SS 316L, Al/DIW, and Cu_2O/DIW nanofluids.

Temperature (°C)	SS 316L/DIW			Al/DIW			Cu_2O/DIW		
	c_0	c_1	c_2	c_0	c_1	c_2	c_0	c_1	c_2
10	7.52	-0.300	1.333	8.98	1.218	-0.239	10.83	1.367	-0.778
20	7.46	-0.112	1.061	8.72	1.663	-0.522	10.89	0.5	4.428×10^{-15}
30	7.40	-0.275	1.250	8.53	2.223	-1.122	10.85	0.627	-0.378
40	7.46	-1.007	1.844	8.37	1.843	-0.656	10.53	1.473	-0.956
50	7.35	-0.730	1.633	8.17	2.438	-1.106	10.52	0.218	0.094
60	7.16	-0.012	0.728	7.30	4.410	-2.433	9.74	1.713	-1.022

3.4 Correlation development

From analysing the experimental results of Fig. 3.5 and Fig. 3.6, it was found that the pH value of each type of nanofluid examined depends on the volumetric concentration of the NPs used and the temperature of suspension fabrication. In order to establish a joint link between the two parameters (i.e. T and ϕ) and the nanofluid pH value, an analysis of the variation of these parameters independently was carried out. Having the correlation independent of any units, the pH_{nf} was nondimensionalised by that of the basefluid, at room temperature conditions, using the parameters pH_{bf0} and T_0 values.

3.5 Influence of temperature

The pH values of SS 316L/DIW, Al/DIW, and Cu_2O/DIW nanofluids in Fig. 3.5 were nondimensionalised using the value of pH_{bf0} then plotted in contrast to the nondimensionalised temperature ($\frac{T}{T_0}$), for each of the three nanoparticle concentrations. It can be observed from Fig. 3.7 that the pH ratio ($\frac{pH_{nf}}{pH_{bf0}}$) against ($\frac{T}{T_0}$) corresponds to a 3rd order polynomial relation. Thus, the correlation for ($\frac{pH_{nf}}{pH_{bf0}}$) as a function of ($\frac{T}{T_0}$) can be best represented as:

$$\frac{pH_{nf}}{pH_{bf0}} = d_0 + d_1(\frac{T}{T_0}) + d_2(\frac{T}{T_0})^2 + d_3(\frac{T}{T_0})^3 \quad (6)$$

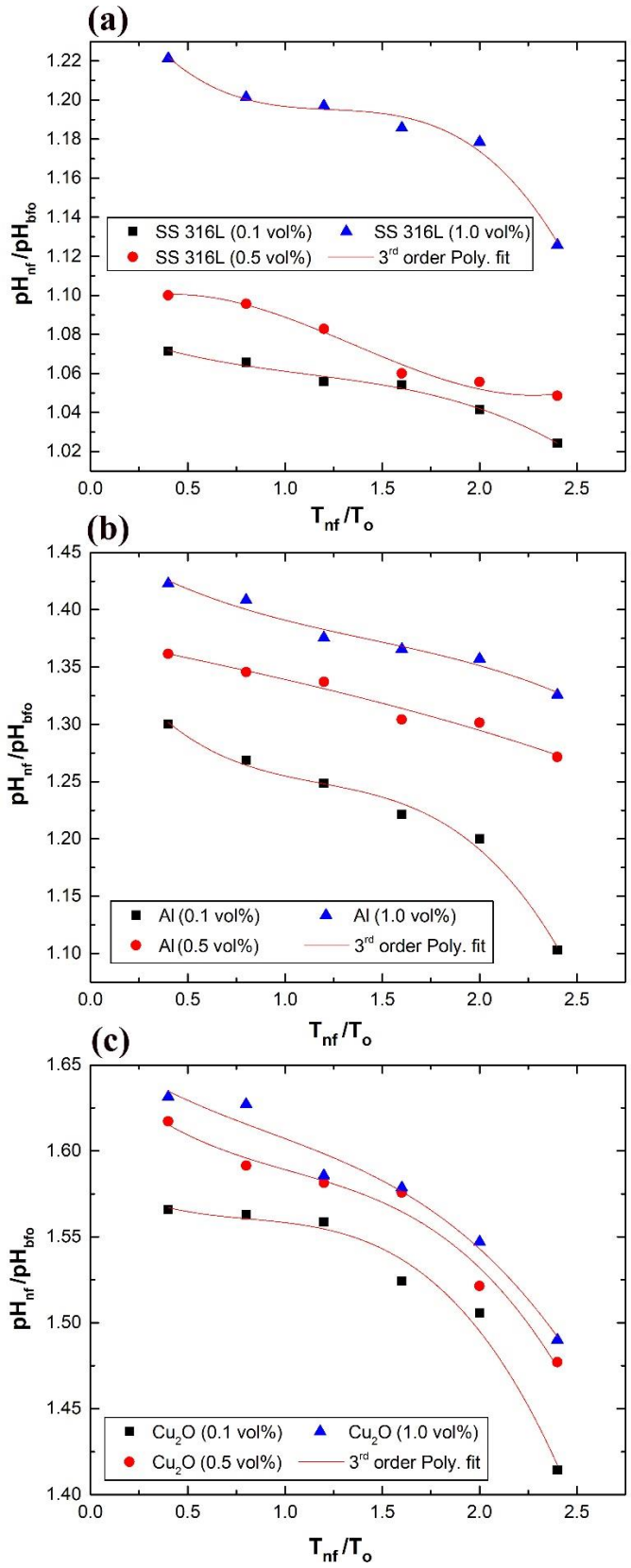

Fig. 3.7. Nanofluids, of 0.1, 0.5, and 1.0 vol%, nondimensionalised pH variation against $(\frac{T}{T_0})$ for: (a) SS 316L/DIW, (b) Al/DIW, and (c) Cu_2O/DIW.

3.6 Influence of concentration

From Fig. 3.6 and Eq. 5, it was demonstrated that the variation in pH_{nf} as a function of ϕ followed a 2nd order polynomial relation at a fixed fabrication temperature. This was examined for all three types of nanofluids that were produced from a controlled sonication bath temperature that ranged from 10°C to 60°C. Due to the nature of Eq. 5, the appropriate nondimensionalisation representation of the correlation can be shown as following:

$$\frac{pH_{nf}}{pH_{bf0}} = e_0 + e_1\phi + e_2\phi^2 \tag{7}$$

3.7 Proposed correlation

From the previous two analysis of the influence of each parameter (i.e. section 3.5 and 3.6), it was found that a general pH_{nf} correlation can be illustrated by combining Eq. 6 and Eq. 7 in the following format:

$$\frac{pH_{nf}}{pH_{bf0}} = \left[d_o + d_1\left(\frac{T}{T_0}\right) + d_2\left(\frac{T}{T_0}\right)^2 + d_3\left(\frac{T}{T_0}\right)^3\right].[e_0 + e_1\phi + e_2\phi^2] \tag{8}$$

Equation 8 was then extended to Eq. 9 because of the infinite number of solutions that can be obtained at the current state to the regression coefficients.

$$\frac{pH_{nf}}{pH_{bf0}} = X_0 + X_1\left(\frac{T}{T_0}\right) + X_2\left(\frac{T}{T_0}\right)^2 + X_3\left(\frac{T}{T_0}\right)^3 + X_4\phi + X_5\phi\left(\frac{T}{T_0}\right) + X_6\phi\left(\frac{T}{T_0}\right)^2 + X_7\phi\left(\frac{T}{T_0}\right)^3 + X_8\phi^2 + X_9\phi^2\left(\frac{T}{T_0}\right) + X_{10}\phi^2\left(\frac{T}{T_0}\right)^2 + X_{11}\phi^2\left(\frac{T}{T_0}\right)^3 \tag{9}$$

Where the correspondence of the new regression coefficients (i.e. X_0 to X_{11}) are shown in Table 3.5.

Table 3.5. Regression coefficients of Eq. 9 and their correspondence.

Regression coefficient	**Representation**	**Regression coefficient**	**Representation**	**Regression coefficient**	**Representation**
X_0	$d_o.e_0$	X_4	$d_o.e_1$	X_8	$d_o.e_2$
X_1	$d_1.e_0$	X_5	$d_1.e_1$	X_9	$d_1.e_2$
X_2	$d_2.e_0$	X_6	$d_2.e_1$	X_{10}	$d_2.e_2$

X_3	$d_3.e_0$	X_7	$d_3.e_1$	X_{11}	$d_3.e_2$

The Excel 2016 data analysis regression tool was then used to determine the values of the unknown regression coefficients of Eq. 9 for the different types of nanofluids from their nondimensionalised pH_{nf} measured data and $(\frac{T}{T_0})$. Table 3.6 shows the statistical analysis tabulation of the regression coefficients, where Eq. 9 with the coefficients of Table 3.6 has a range of validity of 10°C ≤ T ≤ 60°C, and 0.1 vol% ≤ ϕ ≤ 1.0 vol%.

Table 3.6. Regression coefficients of Eq. 9 values for different as-fabricated nanofluids.

Regression constant	**SS 316L/DIW**	**Al/DIW**	**Cu_2O/DIW**
X_0	1.104	1.395	1.562
X_1	-0.107	-0.376	-0.053
X_2	0.090	0.289	0.072
X_3	-0.025	-0.081	-0.033
X_4	-0.227	-0.144	0.255
X_5	0.703	1.099	-0.229
X_6	-0.685	-0.922	0.073
X_7	0.180	0.249	0.007
X_8	0.397	0.212	-0.154
X_9	-0.781	-0.837	0.197
X_{10}	0.741	0.686	-0.097
X_{11}	-0.195	-0.181	0.009

R^2	0.995	0.985	0.953
Maximum deviation	-0.90%	-1.24%	+0.95%
Average deviation	0.28%	0.50%	0.38%

3.8 Validation of the new correlation

In order to validate the newly developed correlation, the pH of the as-prepared 0.3 and 0.7 vol% nanofluids of different fixed fabrication temperatures were compared with the proposed correlation in terms of experimental measurement against theoretical computation as demonstrated in Fig. 3.8. The central line in Fig. 3.8(a-b) represents a perfect match between the new correlation values and the experimental data. It can be notice that there exists some level of deviation between the measured data and the correlation prediction, especially with the measured data of SS 316L/DIW nanofluid. Nevertheless, the correlation shows very good estimation towards the pH_{nf} for all three types of nanofluids, where the highest prediction error was shown to be -8.09% (at T = 40°C and ϕ = 0.7 vol%) for SS 316L/DIW, +5.08% (at T = 60°C and ϕ = 0.7 vol%) for Al/DIW, and +2.31% (at T = 60°C and ϕ = 0.7 vol%) for Cu_2O/DIW. The average error of the newly proposed correlation, for the 0.1-1.0 vol% SS 316L/DIW, Al/DIW, and Cu_2O/DIW samples, was found to be 2.18%, 0.92%, and 0.63%, respectively. Given a specific controlled sonication bath temperature and NPs concentration, the correlation of Eq. 9 insures at least 91% confidence that the value will be between the upper and lower prediction error limits of the curve-fit range. Such level of error is acceptable for many industrial applications, since the highest deviation from the actual pH_{nf} measurement would be within a value of ±0.57 (i.e. less than 1).

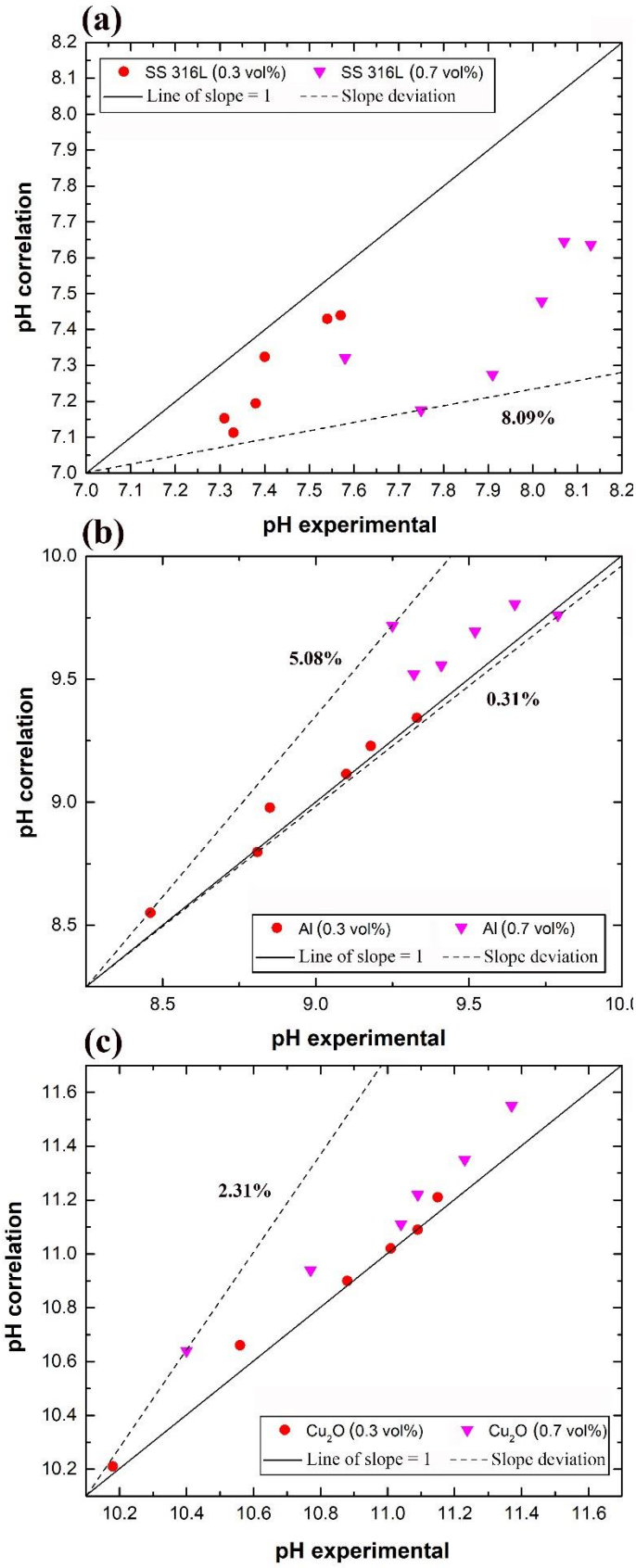

Fig. 3.8. Comparison between the new correlation prediction (Eq. 9) and the measured pH of: (a) SS 316L/DIW, (b) Al/DIW, and (c) Cu_2O/DIW.

4. Summary

Measurements of the pH value of three types of nanofluids, namely, SS 316L/DIW, Al/DIW, and Cu_2O/DIW were performed in order to develop a general correlation that can predict the pH_{nf} value, within the conducted experiments range, from the liquid production temperature and nanoparticle volumetric concentration. All three types of nanofluids were fabricated using a controlled sonication bath temperature two-step approach, with 0.1 to 1.0 vol% of NPs. The following conclusions are drawn:

- The experimental findings have indicated that, increasing the NPs concentration in the basefluid had an alkaline effect, while rising the temperature caused the nanofluid to be more acidic. Such behaviours are expected to be a result of: 1- the NPs attraction of free hydrogen ions within the basefluid, and 2- the increase in the amount of ions been freed from their water molecules caused by the rise in fluid temperature.
- In addition, depending on the nanoparticle material, the pH_{nf} can be strongly influenced by either the controlled sonication bath temperature, as in the case of Cu_2O/DIW, or the changes in nanofluid particle concentration (e.g. SS 316L/DIW, and Al/DIW). For instant, by analysing the pH value of Al/DIW for the two aforementioned parameters, the average change in pH_{nf} due to increasing the particles volumetric concentration alone over the fixed bath temperatures have shown to be 11.13%, whereas varying the processing controlled temperatures for each volumetric concentration has resulted in a 9.53% average change in pH.
- Using the experimental data, a new pH_{nf} correlation was developed as a function of fabrication bath temperature and NPs volume concentration to estimate the pH value of the three previous types of nanofluids. The proposed correlation has illustrated a high prediction capability, where its average error for SS 316L/DIW, Al/DIW, and Cu_2O/DIW have shown to be 2.18%, 0.92%, and 0.63%, respectively.

Nevertheless, it should be acknowledged that, due to the variation in nanofluid dispersant methods and their NPs crystal structures, the presented correlation are very helpful and reliable for applications that uses nanofluids fabricated similarly to the conducted study approach and parametric range. These correlations will be advanced for additional parameters such as NPs average size, shape, and the existence of surfactants.

References

1. Choi, S.U.S.; Eastman, J.A. *Enhancing thermal conductivity of fluids with nanoparticles.* ; Argonne National Lab., IL (United States): 1995; p Medium: ED; Size: 8 p.

2. Keblinski, P.; Eastman, J.A.; Cahill, D.G. Nanofluids for thermal transport. *Materials Today* **2005**, *8*, 36-44.

3. Anushree, C.; Philip, J. Assessment of long term stability of aqueous nanofluids using different experimental techniques. *Journal of Molecular Liquids* **2016**, *222*, 350-358.

4. Ilyas, S.U.; Pendyala, R.; Shuib, A.S.; Marneni, N. A review on the viscous and thermal transport properties of nanofluids. In *International Conference on Process Engineering and Advanced Materials, ICPEAM 2012*, Trans Tech Publications Ltd: Kuala Lumpur, 2014; Vol. 917, pp 18-27.

5. Shanthi, R.; Anandan, S.S.; Ramalingam, V. Heat transfer enhancement using nanofluids an overview. *Therm. Sci.* **2012**, *16*, 423-444.

6. Wen, D.S.; Lin, G.P.; Vafaei, S.; Zhang, K. Review of nanofluids for heat transfer applications. *Particuology* **2009**, *7*, 141-150.

7. Vekas, L.; Bica, D.; Avdeev, M.V. Magnetic nanoparticles and concentrated magnetic nanofluids: Synthesis, properties and some applications. *China Particuology* **2007**, *5*, 43-49.

8. Reddy, K.S.; Kamnapure, N.R.; Srivastava, S. Nanofluid and nanocomposite applications in solar energy conversion systems for performance enhancement: A review. *Int. J. Low Carbon Technol.* **2017**, *12*, 1-23.

9. Sheikholeslami, M.; Ganji, D.D. Chapter 1 - application of nanofluids. In *Applications of semi analytical methods for nanofluid flow and heat transfer*, Sheikholeslami, M.; Ganji, D.D., Eds. Elsevier: 2018; pp 1-44.

10. Mansoury, D.; Faramarz, I.D.; Kiani, A.; Chamkha, A.J.; Sharifpur, M. Heat transfer and flow characteristics of al2o3/water nanofluid in various heat exchangers: Experiments on counter flow. *Heat Transfer Eng* **2018**, 1-36.

11. Chamkha, A.J.; Molana, M.; Rahnama, A.; Ghadami, F. On the nanofluids applications in microchannels: A comprehensive review. *Powder Technol.* **2018**, *332*, 287-322.

12. Ilyas, S.U.; Pendyala, R.; Marneni, N. In *Stability and agglomeration of alumina nanoparticles in ethanol-water mixtures*, 4th International Conference on Process Engineering and Advanced Materials, ICPEAM 2016, 2016; Bustam, M.A.; Keong, L.K.; Man, Z.; Hassankiadeh, A.A.; Fong, Y.Y., Eds. Elsevier Ltd: pp 290-297.

13. Ilyas, S.U.; Pendyala, R.; Marneni, N. Preparation, sedimentation, and agglomeration of nanofluids. *Chemical Engineering & Technology* **2014**, *37*, 2011-2021.

14. Mukherjee, S.; Mishra, P.C.; Chaudhuri, P. Stability of heat transfer nanofluids – a review. *ChemBioEng Reviews* **2018**, *5*, 312-333.

15. Bushehri, M.K.; Mohebbi, A.; Rafsanjani, H.H. Prediction of thermal conductivity and viscosity of nanofluids by molecular dynamics simulation. *J. Eng. Thermophys.* **2016**, *25*, 389-400.

16. Ali, N.; Teixeira, J.A.; Addali, A. A review on nanofluids: Fabrication, stability, and thermophysical properties. *J. Nanomater.* **2018**, *2018*, 33.

17. Hong, J.; Kim, D. Effects of aggregation on the thermal conductivity of alumina/water nanofluids. *Thermochim Acta* **2012**, *542*, 28-32.

18. Arthur, O.; Karim, M.A. An investigation into the thermophysical and rheological properties of nanofluids for solar thermal applications. *Renewable & Sustainable Energy Reviews* **2016**, *55*, 739-755.

19. Suganthi, K.S.; Rajan, K.S. Metal oxide nanofluids: Review of formulation, thermo-physical properties, mechanisms, and heat transfer performance. *Renewable & Sustainable Energy Reviews* **2017**, *76*, 226-255.

20. Mahbubul, I.M.; Elcioglu, E.B.; Saidur, R.; Amalina, M.A. Optimization of ultrasonication period for better dispersion and stability of tio2-water nanofluid. *Ultrason Sonochem* **2017**, *37*, 360-367.

21. Das, P.K. A review based on the effect and mechanism of thermal conductivity of normal nanofluids and hybrid nanofluids. *Journal of Molecular Liquids* **2017**, *240*, 420-446.

22. Peng, X.F.; Yu, X.L.; Xia, L.F.; Zhong, X. Influence factors on suspension stability of nanofluids. *Zhejiang Daxue Xuebao (Gongxue Ban)* **2007**, *41*, 577-580.

23. Choudhary, R.; Khurana, D.; Kumar, A.; Subudhi, S. Stability analysis of al2o3/water nanofluids. *J. Exp. Nanosci.* **2017**, *12*, 140-151.

24. Zhu, H.; Zhang, C.; Tang, Y.; Wang, J.; Ren, B.; Yin, Y. *Preparation and thermal conductivity of suspensions of graphite nanoparticles*. 2007; Vol. 45, p 226-228.

25. Li, X.; Zhu, D.; Wang, X. Evaluation on dispersion behavior of the aqueous copper nano-suspensions. *J Colloid Interface Sci* **2007**, *310*, 456-463.

26. Haghighi, E.B.; Nikkam, N.; Saleemi, M.; Behi, M.; Mirmohammadi, S.A.; Poth, H.; Khodabandeh, R.; Toprak, M.S.; Muhammed, M.; Palm, B. Shelf stability of nanofluids and its effect on thermal conductivity and viscosity. *Meas. Sci. Technol.* **2013**, *24*.

27. Askari, S.; Koolivand, H.; Pourkhalil, M.; Lotfi, R.; Rashidi, A. Investigation of fe3o4/graphene nanohybrid heat transfer properties: Experimental approach. *Int. Commun. Heat Mass Transf.* **2017**, *87*, 30-39.

28. Mohammadi, M.; Dadvar, M.; Dabir, B. Tio2/sio2 nanofluids as novel inhibitors for the stability of asphaltene particles in crude oil: Mechanistic understanding, screening, modeling, and optimization. *Journal of Molecular Liquids* **2017**, *238*, 326-340.

29. Leong, K.Y.; Najwa, Z.A.; Ahmad, K.Z.K.; Ong, H.C. Investigation on stability and optical properties of titanium dioxide and aluminum oxide water-based nanofluids. *Int J Thermophys* **2017**, *38*.

30. Kumar, P.C.M.; Muruganandam, M. Stability analysis of heat transfer mwcnt with different base fluids. *J. Appl. Fluid Mech.* **2017**, *10*, 51-59.

31. Menbari, A.; Alemrajabi, A.A.; Ghayeb, Y. Investigation on the stability, viscosity and extinction coefficient of cuo-al2o3/water binary mixture nanofluid. *Exp. Therm. Fluid Sci.* **2016**, *74*, 122-129.

32. Hwang, Y.; Lee, J.K.; Lee, J.K.; Jeong, Y.M.; Cheong, S.I.; Ahn, Y.C.; Kim, S.H. Production and dispersion stability of nanoparticles in nanofluids. *Powder Technol.* **2008**, *186*, 145-153.

33. Yu, W.; Xie, H.Q. A review on nanofluids: Preparation, stability mechanisms, and applications. *J. Nanomater.* **2012**, *2012*.

34. Wang, X.J.; Zhu, D.S.; Yang, S. Investigation of ph and sdbs on enhancement of thermal conductivity in nanofluids. *Chem. Phys. Lett.* **2009**, *470*, 107-111.

35. Li, X.F.; Zhu, D.S.; Wang, X.J.; Wang, N.; Gao, J.W.; Li, H. Thermal conductivity enhancement dependent ph and chemical surfactant for cu-h2o nanofluids. *Thermochim Acta* **2008**, *469*, 98-103.

36. Witharana, S.; Palabiyik, I.; Musina, Z.; Ding, Y.L. Stability of glycol nanofluids - the theory and experiment. *Powder Technol.* **2013**, *239*, 72-77.

37. Lee, J.; Han, K.; Koo, J. A novel method to evaluate dispersion stability of nanofluids. *Int. J. Heat Mass Transf.* **2014**, *70*, 421-429.

38. Zhu, D.S.; Li, X.F.; Wang, N.; Wang, X.J.; Gao, J.W.; Li, H. Dispersion behavior and thermal conductivity characteristics of al2o3-h2o nanofluids. *Curr. Appl. Phys.* **2009**, *9*, 131-139.

39. Modak, M.; Chougule, S.S.; Sahu, S.K. An experimental investigation on heat transfer characteristics of hot surface by using cuo-water nanofluids in circular jet impingement cooling. *Journal of Heat Transfer-Transactions of the Asme* **2018**, *140*.

40. Manjula, S.; Kumar, S.M.; Raichur, A.M.; Madhu, G.M.; Suresh, R.; Raj, M.A.L.A. A sedimentation study to optimize the dispersion of alumina nanoparticles in water. *Cerâmica* **2005**, *51*, 121-127.

41. Witharana, S.; Hodges, C.; Xu, D.; Lai, X.J.; Ding, Y.L. Aggregation and settling in aqueous polydisperse alumina nanoparticle suspensions. *J. Nanopart. Res.* **2012**, *14*.

42. Lee, D.; Kim, J.W.; Kim, B.G. A new parameter to control heat transport in nanofluids: Surface charge state of the particle in suspension. *J Phys Chem B* **2006**, *110*, 4323-4328.

43. Song, Y.Y.; Bhadeshia, H.K.D.H.; Suh, D.W. Stability of stainless-steel nanoparticle and water mixtures. *Powder Technol.* **2015**, *272*, 34-44.

44. Ali, N.; Teixeira, J.A.; Addali, A.; Al-Zubi, F.; Shaban, E.; Behbehani, I. The effect of aluminium nanocoating and water ph value on the wettability behavior of an aluminium surface. *Applied Surface Science* **2018**, *443*, 24-30.

45. Ali, N.; Teixeira, J.A.; Addali, A.; Saeed, M.; Al-Zubi, F.; Sedaghat, A.; Bahzad, H. Deposition of stainless steel thin films: An electron beam physical vapour deposition approach. *Materials* **2019**, *12*, 571.

46. Nanomaterials, S. Stainless steel nanoparticles/ nanopowder. http://ssnano.com/inc/sdetail/stainless_steel_nanoparticles/2760 (October),

47. Hach. User manual - general use ph probe: Models phc20101, phc20103 (doc022.53.80197). https://www.hach.com/asset-get.download.jsa?id=8027841104 (14th of December),

48. Hach. Application note - temperature compensation with ph measurement (14 November),

49. US Research Nanomaterials, I. Copper(i) oxide (cuprous oxide) nanopowder / cu2o nanoparticles. http://www.us-nano.com/inc/sdetail/4128 (October),

50. Ai, X.W.; Lin, J.X.; Chang, Y.F.; Zhou, L.Q.; Zhang, X.M.; Qin, G.W. Phase modification of copper phthalocyanine semiconductor by converting powder to thin film. *Applied Surface Science* **2018**, *428*, 788-792.

51. Raleaooa, P.V.; Roodt, A.; Mhlongo, G.G.; Motaung, D.E.; Ntwaeaborwa, O.M. Analysis of the structure, particle morphology and photoluminescent properties of zns:Mn2+ nanoparticulate phosphors. *Optik* **2018**, *153*, 31-42.

52. Rabiee, M.; Mirzadeh, H.; Ataie, A. Processing of cu-fe and cu-fe-sic nanocomposites by mechanical alloying. *Adv Powder Technol* **2017**, *28*, 1882-1887.

53. Minaei, S.; Haghighi, M.; Jodeiri, N.; Ajamein, H.; Abdollahifar, M. Urea-nitrates combustion preparation of ceo2-promoted cuo/zno/al2o3 nanocatalyst for fuel cell grade hydrogen production via methanol steam reforming. *Adv Powder Technol* **2017**, *28*, 842-853.

54. Pak, B.C.; Cho, Y.I. Hydrodynamic and heat transfer study of dispersed fluids with submicron metallic oxide particles. *Exp. Heat Transf.* **1998**, *11*, 151-170.

55. Marshall, W.L.; Franck, E.U. Ion product of water substance, 0–1000 °c, 1–10,000 bars new international formulation and its background. *J. Phys. Chem. Ref. Data* **1981**, *10*, 295-304.

Chapter 4

Publication 3: Aluminium Nanofluids Stability: A Comparison Between The Conventional Two-Step Fabrication Approach And The Controlled Sonication Bath Temperature Method

(Ali, N.; Teixeira, J.A.; Addali, A. Aluminium Nanofluids Stability: A Comparison Between The Conventional Two-Step Fabrication Approach And The Controlled Sonication Bath Temperature Method, *J. Nanomater.*, In Press)

Aluminium Nanofluids Stability: A Comparison Between The Conventional Two-Step Fabrication Approach And The Controlled Sonication Bath Temperature Method

A B S T R A C T

This study investigates the shelving stability of dispersed aluminium nanoparticles in water mixtures fabricated by the conventional and the controlled bath temperature two-step methods. The nanofluids were prepared with water of pH 9 and nanoparticles of 0.1 – 1.0 vol.%. A bath type ultrasonicator was employed for dispersing the nanoparticles into the basefluid. The sonication process, for all as-prepared samples, lasted for 4 hours and was either device bath temperature uncontrolled or controlled in the range of 10 – 60^{o}C. Furthermore, the stability of the as-produced nanosuspensions was evaluated using the sedimentation photograph capturing method by capturing images at equal intervals of time for 12 hours then analysing the data based on the samples sedimentation height ratios. It was found that the sedimentation behaviour of the nanofluids fabricated via the controlled temperatures of less than 30^{o}C were of dispersed sedimentation type, while those produced by the conventional method and the fixed temperatures of 30^{o}C and higher were of flocculated sedimentation type. In addition, increasing the controlled sonication temperature has shown to increase the settling process of the sediments. Moreover, the rise in nanoparticles concentration was seen to reduce the variation in sedimentation height ratio between the fixed temperature samples. A comparison between the two fabrication methods has shown that the 30^{o}C nanofluids had better short and long-term stability than the conventionally produced suspensions.

Keywords: Colloidal; dispersed sedimentation; flocculated sedimentation; sedimentation height ratio; sedimentation photograph capturing method; shelving stability.

1. Introduction

Aluminium (Al) is one of the most abundant crustal metal found on earth, which due to its capability of being fully recyclable, it is considered as a very sustainable material. The element itself and its alloys possess valuable electrical, mechanical, and thermal properties, which make their usages in various fields, such as construction and building, electrical engineering, and

packaging favourable to the industry. Because of its relatively low density of 2700 kg/m^3, Al is known to be the lightest among most, if not all, commonly used metals [1]. The low density and promising properties of Al have, for long time, attracted manufacturers, especially in the automotive sector, to employ this element in fabricating their constructions and machined parts, so that the overall weight of the vehicles can be significantly reduced, and hence the fuel consumption and CO_2 emissions consequently get reduced alongside [2]. On the nanoscale, colloidal solutions containing Al nanoparticles (NPs) or its oxides (known as nanofluids) have been frequently reported as promising advanced working fluids that exceed conventional liquids in their heat transfer performance [3]. This is because the nanofluid effective thermal conductivity, which is the net thermal conductivity of the mixture, is seen to have a value within the range of the particles and the hosting fluid thermal conductivities. The highest effective thermal conductivity in any fabricated nanofluid can be achieved by optimizing the colloidal stability, which means that the dispersion of NPs needs to be maintained in a homogeneous manner at all time otherwise its thermal, along with the physical, properties will gradually degrade [4].

Often this is hardly even possible, as one of the main challenges that is associated with nanofluids is their poor stability, whereby the NPs tends to attract each other into forming different sizes of clusters of particles or agglomerations. The reason behind such attraction behaviour was previously found to be due to the imbalance between the electrostatic repulsion force caused by the electrical double layers on the particles large surface area and the strong Van der Waals force of attraction among the NPs [5].

Furthermore, the gravitational force tends to separate the agglomerated particles from the basefluid causing the sediments to settle at the bottom of the hosting fluid, and hence the kinetic stability of the nanofluid gets negatively impacted. There are three types of sedimentation behaviours that can be observed in any unstable nanofluid [6], which are: 1- dispersed sedimentation, 2- flocculated sedimentation, and 3- mixed sedimentation. An illustration of the three different types of sedimentation behaviours is shown in Fig. 4.1.

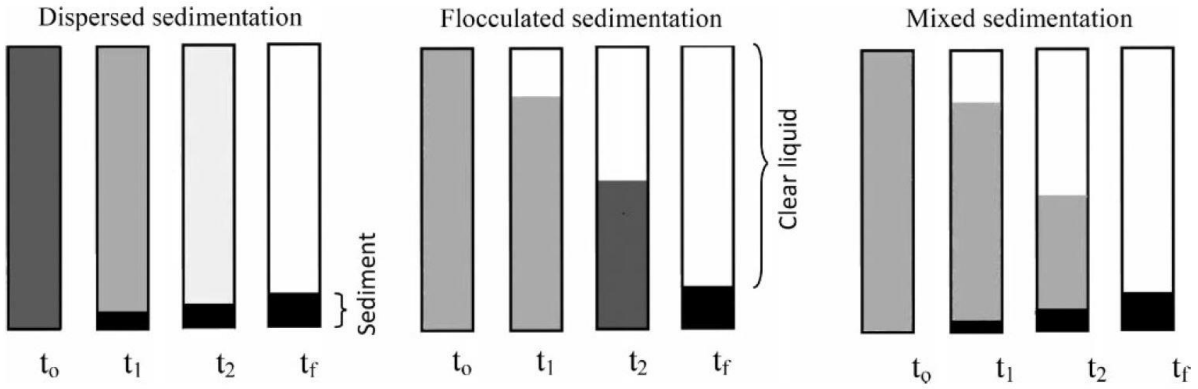

Fig. 4.1. Forms of sedimentation mechanism in unstable nanofluids, where t represent the settling time and $t_o<t_1<t_2<t_f$ [6].

Several methods were developed to evaluate the stability of nanofluids, such as: 1- zeta potential analysis, 2- centrifugation method, 3- spectral analysis approach, 4- 3ω-method, 5- electron microscopy analysis, and 6- sedimentation photograph capturing method [4]. From all of the aforementioned evaluation approaches, the sedimentation photograph capturing method is considered to be the simplest, cheapest, and is a reliable approach for measuring nanofluids stability [7, 8]. In this technique, images of the change in sedimentation settling behaviour, due to gravitational force, are captured within equal intervals of time, thus visual estimation of nanofluids shelf-life can therefore be obtained [9]. It is important to note that this approach is considered as a qualitative method rather than a quantitative one. On the other hand, the parameters that influence the stability of any fabricated nanofluids are the type of nanomaterial used, concentration, particles size, morphology, and density of the solid particles, as well as the kind of basefluid used and its temperature; while the shape and size of the cluster depends greatly on the liquid pH value, surfactant (if added), sonication power intensity, and duration of mixing. Modifying one or more of the previously mentioned parameters can help in improving the homogeneity and dispersion of the NPs within the nanofluid.

Our review of the available literature [10, 11] has shown that, when using an ultrasonicator for preparing nanofluids, the device bath temperature gradually rises with time, and that the highest temperature is constrained by the surrounding atmospheric conditions of the site. This fact needs to be factored in when considering the reproducibility and commercial production of the nanofluids in large scale as different ultrasonic devices and/or surrounding atmospheric

conditions would lead to varying the thermophysical properties and stability of the fabricated colloidal.

Therefore, in this study, an evaluation of the stability of dispersed Al NPs in water fabricated via the conventional two-step method and the controlled sonication bath temperature approaches was performed. The sedimentation photograph capturing method was employed to determine the nanofluids stability variation with time. The examined nanofluids were prepared at equal sonication time using different concentrations of NPs, in the range of 0.1 – 1.0 vol.%. Furthermore, for the controlled temperature method, the ultrasonicator bath temperature was fixed at a set of temperatures of 10^{o}C to 60^{o}C; while the conventional fabrication route was initiated at room temperature conditions. Stability monitoring for all as-prepared samples lasted for the same duration of time. The outcome of this research is expected to widen the understanding of both researchers and manufactures of the significant and importance role of the production process on the stability of nanofluids.

2. Experimental procedure

2.1 Materials

A purity of 99.9% Al NPs, of spherical particles shape and size between 40 to 60 nm, were purchased from SkySpring Nanomaterials Incorporated. A set of 60 mL clear glass vials, of 27.5 mm outer diameter and 140 mm height, with screwed top were provided by SIGMA-ALDRICH. Polypropylene holed caps, which includes a polytetrafluoroethylene (PTFE)/silicone septa for each, were obtained from SIGMA-ALDRICH to seal the aforementioned vials. Deionised water, produced by an Elga PR030BPM1-US Purelab Prima 30 water purification system, was used as the basefluid for the nanofluids preparation after adjusting its pH value to 9, at an in-lab temperature of 25^{o}C. The reason behind selecting the liquid pH value to be 9 is because other authors have reported high alumina nanofluid stability when using water of pH $\leq$ 8 [12-14]. Therefore, a pH of 9 would provide an unstable nanofluid that is close to the stability level, which will enable us to conduct our research investigation. Modification of the water pH was achieved by adding sodium hydroxide (NaOH) solution (1.09956. Titrisol®) to the liquid, while been monitored by a calibrated HACH HQ11D portable pH meter that is connected to a PHC20101 Intellical gel filled Ph electrode. The accuracy of the pH meter, as-reported by the manufacturer, is of ±0.002 pH and the initial calibration of the

device was performed using commercial calibration fluids of pH 4, 7, and 10 that were purchased from Metrohm USA Incorporated.

2.2 Nanoparticles characterization

Phase constitution test was performed for the Al NPs through a 9 kW Rigaku SmartLab, Japan, X-ray diffraction (XRD) analyser and its software, SmartLab Guidance, using a Cu K_α X-ray source with a diffraction angle of 2θ and an incidence beam step of 0.2° to determine the Bragg's peaks of the crystal structure of the examined sample. The diffraction scanning angle range was from 20° to 80°, with a scanning rate of 1°/min. A JEOL JSM-6010LA InTouchScope™ scanning electron microscopy (SEM) device and its integrated energy dispersive x-ray spectroscopy (EDS) analyser were used to check the morphology, size, and level of oxidisation of the as-received Al powder. The SEM images were recorded at two different magnifications by the secondary electron mode from the surface region of the tested sample. It is important to note that the SEM and EDS analysis were conducted at a working distance of 10 mm from the sample with an accelerating voltage of 20 kV to reduce any possible damages to the examined powder, and that the operating software used was InTouchScope 1.12. The density of the NPs (ρ_{np}) was obtained to calculate the Al powder volumetric concentration, which is part of the nanofluids fabrication process requirement. This was done by first measuring the Al sample weight, using an ae-ADAM PW 214 analytical balance of 0.0001 g readability and ±0.0002 g accuracy. Then, the weighted powder was placed inside a HumiPyc trademark Model 1 gas pycnometer – volumetric analyser, which operated at 25ºC, to obtain the density of the sample from its input mass and the volume measured by the instrument.

2.3 Nanofluids fabrication

Each nanofluid sample was prepared by placing the NPs first inside the vial then injecting 20 mL of as-prepared water, using a disposable syringe, on top of the nanopowder after which the vial was tightly sealed using the provided caps. The concentration of NPs used were 0.1, 0.5, and 1.0 vol.%, for each experimental set up, which was calculated by using the mixing theory (Eq. 1 and 2) that is widely used by many researchers in the field [4, 15].

$$V_{np} = \frac{m_{np}}{\rho_{np}} \quad (1)$$

$$f_V = \frac{V_{np}}{V_{np}+V_{bf}} \quad (2)$$

Where f_V, V_{np}, V_{bf}, and m_{np} are the NPs concentration, volume of NPs, volume of basefluid, and mass of NPs, respectively. The vial containing the solution was then placed gently in a Soniclean company benchtop bath type ultrasonic vibrator, running at 100% power (43 kHz pulse) and filled with water to the recommended operating level by the manufacturer, to agitate the mixture. This kind of particles dispersion method is known as the two-step approach, which is a common procedure used for the production of nanofluids by many researchers [4, 16]. The fabrication process then took one of the following two routes: 1- conventional two-step method, where the sonicator bath temperature initially starts at 25°C and ends at 54°C, without external interference (Fig. 4.2); and 2- controlled temperature two-step approach, where the device bath temperature was controlled for a set of temperatures from 10°C to 60°C, with a margin of ±1°C. It is worth noting that the lab temperature where the nanofluids preparations were conducted at was 25°C, surfactants or dispersing materials/chemicals were not used, sonication duration was 4 hours for all as-fabricated nanofluids, and the bath temperature was maintained by gradually adding hot or cold water inside the ultrasonic tank and extracting any access water from the device via the attached ejection valve. Fig. 4.3 demonstrates the schematic procedure used for the nanofluids preparation.

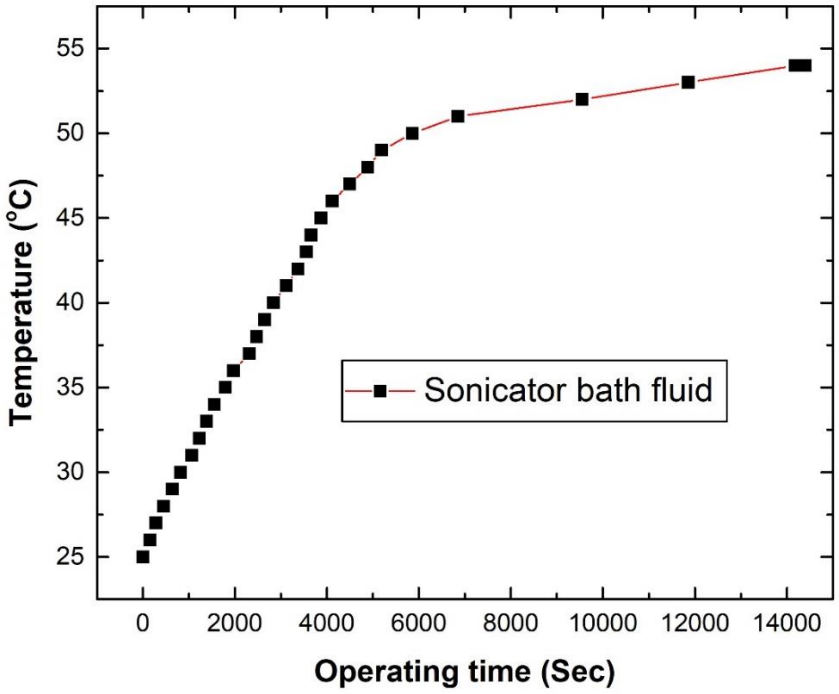

Fig. 4.2. Ultrasonicator bath temperature changes with operation time.

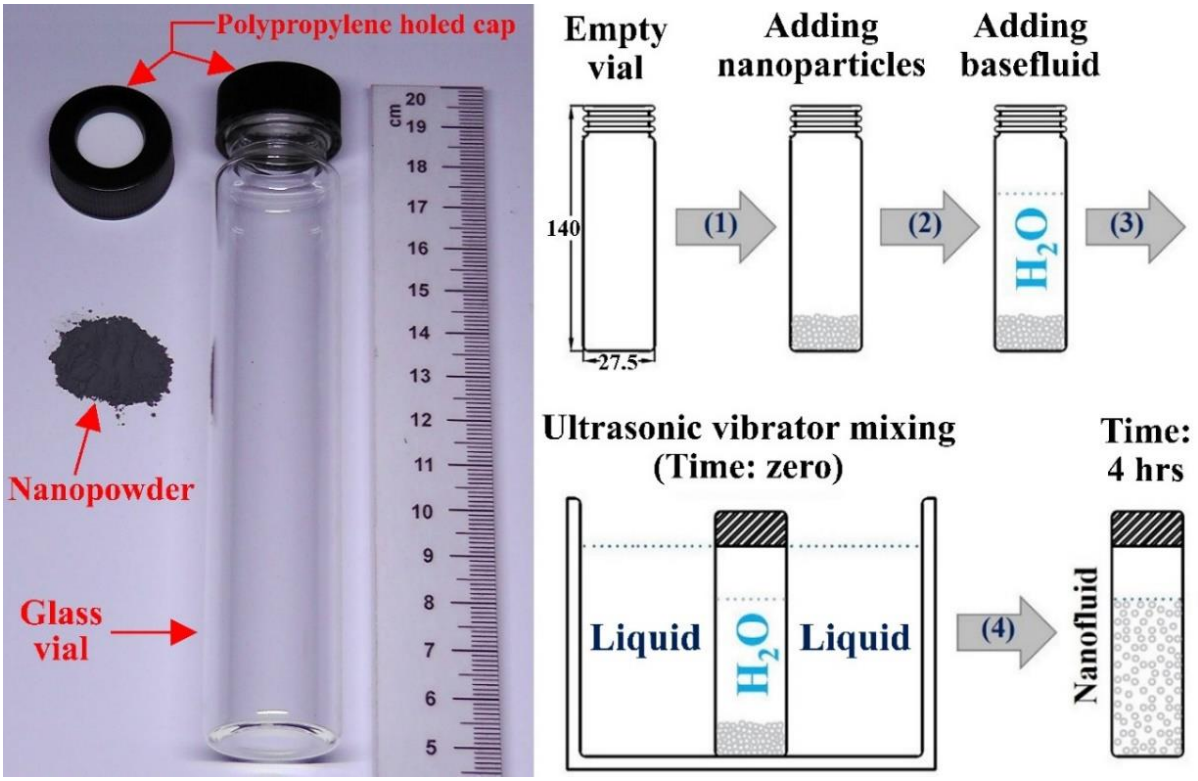

Fig. 4.3. Schematic procedure for the two-step nanofluids preparation.

2.4 Stability measurements

To determine the natural settling behaviour of the nanosuspensions, the as-sonicated nanofluids were placed individually on a measuring stand to allow the separation mechanism to take place under gravitational force after which their sedimentation heights were measured with respect to time by capturing their photographical images, using a Canon EOS 700D professional camera that is equipped with a Sigma 105mm F2.8 EX DG micro lens and a Phottix Company TR-90 remote switch with digital timer, at the start then for every 30 seconds for a total duration of 12 hours. The configuration used for the stability measurements is shown in Fig. 4.4. Sediment height ratio (SHR) was later calculated in terms of the average sediment height (H_S) (i.e. the average of both left and right sides of the sediment) and total liquid height (H_T), as illustrated in Eq. 3.

$$SHR = \frac{H_S}{H_T} \tag{3}$$

The accuracy of the two previously mentioned heights (i.e H_S and H_T) were within ±0.5 mm. Furthermore, a comparison between the different preparation methods was performed, via the obtained SHR's, to evaluate the nanofluids natural settling behaviour with time.

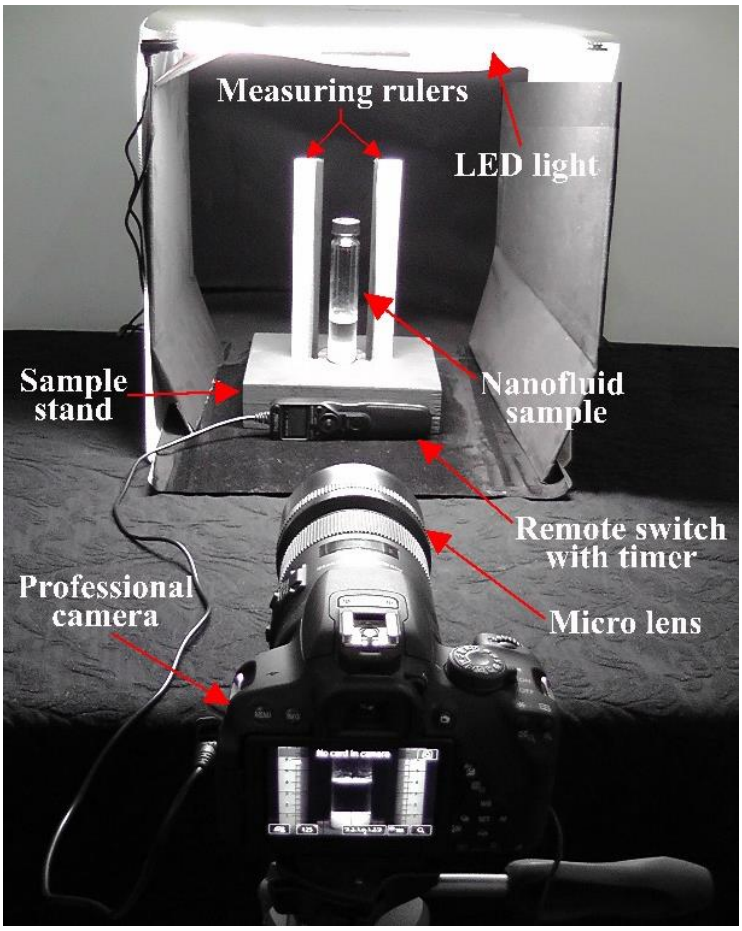

Fig. 4.4. Set up for nanofluid stability measurements.

3. Results and discussion

3.1 X-ray diffraction analysis

The diffraction pattern of the as-received Al NPs is shown in Fig. 4.5. It can be observed from the analysis, at angles 2θ = 20.46°, 40.80°, and 48.82°, that the Al sample contains traces of oxidation. The aforementioned angles are indexed in the XRD pattern as (020), (041), and (042), respectively. Furthermore, the crystallite sizes (D_{hkl}) of the highest peaks of Al and α-Al_2O_3 have shown to be about 50 nm, at (111), and 91 nm, at (042), respectively. The D_{hkl} values were obtained using the Scherrer formula [17-20], which is demonstrated in Eq. 4.

$$D_{hkl} = \frac{F\lambda}{\beta_{hkl} cos\theta_{hkl}} \quad (4)$$

Where F represents a constant value of 0.9, λ signifies the wavelength of the Cu K_α X-ray radiation source and is equal to 0.15405 nm, β_{hkl} is the full width at half the maximum of the (hkl) diffraction peak, and θ_{hkl} is the Bragg angle at the (hkl) peak.

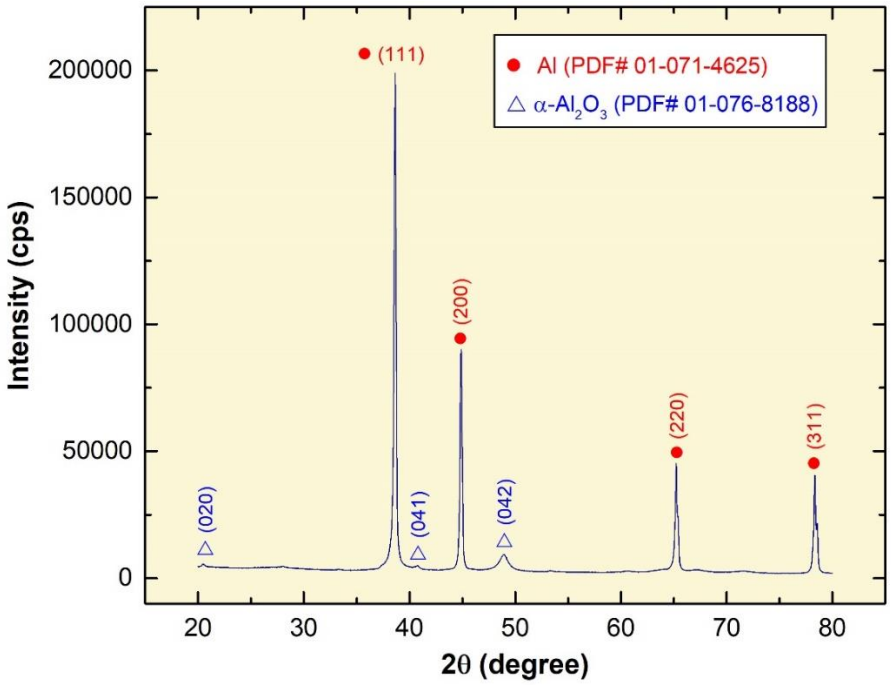

Fig. 4.5. X-ray diffraction patterns of as-received aluminium nanoparticles.

3.2 Aluminium nanoparticles morphology, level of oxidisation, and density

The SEM analysis of the as-received nanopowder has shown that the morphology of the examined NPs are of spherical shape and that some agglomerations between the particles do exist, as illustrated by the SEM patterns (Fig. 4.6a – b). Moreover, the size of the particles was seen to be roughly in the range of 50 to 95 nm. The observed growth in some of the NPs sizes (i.e. larger than the reported by the manufacturer) is due to the formation of α-Al_2O_3 caused by the unavoidable exposure of the sample to the surrounding atmosphere, when performing the characterisation tests. This was also confirmed by the previous XRD analysis and the EDS x-ray spectrum (Fig. 4.6c), which shows the present of oxygen within the specimen. The EDS elemental percentages of the characterised nanopowder is tabulated in Table 4.1. Furthermore, the measured density of the Al NPs was found to be 3.22 g/cm^3, with a standard deviation of 0.81×10^{-2} g/cm^3. Thus, using Eq. 1 and 2, the amount of NPs required to fabricate the 0.1, 0.5, and 1.0 vol.% of nanofluids with 20 mL of water are 64, 323, and 650 mg, respectively.

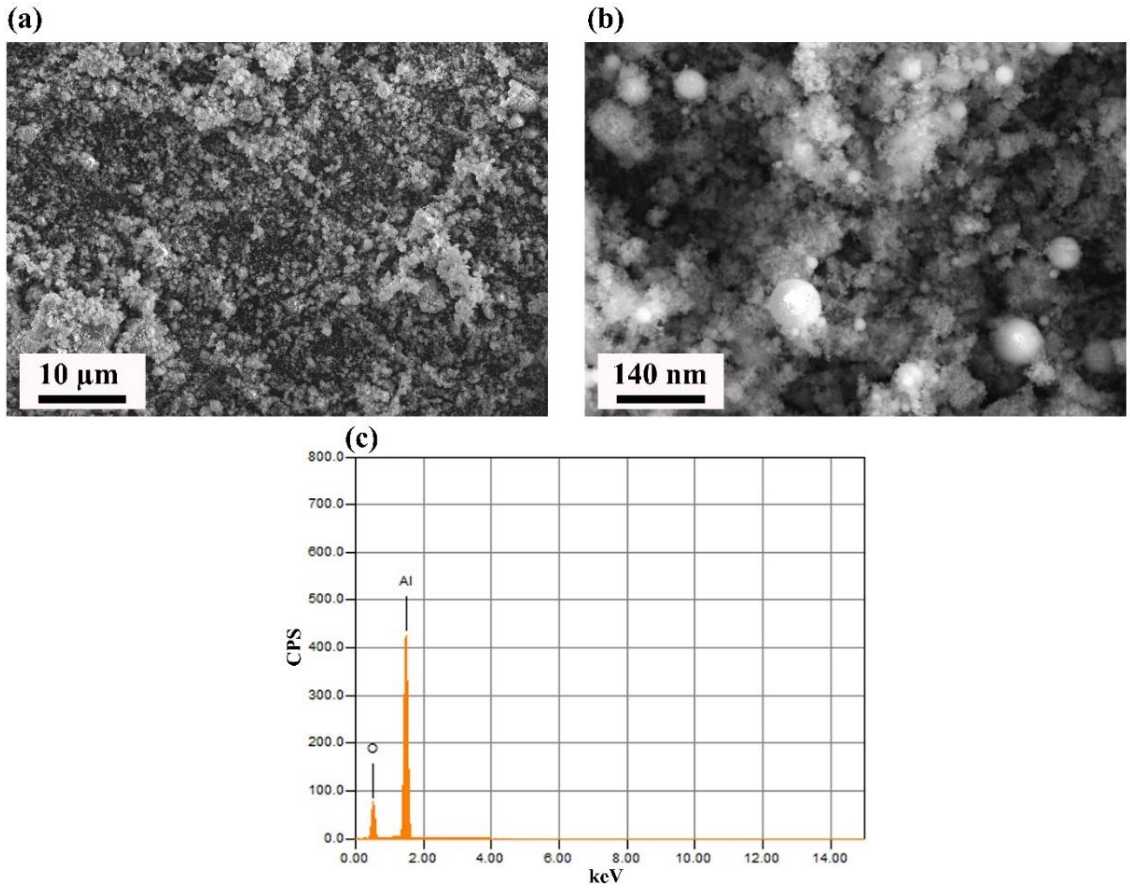

Fig. 4.6. SEM and EDS analysis of the as-received Al nanopowder, where (a – b) are the SEM images of the sample at low and high magnifications, respectively, and (c) is the EDS x-ray spectrum of the elements within the characterised specimen.

Table 4.1. EDS elemental percentage of the as-received Al nanopowder.

Element	Mass %	Atom %	Sigma	Net	K ratio
Aluminium	62.35	49.55	0.09	1582595	0.3617546
Oxygen	37.65	50.45	0.07	210593	0.1499887
Total	100	100	–	–	–

3.3 Nanofluids settling behaviour

Settling characterisation of the as-fabricated nanofluids have shown two types of sedimentation behaviours, which are the dispersed sedimentation and the flocculated sedimentation. The dispersed sedimentation was observed by the nanofluids prepared with 0.1 and 1.0 vol.% at

controlled temperatures of 10°C and 20°C, while the other samples have illustrated a flocculated sedimentation settling mechanism. Such variation in settling behaviour is believed to be caused by the timing of NPs oxidation, where the reaction rate of the particles start to prominently increase, within the aforementioned samples of dispersed sedimentation, after the sonication phase, in contrast to the nanofluids of flocculated sedimentation behaviour which most of its particles oxidise during the preparation stage. This is clearly seen by the notable hydrogen generation in the nanofluids that had experienced a dispersed sedimentation mechanism in comparison to the other as-fabricated suspensions. The hydrogen production is due to the following two possible reactions between the Al NPs and the hosting solution.

$$Al + 3H_2O + NaOH \rightarrow NaAl(OH)_4 + 3/2H_2 \quad (5)$$

$$NaAl(OH)_4 \rightarrow Al(OH)_3 + NaOH \quad (6)$$

Eq. 5 and 6 can be summed up into the following overall reaction.

$$Al + 3H_2O \rightarrow Al(OH)_3 + 3/2H_2 \quad (7)$$

An example of the two previous settling behaviours is demonstrated in Fig. 4.7, and an in-depth discussion and explanation of the significant role of water temperature on the hydrogen production rate from dispersing Al can be found in Hiraki et al. published work [21].

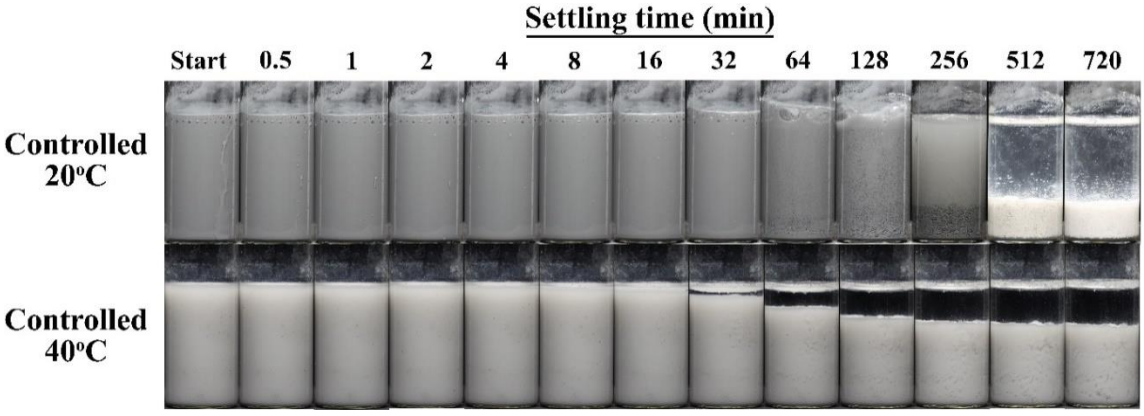

Fig. 4.7. Settling behaviour of the 0.5 vol.% nanofluids fabricated by a controlled ultrasonicator bath temperature of 20°C (top) and 40°C (bottom).

Furthermore, the changes in the SHR of the as-prepared nanofluids during the photographical analysis is shown in Fig. 4.8. It can be seen that the settling data of the nanofluids sonicated at controlled 10 – 20°C has a different trend behaviour than the suspensions that were fabricated

with higher temperatures. This is expected and is associated to, as previously mentioned, the different type of sedimentation mechanism formed due to the timing of highest oxidation rate occurrence within the samples. It was also found that rising the fabrication temperature, of the 0.1 and 0.5 vol.% nanofluids, caused the NPs settling mechanism to escalate (Fig. 4.8a – b), and hence increases the separation between the water molecules and the hosted NPs. In addition, the SHR was seen to rapidly decrease at the early stages of the nanofluids shelving time, reaching values as low as 0.44 and 0.47 within 64 min, for the 0.1 and 0.5 vol.% suspensions produced at 60^{o}C, respectively. Such observation is expected in most nanofluids and is known as the rapid settling region, as reported by other researchers [4, 22]. In general, there exist two phase separation speed regions, the first is the previously introduced rapid settling region and the one beyond it is called the slow settling region, where the settling speed highly reduces along the shelving time period. On the other hand, the effect of sonication temperatures, between 30 – 60^{o}C, on the suspensions of higher NPs concentration (i.e. 1.0 vol.%), has shown to have less influence on the stability of the as-prepared nanofluids (Fig. 4.8c). The divergence in SHR between the conventional method and the controlled temperature approach for the nanofluids, of 1.0 vol.%, have shown to be at the end of the settling experiment (i.e. at time 720 min) -44.4% (10^{o}C), -31.3% (20^{o}C), +10% (30^{o}C), -6.1% (40^{o}C), -2.2% (50^{o}C), and +2.3% (60^{o}C) than the nanosuspension of uncontrolled bath temperature.

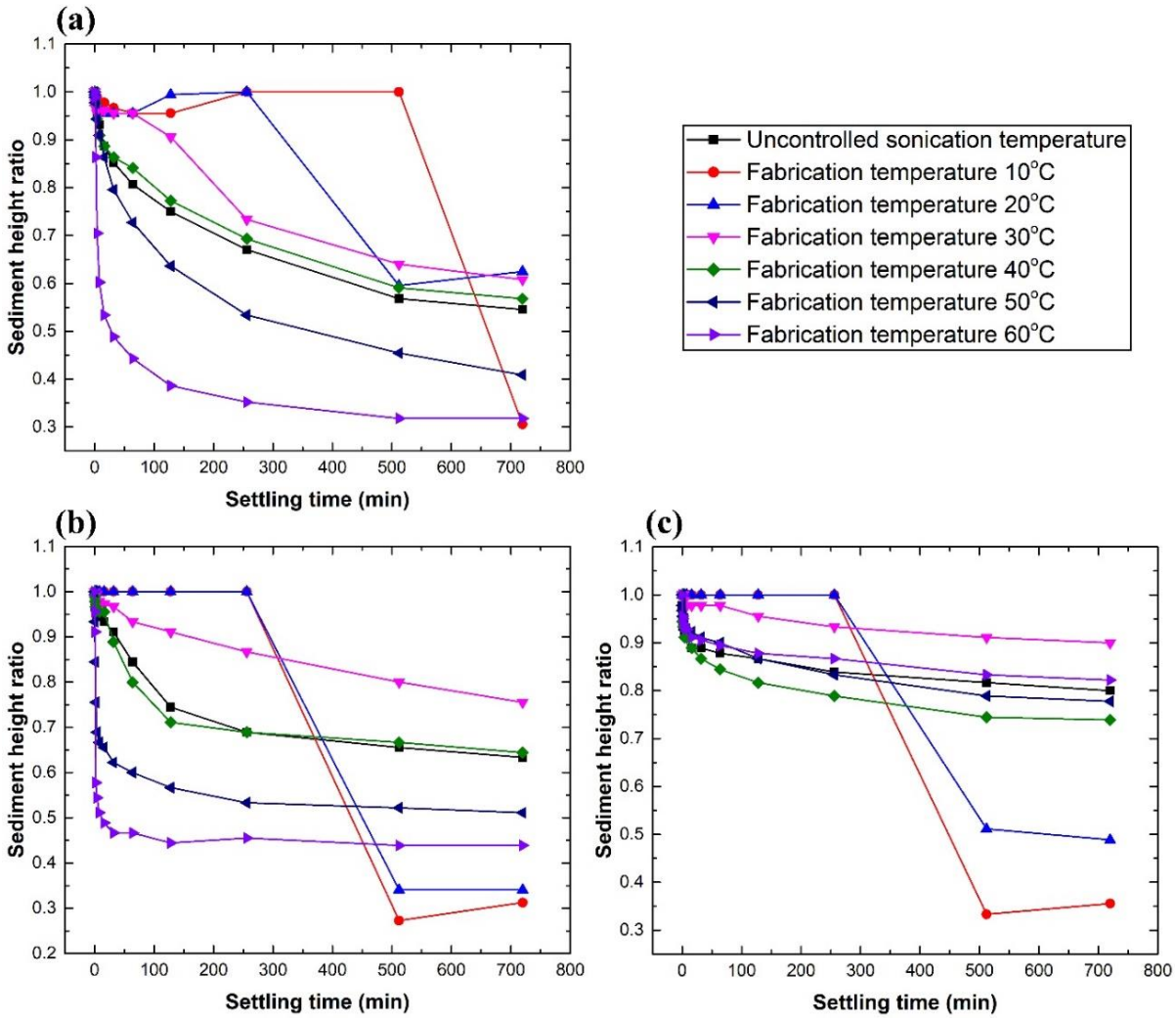

Fig. 4.8. Sediment height ratio variation with settling time for the nanofluids fabricated with (a) 0.1 vol.%, (b) 0.5 vol.%, and (c) 1.0 vol.%.

In general, the nanofluids that were fabricated at 30°C have demonstrated better short and long-term stability than the ones produced by the conventional two-step approach, as illustrated by the data in Fig. 4.8 and the photographical images shown in Fig. 4.9, with the advantage of being reproducible at different atmospheric conditions, as this is not possible with the uncontrolled temperature scheme.

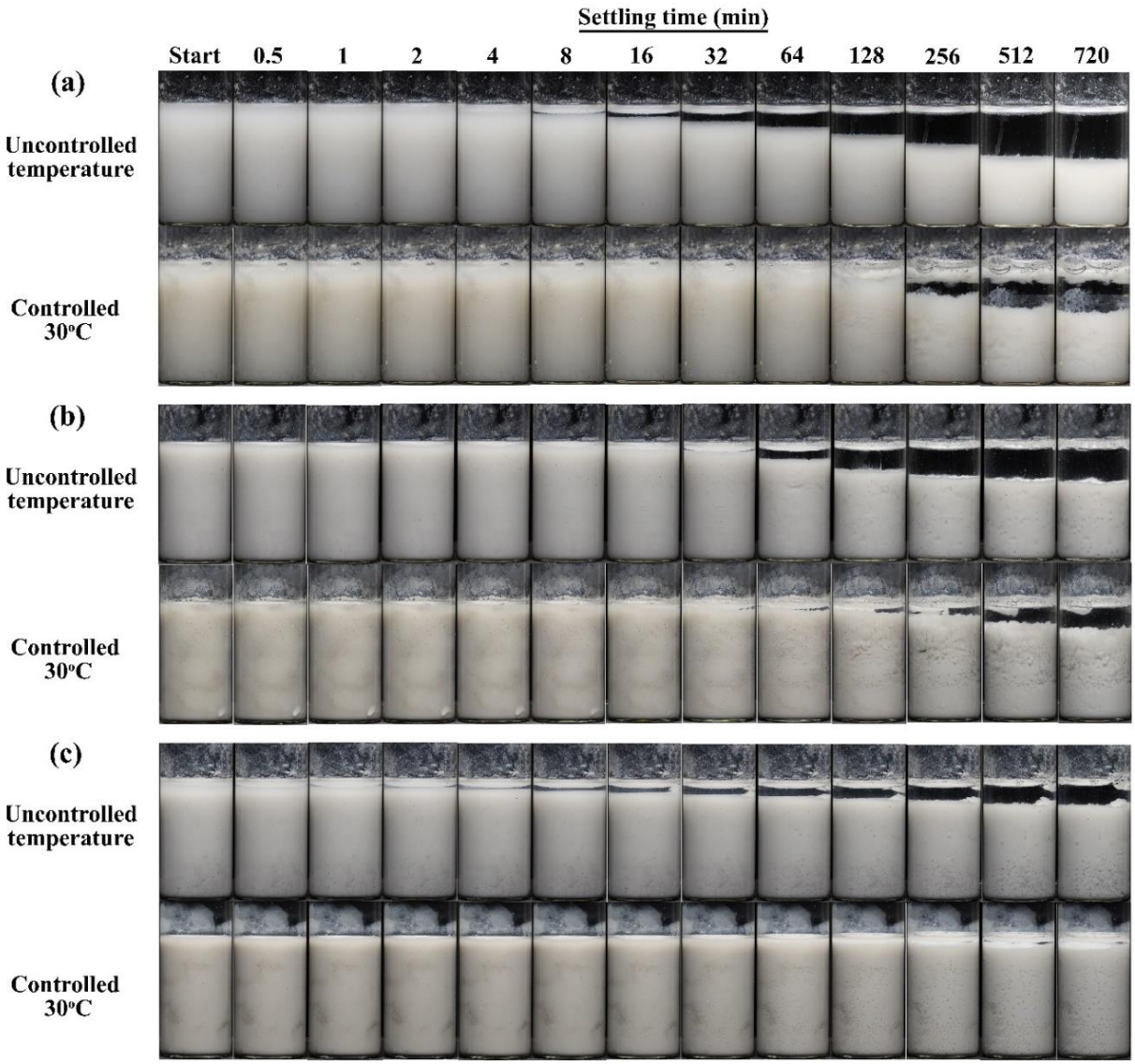

Fig. 4.9. Photographical images of the nanofluids settling behaviour with time using the uncontrolled and 30°C controlled sonication temperature approaches, where the NPs concentrations used were: (a) 0.1 vol.%, (b) 0.5 vol.%, and (c) 1.0 vol.%.

4. Conclusion

Water based colloidal containing dispersed Al nanoparticles has been characterised via the sedimentation photograph capturing method to emphasize the role of the fabrication approach on the stability of the mixture. Two procedures were undertaken for the production of the as-prepared nanofluids, which are the conventional two-step approach and the two-step controlled sonication bath temperature method. The parameters studied include the nanoparticles concentration, nanofluid fabrication temperature, and sediment height ratio in the fluid.

Sodium hydroxide was used to adjust the pH value of the basefluid to 9, as lower pH values were reported in the literature to highly stabilise similar types of nanofluids. Mixing of the colloidal was performed using an ultrasonic bath type device to induce the dispersion of the particles. It was found that the conventional two-step approach caused the bath temperature to increase with time, thus confirming other researchers findings. Moreover, the experiments have revealed that nanofluids produced at controlled temperatures lower than 30^{o}C follows a dispersed sedimentation behaviour, whereas those fabricated at 30^{o}C and above obeyed a flocculated sedimentation settling mechanism.

Evaluation of the nanofluids prepared by the controlled temperature method has generally shown a decrease in their stability with the increase in fabrication temperature. In addition, the increase in nanoparticles concentration has shown to reduce the variation in sedimentation height ratio between the samples that were produced at different fixed temperatures. Furthermore, when comparing the nanofluids fabricated by the two aforementioned preparation methods, it was seen that the stability of the 30^{o}C colloidal have exceeded all other controlled temperature samples, which obeyed the same sedimentation mechanism, beyond the rapid settling region. The 30^{o}C nanosuspensions have also demonstrated better short and long-term stability behaviour than the conventionally fabricated nanofluids. Thus, confirming that the controlled temperature two-step nanofluid fabrication approach is much promising in terms of the colloidal shelving stability than the conventional method.

References

1. Vargel, C. Chapter a.2 - physical properties of aluminium. In *Corrosion of aluminium*, Ed. Elsevier: Amsterdam, 2004; pp 19-20.

2. Hirsch, J. Recent development in aluminium for automotive applications. *Transactions of Nonferrous Metals Society of China* **2014**, *24*, 1995-2002.

3. Farhana, K.; Kadirgama, K.; Rahman, M.M.; Noor, M.M.; Ramasamy, D.; Samykano, M.; Najafi, G.; Sidik, N.A.C.; Tarlochan, F. Significance of alumina in nanofluid technology: An overview. *Journal of Thermal Analysis and Calorimetry* **2019**.

4. Ali, N.; Teixeira, J.A.; Addali, A. A review on nanofluids: Fabrication, stability, and thermophysical properties. *J. Nanomater.* **2018**, *2018*, 33.

5. Babick, F.; Schießl, K.; Stintz, M. Van-der-waals interaction between two fractal aggregates. *Adv Powder Technol* **2011**, *22*, 220-225.

6. Ilyas, S.U.; Pendyala, R.; Marneni, N. Settling characteristics of alumina nanoparticles in ethanol-water mixtures. In *2013 2nd International Conference on Advanced Materials Design and Mechanics, ICAMDM 2013*, Kuala Lumpur, 2013; Vol. 372, pp 143-148.

7. Li, X.; Zhu, D.; Wang, X. Evaluation on dispersion behavior of the aqueous copper nano-suspensions. *J. Colloid Interface Sci.* **2007**, *310*, 456-463.

8. Wei, X.H.; Wang, L.Q. Synthesis and thermal conductivity of microfluidic copper nanofluids. *Particuology* **2010**, *8*, 262-271.

9. Ilyas, S.U.; Pendyala, R.; Marneni, N. In *Stability and agglomeration of alumina nanoparticles in ethanol-water mixtures*, 4th International Conference on Process Engineering and Advanced Materials, ICPEAM 2016, 2016; Bustam, M.A.; Keong, L.K.; Man, Z.; Hassankiadeh, A.A.; Fong, Y.Y., Eds. Elsevier Ltd: pp 290-297.

10. Song, Y.Y.; Bhadeshia, H.K.D.H.; Suh, D.-W. Stability of stainless-steel nanoparticle and water mixtures. *Powder Technol.* **2015**, *272*, 34-44.

11. Ali, N.; Teixeira, J.A.; Addali, A. New ph correlations for stainless steel 316l, alumina, and copper(i) oxide nanofluids fabricated at controlled sonication temperatures. *J. Nano. Res.* **2019**, *58*, 125-138.

12. Ghadimi, A.; Saidur, R.; Metselaar, H.S.C. A review of nanofluid stability properties and characterization in stationary conditions. *Int. J. Heat Mass Transf.* **2011**, *54*, 4051-4068.

13. Mukherjee, S.; Paria, S. Preparation and stability of nanofluids-a review. *IOSR Journal of Mechanical and civil engineering* **2013**, *9*, 63-69.

14. Manjula, S.; Kumar, S.M.; Raichur, A.M.; Madhu, G.M.; Suresh, R.; Raj, M.A.L.A. A sedimentation study to optimize the dispersion of alumina nanoparticles in water. *Cerâmica* **2005**, *51*, 121-127.

15. Pak, B.C.; Cho, Y.I. Hydrodynamic and heat transfer study of dispersed fluids with submicron metallic oxide particles. *Exp. Heat Transf.* **1998**, *11*, 151-170.

16. Yu, W.; Xie, H.Q. A review on nanofluids: Preparation, stability mechanisms, and applications. *J. Nanomater.* **2012**, *2012*.

17. Ai, X.W.; Lin, J.X.; Chang, Y.F.; Zhou, L.Q.; Zhang, X.M.; Qin, G.W. Phase modification of copper phthalocyanine semiconductor by converting powder to thin film. *Applied Surface Science* **2018**, *428*, 788-792.

18. Raleaooa, P.V.; Roodt, A.; Mhlongo, G.G.; Motaung, D.E.; Ntwaeaborwa, O.M. Analysis of the structure, particle morphology and photoluminescent properties of zns:Mn2+ nanoparticulate phosphors. *Optik* **2018**, *153*, 31-42.

19. Rabiee, M.; Mirzadeh, H.; Ataie, A. Processing of cu-fe and cu-fe-sic nanocomposites by mechanical alloying. *Adv Powder Technol* **2017**, *28*, 1882-1887.

20. Minaei, S.; Haghighi, M.; Jodeiri, N.; Ajamein, H.; Abdollahifar, M. Urea-nitrates combustion preparation of ceo2-promoted cuo/zno/al2o3 nanocatalyst for fuel cell grade hydrogen production via methanol steam reforming. *Adv Powder Technol* **2017**, *28*, 842-853.

21. Hiraki, T.; Takeuchi, M.; Hisa, M.; Akiyama, T. Hydrogen production from waste aluminum at different temperatures, with lca. *Mater. Trans.* **2005**, *46*, 1052-1057.

22. Witharana, S.; Hodges, C.; Xu, D.; Lai, X.J.; Ding, Y.L. Aggregation and settling in aqueous polydisperse alumina nanoparticle suspensions. *J. Nanopart. Res.* **2012**, *14*.

Chapter 5

Publication 4: The Effect of Aluminium Nanocoating and Water pH Value on The Wettability Behavior of an Aluminium Surface

(Ali, N.; Teixeira, J.A.; Addali, A.; Al-Zubi, F.; Shaban, E.; Behbehani, I. The effect of aluminium nanocoating and water ph value on the wettability behavior of an aluminium surface. *Applied Surface Science* **2018**, *443*, 24-30. DOI: 10.1016/j.apsusc.2018.02.182)

The Effect of Aluminium Nanocoating and Water pH Value on The Wettability Behavior of an Aluminium Surface

A B S T R A C T

Experimental investigation was performed to highlight the influence of ionic bounding and surface roughness effects on the surface wettability. Nanocoating technique via electron beam physical vapour deposition process was used to fabricate aluminium (Al) metallic films of 50, 100, and 150 nm on the surface of an Al substrate. Microstructures of the samples before and after deposition were observed using an atomic force microscopy. A goniometer device was later on used to examine the influence of surface topography on deionised water of pH 4, 7 and 9 droplets at a temperature ranging from 10°C to 60°C through their contact angles with the substrate surface, for both coated and uncoated samples. It was found that, although the coated layer has reduced the mean surface roughness of the sample from 10.7 nm to 4.23 nm, by filling part of the microstructure gaps with Al, the wettability is believed to be effected by the ionic bounds between the surface and the free anions in the fluid. As the deionised water of pH 4, and 9 gave an increase in the average contact angles with the increase of the coated layer thickness. On the other hand, the deionised water of pH 7 has showed a negative relation with the film thickness, where the contact angle reduced as the thickness of the coated layer was increased. The results from the aforementioned approach had showed that nanocoating can endorse the hydrophobicity (unwitting) nature of the surface when associated with free ions hosted by the liquid.

Keywords: Hydrophobic; hydrophilic; surface topography; element analysis; coating; contact angle.

1. Introduction

Nanoparticles have gained wide recognition in a variety of industrial and commercial applications over the years, such as sunscreen products [1] , medicine [2, 3], electronics [4], transportation [5], reduction of buildings pollution [6], magnetic sealing [7], microbial fuel cells [8], space and defence [9], and structural applications [10].

Alumina (Al_2O_3), in specific, possesses a variety of industrial and commercial uses and has become one of the important elements that is used in manufacturing commercial ceramic materials [11, 12]. On the nano scale, nanoparticles of Al_2O_3 have been used to produce nanocomposites [13, 14], polymer modification [15], textiles functionalization [16], wastewater treatment [17], heat transfer fluids [18], surface coating [19], and as catalysis [20-22].

Surface friction and wettability are important in many of these applications, however, they require further advancement. Whereas in piping systems, the inner pipe surface friction plays a prominent role in the determination of the pressure drop through the head losses along the pipelines for flows of turbulent state. This is theoretically proven using the non-linear relationship between the Reynold number (Re) and the implicit Colebrook–White equation [23], which are expressed in form of a formulation as,

$$Re = \frac{V.D}{\upsilon} \tag{1}$$

$$\frac{1}{\sqrt{f}} = 1.14 - 2\,log_{10}\left(\frac{\varepsilon/D}{3.7} + \frac{2.523}{Re\sqrt{f}}\right) \tag{2}$$

Where υ, D, V, f, and ε are kinematic viscosity, inner pipe diameter, inner pipe average flow velocity, Darcy-Welsbach friction factor, and roughness height, respectively.

On the other hand, surface wettability is determined by the angle of contact between a liquid droplet and the surface in contact to it [24]. Where the surface is called “super-hydrophilic” if the angle is less than 5º, “hydrophilic” if the angle is between 5º and 90º, “hydrophobic” if the angle is between 90º and 150º, and “super-hydrophobic” if the angle is greater than 150º [24, 25]. The term hydrophilic reflects the tendency of the fluid to form a strong bond with the surface, where the term hydrophobic indicates the propensity of the fluid to repel from the surface. Once a liquid of an ionic nature, such as water, comes in contact with an aluminium (Al) surface, an ionic reaction occurs in any of the following forms [26, 27].

$$Al + 3H_2O \rightarrow Al(OH)^3 + 3H^+ + 3e^- \tag{3}$$

$$Al + 3/2H_2O \rightarrow Al_2O_3 + 3H^+ + 3e^- \tag{4}$$

$$Al + 2H_2O \rightarrow AlO(OH) + 3H^+ + 3e^- \tag{5}$$

Such reaction leads to a reduction of oxygen (O_2) atoms and production of hydroxyl ions (H^+) and hence changes the hydrophobicity/hydrophilicity nature of the surface [19].

Fluid – solid interaction has its own importance in a range of applications such as designing of water repelling surfaces [28] to fluid flow manipulation in piping systems [24] and inhabitation of machinery corrosion [29].

Kang et al. [24] studied in their work the effect of surface nanocoating on the reduction of liquid pumping power by modifying the contact angle (CA) of the riser surface. The CA's examined were between 23.7° and 153.8° with the highest pumping power efficiency obtained at a CA of 90.3° for the silicon dioxide (SiO_2) coating of concentration 6.67×10^{-3} wt%.

Zhang et al. [30] considered the improvement of heat exchanger, which consist of fins and tubes, thermal performance by depositing titanium dioxide (TiO_2) film on an Al substrate. Baking temperatures of 150°C, 250°C, 350°C, 450°C, and 600°C were implemented using an electric muffle furnace for surface treatment. For the same Re and relative air humidity (RH) condition, the heat transfer coefficient was found to be the highest after baking the coated substrate at a temperature of 250°C. But decreased when the baking temperature increased above 250°C due to the reduction in coated film area.

Phan et al. [31] investigated experimentally, using nanocoating techniques, the surface wettability effect on nucleate boiling heat transfer. Water CA on a stainless steel grad 301 substrates was varied from 22° to 112° by depositing different coating materials. They found that greater surface wettability decreased the bubble emission frequency but raised the vapor bubble departure radius. Moreover, lower superheat temperature was required to generate the bubbles growth on a hydrophobic surfaces. They also noticed the tendency of bubbles to merge together forming a vapor blanket on the hydrophobic surface leading to critical heat flux (CHF).

Akbari et al. [32] studied the enhancement of saturated pool boiling of distilled water under atmosphere pressure where they formed a layer of silver nanoparticles on a copper substrate by boiling silver nanofluid of 0.025 and 0.05 vol%. They found that higher particles concentration increased the clustering deposition and surface hydrophobicity, however stability of the deposition was reduced. Their results also showed that, the heat transfer coefficient (HTC) and CHF improved by reaching a nanocoated polished surface state.

In this study, the CA and surface roughness of an Al substrate were modified through electron beam physical vapor deposition (EB-PVD) coating technique to enhance the ionic interaction between the surface and the water droplet. An atomic force microscopy (AFM) device was used to measure the reduction in surface roughness after coating the substrate with 50, 100, and 150 nm thick layers. Furthermore, a goniometer devices was used in an attempt to understanding the influence of free ions imbedded in the liquid on the attached surface CA.

2. Experimental

2.1 Materials

All chemicals were used as-received without further purification. Hydrochloric acid (HCl ~37%) grad ACS reagent and acetone (CH_3COCH_3 ≥ 99.5%) grad ACS reagent were purchased from SIGMA-ALDRICH, and sodium hydroxide pellets (NaOH ~98%) grad AR was purchased from LOBA Chemie. Al pellets, 3.175 mm diameter and 6.35 mm height, of 99.99% purity was purchased from Kurt J. Lesker Co. Four cylindrical shaped, 25 mm diameter and 15 mm height, substrates of 92.5% Al were manufactured using a computer numerical control (CNC) machine.

2.2 Preparation of aluminium coatings

Aluminium pellets were placed in a 8 cm^3 graphite crucible to be used as the coating material source and the Al substrate was cleaned by a Soniclean company digital benchtop ultrasonic cleaner filled with acetone for 20 min after which it was wiped carefully before tightly adjusted to the sample holder and positioned vertically inside the EB-PVD device. The EB-PVD device chamber was then vacuumed to a pressure of 6×10^{-6} Torr to insure the removal of all particle contaminations within it and to control the level of evaporation. The Al pellets were later on partially evaporated from the crucible and the Al vapor deposited on the substrate surface with a deposition rate of 0.1 Å/s to form a 50, 100, and 150 nm thick layers. After the deposition process completion, the substrate was left in the chamber for 4 h to cool down before removal. The coating procedure used for the preparation of the Al metallic layer on the substrate is shown in Fig. 5.1.

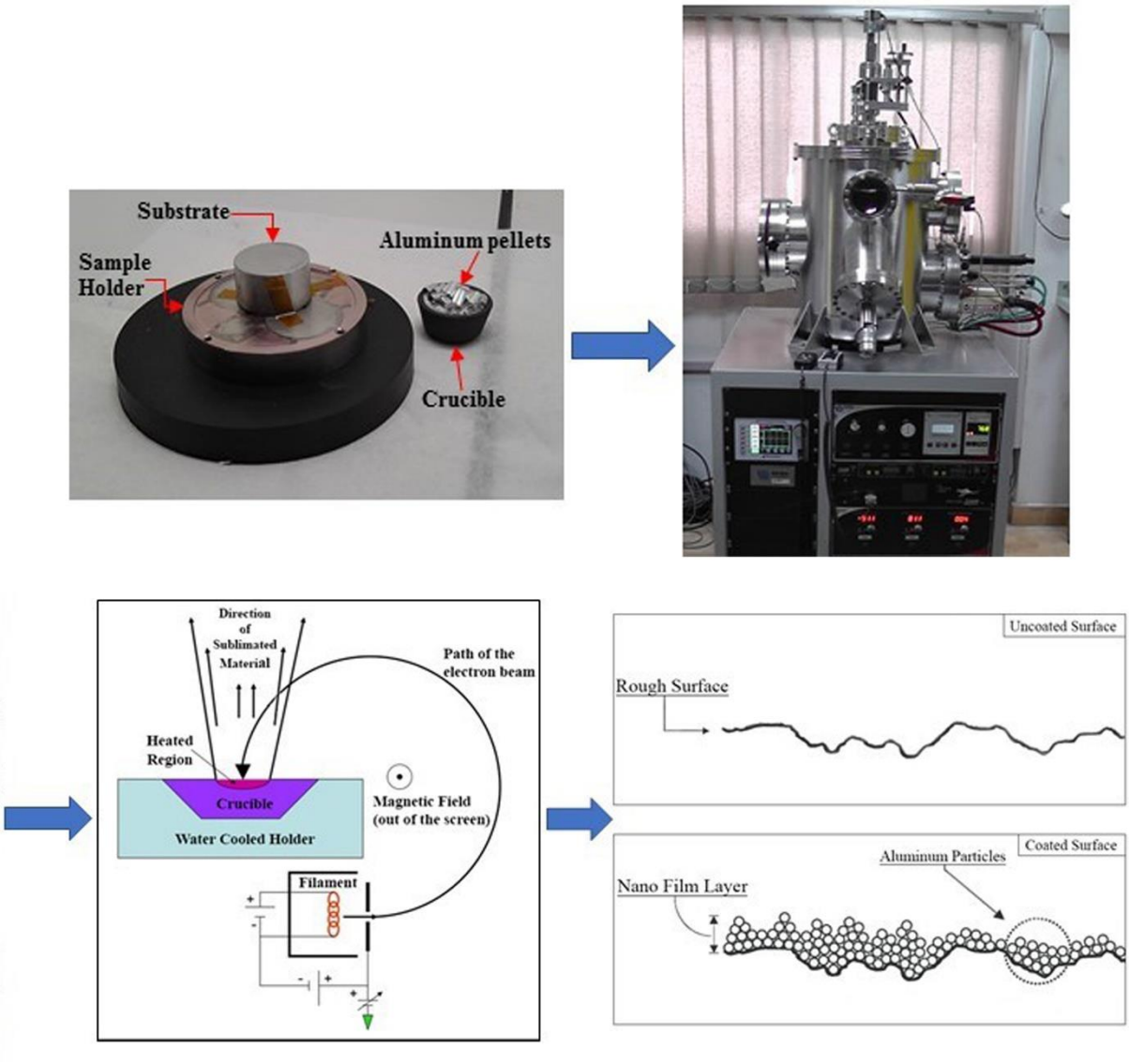

Fig. 5.1. Aluminium particle deposition procedure.

2.3 Characterization

Elemental analysis of the Al substrates was performed three times and averaged using a BRUKER TITAN S1 x-ray fluorescent (XRF) handheld analyser to insure that the bulk components in the manufactured substrate were of Al base. This was done by placing the substrate on the working station and adjusting the XRF device lens vertically on the substrate before starting the measurements which required 10 seconds to complete for each measurement. Additionally, a crystal structure test was performed through a 9 kW Rigaku SmartLab, Japan, x-ray diffraction (XRD) analyser and its software, SmartLab Guidance, using a Cu K_α X-ray source with a diffraction angle of 2Θ and an incidence beam angle of 0.02° to determine the phase constitution of the examined substrate. The diffraction scanning angle

ranges were from 20° to 80° at a scanning rate of 2°/min. A Keysight Technologies 5600LS AFM in tapping mode was used to illustrate the changes in surface topography of the coated and uncoated substrates. The particles size of Al_2O_3 film and surface roughness were determined using Mountview software. Surface wettability was measured by preparing three beakers of 250 ml that were filled with 150 ml of deionised water (DIW) of pH 7 in each. Two of the three DIW, contained in the beakers, pH levels were adjusted to 4 by adding HCl and 9 by adding NaOH. The pH level in each beaker was measured using a HACH HQ11D portable pH meter with accuracy of 0.002 pH. The samples were then used separately to fill one of three 500 µl glass syringes, purchased from Hamilton company, each time. The three syringes containing DIW of pH 4, 7, and 9 were then placed on the Dataphysics OCA 100 contact angle goniometer device automatic multi liquid dispenser. The surface wettability was then measured at a liquid temperature of 10, 20, 25, 30, 40, 50, and 60°C, by heating/cooling the fluid sample using a Dataphysics SHD syringe temperature controller, for the coated and uncoated substrates through the determination of liquid – surface CA using the device supplied software, SCA 20. For each test, the volume of 3 µl liquid drop was carefully dropped on the surface of the test samples with a dosing rate of 3 µl/s and under ambient conditions. The average angle value for each sample was later on reported with a precision value of ± 0.1°. The image of the drop was captured by a high speed video camera provided with the device.

3. Results and discussion

3.1 X-ray fluorescent and x-ray diffraction analysis

The elemental content of the substrates manufactured, as examined by the XRF for three times and averaged, are given in Table 5.1. In addition to the XRF results, the XRD pattern showed good agreement with the XRF analysis as suggested by the sharp diffraction Bragg's peaks (PDF Card No.: 01-089-2837) shown in Fig. 5.2. This conforms that the bulk formation of the substrate is of Al base.

Table 5.1. Averaged XRF elemental analysis of the aluminium substrate.

Element	**wt.%**			
	Minimum	**Maximum**	**Content**	**(+/-) Error**
Aluminium	90	96	92.5	0.04
Iron	0	0.7	0.56	0.03

Copper	5	6	5.82	0.06
Zinc	0	0.3	0.05	0.01
Lead	0.2	0.6	0.43	0.02

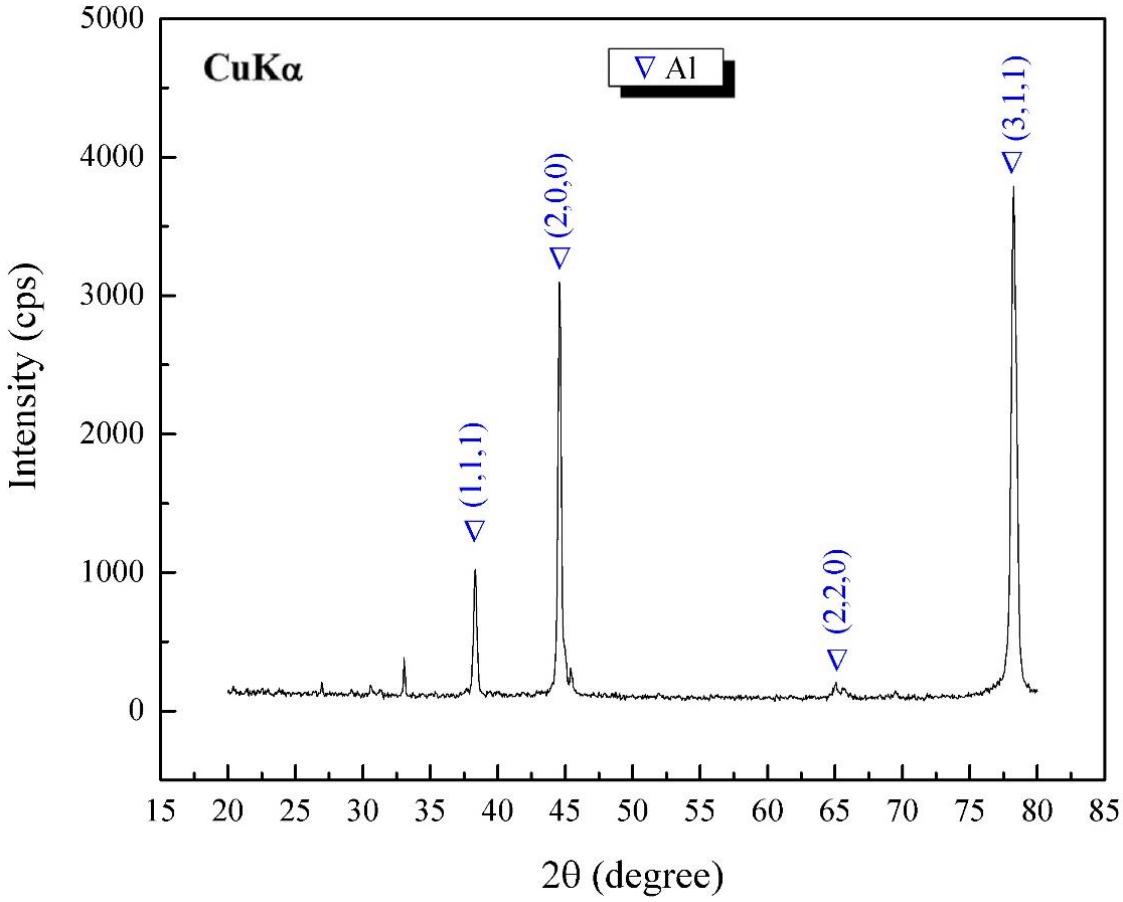

Fig. 5.2. X-ray diffraction pattern of Al substrate.

3.2 Surface characterization

Fig. 5.3 represents the topographical two and three dimensional images obtained from the AFM device for the coated and uncoated samples. The 3D profile shown in Fig. 5.3(B, D, F, and H) clearly reveals the reduction in surface roughness of the substrate caused from the increase in Al film thickness in comparison to the uncoated substrate shown in Fig. 5.3(B). This is because the surface roughness depends on the height variation on the surface which can be classified into micro gaps, hills, and valleys [33].

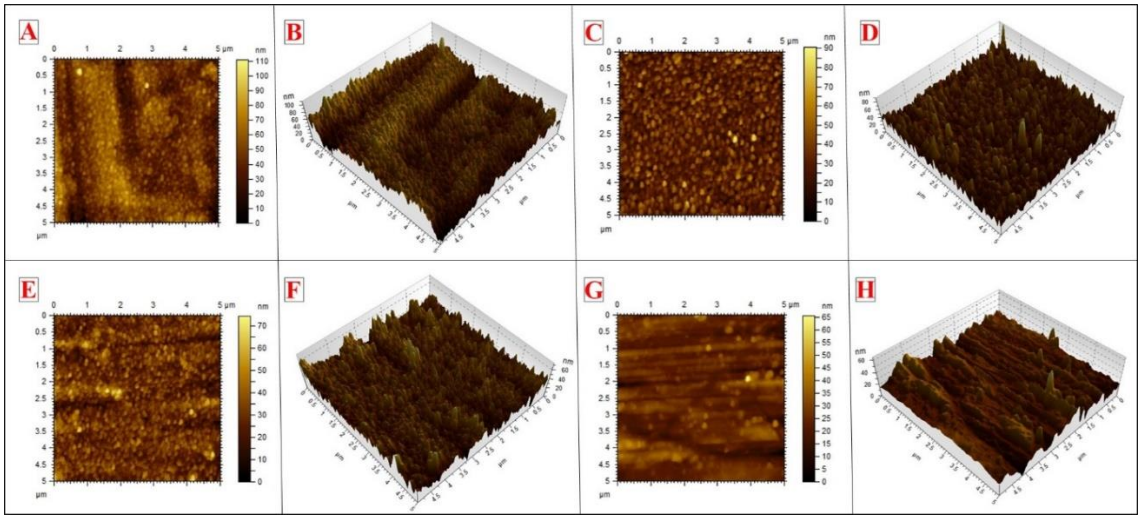

Fig. 5.3. Atomic force microscopy images of: (A) 2D profile of uncoated sample, (B) 3D profile of uncoated sample, (C) 2D profile of 50 nm coated sample, (D) 3D profile of 50 nm coated sample, (E) 2D profile of 100 nm coated sample, (F) 3D profile of 100 nm coated sample, (G) 2D profile of 150 nm coated sample, and (H) 3D profile of 150 nm coated sample.

In the case of the uncoated sample, the hills are found to be high which implies that the surface is of greater surface roughness. This is because the nanostructures on the surface have a range of height between 33.3 to 99.8 nm and a root mean square height (RMSH) of 13.4 nm which shows a wide variety of disparity as seen in Fig. 5.4(A). On the other hand, the coated samples exhibited less hills and valleys with minimum micro gaps, as the film thickness increases, compared to the uncoated sample. This can be attributed to the sealing of the micro gaps as a result of the deposition of Al on the surface, where at a coated thickness of 150 nm, about 95% of the nanostructures on the surface have height between 32.8 and 52.4 nm with the maximum height found to be 59 nm as illustrated in Fig. 5.4(D) and a RMSH value of 5.56 nm. This clear difference in height distribution and values is an indication of rougher surface of the uncoated sample which was smoothened out by the deposition of the nanofilm on the surface. The mean surface roughness values were found to be 10.7, 7.51, 6.32, and 4.23 nm for the uncoated, 50 nm, 100nm, and 150 nm coated substrates, respectively as shown in Fig. 5.4(A-D).

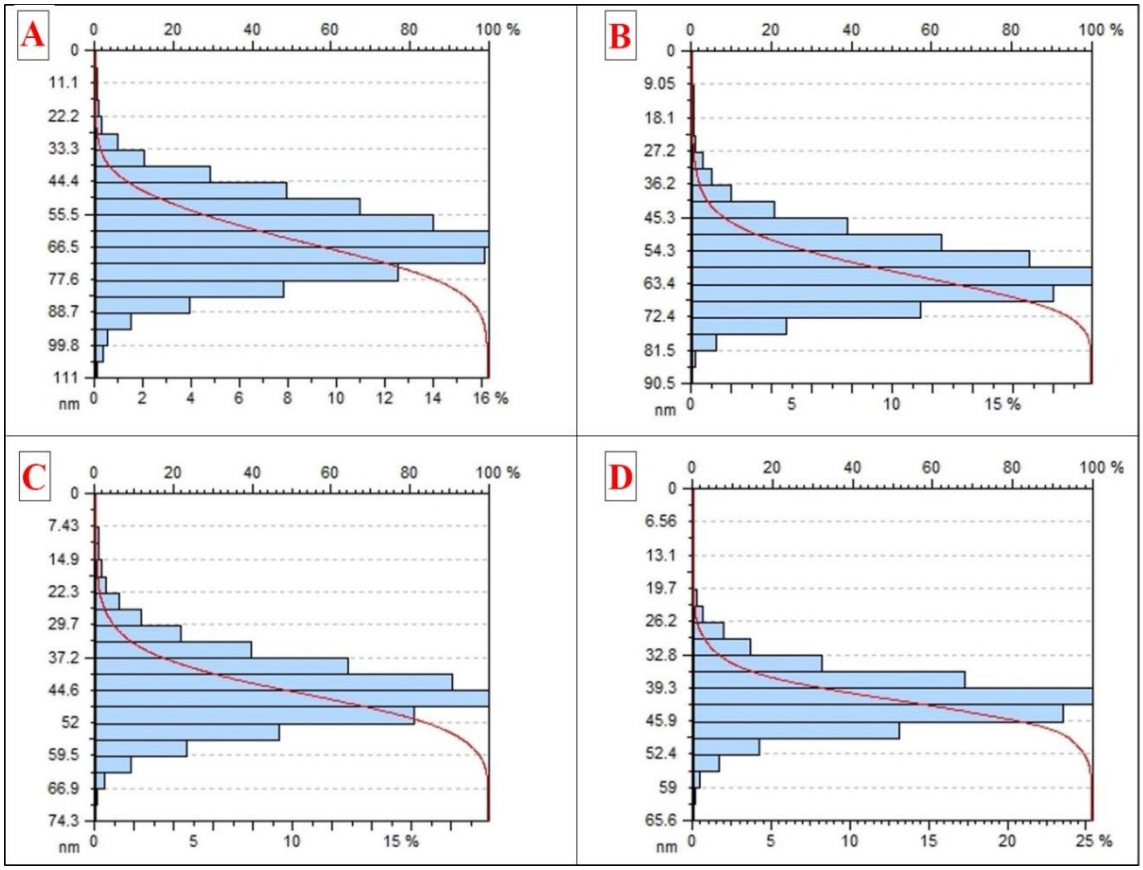

Fig. 5.4. Particles height distribution of: (A) Uncoated substrate surface, (B) 50 nm coated substrate surface, (C) 100 nm coated substrate surface, and (D) 150 nm coated substrate surface.

3.3 Water contact angle measurement

The surface wettability of the Al substrates, both coated and uncoated, were examined via liquid – surface CA measurements at different liquid temperatures and film thickness with the results demonstrated in Fig. 5.5. In the case where DIW of pH 7 was used as the testing fluid, the CA of the uncoated sample showed a higher average value than the coated samples in all cases. This suggest that the surface wettability nature was changed to a higher hydrophilic surface caused from the deposited Al and the neutral charged liquid. The minimum CA was recorded at a temperature of 25°C with a value of 55.3°, as demonstrated in Fig. 5.5(C). On the other hand, when tested the samples with DIW of pH 4 and 9, the hydrophilicity nature of the surface diverged more towards the hydrophobicity region, and in some cases, achieving a fully hydrophobic surface nature as seen in Fig. 5.5(A-G). The maximum increase in CA was

obtained at a temperature of 60°C, a pH of 9, and a film thickness of 150 nm where the CA raised from 71° to 100.1° as illustrated in Fig. 5.5(G).

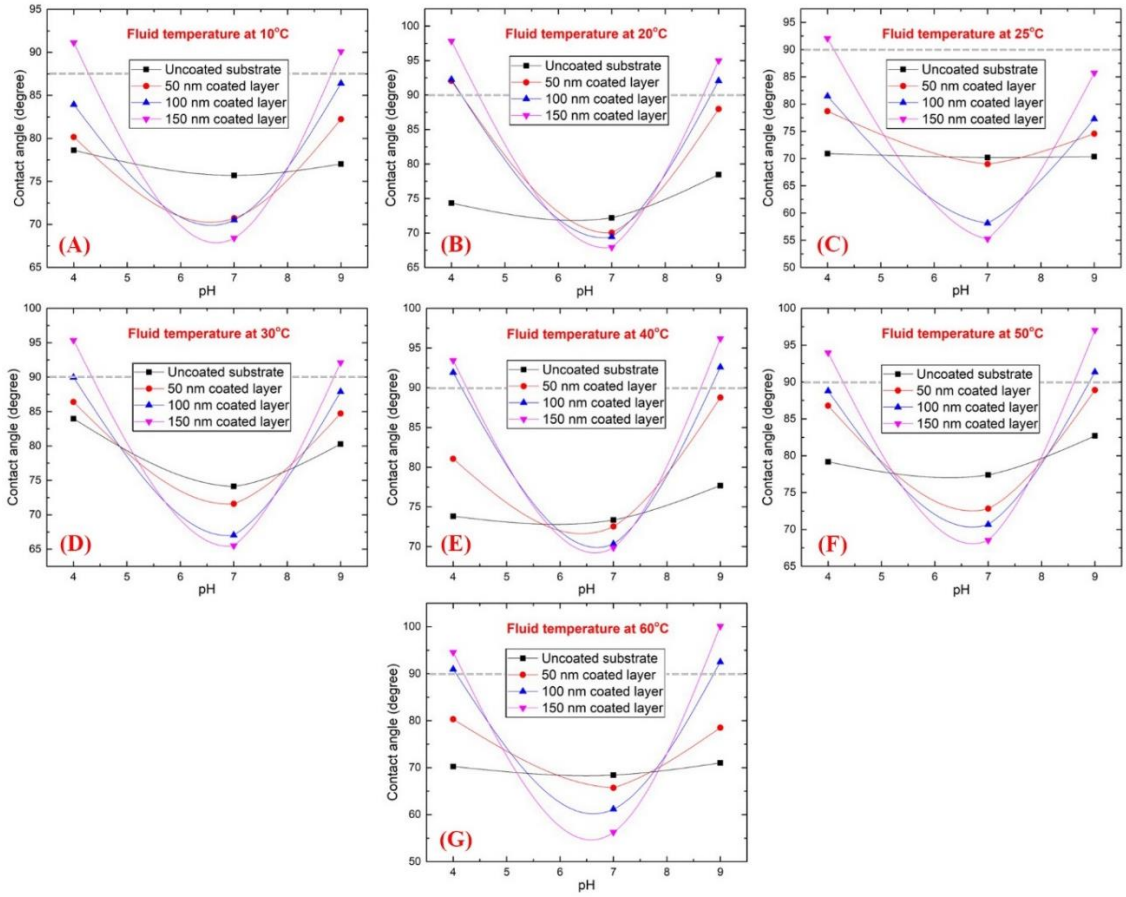

Fig. 5.5. Contact angle measurements of coated and uncoated Al substrates with DIW of pH 4, 7, and 9 at: (A) 10°C fluid temperature, (B) 20°C fluid temperature, (C) 25°C fluid temperature, (D) 30°C fluid temperature, (E) 40°C fluid temperature, (F) 50°C fluid temperature, and (G) 60°C fluid temperature.

The achieved changes in surface wettability reveals the reduction in surface energy which can be linked to the physical chemistry phenomena of Hofmeister effect which suggests an increase in propensity of large ions toward hydrophobic surfaces [34]. These large ions tend to accumulate at the air/water interface causing an enhancement in surface hydrophobicity due to their weak interaction with the liquid compared with the liquid neighbouring molecules interaction [35-37]. Table 5.2 summarises the testing parameters with their obtained contact angles.

Table 5.2. Testing parameters and obtained contact angles.

Temperature (°C)	pH	Surface coating thickness (nm)	Average contact angle (degree)
10	4	0	78.62
10	4	50	80.15
10	4	100	83.94
10	4	150	91.13
10	7	0	75.7
10	7	50	70.72
10	7	100	70.51
10	7	150	68.42
10	9	0	77.02
10	9	50	82.23
10	9	100	86.39
10	9	150	90.1
20	4	0	74.34
20	4	50	92.06
20	4	100	92.25
20	4	150	97.83
20	7	0	72.2
20	7	50	70.04
20	7	100	69.46
20	7	150	67.94
20	9	0	78.46
20	9	50	87.97
20	9	100	92.07
20	9	150	94.99
25	4	0	70.92
25	4	50	78.69
25	4	100	81.47
25	4	150	92.07
25	7	0	70.19

25	7	50	69
25	7	100	58.15
25	7	150	55.26
25	9	0	70.35
25	9	50	74.57
25	9	100	77.3
25	9	150	85.72
30	4	0	83.97
30	4	50	86.4
30	4	100	89.97
30	4	150	95.36
30	7	0	74.13
30	7	50	71.6
30	7	100	67.05
30	7	150	65.51
30	9	0	80.27
30	9	50	84.72
30	9	100	87.88
30	9	150	92.12
40	4	0	73.82
40	4	50	81.05
40	4	100	91.92
40	4	150	93.43
40	7	0	73.35
40	7	50	72.54
40	7	100	70.34
40	7	150	69.85
40	9	0	77.67
40	9	50	88.75
40	9	100	92.6
40	9	150	96.19
50	4	0	79.16

50	4	50	86.78
50	4	100	88.8
50	4	150	93.98
50	7	0	77.4
50	7	50	72.81
50	7	100	70.67
50	7	150	68.54
50	9	0	82.69
50	9	50	88.9
50	9	100	91.34
50	9	150	97.03
60	4	0	70.25
60	4	50	80.3
60	4	100	90.94
60	4	150	94.55
60	7	0	68.42
60	7	50	65.71
60	7	100	61.17
60	7	150	56.25
60	9	0	71.02
60	9	50	78.49
60	9	100	92.48
60	9	150	100.13

4. Conclusion

Surface wettability experiments were conducted for a set of aluminium coated and uncoated substrates of aluminium origin at room temperature and DIW, of pH 4, 7, and 9, temperature ranging from 10°C up to 60°C. The elemental and phase constitution analysis were examined using X-ray fluorescent and x-ray diffraction analysers, respectively. From both analysers, it was conformed that the substrates was aluminium. The surface topography and liquid contact angle were also examined using an atomic force microscopy and a contact angle goniometer devices. From the atomic force microscopy tests, it was shown that the mean surface roughness

was reduced by 60.46% to a value of 4.23 nm after depositing 150 nm layer of aluminium on the substrate surface with the height range of the structures on the surface decreasing from 33.3 – 99.8 nm to 32.8 – 52.4 nm.

Contact angle studies on the substrates using DIW of pH 4, 7, and 9, at different liquid temperatures (i.e. 10°C to 60°C), showed changes in the surface behaviours which is believed to be influenced by the free ions hosted by the adjacent liquid and the contact surface as explained by the Hofmeister theory. Thus water with large free ions tends to reduce the surface energy and hence increasing the repellence level toward the liquid. This was concluded from previous researchers work [34-37] and our obtained data, as the contact angle of DIW showed a minimum CA value of 55.3° at a pH of 7, fluid temperature of 25°C, and film thickness of 150 nm. A maximum CA value of 100.1° was obtained when the DIW was adjected to a pH value of 9, fluid temperature of 60°C, and deposition thickness of 150 nm. In general, our results showed that water, of neutral charge, tends to form a higher hydrophilic relation with the surface. This attraction increases as the difference in surface structural heights decreases, and vice versa. It also suggest that hydrophilic surfaces tend to change their nature towards hydrophobicity when smoothen and coming in contact with water hosting free charges.

In conclusion, this article has focused on integrating an EB-PVD deposition method with surface topography experiments and contact angle measurements for aluminium substrates with diverse DIW pH values and temperatures. It was shown that each of these techniques counterpart one another in providing an understanding towards the nature of activities occurring between the liquid and the surface in contact to it. In the future, it would be interesting to study and monitor the wettability behavior of aluminium – DIW nanofluids on nanocoated substrates. The impact of important parameters such as particle shape, volume percentage, fluid temperature, and sonication time on the hydrophobicity and hydrophilicity of the surface will be investigated. These experiments would be very useful into promoting the usage of nanofluids in industrial applications. This article represents the steps needed toward this direction.

References

1. Burnett, M.E.; Wang, S.Q. Current sunscreen controversies: A critical review. *Photodermatol Photoimmunol Photomed* **2011**, *27*, 58-67.

2. Lapotko, D. Corrigendum. *Nanomedicine (Lond)* **2016**, *11*, 566.

3. Maier-Hauff, K.; Rothe, R.; Scholz, R.; Gneveckow, U.; Wust, P.; Thiesen, B.; Feussner, A.; von Deimling, A.; Waldoefner, N.; Felix, R., *et al.* Intracranial thermotherapy using magnetic nanoparticles combined with external beam radiotherapy: Results of a feasibility study on patients with glioblastoma multiforme. *J Neurooncol* **2007**, *81*, 53-60.

4. Xu, B.X.; Qiao, Y.; Li, Y.B.; Zhou, Q.L.; Chen, X. An electroactuation system based on nanofluids. *Appl. Phys. Lett.* **2011**, *98*.

5. Routbort, J.; Singh, D.; Chen, G. Heavy vehicle systems optimization merit review and peer evaluation. *Annual Report, Argonne National Laboratory, Chicago, Illinois, USA* **2006**.

6. Kulkarni, D.P.; Das, D.K.; Vajjha, R.S. Application of nanofluids in heating buildings and reducing pollution. *Appl. Energy* **2009**, *86*, 2566-2573.

7. Vekas, L.; Bica, D.; Avdeev, M.V. Magnetic nanoparticles and concentrated magnetic nanofluids: Synthesis, properties and some applications. *China Particuology* **2007**, *5*, 43-49.

8. Sharma, T.; Reddy, A.L.M.; Chandra, T.S.; Ramaprabhu, S. Development of carbon nanotubes and nanofluids based microbial fuel cell. *Int J Hydrogen Energy* **2008**, *33*, 6749-6754.

9. Taylor, R.; Coulombe, S.; Otanicar, T.; Phelan, P.; Gunawan, A.; Lv, W.; Rosengarten, G.; Prasher, R.; Tyagi, H. Small particles, big impacts: A review of the diverse applications of nanofluids. *J. Appl. Phys.* **2013**, *113*.

10. Çolak, Ş.; Aktürk, C. Synthesis and characterization of undoped and doped (mn, cu, co) zno nanoparticles: An epr study. In *Emr/esr/epr spectroscopy for characterization of nanomaterials*, Shukla, A.K., Ed. Springer India: New Delhi, 2017; pp 151-179.

11. Uyeda, R. Studies of ultrafine particles in japan - crystallography - methods of preparation and technological applications. *Prog Mater Sci* **1991**, *35*, 1-96.

12. Ichinose, N.; Ozaki, Y.; Kashū, S. Applications of superfine particles. In *Superfine particle technology*, Springer London: London, 1992; pp 163-219.

13. Gleiter, H. Nanostructured materials: Basic concepts and microstructure. *Acta Mater* **2000**, *48*, 1-29.

14. Bertsch, A.; Jiguet, S.; Renaud, P. Microfabrication of ceramic components by microstereolithography. *J Micromech Microengineering* **2004**, *14*, 197-203.

15. Cho, J.; Joshi, M.S.; Sun, C.T. Effect of inclusion size on mechanical properties of polymeric composites with micro and nano particles. *Compos. Sci. Technol.* **2006**, *66*, 1941-1952.

16. Vigneshwaran, N.; Varadarajan, P.V.; Balasubramanya, R.H. Application of metallic nanoparticles in textiles. In *Nanotechnologies for the life sciences*, Wiley-VCH Verlag GmbH & Co. KGaA: 2010.

17. Sharma, Y.C.; Srivastava, V.; Upadhyay, S.N.; Weng, C.H. Alumina nanoparticles for the removal of ni(ii) from aqueous solutions. *Industrial & Engineering Chemistry Research* **2008**, *47*, 8095-8100.

18. Ding, Y.; Chen, H.; Musina, Z.; Jin, Y.; Zhang, T.; Witharana, S.; Yang, W. In *Relationship between the thermal conductivity and shear viscosity of nanofluids*, 3rd International Symposium on Functional Materials 2009, ISFM 2009, Jinju, 2010; Jinju.

19. Vignesh, R.B.; Balaji, J.; Sethuraman, M.G. Surface modification, characterization and corrosion protection of 1,3-diphenylthiourea doped sol-gel coating on aluminium. *Prog Org Coatings* **2017**, *111*, 112-123.

20. Jodin, L.; Dupuis, A.C.; Rouviere, E.; Reiss, P. Influence of the catalyst type on the growth of carbon nanotubes via methane chemical vapor deposition. *J Phys Chem B* **2006**, *110*, 7328-7333.

21. Cai, W.Q.; Yu, J.G.; Cheng, B.; Su, B.L.; Jaroniec, M. Synthesis of boehmite hollow core/shell and hollow microspheres via sodium tartrate-mediated phase transformation and their enhanced adsorption performance in water treatment. *J. Phys. Chem. C* **2009**, *113*, 14739-14746.

22. Yu, X.; Yu, J.; Cheng, B.; Jaroniec, M. Synthesis of hierarchical flower-like alooh and tio2/alooh superstructures and their enhanced photocatalytic properties. *The Journal of Physical Chemistry C* **2009**, *113*, 17527-17535.

23. Najafzadeh, M.; Shiri, J.; Sadeghi, G.; Ghaemi, A. Prediction of the friction factor in pipes using model tree. *ISH Journal of Hydraulic Engineering* **2017**, *24*, 9-15.

24. Kang, M.; Lee, J.W.; Kang, Y.T. Reduction of liquid pumping power by nanoscale surface coating. *International Journal of Refrigeration-Revue Internationale Du Froid* **2016**, *71*, 8-17.

25. Rodrigues, S.P.; Alves, C.F.A.; Cavaleiro, A.; Carvalho, S. Water and oil wettability of anodized 6016 aluminum alloy surface. *Applied Surface Science* **2017**, *422*, 430-442.

26. Ahmad, Z. Effect of velocity on the open circuit potential and corrosion rate of aluminium alloys. *Met Corros Ind* **1985**, *60*, 289-296.

27. Ahmad, Z. The kinetics of anodic and cathodic polarization of aluminium and its alloys. *Anti-Corros. Methods Mater.* **1986**, *33*, 4-11.

28. Tian, X.F.; Li, Y.P.; Wan, S.K.; Wu, Z.Q.; Wang, Z.W. Functional surface coating on cellulosic flexible substrates with improved water-resistant and antimicrobial properties by use of zno nanoparticles. *J. Nanomater.* **2017**, *2017*.

29. Caldona, E.B.; de Leon, A.C.; Pajarito, B.B.; Advincula, R.C. Novel anti-corrosion coatings from rubber-modified polybenzoxazine-based polyaniline composites. *Applied Surface Science* **2017**, *422*, 162-171.

30. Zhang, X.L.; Wang, Y.C.; Zhao, D.W.; Guo, J. Improved thermal performance of heat exchanger with tio2 nanoparticles coated on the surfaces. *Appl Therm Eng* **2017**, *112*, 1153-1162.

31. Phan, H.T.; Caney, N.; Marty, P.; Colasson, S.; Gavillet, J. Surface wettability control by nanocoating: The effects on pool boiling heat transfer and nucleation mechanism. *Int. J. Heat Mass Transf.* **2009**, *52*, 5459-5471.

32. Akbari, E.; Gheitaghy, A.M.; Saffari, H.; Hosseinalipour, S.M. Effect of silver nanoparticle deposition in re-entrant inclined minichannel on bubble dynamics for pool boiling enhancement. *Exp. Therm. Fluid Sci.* **2017**, *82*, 390-401.

33. Hariprasad, S.; Gowtham, S.; Arun, S.; Ashok, M.; Rameshbabu, N. Fabrication of duplex coatings on biodegradable az31 magnesium alloy by integrating cerium conversion (cc) and plasma electrolytic oxidation (peo) processes. *J Alloys Compd* **2017**, *722*, 698-715.

34. Sivan, U. The inevitable accumulation of large ions and neutral molecules near hydrophobic surfaces and small ions near hydrophilic ones. *Current Opinion in Colloid & Interface Science* **2016**, *22*, 1-7.

35. Morag, J.; Dishon, M.; Sivan, U. The governing role of surface hydration in ion specific adsorption to silica: An afm-based account of the hofmeister universality and its reversal. *Langmuir* **2013**, *29*, 6317-6322.

36. Schlesinger, I.; Sivan, U. New information on the hydrophobic interaction revealed by frequency modulation afm. *Langmuir* **2017**, *33*, 2485-2496.

37. Schwierz, N.; Horinek, D.; Sivan, U.; Netz, R.R. Reversed hofmeister series—the rule rather than the exception. *Current Opinion in Colloid & Interface Science* **2016**, *23*, 10-18.

Chapter 6

Publication 5: Effect of Water Temperature, pH Value, and Surface Roughness on the Wettability Behaviour of Copper Surfaces Coated with Copper Using EB-PVD Technique

(Ali, N.; Teixeira, J.A.; Addali, A. Effect of Water Temperature, pH Value, and Surface Roughness on the Wettability Behaviour of Copper Surfaces Coated with Copper Using EB-PVD Technique, *J. Nano. Res.*, In Press)

Effect of Water Temperature, pH Value, and Surface Roughness on the Wettability Behaviour of Copper Surfaces Coated with Copper Using EB-PVD Technique

A B S T R A C T

This research investigates the effect of surface roughness, water temperature, and pH value on the wettability behaviour of copper surfaces. An electron beam physical vapour deposition technique was used to fabricate 25, 50, and 75 nm thin films of copper on the surface of copper substrates. Surface topographical analysis, of the uncoated and coated samples, was performed using an atomic force microscopy device to observe the changes in surface microstructure. A goniometer device was then employed to examine the surface wettability of the samples by obtaining the static contact angle between the liquid and the attached surface using the sessile drops technique. Waters of pH 4, 7, and 9 were employed as the contact angle testing fluids at a set of fixed temperatures that ranged from 20^{o}C to 60^{o}C. It was found that increasing the deposited film thickness reduces the surface roughness of the as-prepared copper surfaces and thus causing the surface wettability to diverge from its initial hydrophobic nature towards the hydrophilic behaviour region. A similar divergence behaviour was seen with the rise in temperature of water of pH 4, and 9. In contrast, the water of pH 7, when tested on the uncoated surface, ceased to reach a contact angle below 90^{o}. It is believed that the observed changes in surface wettability behaviour is directly linked to the liquid temperature, pH value, surface roughness, along with the Hofmeister effect between the water and the surface in contact.

Keywords: Coating; contact angle; pH value; surface topography; wettability.

1. Introduction

Heat exchangers (HEs) are heat transfer devices that exchange thermal energy between two or more mediums. They play a significant role in the operation of many systems such as heat recovery units, process industries, and power plants. The working fluids used in HEs can be of single phase (e.g. liquid-to-liquid or gas-to-gas), or of two phase (i.e. gas-to-liquid). The general classification of HEs is seen as either a direct or indirect-contact type [1]. In the direct-

contact configuration, the heat transfer fluids undergoes direct contact with each other due to the absence of physical separators (e.g. cooling towers), while in the indirect-contact category, the fluids streams are segregated apart via a solid surface in the form of tubular, plate, or other suitable designed geometry. Plate (also known as plate-and-frame) and shell-and-tube are two examples of commonly used indirect-contact HEs. In comparison to the shell-and-tube HE, the plate-and-frame type tends to have a relatively small surface area to volume ratio, enhanced thermal-hydraulic performance, flexible thermal sizing, and higher energy efficiency [2]. For the aforementioned reasons, today, many well-known manufacturers across the globe are offering adapted or improved versions of the plate HE design. Although the plates used can be manufactured from any metal or alloy that has the capability of being welded or cold formed, the most common commercial devices uses copper (Cu), stainless steel, and aluminium in fabricating the plates [3]. Between the three previous materials, Cu has the highest thermal conductivity (386 W/m.^{o}C at 20^{o}C), is relatively low in price, and has favourable processing properties [4, 5]. The common heat transfer fluid hosted by the plate HE is water as it is cheap to obtain and acquires high enthalpy of vaporization; but other advanced types of fluids, such as nanofluids, can also be employed to enhance the heat transfer operation of the system [6-10]. In addition, the performance of the plate HE has been known to depend on a number of factors, including, plate structural design, surface characteristics, liquid properties, … etc. Furthermore, similar to other types of HEs, plate HEs suffer from pressure drop within its system which can be reduced via modifying the previously mentioned factors [11-13].

On the other hand, surface wettability, which is a liquid – surface interaction mechanism that depends greatly on the chemical compositions and surface structures, can play a vital role in improving the efficiency of plate HEs via enhancing the critical heat flux and fluid dynamics of the system [14-16]. Surface wettability can be determined through the contact angle (CA) formed between a static droplet of liquid (e.g. water) and the surface in contact to it. Moreover, the minimum and maximum values a liquid static contact angle can have on a surface can be determined by the difference between the receding and advancing contact angles, in what is known as the dynamic or hysteresis contact angle [17]. Such contact angle measurement is important when dealing with a liquid – solid system of metastable state (e.g. porous media), where the contact lines of the liquid – vapour, liquid – solid, and solid – vapour are in actual motion (i.e. the three phase contact lines are not in a static condition). An in-depth discussion and explanation of the significant role of contact angle hysteresis on coated surfaces can be

found in Gatapova et al. [18] work. It is important to note that: 1- the contact angle hysteresis depends on a variety of parameters, including liquid penetration rate on the solid surface, formed droplet size relative to the surface physical topography, employed liquid evaporation rate, examined surface heterogeneity and impurity, operator consistency, … etc; and 2- the measurements have very low accuracy and reproducibility, thus requiring the repetition of the test, sometime up to ten times, for better interpretation of the data [19]. The surface is classified by its static contact angle as super-hydrophilic if the CA is less than 5^o, hydrophilic if the CA is between 5^o to 90^o, hydrophobic if the CA is between 90^o to 150^o, and super-hydrophobic if the CA is greater than 150^o [20]. The term hydrophobic represent the tendency of the liquid to repel away from the surface, whereas hydrophilic reflects the propensity of the liquid to wet the surface. Different models have been developed and are used for the calculation of the CA, such as the Wenzel [21], Cassie and Baxter [22], and Young [23] models. Both Wenzel, and Cassie and Baxter theories take into account the surface roughness effect on hydrophobicity. The Wenzel model considers the influence of surface roughness when the pores are fully associated with the liquid, where it assumes that the surface hydrophobicity is proportional with the surface roughness. Furthermore, the model is known to be limited to hydrophobic surfaces of CA of up to 120^o, and hence cannot be used for predicting super-hydrophobicity. As for the Cassie and Baxter model, their theory is based on the assumption of the existence of trapped air within the hollow spaces of the surface structure, which leads to a reduction in the liquid – surface area of interaction. On the other hand, the Young model is widely seen used in both industry and research for measuring the CA of flat homogeneous surfaces, except for a complete wetting condition, where the model ceases to hold [24]. Fig. 6.1 shows all three models, where θ_{CB}, θ_w, θ_y, γ_S, γ_L, and γ_{SL} are the Cassie and Baxter apparent CA, apparent CA on a rough surface, CA on a smooth surface, surface free energy of the solid, surface free energy of the liquid, and surface free energy of the solid – liquid interface, respectively.

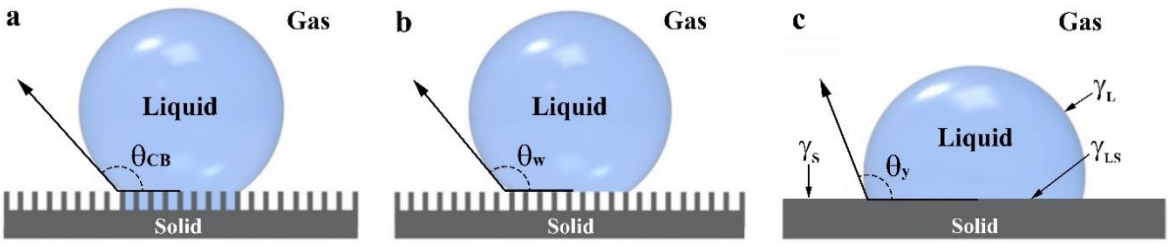

Fig. 6.1. Contact angle measurement theories illustrations; (a) the Wenzel model, (b) the Cassie and Baxter model, and (c) the Young model.

In general, the wettability behaviour of water on Cu surfaces is often seen to exceed a CA of 70^{o}, when exposed to ambient conditions [5, 25]. Surface modification approaches, such as thin film coatings, can be applied to help manipulate the surface wettability, thus changing or enhancing the liquid attraction nature of the surface. Among the available thin films deposition techniques, electron beam physical vapour deposition (EB-PVD) is considered to be one of the favourable coating approaches as it provides high deposition purity, large coating coverage area, uniform elemental distribution on surface, in-situ growth monitoring, precise film thickness, and smoothness control [26, 27]. The EB-PVD process is a thermal coating method, where the deposition takes place inside a high-vacuum chamber via concentrating a high energy electron beam on a material causing it to partially evaporate and then condense on the exposed substrate surface to form the coated layer [26]. On the industrial scale, EB-PVD have been, for more than 40 years, broadly employed in coating surfaces of different geometrical configurations, not only due to its capability of altering the wettability behaviour of the surface but also the fabricated coatings exhibits improved thermal shock resistance and strain tolerance, which significantly enhances the deposited film service life [28]. Moreover, the coating columnar microstructure that results from the process has higher thermal conductivity compared to other techniques (e.g. air plasma spray) [29].

Herein, we demonstrate the deposition of Cu thin films on Cu substrates using an EB-PVD approach. The reason behind investigating Cu was to cover the three common plate HEs materials that were earlier mentioned, where we have previously explored the deposition of stainless steel 316L and aluminium films on substrates of similar bulk materials [20, 30]. The fabrication method consists of thin film deposition, at constant deposition rate, on a stationary substrate surface. Furthermore, to illustrate the crucial role of the deposition on the surface height distribution and root mean square roughness, a comparison between the surfaces topography measurement of the uncoated, 25, 50, and 75 nm coated substrates was performed using an atomic force microscopy (AFM) device. In addition, the influence of both film thickness and water, of pH 4, 7, and 9 at temperatures ranging from 20^{o}C to 60^{o}C, on the static CA measurement was also reported. To the best of the authors knowledge, this study is considered to be the first of its kind, where other researchers have illustrated Cu deposition on Cu substrates using sputtering deposition technique and have not covered the EB-PVD film deposition approach or the combinational effect of water temperature changes and pH value on the Cu surface wettability behaviour [31, 32].

2. Experimental

2.1 Materials

All chemicals were used as-received from the suppliers without further purification. Acetone ($CH_3COCH_3 \geq 99.5\%$) grade ACS reagent and hydrochloric acid (HCl ~37%) grade ACS reagent were purchased from SIGMA-ALDRICH, and sodium hydroxide pellets (NaOH ~98%) grade AR was obtained from LOBA Chemie. Cylindrical 99.99% pure Cu pellets, of 3.175 mm diameter and 3.175 mm long, were purchased from Kurt J. Lesker Company. Four square-shaped Cu substrates, of 3 cm^2 surface area and 1 cm thickness, were mechanically prepared from a 99.99% pure Cu bullion bar, and bought from the United Kingdom RICE METALS Company, using a computer numerical control (CNC) machine. The substrates were afterwards cleaned with acetone, using a bath type Soniclean Limited 250TD ultrasonicator, for 30 min at room temperature then carefully wiped to remove any remaining residuals. Three litres of deionised water, of pH 6.11, produced at room temperature by an Elga PR030BPM1-US Purelab Prima 30 water purification system were divided into 3 sets of 1 L's. The liquids pH value were then adjusted at 25^oC to 4, 7, and 9, respectively, by either adding the as-received HCl or NaOH, while monitoring the changes in pH value via a HACH HQ11D portable pH meter of 0.002 pH accuracy.

2.2 X-ray fluorescence and x-ray diffraction characterisation

Elemental analysis of the as-prepared Cu substrates were performed three times and averaged, using a BRUKER TITAN S1 x-ray fluorescent (XRF) handheld analyser, to insure that the bulk components of the fabricated substrates matches with that one provided by the manufacturer. This was done by placing the substrate on the working station then adjusting the XRF device lens vertically on top of the examined substrate before starting the measurements, which required 10 seconds per measurement. Additionally, a crystal structure test was performed using a 9 kW Rigaku SmartLab, Japan, x-ray diffraction (XRD) analyser and its software, SmartLab Guidance, using a Cu K_α x-ray source with a diffraction angle of 2Θ and an incidence beam angle of 0.02° to determine the phase constitution of the examined substrate. The diffraction scanning angle was set to be from 20° to 80°, with a scanning rate of 2°/min.

2.3 Fabrication of copper films

Three of the four substrates were individually placed inside an EB-PVD device chamber, after tightly adjusted on the sample holder then screwed vertically on top of the evaporation source. The remaining Cu substrate was sealed and stored as references for characterization and comparison purposes. Copper pellets, which were used as the deposition source, were placed inside a water cooled Kurt J. Lesker company 5.87 mm^3 inner volume graphite crucible liner located at the bottom of the EB-PVD chamber. The EB-PVD device chamber was then sealed and evacuated to a pressure of 6 x 10^{-6} Torr, to insure that any particles contamination within the chamber were removed. An INFICON SQC-310 electronic thickness monitoring system, which is connected to a sensor placed inside the chamber, was used to control the deposited film thickness. Next, the deposition process was initiated and fixed at a rate of 0.05 Å/s to form a set of 25, 50, and 75 nm thick films, respectively. It is important to note that, while depositing the films, each substrate was fixed at a target-to-sample distance of 26 cm and that the EB-PVD chamber used had a 40 cm inner diameter × 50 cm inner height. After completing each deposition process, the coated substrate was left in the chamber for 4 h to cool down before it was removed from the EB-PVD chamber and used for further analysis. The films fabrication procedure used for the preparation of the Cu depositions on the substrates is shown in Fig. 6.2a – c.

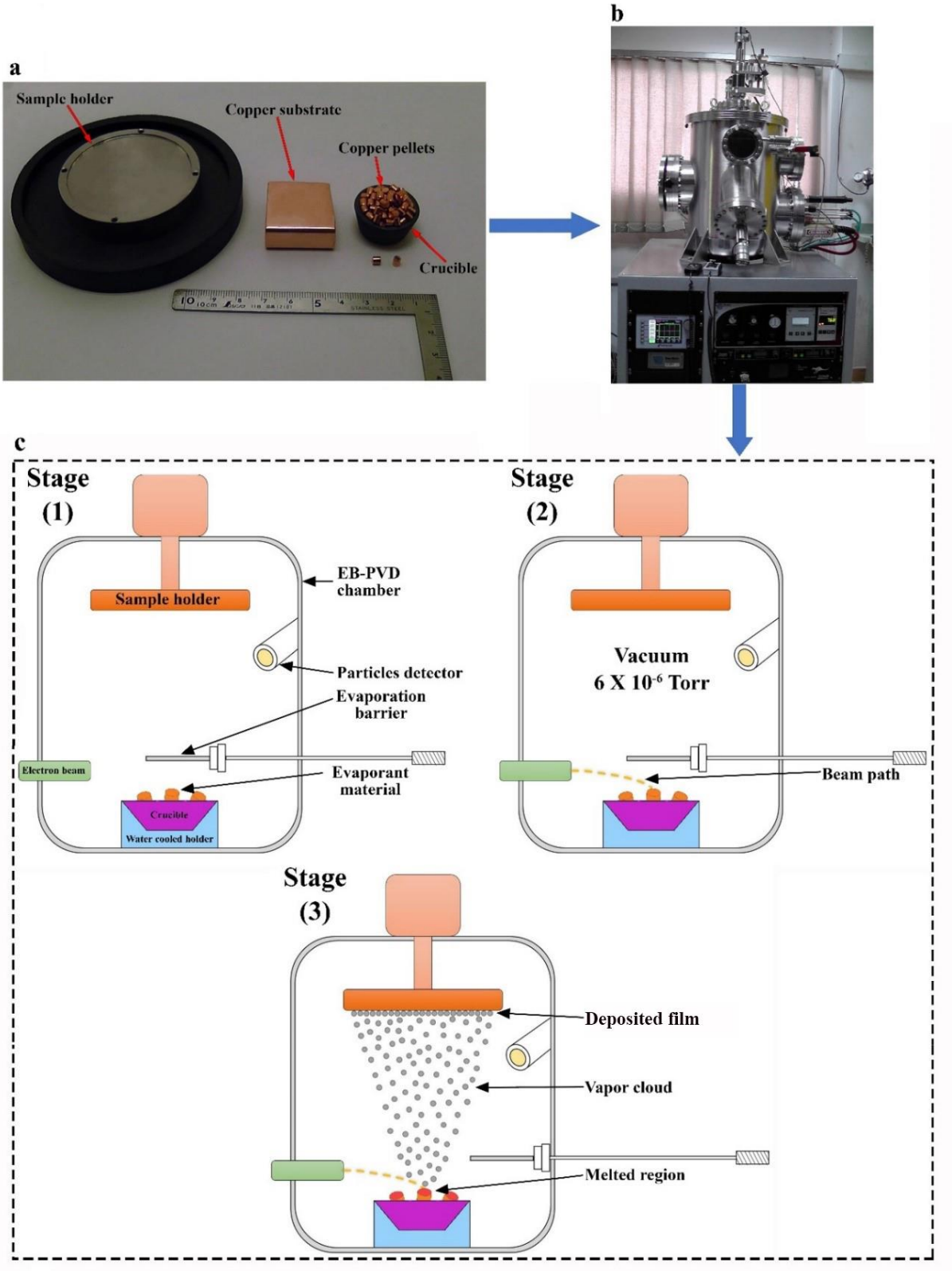

Fig. 6.2. Electron beam physical vapour deposition process; (a) the Cu substrate, Cu evaporated source, and sample holder, (b) EB-PVD device used for the deposition, and (c) the high vacuum EB-PVD coating procedure.

2.4 Surface characterization

Agilent Technologies 5600LS AFM instrument, equipped with a 90 µm N9521A multipurpose scanner in tapping mode, was used to obtain the surface topographical images of the coated and uncoated Cu substrates at room temperature, via a PicoView 1.14.4 software, at 10 µm2, 1,024 × 1,024 pixels, and 0.84 line/s. A NANOSENSORSTM silicon tips (type: PPP-CONTPt-20; resonance frequency 6 – 21 kHz) were employed for the surface characterization. Data analysis was performed, using a Pico Image Basic 6.2 software, through first enabling the gaussian filter with the 0.25 μm^2 cut-off feature, for the background corrections, then having the software calculate the main height parameters and particles height distribution of the samples.

2.5 Water properties measurements and theoretical calculation

Water, of pH 4, 7, and 9, kinematic viscosity and density changes with temperature were characterized at a temperature range from 20°C to 60°C, via an Anton Paar DMA 4500M density meter of accuracy 5 x 10^{-5} g/cm³ and a PAC Herzog HVM 472 multirange viscometer device, respectively. It is worth noting that both of the previously mentioned devices have built-in calibration systems that are initiated before starting the measurements. Furthermore, the variation in pH value, of the as-prepared liquids, with temperature was theoretically calculated, for the same range of temperatures, using the following equation [33, 34]:

$$pH_T = pH_{25^oC} + [(T - 25^oC) \times solution\ temperature\ coefficient] \quad (1)$$

Where pH_T, pH_{25^oC}, and T are the solution pH value for the targeted temperature, the solution pH value at 25°C, and the targeted temperature in Celsius, respectively. The solution temperature coefficient for water of pH 7 and 9 was selected to be -0.016 pH/°C and -0.029 pH/°C, respectively, based on analysing previous literature data [34-36]. As for the water of pH 4, due to the lack of published data as far as the authors knowledge, the solution temperature coefficient was obtained by extrapolating the two aforementioned ones and choose to be -0.004 pH/°C, which provides a very close trend behaviour as water of pH 5 [37]. In addition, published measurements on the variation of water pH value with temperature were also included for comparison with the theoretical results. A tabulation of the calculated, measured and published parameters of the liquids in terms of temperature are illustrated in Table 6.1, and the in-depth explanation of the data can be found in ref [30].

2.6 Surface wettability characterization

Three Hamilton 1000 series 1 mL syringes containing the liquids, of pH 4, 7, and 9, respectively, were individually placed inside a Dataphysics SHD syringe temperature controller, which is integrated with the Dataphysics OCA 100 automatic multi-liquid dispenser contact angle goniometer device. This was done in order to raise or lower the fluids temperature hosted by the syringes, while monitoring the liquid temperature changes. The surface wettability, of the coated and uncoated Cu substrates, was measured through the Sessile drop approach [38] by carefully dispersing a 5 µL droplet, at a dosing rate of 5 µL/s, on each atmospherically exposed sample surface. Liquid – surface average CA (ACA) was then obtained by capturing three droplets images while being at static condition and averaging their results, using the goniometer high speed video camera and the software (SCA 20) provided with the device that relies on the Young equation in calculating the CA [17, 39]. The measurements were performed for the fluids temperatures between 20 – 60^{o}C, with an increment of 10^{o}C and a ± 0.1^{o} CA precision. Comparison between the ACA measurements at room temperature and published data was also performed.

Table 6.1. Water density, kinematic viscosity, and pH value variation with temperature.

Temperature (°C)	Measured density (g/cm^3)			Published density (g/cm^3) [38]	Measured kinematic viscosity (mm^2/s)			Published kinematic viscosity (mm^2/s) [38]	Calculated pH			Published pH [35, 36]	
	pH 4	pH 7	pH 9	Pure water	pH 4	pH 7	pH 9	Pure water	pH 4	pH 7	pH 9	pH 7	pH 9
20	0.99821	0.99822	0.99821	0.99823	1.01140	1.01140	1.01140	1.00378	4.02	7.08	9.15	7.08	9.17
25	0.99701	0.99699	0.99702	0.99707	0.90134	0.90075	0.90075	0.89292	4.00	7.00	9.00	7.00	9.00
30	0.99564	0.99562	0.99563	0.99567	0.80927	0.80951	0.80967	0.80087	3.98	6.92	8.86	6.92	8.88
40	0.99219	0.99217	0.99219	0.99224	0.69724	0.69381	0.68507	0.65821	3.94	6.76	8.57	6.77	8.54
50	0.98800	0.98799	0.98800	0.98807	0.59003	0.58356	0.59501	0.55371	3.90	6.60	8.28	6.63	8.26
60	0.98293	0.98264	0.98293	0.98324	0.50320	0.51537	0.51986	0.47486	3.86	6.44	7.99	6.51	8.02

3. Results and Discussion

3.1 Substrates analysis

The elemental content of the as-machined Cu substrates, after being examined by the XRF device for three times then averaged, are given in Table 6.2. It can be seen that the Cu content was 0.17% less than the one reported by the raw material supplier (i.e. 99.99% Cu). This is believed to be part of the device error margin (i.e. 0.39%). Furthermore, the XRD analysis of the samples showed three sharp Cu diffraction Bragg's peaks in the XRD pattern (PDF Card No.: 03-065-9026), as seen in Fig. 6.3. Thus, confirming that the bulk formation of the substrates was of Cu base, and hence matching well with the XRF findings.

Table 6.2. Averaged XRF elemental analysis of the copper substrate.

Analysis	**Element**	**wt.%**			
		Content	**Maximum**	**Minimum**	**+/− Error**
1st run	Copper	99.79	100	90	0.39
	Zirconium	0.01	–	–	0.01
	Bismuth	0.02	–	–	0.02
2nd run	Copper	99.82	100	90	0.39
	Zirconium	0.02	–	–	0.01
3rd run	Copper	99.86	100	90	0.39
	Zirconium	0.02	–	–	0.01
	Silver	0.03	–	–	0.03
Runs average	Copper	99.82	100	90	0.39
	Zirconium	0.02	–	–	0.01

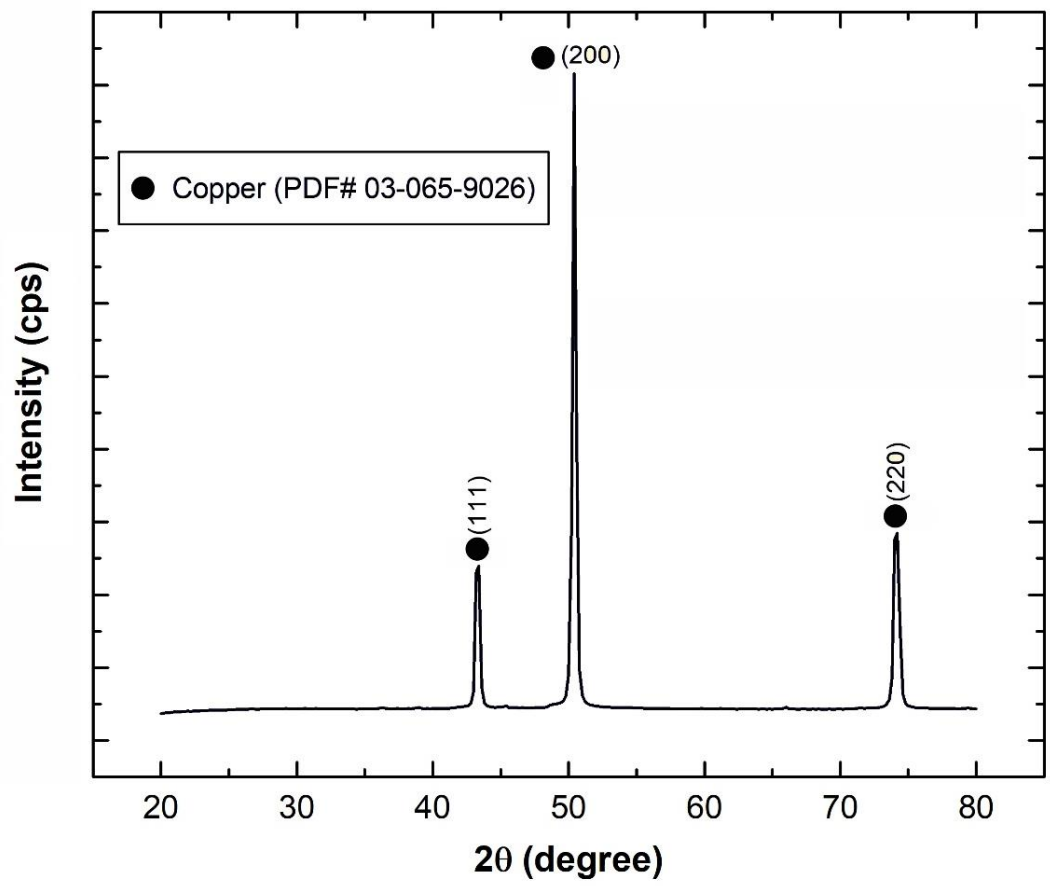

Fig. 6.3. X-ray diffraction pattern of copper substrate.

3.2 Surface characterization

Surface topographical analysis of the uncoated and coated Cu substrates, obtained by the AFM device, is shown in the form of two and three dimensional profiles, as illustrated in Fig. 6.4a–h. The experimental results have revealed that the nanostructures on the undeposited surface have a range of height between ~ 205 to 308 nm (Fig. 6.5a), with almost 75% of the structure height being in the range of 240–257 nm. Maximum height of surface (MHS) and root mean square roughness (RMSR) have values of 342 nm and 9.47 nm, respectively. On the other hand, deposition of the Cu film on the substrate surface and increasing its thickness (Fig. 6.4c–h) led the structure height on the surface, MHS, and RMSR to reduce, reaching values between ~ 31.2 to 72.7 nm (Fig. 6.5d), 104 nm, and 5.29 nm, respectively. Furthermore, the average roughness values were found to be 6.05, 5.01, 4.39, and 3.71 nm for the uncoated, 25, 50, and 75 nm coated substrates, respectively.

The reason behind the aforementioned changes in surface parameters cannot be attributed to the deposited film alone because in reality Cu films are never flat [39]. This means that when depositing Cu on a smooth surface (i.e. a surface of very low roughness) of roughly uniformed structural height distribution, the film would tend to form an island-like structure of layers as a result of undergoing a Volmer-Weber growth mode, and hence the roughness of the surface consequently increases [40]. Therefore, the seen reduction in height parameters can be better explained by the combination of the following key factors [41-46]:

1- The examined surface originally contained defects in the form of deep valleys, hills (i.e. high peaks), and micro sized gaps, and thus the evaporated material tend to occupy the lower structure of the surface (e.g. gaps), phase change into droplets due to the temperature difference between the surface and the vapour in contact, then solidifies as a result of been further cooled down, and hence the variation in structural height of the surface is reduced.
2- The very low deposition rate employed in the EB-PVD process lowers the film particles clustering size; otherwise, if high deposition rates were alternatively used then the amount of atoms arriving per unit time on to the substrate surface would have been higher and thereby resulting in the formation of larger sized clusters.
3- The deposited film is not thick enough to completely eliminate the memory of the initial substrate roughness, thus the dynamic growth process of the coated layer will have a relative reduction influence on the surface roughness.

In general, the results have shown that the EB-PVD deposited film had led to a much smoother surface in comparison to the uncoated substrate, and hence the as-prepared substrates surfaces would have exhibited less height variation within its structure. Additional height parameters values obtained from the AFM analysis of the substrates (i.e. coated and uncoated samples) can be seen in Table 6.3.

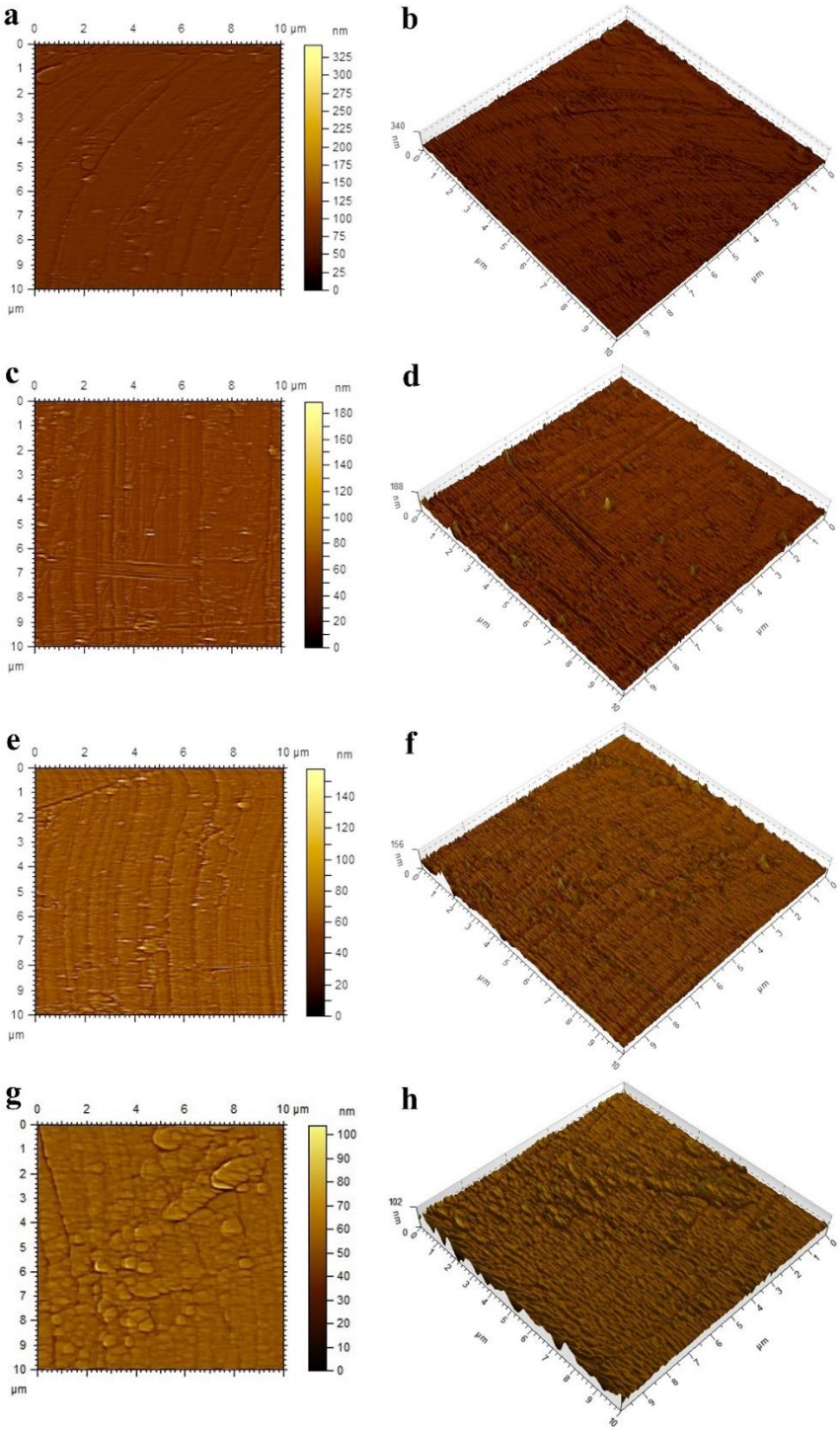

Fig. 6.4. Atomic force microscopy images; (a) 2D profile of uncoated sample, (b) 3D profile of uncoated sample, (c) 2D profile of 25 nm coated sample, (d) 3D profile of 25 nm coated sample, (e) 2D profile of 50 nm coated sample, (f) 3D profile of 50 nm coated sample, (g) 2D profile of 75 nm coated sample, and (h) 3D profile of 75 nm coated sample.

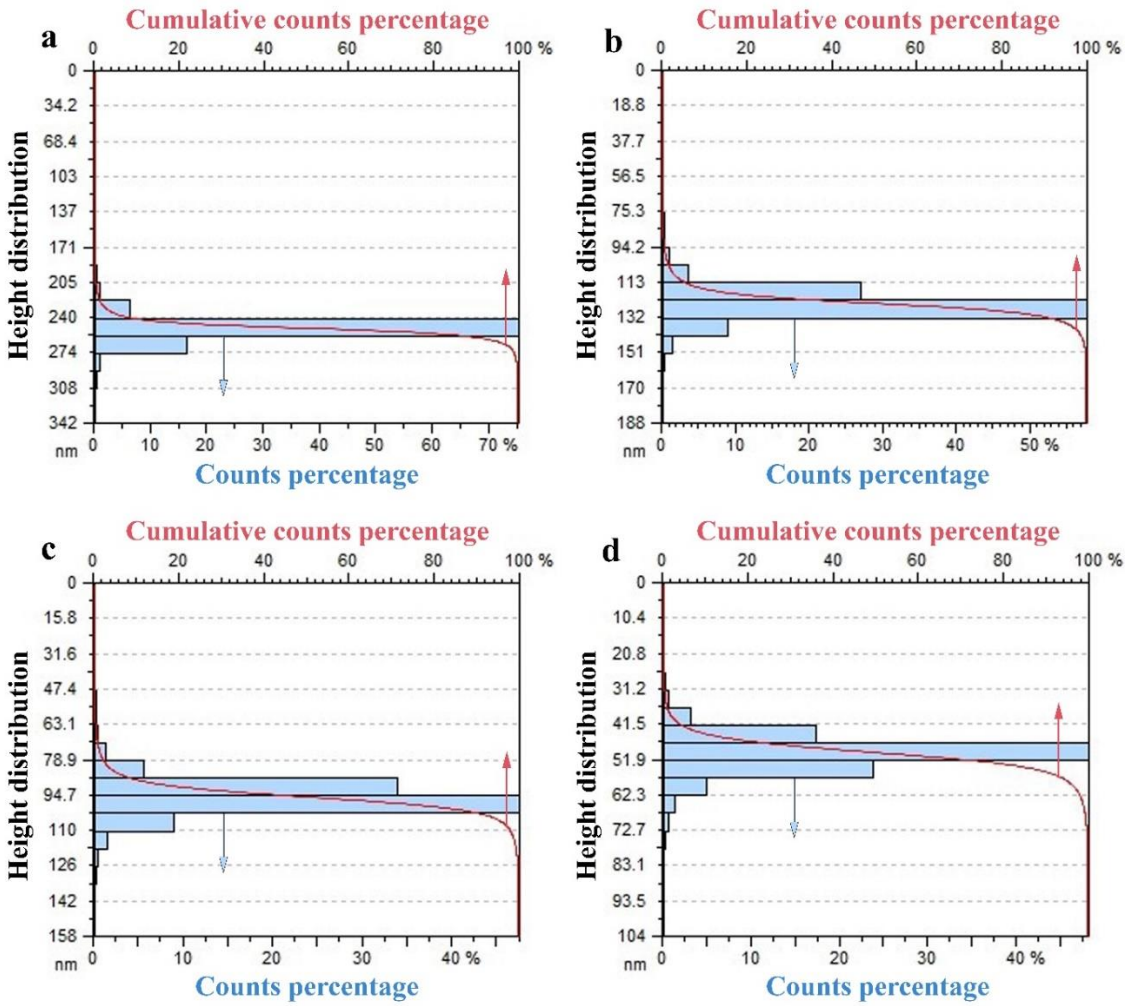

Fig. 6.5. Particles height distribution; (a) uncoated substrate surface, (b) 25 nm coated substrate surface, (c) 50 nm coated substrate surface, and (d) 75 nm coated substrate surface.

Table 6.3. Height parameters of the AFM analysis of the uncoated, 25, 50, and 75 nm coated copper substrates.

Height parameters	**Film thickness (nm)**			
	0	**25**	**50**	**75**
Skewness	1.73	1.38	0.83	-0.39
Kurtosis	29.10	15.80	12.60	9.11
Maximum peak height (nm)	250.0	124.0	95.5	50.0
Maximum valley depth (nm)	92.0	64.0	62.3	53.8

3.3 Contact angle measurement

The surface The surface wettability of the Cu substrates, both coated and uncoated, were examined via liquid – surface CA measurements at different liquid pH value, liquid temperature, and deposited film thickness. Fig. 6.6 shows photographic images of the variation in liquids ACA at the lowest and highest limits (i.e. at liquid temperature of 20^{o}C and 60^{o}C, and deposited film thickness of 0 nm and 75 nm). It can be noticed from Fig. 6.6 that the deposited Cu film caused the surface ACA, of each examined set of water temperature and pH value, to decrease. This is because the deposited film enhances the surface energy of the substrate, due to the reduction in both surface micro-roughness and air pockets formation at the interface between the liquid and the substrate, and hence causes the ACA to reduce [47, 48]. Moreover, the level of decrease is seen to be linked to the three main parameters; i.e. water pH value, temperature, and changes in surface roughness caused by the deposited film [20, 49, 50]. For example, the ACA of water of pH 4, at 20^{o}C and 60^{o}C, shows a decrease from 101.9^{o} and 81.3^{o} (uncoated) to 88.5^{o} and 79.0^{o} (75 nm film), respectively. Whereas the ACA of as-prepared liquid of pH 7, at the same two aforementioned temperatures, shows a drop down in ACA from 91.9^{o} and 92.5^{o} (uncoated) to 87.1^{o} and 88.3^{o} (75 nm film), respectively. In addition, the ACA changes with liquid temperature and fabricated film thickness, within the full measured range, is demonstrated in Fig. 6.7a–c, where the grey dashed line in the plots represents the transition point between hydrophobic (top) and hydrophilic (bottom) surface behaviour. In the case where water of pH 4 was used as the testing liquid (Fig. 6.7a), the uncoated surface showed a shift in its wettability nature, beyond 25^{o}C, from hydrophobic to hydrophilic. Furthermore, the added film layer on the substrate is clearly seen to cause the same wettability shift throughout the examined liquid temperature range, except when the liquid temperature was fixed at 20^{o}C, where the ACA was observed to be 90.4^{o} (i.e. slightly above the transition point). As for the water of pH 7 (Fig. 6.7b), almost 80% of the obtained data were within the hydrophobic region and have shown some fluctuation in the uncoated substrate ACA results trend across the liquid temperature escalation. The fluctuation in ACA outcome, of the characterized surface, is seen to be higher when employing 20–40^{o}C water of pH 9 (Fig. 6.7c). It is believed that the reason behind the previous results trend can be related to the amount of decrease in each liquid pH value with the rise in temperature, as recorded in Table 6.1. Thus, liquids with less pH sensitivity to temperature tend to have a better wettability trend at fixed surface conditions. Based on Fig. 6.7a–c data, it is also believed that, unlike the water of pH 7, the free ions in the

liquid of pH 4 and 9 have a prominent influence on the surface wettability. This ionic interaction between the liquid and surface was demonstrated by other researches and is known as the Hofmeister effect [51-54]. Besides the aforementioned reasons, possible traces of hydrocarbon contamination from the surrounding atmosphere can also affect the surface wettability [55, 56]. Usually, such contamination is unavoidable in open atmospheric experiments, but would occasionally have a very low impact on the final results.

A comparison between our findings and Nithyanandam and Palanisamy [32] ACA data, clearly shows the impact of water pH value on the surface wettability. The authors reported an ACA of 94.2^{o} when characterizing the wettability of their bare Cu surface, which is very close to our uncoated substrate result (i.e. 93.9^{o}). Altering the liquid pH value to 4 or 9 has shown to reduce the ACA to 91.7^{o} and 90.0^{o}, respectively, without further surface modifications (e.g. surface coating). Supplementary Table S6.1 summarises the testing parameters and obtained contact angles of the characterized samples and published data.

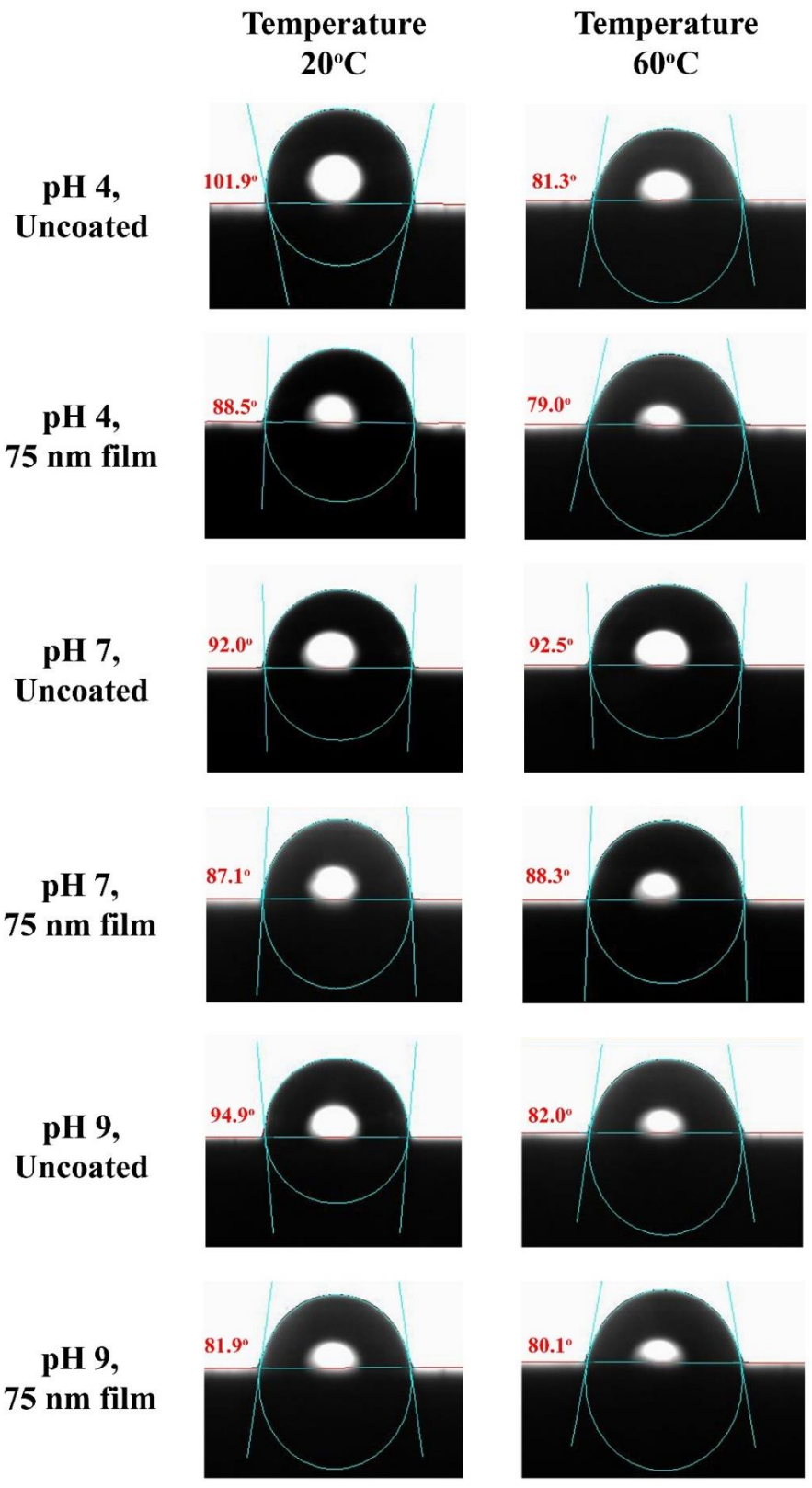

Fig. 6.6. Average contact angle measurements of uncoated and 75 nm coated Cu substrates, using 20°C and 60°C water of pH 4, 7, and 9.

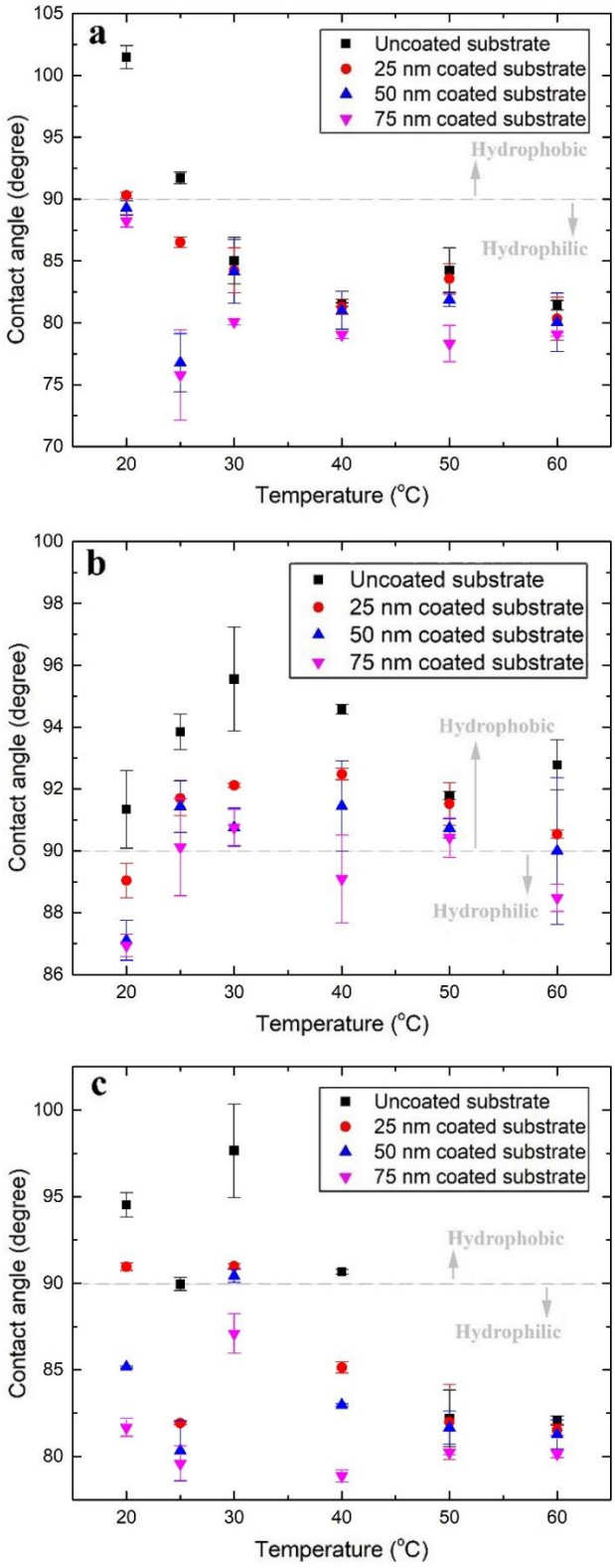

Fig. 6.7. Average contact angle measurements of coated and uncoated Cu substrates using water of (a) pH 4, (b) pH 7, and (c) pH 9. The error bars represent the 95% confidence interval of the plotted data.

4. Future Work

Although this article have demonstrated the important role of water pH value, temperature, and structural changes that the film thickness might cause on the wettability of one of the common plate HEs material (i.e. Cu) surfaces, further investigations is still required. For example, it would be beneficial to study other film deposition techniques (e.g. cold gas dynamic spraying), using the same main parameters included in this article, then compare the influence of the fabrication methods on the surface wettability behaviour. In addition, the dynamic wetting of the surface would also be worth considering as it plays a crucial role in various applications and processes. Thus, linking the liquid pH value and temperature, surface and coating materials, film thickness, and deposition approach to the hysteresis contact angle would advance the understanding of researchers towards this physical phenomenon. Moreover, the evaluation of the degree of oxidation caused by the thin film deposition on the surface should also be investigated in terms of wettability and thermal performance. The outcome of these experiments would be very useful in aiding both researchers and industrial decision makers into selecting the appropriate combination for their manufactured parts or systems.

5. Conclusion

Surface wettability experiments were conducted on a set of EB-PVD coated and uncoated Cu substrates, at atmospheric exposed conditions, using water of different pH values as the CA testing fluid. The XRF and XRD analysis of the substrates confirmed that the bulk formation of the substrates was of Cu. Furthermore, the AFM analysis illustrated a reduction in structure height on the surface, MHS, RMSR, and average roughness from 205 – 308 nm, 342 nm, 9.47 nm, and 6.05 nm (uncoated substrate) to 31.2 – 72.7 nm, 104 nm, 5.29 nm, and 3.71 nm (75 nm coated substrate), respectively. In addition, the surface ACA was seen to decrease with the reduction in surface roughness caused by the increase in deposition film thickness, for all three fabricated liquids. Moreover, the rise in water temperature, for pH 4 and 9, has demonstrated a tendency to change the characteristic of the uncoated and coated surface towards the hydrophilic region. In contrast, 20 – 60^{o}C water of pH 7, when applied on the uncoated substrate, failed to reach an ACA below 90^{o}. It was also seen that the ACA data trend with temperature, of the examined surfaces, had higher fluctuation as the water pH value increased. Comparison between published data and results obtained have exemplified the significant role of water pH value on the ACA, where it was shown that modifying the liquid pH value, from

its neutral state, can reduce the contact angle without further surface modifications. Therefore, the EB-PVD coating and liquid parameter modification approach seems to be quite promising for changing the degree of wettability of Cu surfaces.

References

1. Abou Elmaaty, T.M.; Kabeel, A.E.; Mahgoub, M. Corrugated plate heat exchanger review. *Renewable Sustainable Energy Rev* **2017**, *70*, 852-860.

2. Wang, L.; Sundén, B.; Manglik, R.M. Basic features and development of plate heat exchangers. In *Plate heat exchangers : Design, applications and performance*. WIT Press: Southampton, SO40 7AA, UK, 2007; pp 1-6.

3. Wang, L.; Sundén, B.; Manglik, R.M. Materials and manufacturing. In *Plate heat exchangers : Design, applications and performance*. WIT Press: Southampton, SO40 7AA, UK, 2007; pp 41-49.

4. Holman, J.P. *Heat transfer*. Ninth Edition ed.; McGraw-Hill: New York, 2002; p 648.

5. Nam, Y.; Ju, Y.S. A comparative study of the morphology and wetting characteristics of micro/nanostructured cu surfaces for phase change heat transfer applications. *Journal of Adhesion Science and Technology* **2013**, *27*, 2163-2176.

6. Ali, N.; Teixeira, J.A.; Addali, A. A review on nanofluids: Fabrication, stability, and thermophysical properties. *J. Nanomater.* **2018**, *2018*, 33.

7. Singh Sokhal, G.; Gangacharyulu, D.; Bulasara, V.K. Influence of copper oxide nanoparticles on the thermophysical properties and performance of flat tube of vehicle cooling system. *Vacuum* **2018**, *157*, 268-276.

8. Wong, K.V.; De Leon, O. Applications of nanofluids: Current and future. *Adv. Mech. Eng.* **2010**, *2*, 519659.

9. Kumar, V.; Tiwari, A.K.; Ghosh, S.K. Application of nanofluids in plate heat exchanger: A review. *Energy Conversion and Management* **2015**, *105*, 1017-1036.

10. Huminic, G.; Huminic, A. Application of nanofluids in heat exchangers: A review. *Renewable Sustainable Energy Rev* **2012**, *16*, 5625-5638.

11. Durmuş, A.; Benli, H.; Kurtbaş, İ.; Gül, H. Investigation of heat transfer and pressure drop in plate heat exchangers having different surface profiles. *Int. J. Heat Mass Transf.* **2009**, *52*, 1451-1457.

12. Abu-Khader, M.M. Plate heat exchangers: Recent advances. *Renewable Sustainable Energy Rev* **2012**, *16*, 1883-1891.

13. Zhang, J.; Zhu, X.; Mondejar, M.E.; Haglind, F. A review of heat transfer enhancement techniques in plate heat exchangers. *Renewable Sustainable Energy Rev* **2019**, *101*, 305-328.

14. Takata, Y.; Hidaka, S.; Masuda, M.; Ito, T. Pool boiling on a superhydrophilic surface. *International Journal of Energy Research* **2003**, *27*, 111-119.

15. Choi, C.; Kim, M. Wettability effects on heat transfer. In *Two phase flow, phase change and numerical modeling*, Intechopen: 2011.

16. Kim, T.H.; Chang, Y.S.; Kang, B.H. Regeneration performance of liquid desiccant on the surface of a plate-type heat exchanger. *Journal of Thermal Science and Technology* **2016**, *11*.

17. Yuan, Y.; Lee, T.R. Contact angle and wetting properties. *Springer Series in Surface Sciences* **2013**, *51*, 34.

18. Gatapova, E.Y.; Shonina, A.M.; Safonov, A.I.; Sulyaeva, V.S.; Kabov, O.A. Evaporation dynamics of a sessile droplet on glass surfaces with fluoropolymer coatings: Focusing on the final stage of thin droplet evaporation. *Soft Matter* **2018**, *14*, 1811-1821.

19. Smith, S.M.; Taft, B.S.; Moulton, J. Contact angle measurements for advanced thermal management technologies. *Frontiers in Heat and Mass Transfer (FHMT)* **2014**, *5*, 1-9.

20. Ali, N.; Teixeira, J.A.; Addali, A.; Al-Zubi, F.; Shaban, E.; Behbehani, I. The effect of aluminium nanocoating and water ph value on the wettability behavior of an aluminium surface. *Applied Surface Science* **2018**, *443*, 24-30.

21. Wenzel, R.N. Resistance of solid surfaces to wetting by water. *Industrial and Engineering Chemistry* **1936**, *28*, 988-994.

22. Cassie, A.B.D.; Baxter, S. Wettability of porous surfaces. *Trans. Faraday Society* **1944**, *40*, 546-551.

23. Huh, C.; Mason, S.G. Effects of surface roughness on wetting (theoretical). *J. Colloid Interface Sci.* **1977**, *60*, 11-38.

24. Kumar, G.; Prabhu, K.N. Review of non-reactive and reactive wetting of liquids on surfaces. *Adv Colloid Interface Sci* **2007**, *133*, 61-89.

25. Yang, W.; Li, J.; Zhou, P.; Zhu, L.; Tang, H. Superhydrophobic copper coating: Switchable wettability, on-demand oil-water separation, and antifouling. *Chemical Engineering Journal* **2017**, *327*, 849-854.

26. Singh, J.; Wolfe, D.E. Review nano and macro-structured component fabrication by electron beam-physical vapor deposition (eb-pvd). *Journal of Materials Science* **2005**, *40*, 1-26.

27. Arunkumar, P.; Aarthi, U.; Sribalaji, M.; Mukherjee, B.; Keshri, A.K.; Tanveer, W.H.; Cha, S.-W.; Babu, K.S. Deposition rate dependent phase/mechanical property evolution in zirconia and ceria-zirconia thin film by eb-pvd technique. *J Alloys Compd* **2018**, *765*, 418-427.

28. Johnson, C.A.; Ruud, J.A.; Bruce, R.; Wortman, D. Relationships between residual stress, microstructure and mechanical properties of electron beam–physical vapor

deposition thermal barrier coatings. *Surface and Coatings Technology* **1998**, *108-109*, 80-85.

29. Kumar, V.; Kandasubramanian, B. Processing and design methodologies for advanced and novel thermal barrier coatings for engineering applications. *Particuology* **2016**, *27*, 1-28.

30. Ali, N.; Teixeira, J.A.; Addali, A.; Saeed, M.; Al-Zubi, F.; Sedaghat, A.; Bahzad, H. Deposition of stainless steel thin films: An electron beam physical vapour deposition approach. *Materials* **2019**, *12*, 571.

31. Thornton, J.A. Influence of substrate temperature and deposition rate on structure of thick sputtered cu coatings. *Journal of Vacuum Science and Technology* **1975**, *12*, 830-835.

32. Nithyanandam, T.; Palanisamy, K. Wettability analysis on copper substrate by emery abrasion and copper nano coating. *International Journal of Mechanical and Production Engineering Research and Development* **2018**, *8*, 583-590.

33. Langelier, W.F. Effect of temperature on the ph of natural waters. *Journal (American Water Works Association)* **1946**, *38*, 179-185.

34. Yokogawa. Technical note tna0924. In *Vigilantplant*, 2009; pp 1-3.

35. Light, T.S. Temperature dependence and measurement of resistivity of pure water. *Anal. Chem.* **1984**, *56*, 1138-1142.

36. Down, R.D.; Lehr, J.H. *Environmental instrumentation and analysis handbook*. John Wiley & Sons: 2005.

37. Liptak, B.G. *Analytical instrumentation*. CRC Press: Pennsylvania, 1994.

38. Baboian, R. *Corrosion tests and standards: Application and interpretation*. ASTM international: USA, 2005.

39. Zhang, X.; Han, J.; Plombon, J.J.; Sutton, A.P.; Srolovitz, D.J.; Boland, J.J. Nanocrystalline copper films are never flat. *Science* **2017**, *357*, 397-400.

40. Dennler, G.; Houdayer, A.; Raynaud, P.; Séguy, I.; Ségui, Y.; Wertheimer, M.R. Growth modes of sioxfilms deposited by evaporation and plasma-enhanced chemical vapor deposition on polymeric substrates. *Plasmas and Polymers* **2003**, *8*, 43-59.

41. Amirzada, M.R.; Tatzel, A.; Viereck, V.; Hillmer, H. Surface roughness analysis of sio2 for pecvd, pvd and ibd on different substrates. *Applied Nanoscience* **2016**, *6*, 215-222.

42. Semaltianos, N.G. Thermally evaporated aluminium thin films. *Applied Surface Science* **2001**, *183*, 223-229.

43. Bordo, K.; Rubahn, H.-G. Effect of deposition rate on structure and surface morphology of thin evaporated al films on dielectrics and semiconductors. *Materials Science* **2012**, *18*, 313-317.

44. Yeniyol, S.; #xf6; #xfc; kba; #x15f; #x131; , N.; #xfc; fer; Bilir, A., *et al.* Relative contributions of surface roughness and crystalline structure to the biocompatibility of titanium nitride and titanium oxide coatings deposited by pvd and tps coatings. *ISRN Biomaterials* **2013**, *2013*, 9.

45. da Silva, T.J.; Moreira, J.G. Kinetic roughening on rough substrates. *Phys Rev E.* **1997**, *56*, 4880-4883.

46. Barabási, A.-L.; Stanley, H.E. *Fractal concepts in surface growth*. Cambridge university press: New York, USA, 1995.

47. Steele, A.; Bayer, I.; Moran, S.; Cannon, A.; King, W.P.; Loth, E. Conformal zno nanocomposite coatings on micro-patterned surfaces for superhydrophobicity. *Thin Solid Films* **2010**, *518*, 5426-5431.

48. Wang, S.; Liu, K.; Yao, X.; Jiang, L. Bioinspired surfaces with superwettability: New insight on theory, design, and applications. *Chem. Rev.* **2015**, *115*, 8230-8293.

49. Kubiak, K.J.; Wilson, M.C.T.; Mathia, T.G.; Carval, P. Wettability versus roughness of engineering surfaces. *Wear* **2011**, *271*, 523-528.

50. Petke, F.D.; Ray, B.R. Temperature dependence of contact angles of liquids on polymeric solids. *J. Colloid Interface Sci.* **1969**, *31*, 216-227.

51. Sivan, U. The inevitable accumulation of large ions and neutral molecules near hydrophobic surfaces and small ions near hydrophilic ones. *Current Opinion in Colloid & Interface Science* **2016**, *22*, 1-7.

52. Morag, J.; Dishon, M.; Sivan, U. The governing role of surface hydration in ion specific adsorption to silica: An afm-based account of the hofmeister universality and its reversal. *Langmuir* **2013**, *29*, 6317-6322.

53. Schlesinger, I.; Sivan, U. New information on the hydrophobic interaction revealed by frequency modulation afm. *Langmuir* **2017**, *33*, 2485-2496.

54. Schwierz, N.; Horinek, D.; Sivan, U.; Netz, R.R. Reversed hofmeister series—the rule rather than the exception. *Current Opinion in Colloid & Interface Science* **2016**, *23*, 10-18.

55. Mantel, M.; Wightman, J.P. Influence of the surface chemistry on the wettability of stainless steel. *Surface and Interface Analysis* **1994**, *21*, 595-605.

56. Rupp, F.; Gittens, R.A.; Scheideler, L.; Marmur, A.; Boyan, B.D.; Schwartz, Z.; Geis-Gerstorfer, J. A review on the wettability of dental implant surfaces i: Theoretical and experimental aspects. *Acta Biomaterialia* **2014**, *10*, 2894-2906.

Chapter 7

Publication 6: Deposition of Stainless Steel Thin Films: An Electron Beam Physical Vapour Deposition Approach

(Ali, N.; Teixeira, J.A.; Addali, A.; Saeed, M.; Al-Zubi, F.; Sedaghat, A.; Bahzad, H. Deposition of stainless steel thin films: An electron beam physical vapour deposition approach. *Materials* **2019**, *12*, 571. DOI: 10.3390/ma12040571)

Deposition of Stainless Steel Thin Films: An Electron Beam Physical Vapour Deposition Approach

A B S T R A C T

This study demonstrates an electron beam physical vapour deposition approach as an alternative stainless steel thin films fabrication method with controlled layer thickness and uniform elemental distribution capability. The films were fabricated at a range of starting electron beam power percentages of 3–10%, and thickness of 50–150 nm. Surface topography and wettability analysis of the samples were investigated to observe the changes in surface microstructure and the contact angle behaviour of 20°C to 60°C deionised waters, of pH 4, pH 7, and pH 9, with the as-prepared surfaces. The results indicated that films fabricated at low controlled deposition rates provided uniform elemental distribution and had the closest elemental percentages to stainless steel 316L and that increasing the deposition thickness caused the surface roughness to reduce by 38%. Surface wettability behaviour, in general, showed that the surface hydrophobic nature tends to weaken with the increase in temperature of the three examined fluids.

Keywords: Coating; controlled deposition rate; EB-PVD; morphology; topography; wettability.

1. Introduction

Stainless steels are passive alloys, which due to their chemical composition tend to form a thin oxide layer that inhibits the metal dissolution in corrosive environments [1]. Physical, mechanical, and anticorrosive properties of the alloy are highly related to its microstructure, where one or two phases (i.e., austenitic, ferritic, or both) may be formed [2]. Due to their unique properties, including adaptation to changes in solution salinity and pH level, these alloys are widely used in application areas such as construction and building [3], heat exchangers [4], and biomedicine [5]. In addition to these application areas, stainless steel (SS) in its powder form was reported to be used in fabricating nanofluids [6,7], which are heat transfer fluids; and surface coatings, via the cold spray deposition method [8]. Since the current trend in

engineering industry, such as the automotive sector, is to rely on light construction materials (e.g., aluminium and its alloys) in order to reduce the overall weight of constructions and manufactured parts, hence SS surface coatings on metals are considered to be a promising solution for achieving this target while providing anticorrosion and wear resistance to the bulk material [9,10]. So far, all reported deposition procedures of SS films are seen as adaptation of cold gas dynamic spraying of premixed powders onto the surface [9,11], wire feedstock melt down on surfaces via electron beam solid freeforming (EB-SFF) [12,13], ionic sputtering of a target source [14–21], thermal evaporation of a source and ionic bombardment of the particles by ion beam assisted deposition (IBAD) approach [22], and pulsed laser evaporation technique [23,24]. However, some of these routes can be incompatible for industrial usage because of the lack in precision of controlling the deposited layer thickness, the thin film can be associated with contamination, and the cold spray deposited particles and/or its coated surface can suffer from intensive plastic deformation. Furthermore, the aforementioned methods raise processability and cost concerns due to the large number of parameters involved in the coating procedure. For example, when employing cold gas dynamic spraying approach, parameters such as the nozzle dimensions, jet velocity, particles size, and particles impact temperature need to be considered cautiously before starting the process.

On the other hand, electron beam physical vapour deposition (EB-PVD), which is a high vacuum thermal coating technology, is considered to be a simple and relatively cheap process in which a focused high energy electron beam is directed towards melting an evaporant material inside a vacuumed chamber. The evaporating material is then condensed on the surface of a substrate or component to form the film layer [25]. The distinct advantages of this approach are the high deposition purity, enlarged coating area, precise film thickness, in-situ growth monitoring, and smoothness control [26]. In addition to the associated benefits, the aforementioned technique has proven its capability of depositing alloys, as demonstrated by Almeida et al. [27] with their MCrAlY film fabrication study. On the industrial scale, EB-PVD has been widely employed for coating materials, including SS bulk materials, but to the authors of this article's knowledge, has never been reported as the means to deposit SS thin films [25,28].

Herein, we demonstrate the deposition of SS thin films on metallic substrates using an EB-PVD approach. The present study, based on the conducted literature review, is the first reported EB-

PVD process for forming SS films and does not aim to challenge other film fabrication processes but rather unlocks opportunities for new ways of depositing SS thin films. Furthermore, to illustrate the crucial role of the controlled deposition rates on the uniformity and elemental distribution within the fabricated thin layer, a comparison between the morphologies of the SS films, of 150 nm, coated on copper (Cu) substrates with fixed deposition rates of 0.05 Å/s to 1.45 Å/s was performed. The main reasons behind selecting Cu as the hosting substrate is due to: (1) the fact that Cu is not part of the forming elements of the SS 316L alloy and can therefore be easily diverted from the deposited film when elemental characterisations is performed, and (2) most commercial heat pipes are made of Cu, because of the material high thermal conductivity, but usually faces erosion damages from water flows [29]; so providing an insight into SS coatings on Cu would be desirable for the industry since it can help reduce such common phenomena with minimum degradation effects on the heat transfer properties of the bulk material. Moreover, since there is still a need for further investigation and clarification of the wettability behaviour of SS 316L surfaces and the effect of different parameters on their wetting phenomena [30], the impact of the 0.05 Å/s as-prepared films on the surface topography and water wettability behaviour was explored for 50, 100, and 150 nm SS layers coated on SS 316L substrates. The expected applications that can benefit from this study include, but are not limited to, medical equipment, automotive parts, and heat transfer devices.

2. Experimental

2.1 Materials

All chemicals were used as-received from the manufacturer without further purification. Acetone (CH_3COCH_3 ≥ 99.5%) grade ACS reagent and hydrochloric acid (HCl ~37%) grade ACS reagent were purchased from SIGMA-ALDRICH, and sodium hydroxide pellets (NaOH ~98%) grade AR were purchased from LOBA Chemie (Mumbai, India). Stainless steel AISI 316L bearing balls, of grade 100 and 8.5 mm diameter, were purchased from Bearing Warehouse Limited (Sheffield, UK). Thirteen square shaped substrates, divided into: (1) four of 3 cm^2 surface area and 0.6 mm thickness stainless steel 316L (supplied by YC Inox co., (Chang-Hwa, Taiwan)), (2) four of 0.5 cm^2 surface area and 0.6 mm thickness stainless steel 316L (supplied by YC Inox co.), and (3) five of 1 cm^2 surface area and 0.127 mm thickness copper of 99.9% purity (supplied by Precision Brand Products, Downers Grove, IL, USA),

were manufactured using a computer controlled machine. The substrates were then cleaned with acetone, using a bath type Soniclean limited 250TD ultrasonicator (Thebarton, Australia), for 15 min at room temperature then carefully wiped to remove any remaining residuals. Three litres of deionised water (DIW), of pH 6.11, produced by an Elga PR030BPM1-US Purelab Prima 30 water purification system (Buckinghamshire, UK) was used after being divided into 3 sets of 1 L's, then their pH value at 25°C were adjusted, via a HACH HQ11D portable pH meter (Loveland, CO, USA) of 0.002 pH accuracy, to 4, 7, and 9, respectively.

2.2 X-ray fluorescence and x-ray diffraction characterisation

Elemental analysis of the fabricated substrates was performed three times and averaged using a BRUKER TITAN S1 X-ray fluorescent (XRF) handheld analyser (Coventry, UK) to ensure that the bulk components in the manufactured substrates match the composition standards. This was done by placing the substrate on a working station then adjusting the lens of the XRF device vertically on the substrate before starting the measurements, which required 10 seconds to complete for each single measurement. Moreover, X-ray diffraction (XRD) analysis was performed using a 9 kW Rigaku SmartLab, Tokyo, Japan, XRD device that utilizes a Cu K_α X-ray source at a diffraction angle of 2Θ and an incidence beam angle of 0.02°. This was done in order to identify the Bragg's peaks within the substrates, and hence define the phase of the stainless steel alloy used. The diffraction scanning angle ranged from 20° to 80°, with a scanning rate of 2 °/min.

2.3 Stainless steel film deposition

The thin film production method used consists of fabrication at constant deposition rates, as commonly seen in literature [31], and is demonstrated in Fig. 7.1. Eleven of the thirteen substrates were individually placed inside the EB-PVD device chamber after being tightly adjusted on the sample holder and were screwed vertically above the evaporation source. The remaining two stainless steel 316L substrates were kept as references for characterisation purposes. Stainless steel AISI 316L bearing balls, which were used as the deposition source, were placed in an 8 cm^3 graphite crucible located at the bottom of the EB-PVD chamber, thus having a fixed target-to-sample distance of 26 cm. The EB-PVD device chamber (40 cm inner diameter × 50 cm inner height) was then vacuumed to a pressure of 6×10^{-6} Torr to ensure the removal of all particle contaminations within it, and the film thickness was controlled via an

INFICON SQC-310 electronic thickness monitor system (Bad Ragaz, Switzerland) connected to a sensor located inside the chamber. It is worth noting that there was no external heating or cooling applied to the substrates temperature during the film fabrication process. In the case of the copper substrates, the deposition source was evaporated at a set of starting power percentages after which the deposition rates were maintained so that a film layer of 150 nm thick can be achieved. The starting power percentages employed were of 3, 4, 6, 8, and 10%, and the maintained deposition rates were of 0.05, 0.16, 0.82, 1.07, and 1.45 Å/s, respectively. It is worth noting that power percentages less than 3% had no trace of evaporation and that power percentages higher than 12% are restricted by the manufacturer of the EB-PVD device due to safety concerns. As such, the range of power percentage was selected to be from 3% to 10%, with a maximum deviation of ± 1% to sustain the deposition rate. As for the stainless steel 316L substrates, based on the elemental characterisation of the film coated on the copper substrates, the evaporation was selected to be at the lowest deposition rate (i.e., 0.05 Å/s) for a set of film thickness of 50, 100, and 150 nm. After the completion of each of the aforementioned particle deposition processes, the substrate was kept in the chamber for 4 h to cool down before removal from the EB-PVD chamber for further analysis.

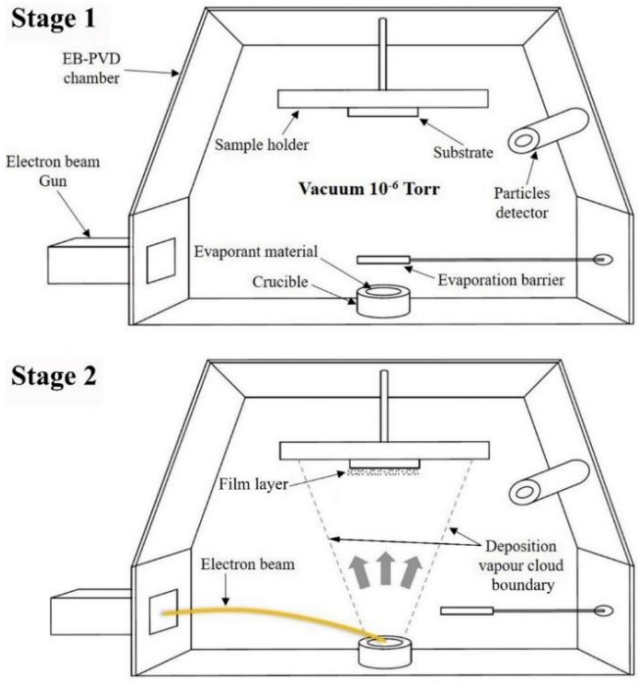

Fig. 7.1. Electron beam physical vapour deposition process, where (Stage 1) shows the schematic illustration of the device configuration, and (Stage 2) demonstrates the source evaporation and film formation process.

2.4 Scanning electron microscopy and elemental mapping

The surface microstructure and the elemental mapping of the chemical composition of the 150 nm stainless steel film coated on the copper substrates at fixed deposition rates (i.e., from 0.05 Å/s to 1.45 Å/s); and the evaporated source before and after 150 nm film deposition at a 0.05 Å/s were studied using a JEOL JSM-6010LA InTouchScopeTM scanning electron microscopy (SEM, Tokyo, Japan) device that is equipped with an integrated energy dispersive x-ray spectroscopy (EDS) analyser and operates via the InTouchScope 1.12 software. All SEM images were recorded by the secondary electron mode from the surface region of the samples and then recorded at different magnifications. Elemental distribution and percentages were obtained by the EDS analyser at a process real time of 100 s. Both SEM and EDS analysis were conducted at a working distance of 10 mm and an accelerating voltage of 20 kV, to reduce any possible damage to the tested samples. It is important to note that elements such as carbon, oxygen, and copper were excluded from the EDS elemental composition due to the presence of carbon in the adhesive tape used for mounting the samples into the device, traces of oxygen can remain in the chamber even at a high vacuum condition while copper was the tested substrate beneath the thin film, this being our area of interest.

2.5 Atomic force microscopy

Topography images of the coated and uncoated stainless steel 316L substrates were recorded at room temperature, using a PicoView 1.14.4 software (Woburn, MA, USA), at 10 μm^2, 1024 × 1024 pixels, and 0.84 line/s via an Agilent Technologies 5600LS atomic force microscopy (AFM, Santa Clara, CA, USA) instrument, equipped with a 90 µm N9521A multipurpose scanner, in tapping mode. NANOSENSORSTM silicon tips (type: PPP-CONTPt-20; resonance frequency 6–21 kHz) were employed for the characterisation. Data analysis was performed, with a Pico Image Basic 6.2 software (Chandler, AZ, USA), via first enabling the gaussian filter with 0.25 μm^2 cut-off feature, for the background corrections, then having the software calculate the main height parameters and particles height distribution of the samples.

2.6 Deionised water properties measurements and theoretical calculation

Deionised water, of pH 4, 7, and 9, kinematic viscosity and density changes with temperature were characterised at a temperature range from 20°C to 60°C, via an Anton Paar DMA 4500M density meter (Graz, Austria) of accuracy 5 × 10−5 g/cm³ and a PAC Herzog HVM 472

multirange viscometer device (Houston, TX, USA), respectively. Both of the aforementioned devices have built-in calibration systems that are initiated before starting the measurements. The variation in pH value, of the DIW's, with temperature was obtained from previously published results [32,33], for pH 7 and 9, and theoretically calculated for pH 4, for the same range of temperatures, using the following equation [34,35]:

$$pH_T = pH_{25^oC} + [(T - 25^oC) \times \text{solution temperature coefficient}] \quad (1)$$

Where pH_T, pH_{25^oC}, and T are the solution pH value for an examined temperature, the solution pH value at 25°C, and the examined temperature in Celsius, respectively. The solution temperature coefficient of DIW of pH 4 was selected to be −0.004 pH/°C, based on the extrapolation of the available data of the two previous DIW's (i.e., pH 7 and 9).

2.7 Surface wettability characterisation

Three 1 mL Hamilton 1000 series syringes, containing DIW of pH 4, 7, and 9, were adjusted to a Dataphysics SHD syringe temperature controller (Reno, NV, USA), which is integrated with the Dataphysics OCA 100 automatic multi-liquid dispenser contact angle goniometer device (San Jose, CA, USA). This was done in order to increase/decrease the liquid temperature inside the syringes, while being monitored. The surface wettability of the coated and uncoated stainless steel 316L samples was measured using the Sessile drop method [36]. This was done by dispersing a 5 µL droplet (5 µL/s dosing rate) on the examined surface then capturing its image, at static condition, which is analysed afterwards through the device provided software SCA 20 to obtain the liquid – surface CA. The CA measurements were conducted three times, for the three types of liquids, at a fixed liquid temperature of 20°C to 60°C, with a ±0.1° contact angle precision.

3. Results and Discussion

3.1 Substrates analysis

The average elemental content of the manufactured SS 316L and Cu substrates, which were each examined three times by the XRF, are given in Table 7.1. In addition, the XRD pattern corresponds well with the XRF analysis as suggested by the sharp diffraction Bragg's peaks shown in Fig. 7.2a and 7.2b, where the SS substrate (Fig. 7.2a) showed peaks at 2θ = 43.6°, 50.9°, and 74.7° corresponding to the planes (111), (200), and (220) austenite gamma phase; and the Cu substrate (Fig. 7.2b) illustrated diffraction peaks at 2θ = 43.2°, 50.4°, and 74.1°

corresponding to the planes (111), (200), and (220) of pattern (PDF Card No.: 03-065-9026). Hence, this confirms that the bulk formation of the as-prepared substrates used for the deposition experiments are of Cu and SS 316L in its austenite phase.

Table 7.1. Averaged XRF elemental analysis of SS 316L and Cu substrates.

Element	Stainless steel 316L				Element	Copper			
	Content (wt.%)	Max. (wt.%)	Min. (wt.%)	+/− Error (wt.%)		Content (wt.%)	Max. (wt.%)	Min. (wt.%)	+/− Error (wt.%)
Iron	69.22	75	60	0.5	Copper	99.82	100	90	0.39
Chromium	16.78	18	16	0.18	Zirconium	0.02	-	-	0.01
Nickel	10.12	14	10	0.21	-	-	-	-	-
Manganese	2.02	3	2	0.04	-	-	-	-	-
Molybdenum	1.32	2	0	0.11	-	-	-	-	-
Silicon	0.27	1	0	0.05	-	-	-	-	-

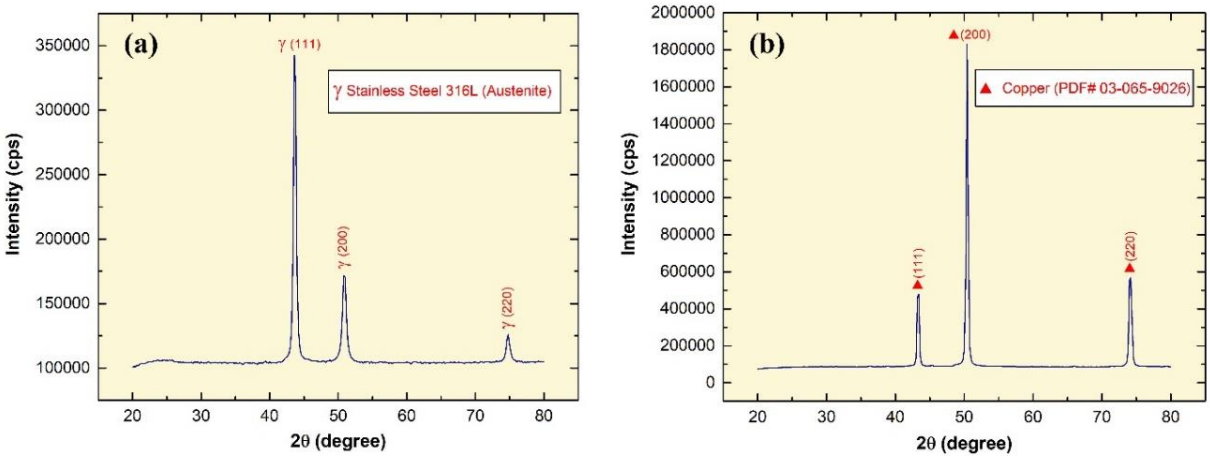

Fig. 7.2. X-ray diffraction pattern of: (a) SS 316L substrate, and (b) Cu substrate.

3.2 Deposition morphology

Fabricated samples of 150 nm SS deposited on Cu substrates, which were synthesised by the EB-PVD starting electron beam powers of 3% to 10%, are shown in Fig. 7.3. The SS thin film layer produced can be visually observed (Fig. 7.3(b2–b6)), except for the corners where the adhesive tapes were placed to adjust the samples on the sample holder. The time required for achieving the film thickness varied from 500 min, at a fixed deposition rate of 0.05 Å/s, down to 17.25 min, via a 1.45 Å/s controlled evaporation rate. Samples were then characterised to determine the effect of the controlled deposition rates on the film and evaporant material (Fig. 7.3(c1–c6)) morphologies, via the SEM and EDS analysis. The SEM characterisation of the

0.05 Å/s and 0.16 Å/s fabricated samples has demonstrated a well-constructed film structure as shown in Fig. 7.3(a1 and a2) (alternatively, Supplementary Fig. S7.1(a1 and a2)), whereas higher deposition rates have resulted in the development of non-uniform films with partial detachments from the surface as seen in Fig. 7.3(a3–a5) (alternatively, Supplementary Fig. S7.1(a3–a5)). Both observations can be linked to the phase of the SS film formed due to the elemental ratio of the deposit, where a well-constructed film structure indicates a ferritic phase and a semi-detached structure illustrates an austenitic phase [37]. In addition, analysing the evaporant source, before and after 0.05 Å/s deposition, has shown a local melt down in the material, due to the electron beam being focused on a single location at a low power (i.e. the beam is fixed and does not follow a movement path across the evaporant source), thus resulting in surface microstructural changes as shown in Fig. 7.3(d1–d4) (alternatively, Supplementary Fig. S7.1(d1–d4)). Further inspection of the samples using the EDS device (Fig. 7.4) has illustrated that, unlike higher controlled deposit rates, the film fabricated via 0.05 Å/s was within the SS 316L elemental composition acceptable ranges, except for the chromium, manganese, and nickel, which showed partial divergences of +3.33%, +1.15%, and −5.24%, respectively. This indicates that the film is indeed SS but of a different category [38–40], whereas to obtain SS 316L thin films the evaporant source would require some modification in its composition (i.e., fabricate our own EB-PVD evaporant source). In addition, the film elemental distribution of the fixed 0.05 Å/s deposition was seen to be uniformly distributed along the substrate surface as shown in Fig. 7.5 (alternatively, Supplementary Fig. S7.2a–b). It is important to note that due to the limitation of the EDS device used, elements of less than 0.5% of the composition mass could not be elementally mapped, as seen in the case of molybdenum. The EDS elemental composition percentages of the 150 nm SS deposited film at a fixed rate of 0.05 Å/s are tabulated in Table 7.2.

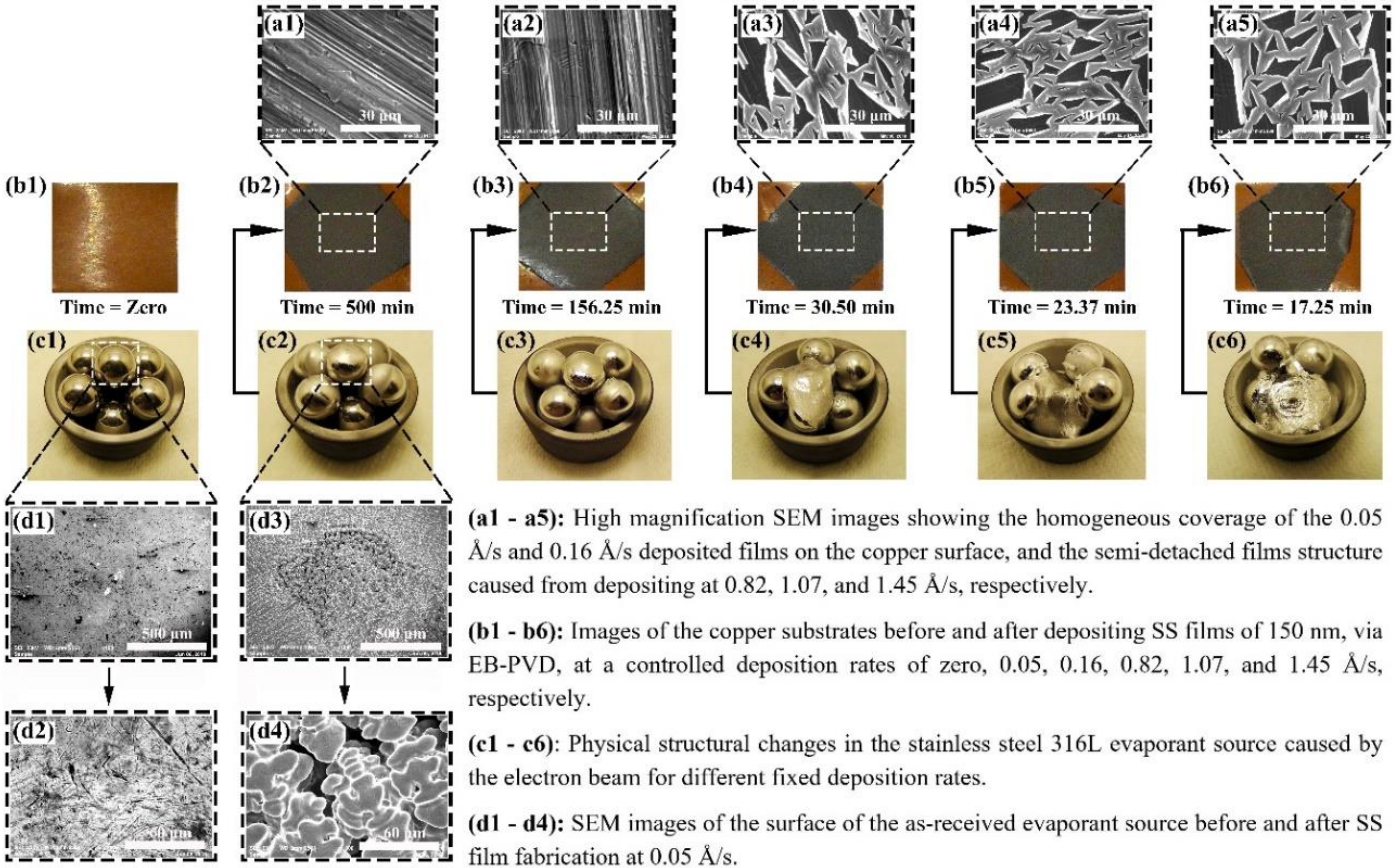

Fig. 7.3. Characterisation of the stainless steel evaporant source and deposited thin films, where (a1– a5) shows the SEM images of the 0.05–1.45 Å/s as-deposited films structure, (b1– b6) illustrates the copper substrates before and after SS deposition, (c1– c6) demonstrates the physical changes in evaporant source caused by different deposition rates, and (d1– d4) shows the SEM images of the evaporant source before and after 0.05 Å/s film deposition.

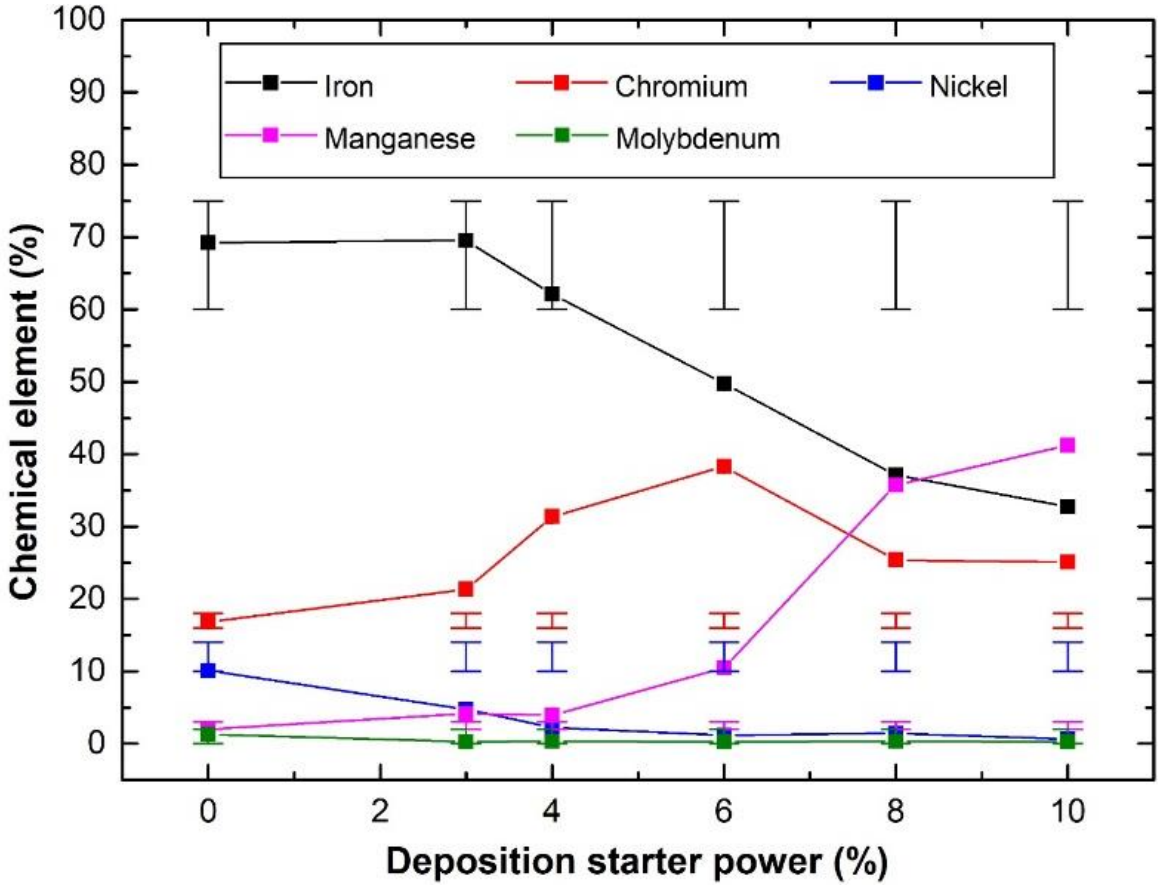

Fig. 7.4. EDS characterisation of the chemical elemental percentages of the evaporant source (0% power), and the SS thin films deposited with a starting beam power of 3% up to 10%. The bars at the top and bottom of each data point indicate the maximum and minimum range of each element percentage of the stainless steel 316L composition and was attained from the XRF device installed database.

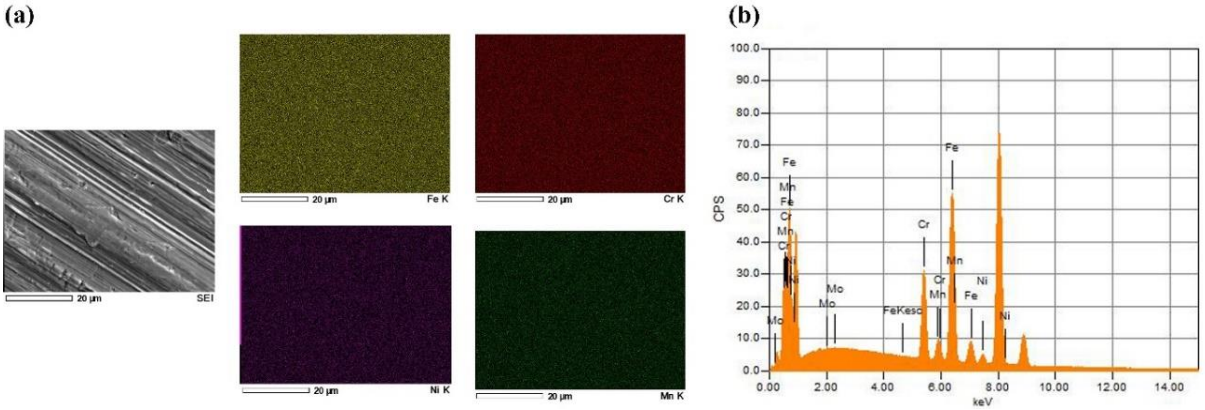

Fig. 7.5. EDS elemental analysis, where (a) is the SEM image and its elemental maps of the characterised 150 nm deposited SS film at 0.05 Å/s on Cu substrate, and (b) demonstrates the EDS X-ray spectrum of the elements within the film shown in (a).

Table 7.2. EDS elemental composition percentage of the 150 nm SS fabricated film at 0.05 Å/s controlled deposition rate.

Element	Mass %	Atom %	Sigma	Net	K ratio
Iron	69.52	68.62	0.05	2879132	0.3919295
Chromium	21.33	22.61	0.03	1347161	0.1368063
Nickel	4.76	4.47	0.03	131065	0.0250911
Manganese	4.15	4.16	0.03	201285	0.0236898
Molybdenum	0.25	0.14	0.03	12922	0.0009314
Total	100	100			

3.3 Surface topography

Surface topography analysis of the uncoated and coated SS 316L samples, which were conducted using an AFM device, is shown in Fig. 7.6 and 7.7 (alternatively to Fig. 7.7, Supplementary Fig. S7.3a–d). The experimental results have revealed that the nanostructures on the uncoated surface have a range of height between 87.3 to 204 nm (Fig. 7.7a), with almost 47.5% of the structure height being in the range of 116 to 130.5 nm. Moreover, the maximum height of surface (MHS), which was obtained by adding up the surface maximum peak height and maximum valley depth, and root mean square roughness (RMSR) of the uncoated sample, were shown to be 291 nm and 12 nm, correspondingly, as demonstrated in Fig. 7.6. On the other hand, as the deposited layer thickness increased (Fig. 7.7b–d), the structure height on the surface, RMSR, and MHS were seen to reduce, reaching values between 35.9 to 83.7 nm, 6.86 nm, and 120 nm, respectively. Furthermore, the degree of symmetry of the surface heights about the mean plane was also seen to improve with the deposited film thickness, as the obtained surface skewness (Ssk) values of the measured samples (Table 7.3) were shown to move closer to the mean plane (i.e. zero) with the increase in fabricated layer thickness. It is worth noting that the sign of Ssk represents the predominance of the comprising surface peaks (Ssk > 0) or valley structures (Ssk < 0). The aforementioned changes in surface conditions can be attributed to the deposited film occupying the vacant spaces on the surface structure, which consist of valleys, hills, and micro gaps, leading to the height variation on the surface to narrow down [41]. Moreover, the presence of inordinately high peaks or deep valleys was also found on the examined substrates, as indicated by the surface kurtosis (Sku) values, where Sku > 3.00 suggests the existence of a peaks/valleys defect on the surface and Sku < 3.00 illustrates a lack

thereof (i.e., insufficient surface information). Such an observation is not surprising as it is commonly present on most surfaces [42]. The average roughness values were found to be 7.87 nm, 7.48 nm, 6.00 nm, and 4.88 nm for the uncoated, 50 nm, 100 nm, and 150 nm coated substrates, respectively. These results confirmed the smoothening effect caused by the increase in EB-PVD deposited film thickness on the SS 316L substrate surface. The roughness results can also be used as a general indication of the corrosion behaviour, as it has been reported by other authors that decreasing the surface roughness of passive alloys tends to reduce the pitting susceptibility and corrosion rate [43,44]. The height parameters values obtained from the AFM analysis of the samples can be seen in Table 7.3.

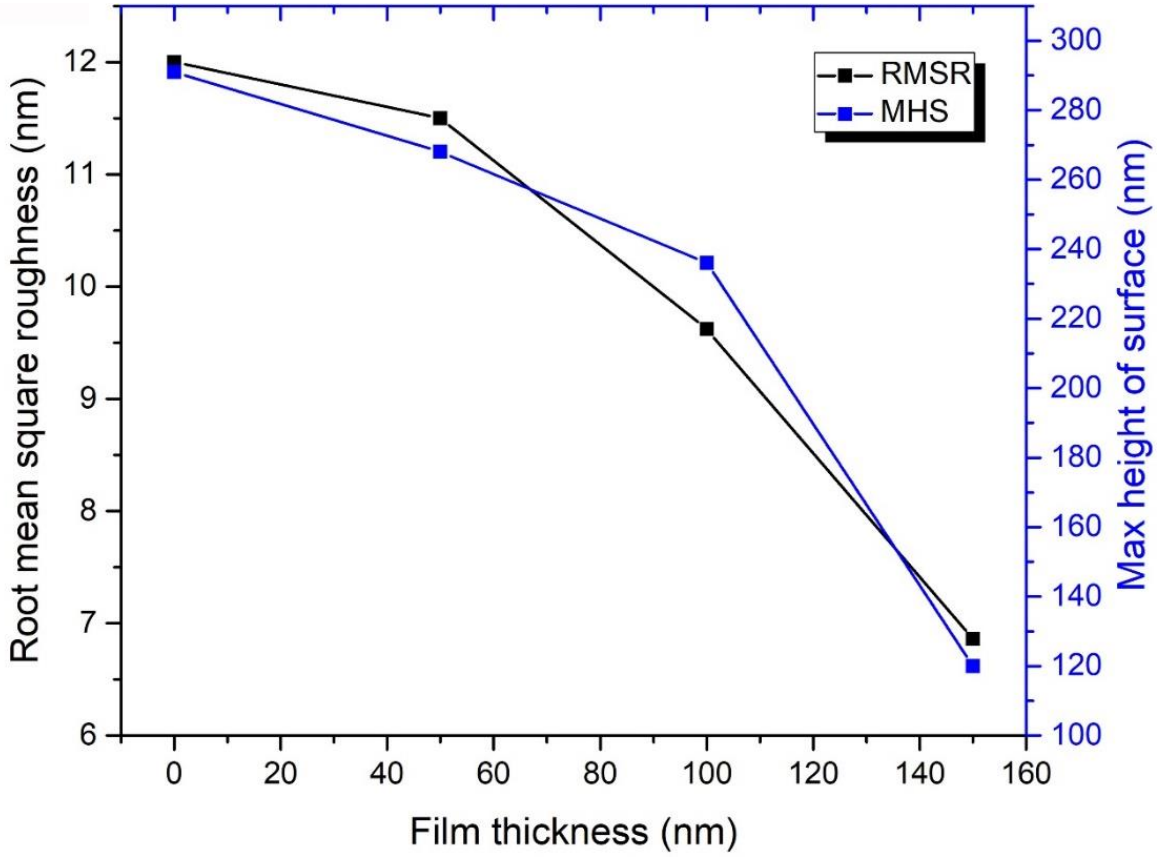

Fig. 7.6. Root mean square roughness and maximum height of surface variation with deposition thickness on SS 316L substrates.

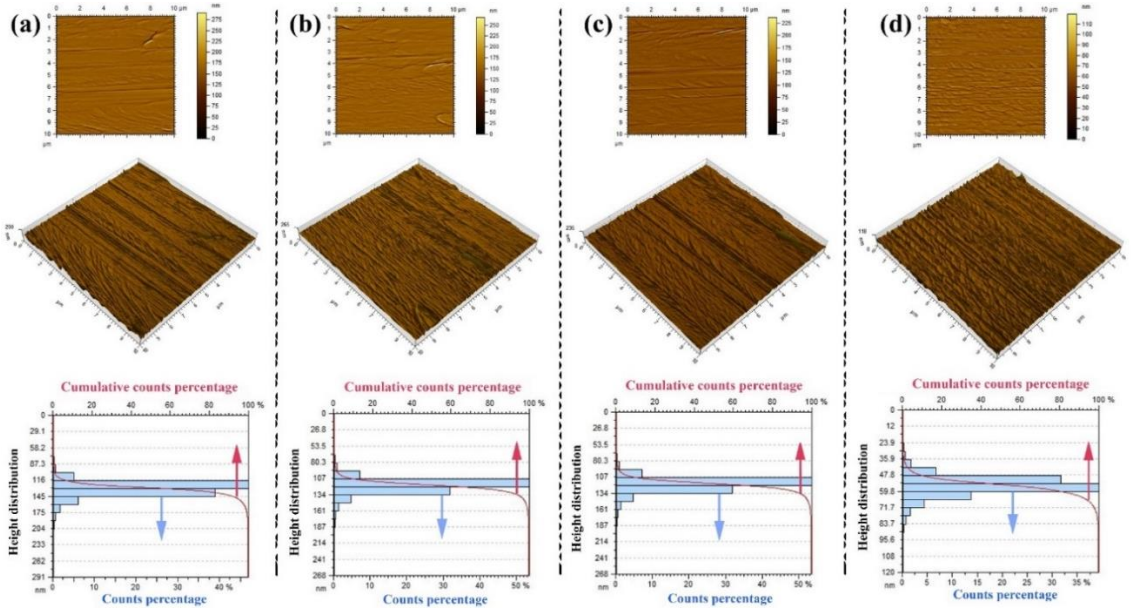

Fig. 7.7. Surface topography analysis of SS films on SS 316L substrates, where (a) 2D and 3D rendered AFM topograph and height distribution of the surface of the uncoated SS 316L substrate, and (b–d) 2D and 3D rendered AFM topograph after 50, 100, and 150 nm SS deposition on substrates and their height distribution.

Table 7.3. Height parameters of the AFM analysis of the uncoated, 50 nm, 100 nm, and 150 nm coated SS substrates.

Height parameters	**Film Thickness (nm)**			
	0	**50**	**100**	**150**
Root mean square roughness (nm)	12	11.5	9.62	6.86
Skewness	−1.08	−1.0	−0.654	−0.535
Kurtosis	16.8	18	19.6	6.39
Maximum peak height (nm)	131	119	119	55.4
Maximum valley depth (nm)	160	149	118	64.1
Maximum height of surface (nm)	291	268	236	120
Average roughness (nm)	7.87	7.48	6.0	4.88

3.4 Deionised water properties variation with temperature

The deionised waters used were selected to have a pH of 4, 7, and 9 to observe the acidity, neutrality, and alkalinity of the liquid effect on the surfaces wettability. Analyses results of the

changes in properties, namely, kinematic viscosity (ν), density (ρ), and pH value of the three liquids, within our temperature range, are shown in Fig. 7.8a. Comparing the ρ and ν characterisation outcomes, of the as-prepared DIW of pH 7, with the available data on pure water in literature [45] has shown a deviation of 0.015% and 3.67%, respectively, thus verifying the measurement approach conducted. Moreover, regardless of the examined DIW pH value, the as-fabricated liquids ν and ρ were seen to have a negligible difference in their values at each investigated point of temperature. For example, at 30°C, the DIW $\rho_{pH\,4}$, $\rho_{pH\,7}$, and $\rho_{pH\,9}$ had an outcome of 0.99564, 0.99562, and 0.99563 g/cm^3, respectively. In contrast, manipulating the temperature was seen to have a notable influence on all three properties of the DIW's (i.e., ν, ρ, and pH value), as demonstrated in Fig. 7.8a. This can be explained by the fact that ν is inversely related to the ρ, and that ρ is a representation of substance mass to its volume, where at a constant volume, the mass is influenced by the bonds distance of the molecules and their forming atoms. Our as-prepared DIW's consist of four types of bonds: 1- Polar covalent bond between a single or a pair of hydrogen atoms and one atom of oxygen, 2- Dative covalent bond between a single atom of H^+ and a H_2O molecule, 3- hydrogen bond between the oxygen atom of a H_2O molecule and a hydrogen atom of a neighbouring H2O molecule, and 4- Ion–dipole interaction between the H_2O molecules and a Cl^- atom (e.g., DIW of pH 4) or Na^+ atom (e.g., DIW of pH 9). The four previous bounds are shown in Fig. 7.8b–d. Based on the obtained data, it is believed that at a point of temperature, the bond distances of the newly introduced dative covalent bond (pH 4) and ion – dipole interaction (pH 9) are very close in distance to the other two initially existing bonds in neutral water, causing this neglectable changes in the liquid mass. On the other hand, raising the temperature weakens all four bonds, because of the increase in molecular vibrations, causing the bonds distance to widen; and hence the liquid mass reduces and becomes more acidic due to the release of H^+ and growth in its concentration [46]. The different formed reactions in our as-prepared DIW's, based on the Bronsted–Lowry theory of acids and bases [47], are demonstrated in Equations (2)–(4) as the following:

pH 4: $HCl + H_2O \rightleftharpoons H_3O^+ + Cl^-$ (Reverse reaction) (2)

pH 7: $2H_2^+ + O_2^- \rightarrow 2H_2O$ (Chemical reaction) (3)

pH 9: $NaOH + H_2O \rightarrow Na^+ + OH^- + H_2O + Heat$ (Exothermic reaction) (4)

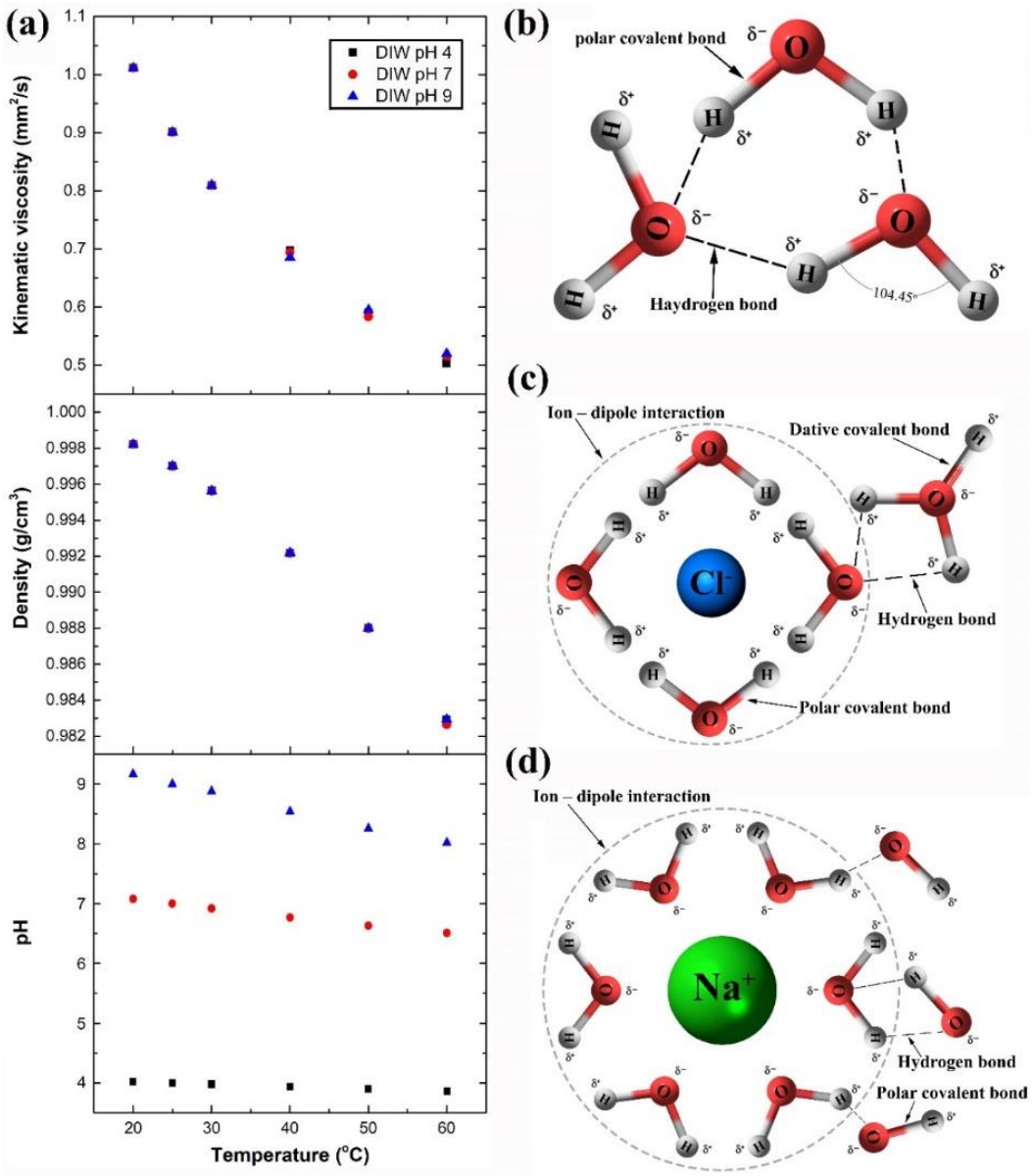

Fig. 7.8**.** Water atoms and molecules bonds, and properties variation with temperature, where (a) shows the DIW's kinematic viscosity, density, and pH value changes with temperature, and (b–d) illustrates the bonds in water of pH 7, 4, and 9, respectively.

3.5 Contact angle measurement

Examining the wettability of the uncoated SS 316L sample (Fig. 7.9a), with 20°C of DIW of pH 7, showed that the surface had an average contact angle (ACA) of 131.7°, which illustrates a hydrophobic behaviour. The high ACA value is believed to be linked to the substrate Cassie–Baxter state via its surface roughness, as reported by other authors [30,48]. In general, there are two common texture states that explain the relationship between surface wettability and

roughness, which are the Cassie-Baxter [49] and Wenzel [50] states. In the Cassie-Baxter state, the surface pores and valleys tend to trap the air, which leads to a reduction in the degree of liquid-surface interaction. On the other hand in the Wenzel state, the liquid fully occupies the pores, thus improving the surface wettability. Applying DIW's of pH 4 and 9 have led the surface ACA to reduce to 124.9^{o} and 117.4^{o}, respectively, without additional surface modifications. Furthermore, it was found that raising the temperature of the as-prepared DIW's tends to weaken the hydrophobic nature of the uncoated surface, as demonstrated by the obtained data in Fig. 7.9b-d. The grey dashed line in the plots (Fig. 7.9b-d) illustrates the transition point between the surface hydrophobic (top) and hydrophilic (bottom) regions. Moreover, the deposition thickness was seen to be inversely related to the CA, where increasing the film thickness caused the ACA to reduce. For example, when examining DIW, of 20°C and pH of 4, the ACA of the uncoated, 50 nm, 100 nm, and 150 nm film gave angles of 124.9°, 119.5°, 116.7°, and 110.9°, respectively. This can be attributed to the reduction in surface micro-roughness and air pockets formation at the interface between the substrate and liquid as a result of the deposited film occupying the surface structure, thus enhancing the substrate surface energy to attract the liquid towards the surface (i.e., reducing the CA) [49,51]. In addition, the level of decrease in CA is seen to correspond to the liquid temperature, pH value, and fabricated film thickness due to their ability to modify the surface mode from a Cassie–Baxter state to a Wenzel state, and vice versa. For instance, the ACA of DIW of pH 4, 7, and 9, at 50°C, showed a decrease from 110.1°, 114.8°, and 112.3° (uncoated) to 93.1°, 95.5°, and 97.0° (150 nm film), respectively. It was also possible to change the substrate surface wettability nature from hydrophobic to hydrophilic by manipulating the three aforementioned parameters, as shown in Fig. 7.9b when investigating the 150 nm coated substrate with DIW of 60°C and pH 4. Such findings are very attractive for heat transfer applications, as lowering the CA can enhance the heat transfer efficiency of SS by providing larger contact area between the liquid and the surface. On the other hand, the fluctuation in the data trend of DIW of pH 4 and 9 across the examined temperature range is believed to be caused by the free ions hosted by the liquid. Since both fluids are considered ionically unstable, attempting to change the surface functional group of the substrate from hydrophobic toward hydrophilic by inducing the transformation in surface charge, in what is known as the Hofmeister series reversal effect, could be the reason behind this kind of behaviour in the data trend [52]. In addition to the previously mentioned reason, there is a possibility that traces of hydrocarbon contamination

from the surrounding atmosphere on the substrate surface are strongly interacting with the two aforementioned liquids free ions, since the DIW of pH 7 did not show such fluctuation in its data trend. Usually, such contamination is unavoidable in open atmospheric experiments, and would have some sort of influence on all the conducted measurements [53,54]. Supplementary Table S7.1 summarises the testing parameters and obtained contact angles of the characterised samples.

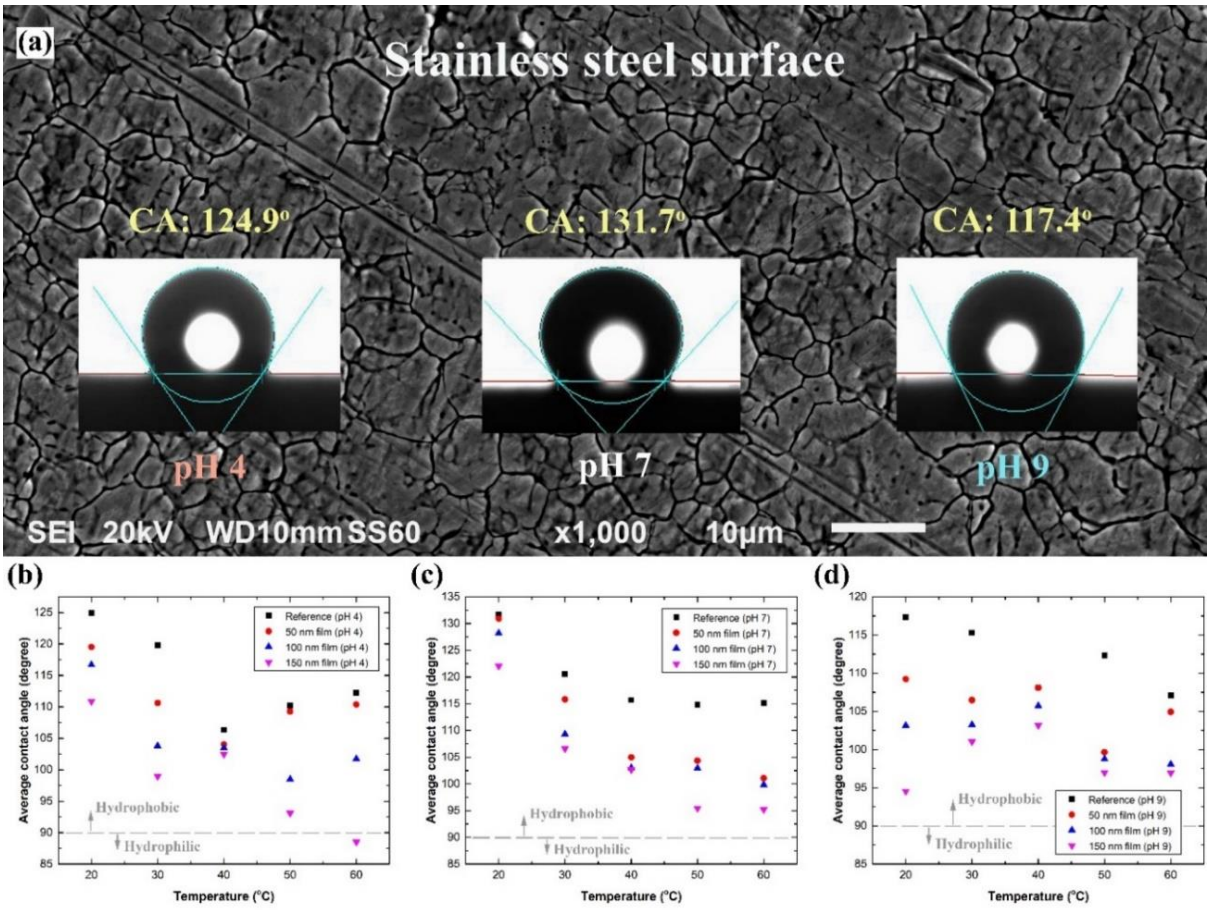

Fig. 7.9. Effect of DIW temperature and pH value on the wettability behaviour of SS 316L surface, where (a) illustrates the contact angles between the 20 °C DIW's, of pH 4, 7, and 9, and the uncoated SS 316L substrate surface, and (b–d) demonstrates the average contact angle measurements of the uncoated and coated samples using the DIW's, at 20–60°C, as the testing fluids.

4. Conclusions

Stainless steel films were fabricated via an electron beam physical vapour deposition method with starting electron beam power percentages of 3%–10%. The thin layers obtained with a

controlled deposition rates of 0.05 Å/s and 0.16 Å/s have shown a uniform elemental distribution with a well-constructed film structure that covered the whole exposed area, while higher deposition rates have illustrated semi-detachments in the film structure. Furthermore, the closest film elemental content to SS 316L was achieved with a 0.05 Å/s, where higher deposition rates were seen to extend the maximum and minimum elemental limits of SS 316L. Surface topography of SS 316L before and after depositing 50 nm, 100 nm, and 150 nm films, using controlled 0.05 Å/s fabrication rate, was then examined. The results illustrated a reduction in structure height on the surface, MHS, RMSR, and average roughness from 87.3–204 nm, 291 nm, 12 nm, and 7.87 nm (uncoated substrate) to 35.9–83.7 nm, 120 nm, 6.86 nm, and 4.88 nm (150 nm coated substrate), respectively. It also showed, via the obtained Ssk values, that the degree of symmetry of the surface heights about the mean plane was improved by ~ 49.5% for the reference substrate after 150 nm film deposition. Surface wettability of the as-prepared samples were afterwards characterised with DIW's, of pH 4, 7, and 9, at a 20–60°C liquid temperatures. The film thickness was seen to be inversely related to the liquid – surface CA, and hence the CA reduced with the increase in film thickness. Moreover, the rise in DIW's temperature has been shown to weaken the hydrophobic nature of the as-prepared substrates. It was also noticed that, unlike the DIW of pH 7, the liquids of pH 4 and 9 demonstrated some fluctuation in their CA data trend.

In summary, this article unlocks a new approach for depositing stainless steel thin films using an electron beam physical vapour deposition technique. The resulting film is ultrathin, uniform, conformal, and controllable. Moreover, an extension towards depositing different grades of stainless steel can be achieved by changing the composition of the evaporant source, based on exploratory experiments; and hence may facilitate a feasible route towards industrial usage of the process after further film properties investigation is provided (e.g., corrosivity, cohesion, hardness, and abrasiveness). Furthermore, as our approach is the first example of any stainless steel EB-PVD coating, the present work marks an important milestone in the future of stainless steel depositions on metallic surfaces and is expected to be beneficial to many applications such as manufacturing medical equipment, automotive parts, and heat transfer devices.

References

1. Landoulsi, J.; Genet, M.J.; Richard, C.; El Kirat, K.; Pulvin, S.; Rouxhet, P.G. Evolution of the passive film and organic constituents at the surface of stainless steel immersed in fresh water. *J. Colloid Interface Sci*. **2008**, *318*, 278–289.

2. Tylek, I.; Kuchta, K. Mechanical properties of structural stainless steels. *Civil Eng*. **2014**, *4-B*, 59–80.

3. Corradi, M.; Di Schino, A.; Borri, A.; Rufini, R. A review of the use of stainless steel for masonry repair and reinforcement. *Constr. Build. Mater*. **2018**, *181*, 335–346.

4. Bowden, D.; Krysiak, Y.; Palatinus, L.; Tsivoulas, D.; Plana-Ruiz, S.; Sarakinou, E.; Kolb, U.; Stewart, D.; Preuss, M. A high-strength silicide phase in a stainless steel alloy designed for wear-resistant applications. *Nat. Commun*. **2018**, *9*, 1–10.

5. Trzaskowska, P.A.; Kuz´min´ ska, A.; Butruk-Raszeja, B.; Rybak, E.; Ciach, T. Electropolymerized hydrophilic coating on stainless steel for biomedical applications. *Colloids Surf. B* **2018**, *167*, 499–508.

6. Song, Y.Y.; Bhadeshia, H.K.D.H.; Suh, D.W. Stability of stainless-steel nanoparticle and water mixtures. *Powder Technol.* **2015**, *272*, 34–44.

7. Ali, N.; Teixeira, J.A.; Addali, A. A Review on Nanofluids: Fabrication, Stability, and Thermophysical Properties. *J. Nanomater.* **2018**, *33*, 1–33.

8. Spencer, K.; Zhang, M.X. Optimisation of stainless steel cold spray coatings using mixed particle size distributions. *Surf. Coat. Technol.* **2011**, *205*, 5135–5140.

9. Sova, A.; Grigoriev, S.; Okunkova, A.; Smurov, I. Cold spray deposition of 316L stainless steel coatings on aluminium surface with following laser post-treatment. *Surf. Coat. Technol.* **2013**, *235*, 283–289.

10. Vitos, L.; Korzhavyi, P.A.; Johansson, B. Stainless steel optimization from quantum mechanical calculations. *Nat. Mater.* **2002**, *2*, 25.

11. Li, W.-Y.; Liao, H.; Douchy, G.; Coddet, C. Optimal design of a cold spray nozzle by numerical analysis of particle velocity and experimental validation with 316L stainless steel powder. *Mater. Des.* **2007**, *28*, 2129–2137.

12. Wanjara, P.; Brochu, M.; Jahazi, M. Electron beam freeforming of stainless steel using solid wire feed. *Mater. Des.* **2007**, *28*, 2278–2286.

13. Davé, V.R.; Matz, J.E.; Eagar, T.W. Electron beam solid freeform fabrication of metal parts. Available online: http://sffsymposium.engr.utexas.edu/Manuscripts/1995/1995-09-Dave.pdf (accessed on 12 February 2019).

14. Sahoo, B.; Schlage, K.; Major, J.; Von Hörsten, U.; Keune, W.; Wende, H.; Röhlsberger, R. Preparation and characterization of ultrathin stainless steel films. *AIP Conf. Proc.* **2011**, *1347*, 57–60.

15. Nomura, K.; Iio, S.; Ujihira, Y.; Terai, T. DCEMS study of thin stainless steel films deposited by RF sputtering of AISI316L. *AIP Conf. Proc.* **2005**, *765*, 108–113.

16. De Baerdemaeker, J.; Van Hoecke, T.; Van Petegem, S.; Segers, D.; Bauer-Kugelmann, W.; Sperr, P.; Terwagne, G. Investigation of stainless steel films sputtered on glass. *Mater. Sci. Forum* **2001**, *363*, 496–498.

17. Kraack, M.; Boehni, H.; Muster, W.; Patscheider, J. Influence of molybdenum on the corrosion properties of stainless steel films. *Surf. Coat. Technol.* **1994**, *68–69*, 541–545.

18. Eymer, J.P. On the hyperfine field of bcc 304 L stainless steel films. *J. Phys. IV France* **1992**, *2*, C3-211–C213-215.

19. Godbole, M.J.; Pedraza, A.J.; Allard, L.F.; Geesey, G. Characterization of sputter-deposited 316L stainless steel films. *J. Mater. Sci.* **1992**, *27*, 5585–5590.

20. Fabis, P.M. Microporosity in 304 stainless steel films prepared by vapor quenching. *Thin Solid Films* **1985**, *128*, 57–66.

21. Pedraza, A.J.; Godbole, M.J.; Bremer, P.J.; Avci, R.; Drake, B.; Geesey, G.G. Stability in aqueous media of 316L stainless steel films deposited on internal reflection elements. *Appl. Spectmsc.* **1993**, *47*, 161–166.

22. Song, Y.S.; Lee, J.H.; Lee, K.H.; Lee, D.Y. Corrosion properties of N-doped austenitic stainless steel films prepared by IBAD. *Surf. Coat. Technol.* **2005**, *195*, 227–233.

23. Nomura, K.; Yamada, Y.; Tomita, R.; Yajima, T.; Shimizu, K.; Mashlan, M. CEMS study of stainless steel films deposited by pulsed laser ablation of AISI316. *Czech J. Phys.* **2005**, *55*, 845–852.

24. Koinkar, V.N.; Chaudhari, S.M.; Kanetkar, S.M.; Ogale, S.B. Deposition of stainless steel film using pulsed laser evaporation. *Thin Solid Films* **1989**, *171*, 335–342.

25. Singh, J.; Wolfe, D.E. Review Nano and macro-structured component fabrication by electron beam-physical vapor deposition (EB-PVD). *J. Mater. Sci.* **2005**, *40*, 1–26.

26. Arunkumar, P.; Aarthi, U.; Sribalaji, M.; Mukherjee, B.; Keshri, A.K.; Tanveer, W.H.; Cha, S.-W.; Babu, K.S. Deposition rate dependent phase/mechanical property evolution in zirconia and ceria-zirconia thin film by EB-PVD technique. *J. Alloys Compd.* **2018**, *765*, 418–427.

27. De Almeida, D.S.; da Silva, C.R.M.; do Carmo, M. Ni Al alloy coating deposition by electron beam physical vapour deposition. In Proceedings of the 17th Brazilian Congress of Engineering and Materials Science, Paraná, Brazil, 15–19 November 2006.

28. Singh, J.; Wolfe, D.; Quli, F. Electron beam-physical vapor deposition technology: Present and future applications. In IMAST Quarterly; Pennsylvania State University: University Park, PA, USA, 2000; pp. 3–6.

29. Nam, Y.; Ju, Y.S. A comparative study of the morphology and wetting characteristics of micro/nanostructured Cu surfaces for phase change heat transfer applications. *J. Adhes. Sci. Technol.* **2013**, *27*, 2163–2176.

30. Cai, Y.; Chang, W.; Luo, X.; Sousa, A.M.L.; Lau, K.H.A.; Qin, Y. Superhydrophobic structures on 316L stainless steel surfaces machined by nanosecond pulsed laser. *Precis. Eng.* **2018**, *52*, 266–275.

31. Ali, N.; Teixeira, J.A.; Addali, A.; Al-Zubi, F.; Shaban, E.; Behbehani, I. The effect of aluminium nanocoating and water pH value on the wettability behavior of an aluminium surface. *Appl. Surf. Sci.* **2018**, *443*, 24–30.

32. Light, T.S. Temperature dependence and measurement of resistivity of pure water. *Anal. Chem.* **1984**, *56*, 1138–1142.

33. Down, R.D.; Lehr, J.H. Environmental Instrumentation and Analysis Handbook; John Wiley & Sons: Hoboken, NJ, USA, 2005.

34. Langelier, W.F. Effect of Temperature on the pH of Natural Waters. *J. Am. Water Works Assoc.* **1946**, *38*, 179–185.

35. Yokogawa Electric Corporation, Technical Note TNA0924. Available online: https://web-material3. yokogawa.com/TNA0924.us.pdf (accessed on 11 February 2019).

36. Villa, F.; Marengo, M.; De Coninck, J. A new model to predict the influence of surface temperature on contact angle. *Sci. Rep.* **2018**, *8*, 6549.

37. Tylek, I.; Kuchta, K. Physical and technological properties of structural stainless steel. *Civil Eng.* **2014**, *4-B*, 81–100.

38. Association, I.M. *Practical Guidelines for the Fabrication of Duplex Stainless Steels*; IMOA: London, UK, 2009; pp. 1–64.

39. Stainless Steel Grade Datasheets. Available online: http://www.worldstainless.org/Files/issf/non-image- files/PDF/Atlas_Grade_datasheet_-_all_datasheets_rev_Aug_2013.pdf (accessed on 12 February 2019).

40. Capus, J. 100 Years of Stainless Steel. *Met. Powder Rep.* **2013**, *68*, 12.

41. Hariprasad, S.; Gowtham, S.; Arun, S.; Ashok, M.; Rameshbabu, N. Fabrication of duplex coatings on biodegradable AZ31 magnesium alloy by integrating cerium conversion (CC) and plasma electrolytic oxidation (PEO) processes. *J. Alloys Compd.* **2017**, *722*, 698–715.

42. King, T.G. rms skew and kurtosis of surface profile height distributions: Some aspects of sample variation. *Precis. Eng.* **1980**, *2*, 207–215.

43. Zuo, Y.; Wang, H.; Xiong, J. The aspect ratio of surface grooves and metastable pitting of stainless steel. *Corros. Sci.* **2002**, *44*, 25–35.

44. Hong, T.; Nagumo, M. Effect of surface roughness on early stages of pitting corrosion of type 301 stainless steel. *Corros. Sci.* **1997**, *39*, 1665–1672.

45. Baboian, R. *Corrosion Tests and Standards: Application and Interpretation*; ASTM International: West Conshohocken, PA, USA, 2005.

46. Dougherty, R.C. Temperature and pressure dependence of hydrogen bond strength: A perturbation molecular orbital approach. *J. Chem. Phys.* **1998**, *109*, 7372–7378.

47. Kauffman, G.B. The Bronsted-Lowry acid base concept. *J. Chem. Edu.* **1988**, *65*, 28.

48. Gregorcˇicˇ, P.; Šetina-Baticˇ, B.; Hocˇevar, M. Controlling the stainless steel surface wettability by nanosecond direct laser texturing at high fluences. Appl. *Phys. A: Mater. Sci. Process.* **2017**, *123*, 1–8.

49. Cassie, A.B.D.; Baxter, S. Wettability of porous surfaces, *Trans. Faraday Soc.* **1944**, *40*, 546–551.

50. Wenzel, R.N. Resistance of solid surfaces to wetting by water. *Ind. Eng. Chem.* **1936**, *28*, 988–994.

51. Steele, A.; Bayer, I.; Moran, S.; Cannon, A.; King, W.P.; Loth, E. Conformal ZnO nanocomposite coatings on micro-patterned surfaces for superhydrophobicity. *Thin Solid Films* **2010**, *518*, 5426–5431.

52. Schwierz, N.; Horinek, D.; Sivan, U.; Netz, R.R. Reversed Hofmeister series—The rule rather than the exception. *Curr. Opin. Colloid Interface Sci.* **2016**, *23*, 10–18.

53. Mantel, M.; Wightman, J.P. Influence of the surface chemistry on the wettability of stainless steel. *Surf. Interface Anal.* **1994**, *21*, 595–605.

54. Rupp, F.; Gittens, R.A.; Scheideler, L.; Marmur, A.; Boyan, B.D.; Schwartz, Z.; Geis-Gerstorfer, J. A review on the wettability of dental implant surfaces I: Theoretical and experimental aspects. *Acta Biomater.* **2014**, *10*, 2894–2906.

Chapter 8 General Discussion

8. General Discussion

The conducted work has explored the changes in nanofluids pH value and stability as a result of the controlled sonication bath temperature two-step approach, and the effect of deposited layers on surfaces of similar materials on their wettability mechanism. In this regard, the major finding of this thesis is that the most effective implementation of the nanofluid two-step fabrication approach is by controlling the sonicator bath temperature throughout the production process (Chapter 3 and 4). Unlike the conventional two-step route used by most researchers in the field [1-3] , such method of construction provides a better suspension stability control and pH value modification capability to the manufacturer within certain limits (i.e. depending on the NPs materials, shape, size, concentration, and basefluid used). Furthermore, one of the major problems experienced with using the conventional two-step sonication method is that the bath temperature is seen to gradually rise with the operating time, as was shown in Chapter 4, Fig. 4.2 and previously acknowledged by Song et al. [4]. This increase in bath temperature is constrained by the atmospheric surrounding and the device working power, and therefore, would usually lead to the production of different nanofluids based on the fabrication process conditions. In addition, the level of alkalinity of the as-prepared dispersions was seen to rise through increasing the concentration of NPs in the basefluid (i.e. water), as illustrated in Chapter 3, Fig. 3.6. Furthermore, modification to the suspensions pH value was shown to be achievable to a given extend by only changing the production process fixed temperature (Chapter 3, Fig. 3.5). Such alteration in nanofluids pH value is believed to be a result of: 1- the NPs attraction of free hydrogen ions within the basefluid, and 2- the increase in the amount of ions been freed from their water molecules caused by the rise in fluid temperature. Fig. 8.1 illustrates how the pH value of the SS 316L, Al, and Cu_2O nanofluids of water base is effected by the controlled sonication temperature and the concentration of NPs. Moreover, an enhancement in the colloidal stability was found possible via the proposed controlled sonication temperature route without the need to add any type of surfactants or dispersing materials/chemicals to the mixture (Chapter 4, Fig. 4.8). Thus, the two-step controlled bath temperature approach can be looked at as a less hazardous and more economical method for providing higher stabilised nanofluids than the conventional way. It was also noticed that the mechanism in which the sediment tends to form within a suspension that is prepared with NPs of pure elements that can oxidise in the hosting environment depends greatly on the stage in

which the particles gets mostly oxidised. For example, dispersed Al NPs in water mixtures that were produced via the controlled sonication temperatures of less than 30^{o}C have shown a dispersed sedimentation type of behaviour due to the majority of NPs being oxidised after the preparation stage, while the same mixtures when fabricated with higher temperatures have shown a flocculated sedimentation mechanism as a result of the contained particles being oxidised within the preparation phase (Chapter 4, Fig. 4.7). In similar cases, where the sedimentation behaviour differs from one set of samples to the other, it is believed that the stability of nanofluids is better evaluated at the slow settling region to represent the colloidal overall stability performance, as estimating the suspensions stability from the rapid settling region at such scenario would be a meaningless approach to conduct.

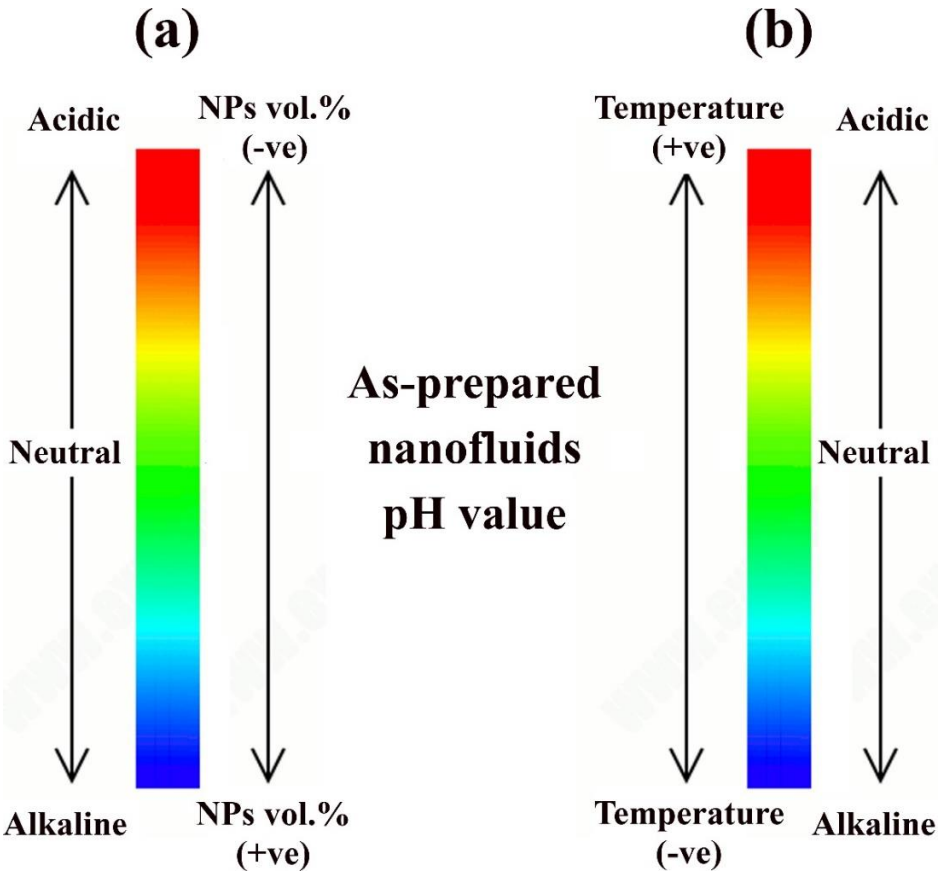

Fig. 8.1. Changes in nanofluids pH value based on: (a) fixed preparation temperature, and (b) fixed NPs concentration.

On the other hand, the change in wettability behaviour caused by the thin film deposition on the surfaces as a result of the colloidal operational performance, were seen to depend on a number of factors, namely, surface roughness, basefluid type, liquid temperature, pH value,

and ionic interaction between the surface and fluid in contact (Chapter 5 – 7). In all the examined surfaces, the deposited layer was seen to reduce the surface roughness with the increase in the fabricated film thickness. Such finding is not always achievable because the aforementioned property is subjected to the initial surface structure, deposited film thickness, and rate of particles deposition. Therefore, the obtained reduction in surface roughness can be attributed to the following key elements:

1- The examined surfaces initially contained defects in the form of deep valleys, high hills, and micro sized gaps; and thus the vaporised particles tend to occupy the lower structure of the surface (e.g. gaps), condense, then solidifies after which the variation in structural height is reduced.
2- The low deposition rate employed in the film fabrication process lowers the particles clustering size on the coated surfaces; otherwise, if high deposition rates were alternatively used then the amount of atoms arriving per unit time to the substrate would have been greater and thereby would result in forming larger scale of particle clusters.
3- The coated layer thickness is not high enough to completely eliminate the memory of the original substrate roughness, and hence the dynamic growth process of the deposited film would cause the roughness of the surface to decrease.

The wettability behaviour of the as-prepared Al surfaces coated with thin films of Al (Chapter 5) showed that neutral water tend to have a hydrophilic effect on the surface, and that the hydrophilicity of the surface increases with the reduction of the substrate surface roughness (Chapter 5, Fig.5.5). In contrast, water of higher and lower pH values was seen to develop a hydrophobic interaction with the surface, which increases with the deposited film thickness (Chapter 5, Fig.5.5). Furthermore, the effect associated with modifying the fluid temperature on the liquid – solid contact angle measurement have shown to be minimum. The reason behind the observed changes in surface wetting is believed to be linked to the physical chemistry phenomena of Hofmeister effect, as concluded from other researchers work [5-8], where the phenomena suggests the following:

1- The propensity of large ions, within the liquid, increase towards hydrophobic surfaces;
2- Next, the large ions start to accumulate at the air – water interface; and

3- Finally, an enhancement in the surface hydrophobicity occurs, due to the weak surface interaction with the liquid compared to the strength of interaction between the liquid neighbouring molecules.

Furthermore, examining the static wetting for substrates made of Cu (Chapter 6), using acidic, neutral, and alkaline waters, have shown that the contact angle decreases with the reduction in surface roughness, which was caused by increasing the deposited Cu film thickness. Moreover, the rise in temperature of the as-prepared acidic and alkaline liquids, has demonstrated a tendency to change the characteristic of the uncoated and coated surface towards the hydrophilic region (Chapter 6, Fig. 6.7a and c). In contrast, 20 – 60oC water of pH 7, when applied on the uncoated substrate, failed to reach a contact angle below 90o (Chapter 6, Fig. 6.7b). It was also noticed that the contact angle data trend with temperature, of the examined surfaces, had higher fluctuation as the water pH value increased. It is likely that such fluctuation in data is attributed to the liquid pH sensitivity to temperature and the resulting ionic interaction between the liquid and the Cu surfaces, which also had an important role in influencing the surface wettability nature.

As for the wettability of SS surfaces deposited with SS, the first challenge was to fabricate the thin films of alloy on the substrates using an electron beam physical vapour deposition technique. This is because such method of deposition was never previously reported in literature [9-23], and therefore initial exploration tests were needed to successfully obtain the alloy in its deposited form [24]. Similar to the Cu surfaces case, the wettability is seen to be mostly effected by the structure of the examined surface (i.e. surface roughness). Although the SS surfaces are hydrophobic in nature as they follows a Cassie – Baxter texture states [25,26] (illustrated in Chapter 6, Fig. 6.1b), the deposited films was seen to reduce the height variation on the surface, and with it the volume of the trapped air in the micro gaps. As a result, the contact angle decreases with the reduction in surface roughness, regardless of the pH value of the water employed. Additionally, it was also found that raising the temperature of the as-prepared water tends to weaken the hydrophobic nature of the uncoated surface, as demonstrated by the obtained data in Chapter 7, Fig. 7.9b-d, which is linked to the change in liquid properties and with it the ionic interaction between the liquid and surface in contact.

Finally, Table 8.1 summarises the influence of water pH value, temperature, and surface roughness on the wettability behaviour of all three aforementioned materials (i.e. Al, Cu, and SS).

Table 8.1. Influence of water pH value, temperature, and surface roughness on the wettability behaviour of Al, Cu, and SS.

Property	**Surface material**		
	Aluminium	**Copper**	**Stainless steel**
Water pH value	At pH = 7 the CA is seen to be less than the obtained from water of pH = 4 and 9. Thus, neutral water has a hydrophilic effect on the surface, while acidic or alkaline water has a hydrophobic influence.	Water of pH 4 and 9 was able to change the surface wettability behaviour from hydrophobic to hydrophilic as the temperature of the fluid increased. Furthermore, increasing the liquid pH value was seen to cause a fluctuation in the data across the temperature trend-line.	Water of pH 7 caused the surface to be more hydrophobic, while the ones of pH 4 and 9 had a hydrophilic effect on the surface. In addition, the liquids of pH 4 and 9 were seen to cause fluctuation in the data across the temperature trend-line.
Water temperature	Increasing the water temperature was shown to enhance the wettability behaviour caused by the liquid pH value.	Rising the liquid temperature showed to reduce the CA for all three water pH values.	Rising the liquid temperature showed to reduce the CA for all three water pH values.
Surface roughness	Reducing the surface roughness was seen to strongly enhance the wettability behaviour caused by the liquid pH value.	For acidic, neutral, and alkaline water, reducing the surface roughness caused the CA to reduce and had the largest effect between the other two properties.	For acidic, neutral, and alkaline water, smoothening the surface resulted in reduce the CA and had the largest influence on the wettability behaviour between the other two properties.

References

1. Ali, N.; Teixeira, J.A.; Addali, A. A review on nanofluids: Fabrication, stability, and thermophysical properties. *J. Nanomater.* **2018**, *2018*, 33.

2. Mukherjee, S.; Mishra, P.C.; Chaudhuri, P. Stability of heat transfer nanofluids – a review. *ChemBioEng Reviews* **2018**, *5*, 312-333.

3. Borode, A.O.; Ahmed, N.A.; Olubambi, P.A. Surfactant-aided dispersion of carbon nanomaterials in aqueous solution. *Phys. Fluids* **2019**, *31*, 071301.

4. Song, Y.Y.; Bhadeshia, H.K.D.H.; Suh, D.-W. Stability of stainless-steel nanoparticle and water mixtures. *Powder Technol.* **2015**, *272*, 34-44.

5. Sivan, U. The inevitable accumulation of large ions and neutral molecules near hydrophobic surfaces and small ions near hydrophilic ones. *Current Opinion in Colloid & Interface Science* **2016**, *22*, 1-7.

6. Morag, J.; Dishon, M.; Sivan, U. The governing role of surface hydration in ion specific adsorption to silica: An afm-based account of the hofmeister universality and its reversal. *Langmuir* **2013**, *29*, 6317-6322.

7. Schlesinger, I.; Sivan, U. New information on the hydrophobic interaction revealed by frequency modulation afm. *Langmuir* **2017**, *33*, 2485-2496.

8. Schwierz, N.; Horinek, D.; Sivan, U.; Netz, R.R. Reversed hofmeister series—the rule rather than the exception. *Current Opinion in Colloid & Interface Science* **2016**, *23*, 10-18.

9. Sova, A.; Grigoriev, S.; Okunkova, A.; Smurov, I. Cold spray deposition of 316L stainless steel coatings on aluminium surface with following laser post-treatment. *Surf. Coat. Technol.* **2013**, *235*, 283–289.

10. Li, W.-Y.; Liao, H.; Douchy, G.; Coddet, C. Optimal design of a cold spray nozzle by numerical analysis of particle velocity and experimental validation with 316L stainless steel powder. *Mater. Des.* **2007**, *28*, 2129–2137.

11. Wanjara, P.; Brochu, M.; Jahazi, M. Electron beam freeforming of stainless steel using solid wire feed. *Mater. Des.* **2007**, *28*, 2278–2286.

12. Davé, V.R.; Matz, J.E.; Eagar, T.W. Electron beam solid freeform fabrication of metal parts. Available online: http://sffsymposium.engr.utexas.edu/Manuscripts/1995/1995-09-Dave.pdf (accessed on 12 February 2019).

13. Sahoo, B.; Schlage, K.; Major, J.; Von Hörsten, U.; Keune, W.; Wende, H.; Röhlsberger, R. Preparation and characterization of ultrathin stainless steel films. *AIP Conf. Proc.* **2011**, *1347*, 57–60.

14. Nomura, K.; Iio, S.; Ujihira, Y.; Terai, T. DCEMS study of thin stainless steel films deposited by RF sputtering of AISI316L. *AIP Conf. Proc.* **2005**, *765*, 108–113.

15. De Baerdemaeker, J.; Van Hoecke, T.; Van Petegem, S.; Segers, D.; Bauer-Kugelmann, W.; Sperr, P.; Terwagne, G. Investigation of stainless steel films sputtered on glass. *Mater. Sci. Forum* **2001**, *363*, 496–498.

16. Kraack, M.; Boehni, H.; Muster, W.; Patscheider, J. Influence of molybdenum on the corrosion properties of stainless steel films. *Surf. Coat. Technol.* **1994**, *68–69*, 541–545.

17. Eymer, J.P. On the hyperfine field of bcc 304 L stainless steel films. *J. Phys. IV France* **1992**, *2*, C3-211–C213-215.

18. Godbole, M.J.; Pedraza, A.J.; Allard, L.F.; Geesey, G. Characterization of sputter-deposited 316L stainless steel films. *J. Mater. Sci.* **1992**, *27*, 5585–5590.

19. Fabis, P.M. Microporosity in 304 stainless steel films prepared by vapor quenching. *Thin Solid Films* **1985**, *128*, 57–66.

20. Pedraza, A.J.; Godbole, M.J.; Bremer, P.J.; Avci, R.; Drake, B.; Geesey, G.G. Stability in aqueous media of 316L stainless steel films deposited on internal reflection elements. *Appl. Spectmsc.* **1993**, *47*, 161–166.

21. Song, Y.S.; Lee, J.H.; Lee, K.H.; Lee, D.Y. Corrosion properties of N-doped austenitic stainless steel films prepared by IBAD. *Surf. Coat. Technol.* **2005**, *195*, 227–233.

22. Nomura, K.; Yamada, Y.; Tomita, R.; Yajima, T.; Shimizu, K.; Mashlan, M. CEMS study of stainless steel films deposited by pulsed laser ablation of AISI316. *Czech J. Phys.* **2005**, *55*, 845–852.

23. Koinkar, V.N.; Chaudhari, S.M.; Kanetkar, S.M.; Ogale, S.B. Deposition of stainless steel film using pulsed laser evaporation. *Thin Solid Films* **1989**, *171*, 335–342.

24. Ali, N.; Teixeira, J.A.; Addali, A.; Saeed, M.; Al-Zubi, F.; Sedaghat, A.; Bahzad, H. Deposition of stainless steel thin films: An electron beam physical vapour deposition approach. *Materials* **2019**, *12*, 571.

25. Cai, Y.; Chang, W.; Luo, X.; Sousa, A.M.L.; Lau, K.H.A.; Qin, Y. Superhydrophobic structures on 316L stainless steel surfaces machined by nanosecond pulsed laser. *Precis. Eng.* **2018**, *52*, 266–275.

26. Gregorc̆ic̆, P.; Šetina-Batic̆, B.; Hoc̆evar, M. Controlling the stainless steel surface wettability by nanosecond direct laser texturing at high fluences. Appl. *Phys. A: Mater. Sci. Process.* **2017**, *123*, 1–8.

Chapter 9 Conclusions and Future Work

9. Conclusions and Future Works

9.1 Conclusions

The present research has investigated nanofluids through two main streams, specifically, the preparation and operation stages. The main aspects explored were associated to the changes in nanofluid stability and pH value, as a result of the two-step controlled sonication bath temperature approach, and the wettability variation caused by the deposition of particles on surfaces of similar materials. In this regard, the following series of conclusions were drawn out from the work conducted in this thesis.

1- When fabricating nanofluids using a specific basefluid with a given particles type, shape, and size, the final pH value of the as-prepared suspension would greatly depend on the NPs concentration and preparation temperature. Furthermore, the pH value of the as-produced colloidal was seen to increase with the increase in NPs concentration, while rising the fabrication temperature causes the pH value to decrease.

2- Comparing the developed nanofluids pH correlation to the experimental data has illustrated a high prediction capability of the property, with very low deviation from the actual measurements. Thus, the proposed correlation can be used as a reliable source for estimating the pH value for similar types of nanofluids that are within the experimental range and fabricated by the two-step controlled temperature approach.

3- In contrast with the conventional two-step suspension production route, the two-step controlled sonication bath temperature approach has demonstrated a better short and long-term stability for the as-fabricated nanofluids at given fixed dispersion conditions, and has the advantage of being capable of reproducing the colloidal, which is not possible with the conventional fabrication method.

4- Unlike metallic oxides, the type of sedimentation behaviour of the suspensions prepared with NPs made of pure metallic elements has shown to be influenced by the stage in which the particles get mostly oxidised (i.e. at the stage of preparation or shelving). Therefore, a stability comparison between different sedimentation mechanisms at the rapid settling region is relatively unfair but should rather be evaluated only at the slow settling region for a better colloidal overall stability representation.

5- Examining the wettability of the coated and uncoated surfaces has revealed that this property depends mostly on the liquid temperature and pH value, surface roughness,

and ionic interaction between the surface and fluid in contact. The surface material and liquid properties determines the type of ionic interaction between the two, while the deposited particles tend to modify the surface roughness and enhance the level of interaction between the substrate and fluid.

9.2 Future work and recommendations

The research work conducted in this thesis, has demonstrated the important role of the two-step controlled sonication bath temperature approach on improving or altering the stability and pH value of nanofluids, and how the wettability behaviour of deposited surfaces can be varied from its initial states. There is still a need for further work, which can be presented in the following points:

1- The influence of surfactant, nanoparticles shape, particles average size, and sonication time needs to be added to the set of effective parameters that have been investigated for the nanofluids stability and pH value.
2- A database of experimental result covering a wider range of parameters used in fabricating different types of nanofluids, via the two-step controlled sonication bath temperature approach, is required to drive a universal correlation that can predict the suspension pH value, stability, and thermophysical properties.
3- As nanofluids are always seen prepared within vials of different sizes, the effect of varying the suspension hosting vial diameter on the characteristics of the colloidal is another area of interest that needs to be explored.
4- A feasibility assessment based on the performance, capital and production costs, sustainability, and environmental impact should be performed for the nanofluids fabricated by the two-step controlled temperature method.
5- Extended research on the stability characterisation of hybrid nanofluids produced by the controlled temperature route is also required in the field.
6- Further investigations on the dynamic wetting, through the hysteresis contact angle measurements, of the examined surfaces is needed for providing a wider understanding on the surface wettability behaviour.
7- Since the work in hand has used an external deposition method to reflect the fouling build-up before evaluating the wettability of the surfaces, a real-life test rig is required to obtain the actual deposited layer from using nanofluids at operating conditions.

APPENDIX A

Publication 6: Supplementary Materials

Supplementary

Table S6.1. Testing parameters and obtained contact angles of the characterized samples and published data.

Water temperature (°C)	Water pH	Surface information	Highest contact angle (degree)	Lowest contact angle (degree)	Average contact angle (degree)	95% confidence interval
20	4	Uncoated Cu substrate	101.9	101.1	101.5	0.93
25	4	Uncoated Cu substrate	91.9	91.7	91.7	0.46
30	4	Uncoated Cu substrate	85.8	84.3	85.0	1.87
40	4	Uncoated Cu substrate	81.5	81.4	81.5	0.15
50	4	Uncoated Cu substrate	85.0	83.6	84.3	1.80
60	4	Uncoated Cu substrate	81.5	81.3	81.4	0.39
20	7	Uncoated Cu substrate	91.9	90.9	91.3	1.25
25	7	Uncoated Cu substrate	94.1	93.7	93.9	0.57
30	7	Uncoated Cu substrate	96.2	94.9	95.6	1.68
40	7	Uncoated Cu substrate	94.6	94.5	94.6	0.16
50	7	Uncoated Cu substrate	91.9	91.8	91.8	0.13
60	7	Uncoated Cu substrate	93.2	92.5	92.8	0.81
20	9	Uncoated Cu substrate	94.9	94.3	94.5	0.71
25	9	Uncoated Cu substrate	90.1	89.8	90.0	0.37
30	9	Uncoated Cu substrate	98.9	97.0	97.7	2.70
40	9	Uncoated Cu substrate	90.7	90.6	90.7	0.13
50	9	Uncoated Cu substrate	83.0	81.7	82.2	1.64

60	9	Uncoated Cu substrate	82.2	82.0	82.1	0.27
20	4	Coated Cu substrate (25 nm film)	90.4	90.2	90.3	0.25
25	4	Coated Cu substrate (25 nm film)	86.7	86.4	86.5	0.41
30	4	Coated Cu substrate (25 nm film)	85.0	83.6	84.3	1.80
40	4	Coated Cu substrate (25 nm film)	81.4	81.0	81.3	0.60
50	4	Coated Cu substrate (25 nm film)	84.0	83.0	83.6	1.24
60	4	Coated Cu substrate (25 nm film)	81.0	79.6	80.3	1.74
20	7	Coated Cu substrate (25 nm film)	89.3	88.9	89.0	0.56
25	7	Coated Cu substrate (25 nm film)	91.9	91.5	91.7	0.57
30	7	Coated Cu substrate (25 nm film)	92.2	92.1	92.1	0.07
40	7	Coated Cu substrate (25 nm film)	92.6	92.4	92.5	0.19
50	7	Coated Cu substrate (25 nm film)	91.7	91.2	91.5	0.69
60	7	Coated Cu substrate (25 nm film)	90.6	90.5	90.5	0.13
20	9	Coated Cu substrate (25 nm film)	91.0	90.9	91.0	0.22
25	9	Coated Cu substrate (25 nm film)	82.0	81.9	81.9	0.07
30	9	Coated Cu substrate (25 nm film)	91.1	91.0	91.0	0.13

40	9	Coated Cu substrate (25 nm film)	85.3	85.0	85.1	0.32
50	9	Coated Cu substrate (25 nm film)	83.0	81.3	82.0	2.16
60	9	Coated Cu substrate (25 nm film)	81.7	81.4	81.5	0.31
20	4	Coated Cu substrate (50 nm film)	89.6	89.1	89.3	0.58
25	4	Coated Cu substrate (50 nm film)	77.7	75.8	76.8	2.36
30	4	Coated Cu substrate (50 nm film)	85.0	83.0	84.2	2.58
40	4	Coated Cu substrate (50 nm film)	81.4	80.3	81.0	1.53
50	4	Coated Cu substrate (50 nm film)	82.1	81.7	81.9	0.56
60	4	Coated Cu substrate (50 nm film)	81.0	79.1	80.1	2.36
20	7	Coated Cu substrate (50 nm film)	87.4	86.9	87.1	0.64
25	7	Coated Cu substrate (50 nm film)	91.8	91.2	91.4	0.83
30	7	Coated Cu substrate (50 nm film)	91.0	90.5	90.8	0.62
40	7	Coated Cu substrate (50 nm film)	92.1	91.0	91.5	1.46
50	7	Coated Cu substrate (50 nm film)	90.9	90.6	90.7	0.31
60	7	Coated Cu substrate (50 nm film)	91.0	89.1	90.0	2.37
20	9	Coated Cu substrate (50 nm film)	85.2	85.2	85.2	0.07

25	9	Coated Cu substrate (50 nm film)	81.0	79.6	80.3	1.74
30	9	Coated Cu substrate (50 nm film)	90.6	90.3	90.4	0.38
40	9	Coated Cu substrate (50 nm film)	83.0	83.0	83.0	0.07
50	9	Coated Cu substrate (50 nm film)	82.1	81.4	81.7	0.95
60	9	Coated Cu substrate (50 nm film)	81.7	81.0	81.3	0.84
20	4	Coated Cu substrate (75 nm film)	88.5	88.1	88.2	0.50
25	4	Coated Cu substrate (75 nm film)	76.8	74.1	75.8	3.66
30	4	Coated Cu substrate (75 nm film)	80.2	80.0	80.1	0.25
40	4	Coated Cu substrate (75 nm film)	79.1	78.9	79.0	0.28
50	4	Coated Cu substrate (75 nm film)	78.9	77.7	78.3	1.47
60	4	Coated Cu substrate (75 nm film)	79.1	79.0	79.1	0.15
20	7	Coated Cu substrate (75 nm film)	87.1	86.8	86.9	0.36
25	7	Coated Cu substrate (75 nm film)	90.9	89.8	90.1	1.57
30	7	Coated Cu substrate (75 nm film)	91.0	90.5	90.8	0.58
40	7	Coated Cu substrate (75 nm film)	89.7	88.6	89.1	1.42
50	7	Coated Cu substrate (75 nm film)	90.7	90.2	90.4	0.64

60	7	Coated Cu substrate (75 nm film)	88.7	88.3	88.5	0.44
20	9	Coated Cu substrate (75 nm film)	81.9	81.5	81.7	0.51
25	9	Coated Cu substrate (75 nm film)	80.0	79.2	79.6	1.02
30	9	Coated Cu substrate (75 nm film)	87.6	86.8	87.1	1.13
40	9	Coated Cu substrate (75 nm film)	79.0	78.7	78.9	0.35
50	9	Coated Cu substrate (75 nm film)	80.3	80.2	80.2	0.15
60	9	Coated Cu substrate (75 nm film)	80.2	80.1	80.2	0.22
Room temperature	–	Bare Cu	95.0	93.7	94.2	–

APPENDIX B

Publication 7: Supplementary Materials

Supplementary

SEM images of the Stainless steel evaporant source and deposited thin films:

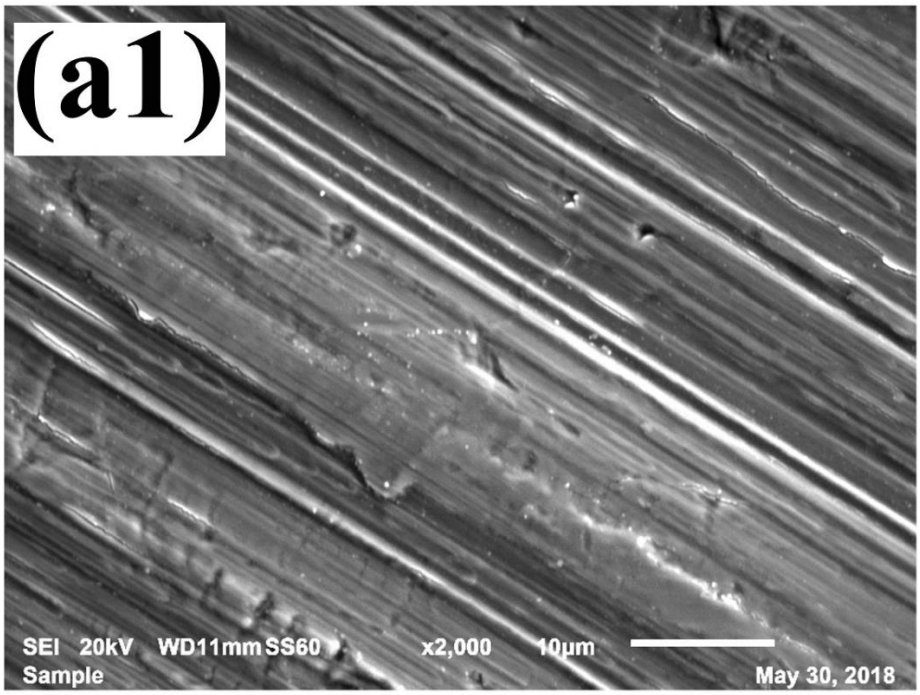

Fig. S7.1a1. SEM image of the 0.05 Å/s deposited film.

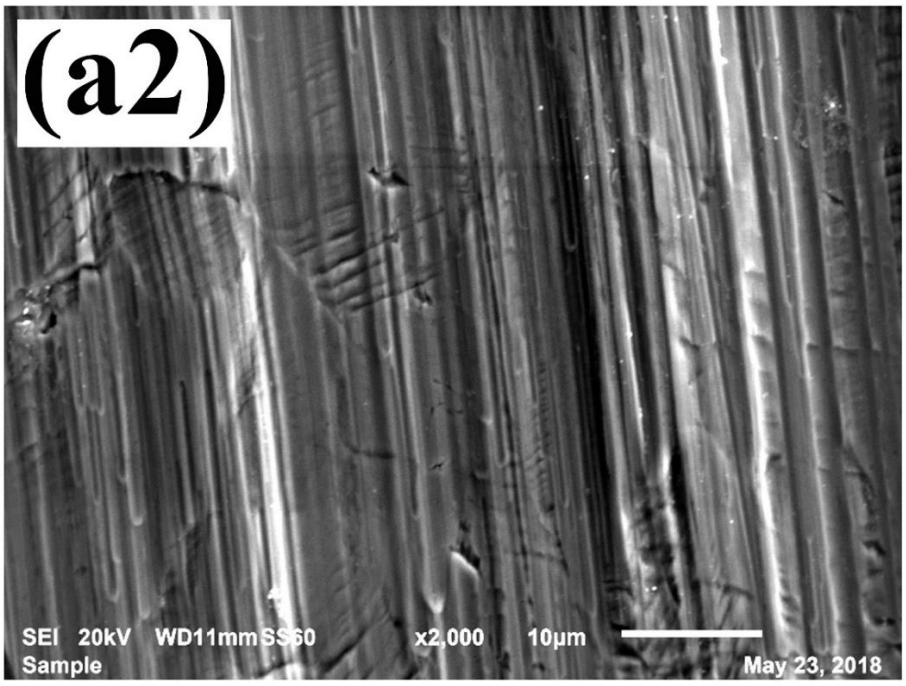

Fig. S7.1a2. SEM image of the 0.16 Å/s deposited film.

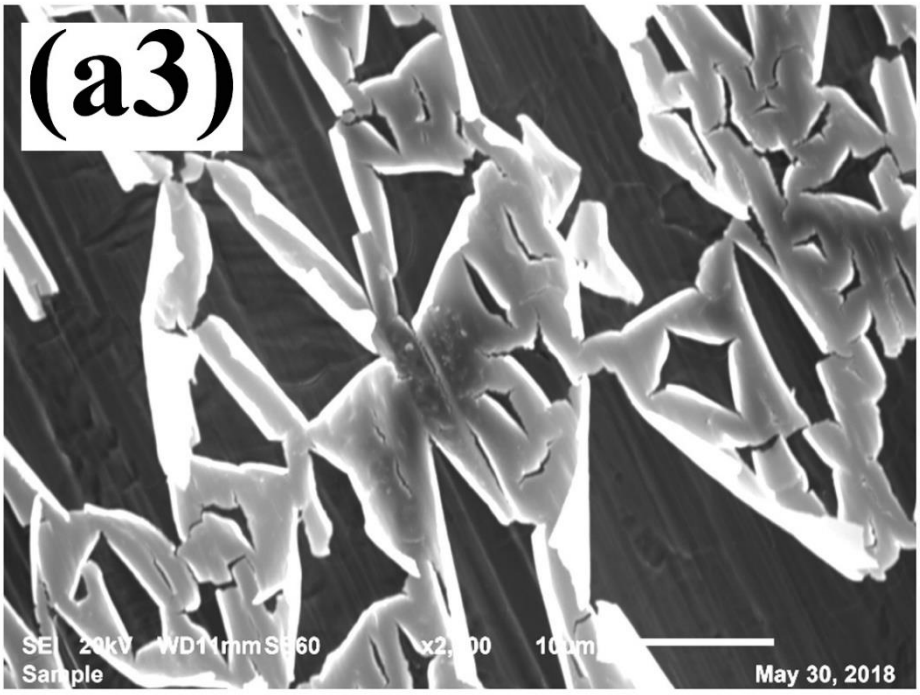

Fig. S7.1a3. SEM image of the 0.82 Å/s deposited film.

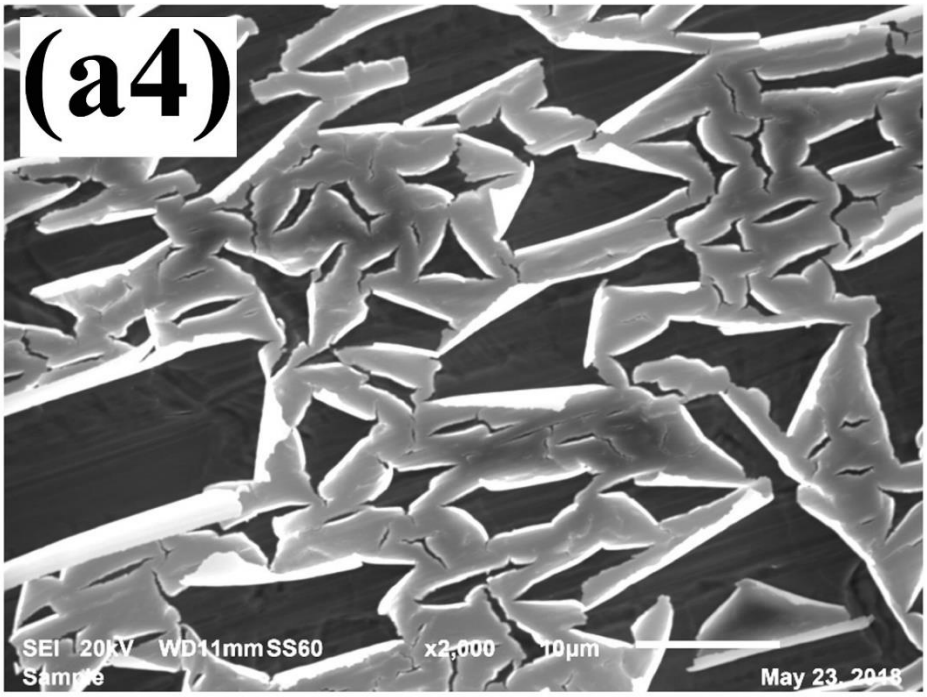

Fig. S7.1a4. SEM image of the 1.07 Å/s deposited film.

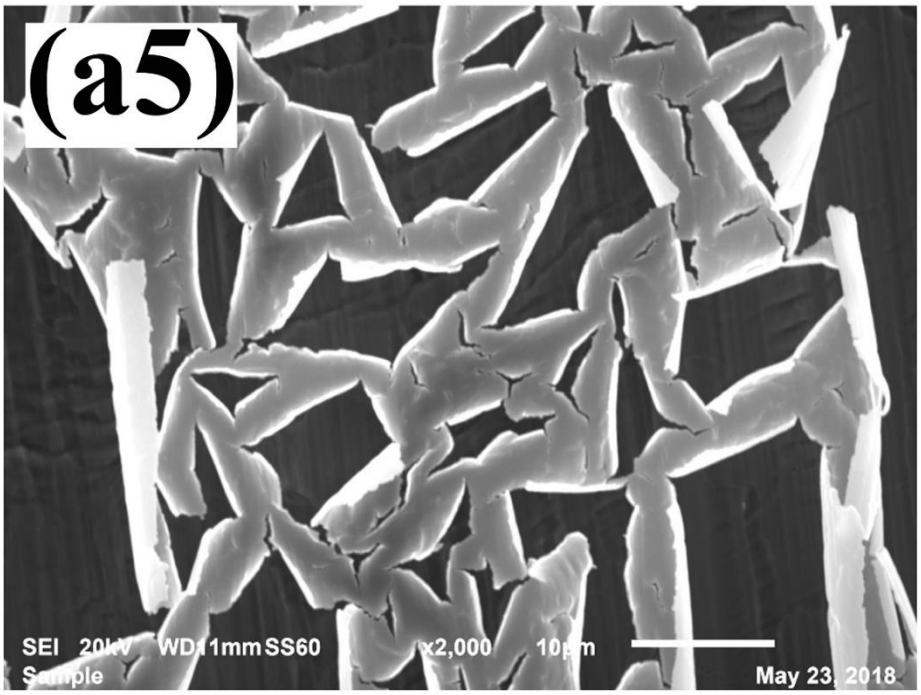

Fig. S7.1a5. SEM image of the 1.45 Å/s deposited film.

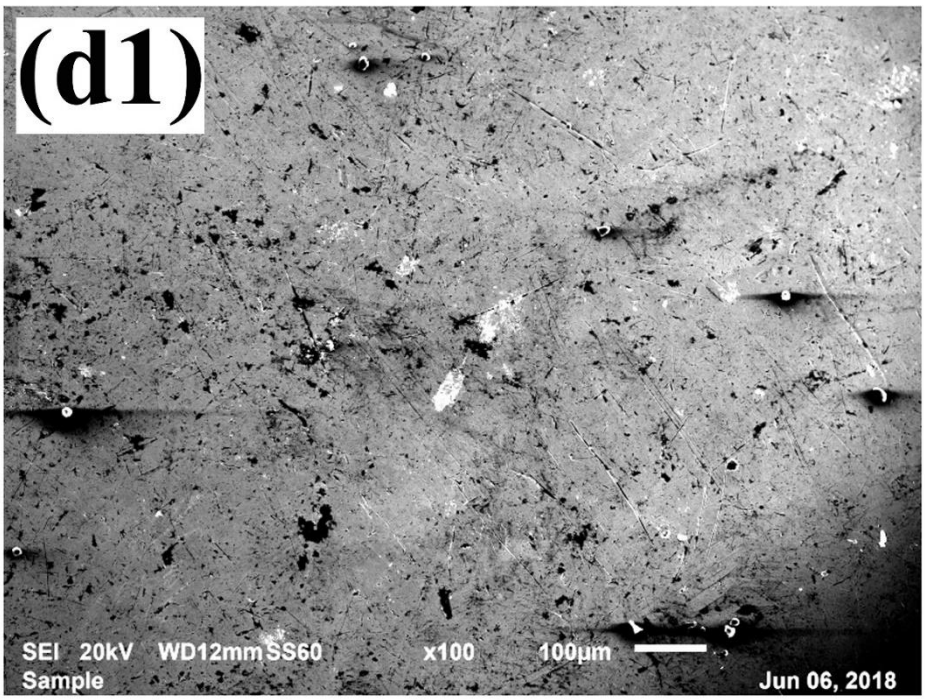

Fig. S7.1d1. SEM image of the as-received evaporant source before film deposition.

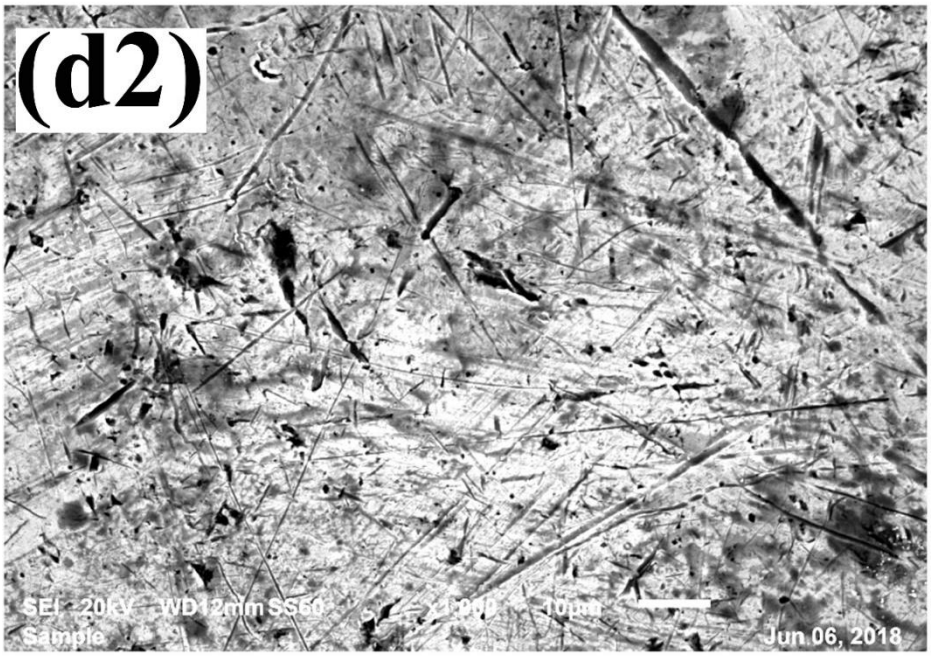

Fig. S7.1d2. Higher resolution SEM image of the as-received evaporant source before film deposition.

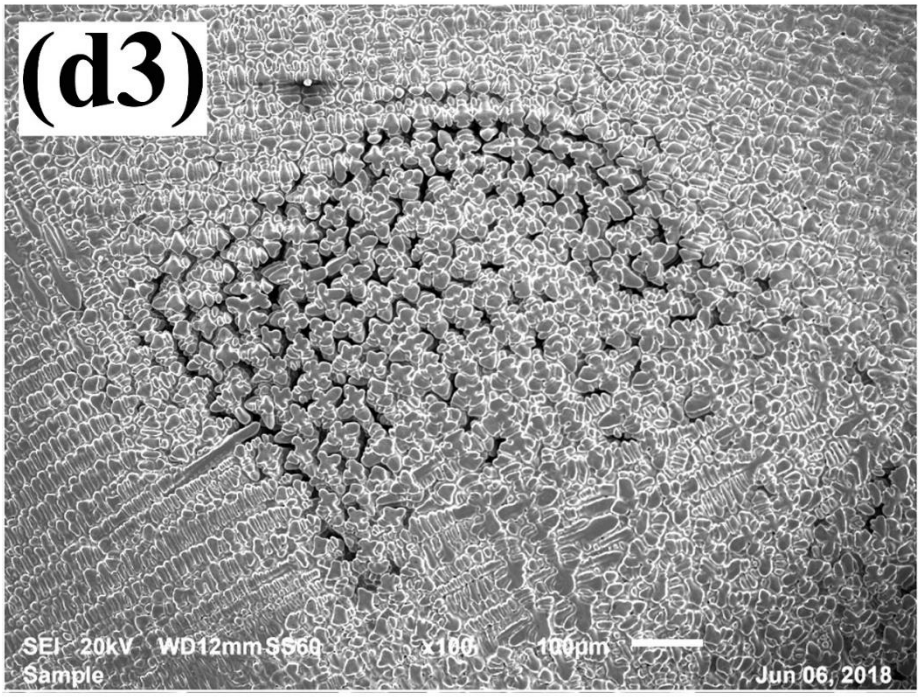

Fig. S7.1d3. SEM image of the as-received evaporant source after 0.05 Å/s film deposition.

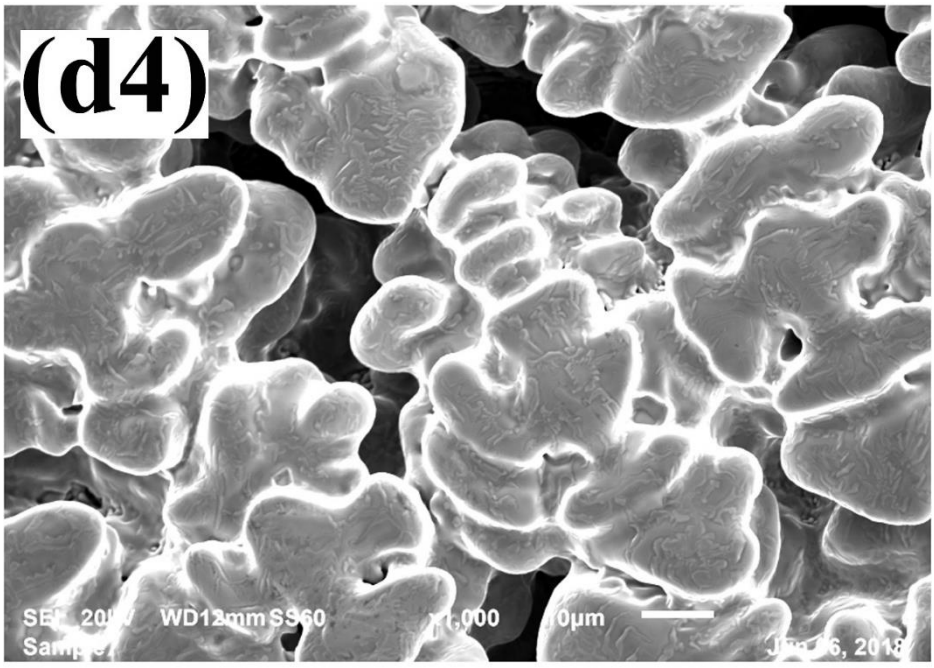

Fig. S7.1d4. Higher resolution SEM image of the as-received evaporant source after 0.05 Å/s film deposition.

Deposited film EDS elemental analysis:

(a)

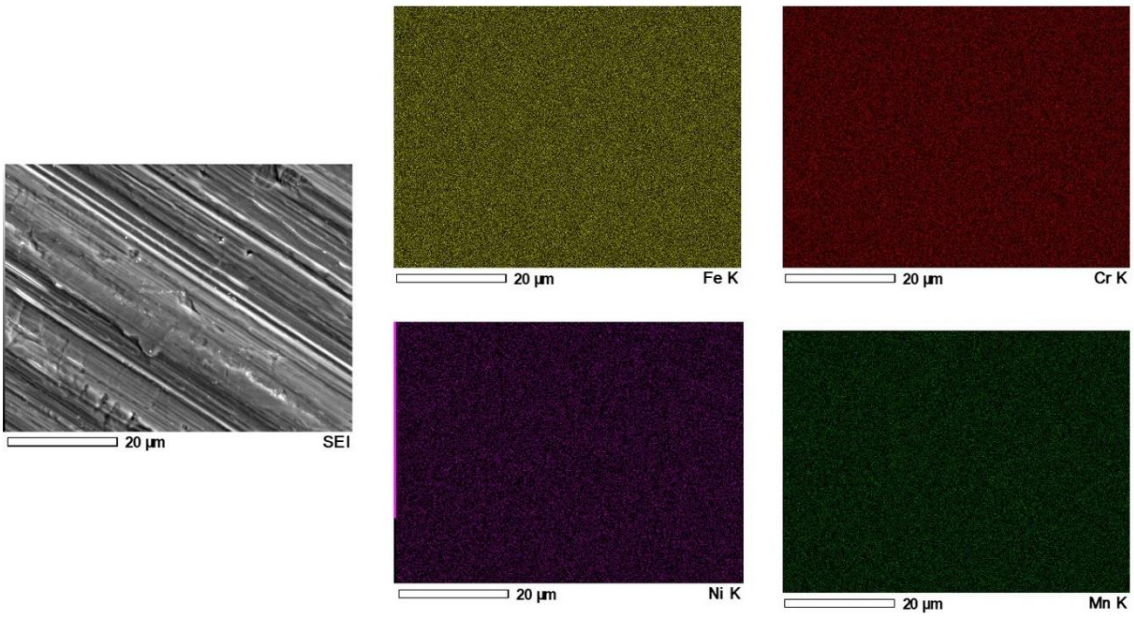

Fig. S7.2a. SEM image and its elemental maps of the characterized 150 nm deposited SS film at 0.05 Å/s on Cu substrate.

(b)

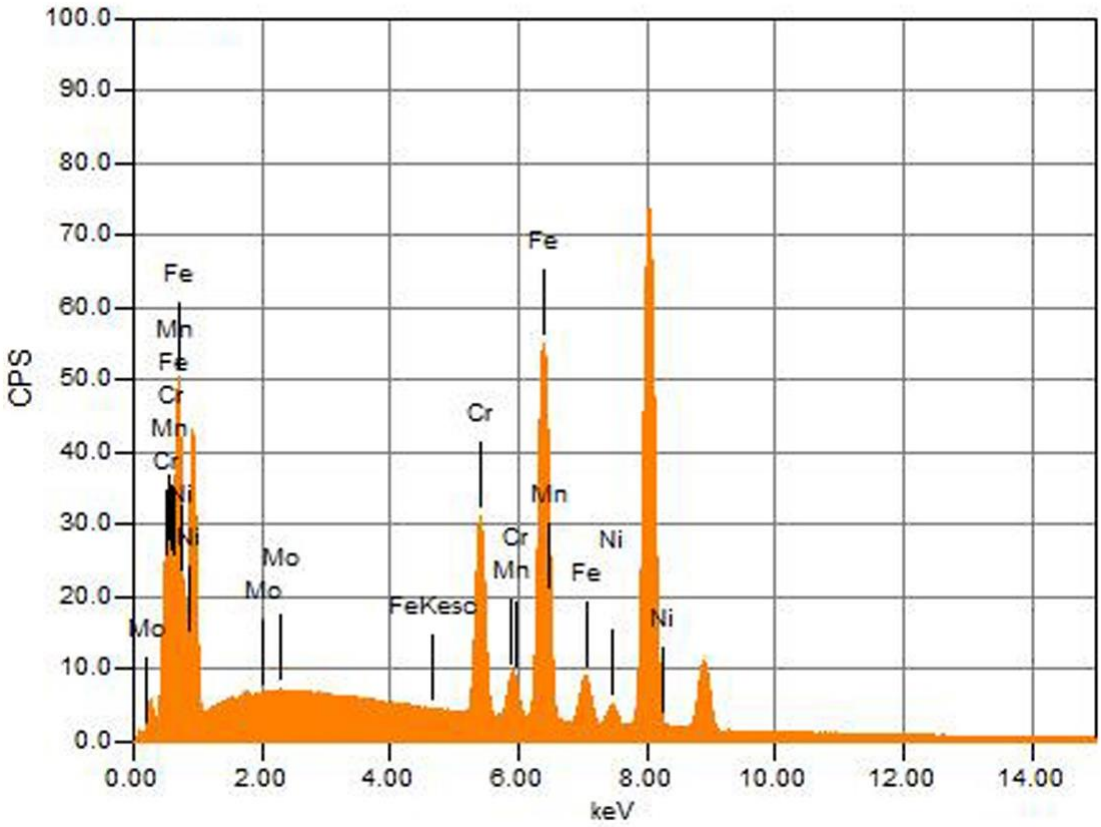

Fig. S7.2b. EDS x-ray spectrum of the elements.

Surface topography analysis of SS films on SS 316L substrates:

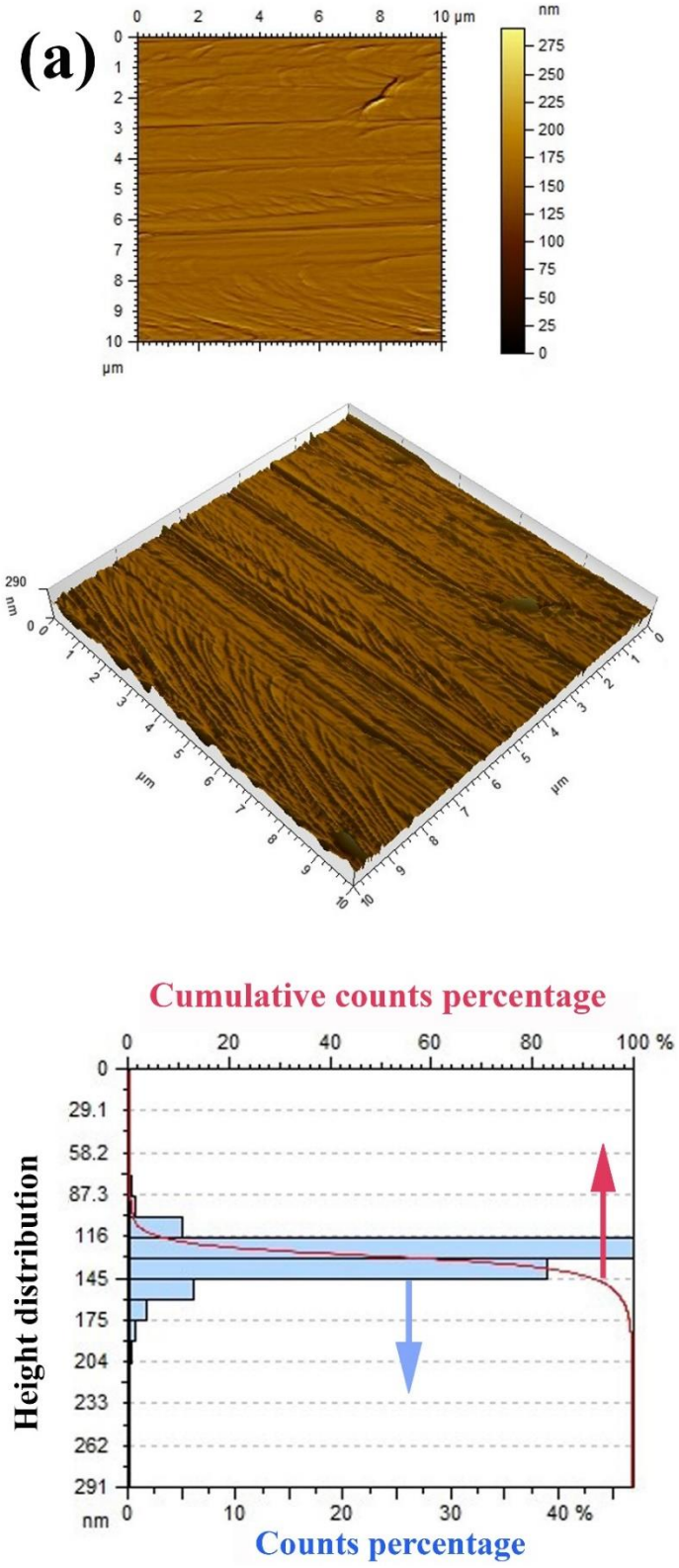

Fig. S7.3a. AFM images and analysis of the uncoated substrate.

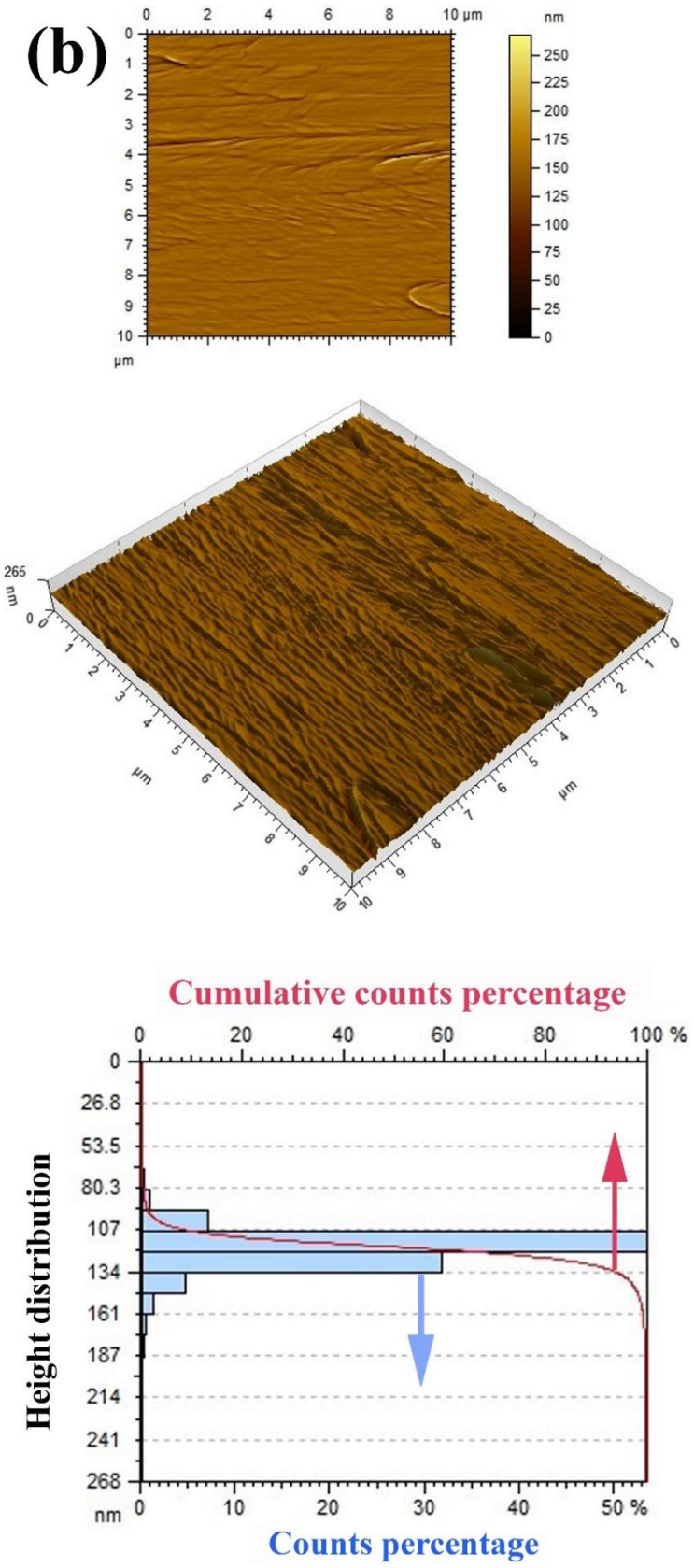

Fig. S7.3b. AFM images and analysis of the 50 nm coated substrate.

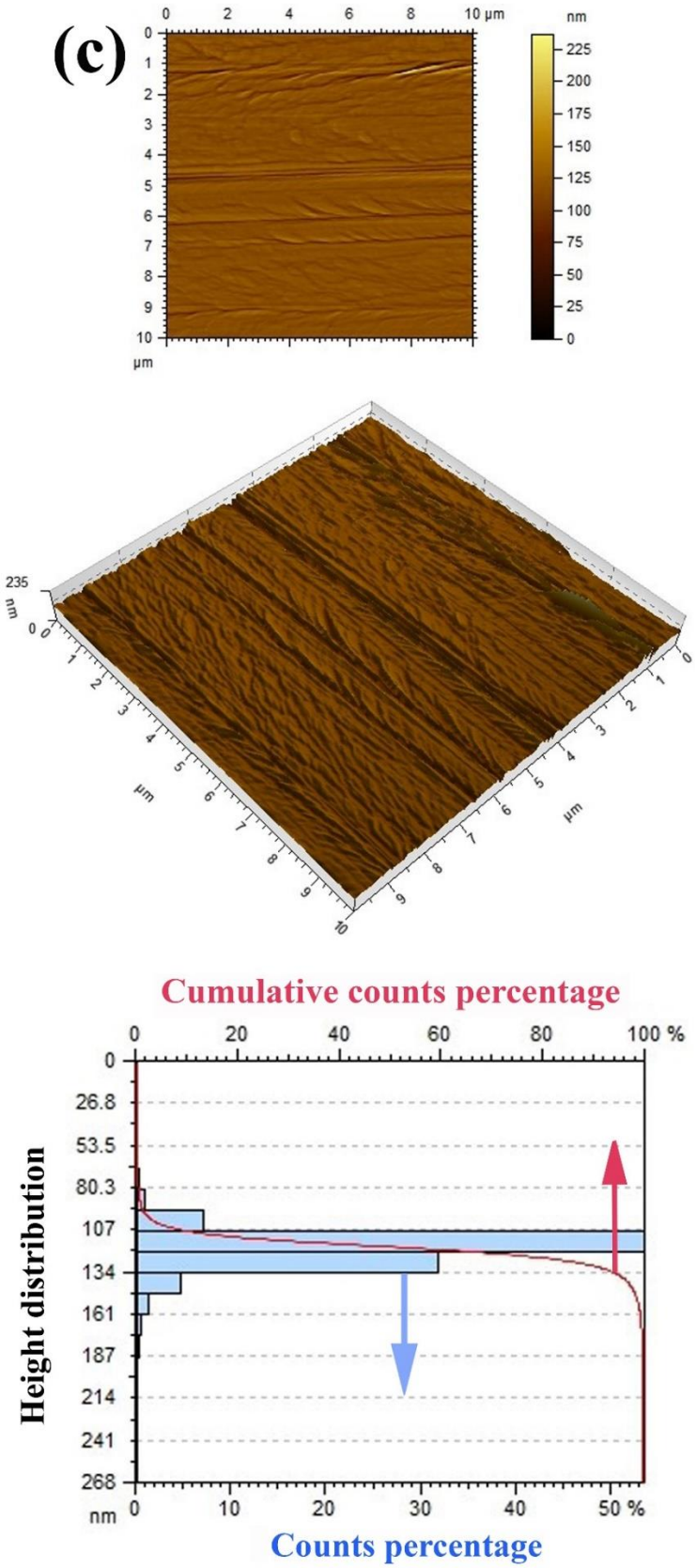

Fig. S7.3c. AFM images and analysis of the 100 nm coated substrate.

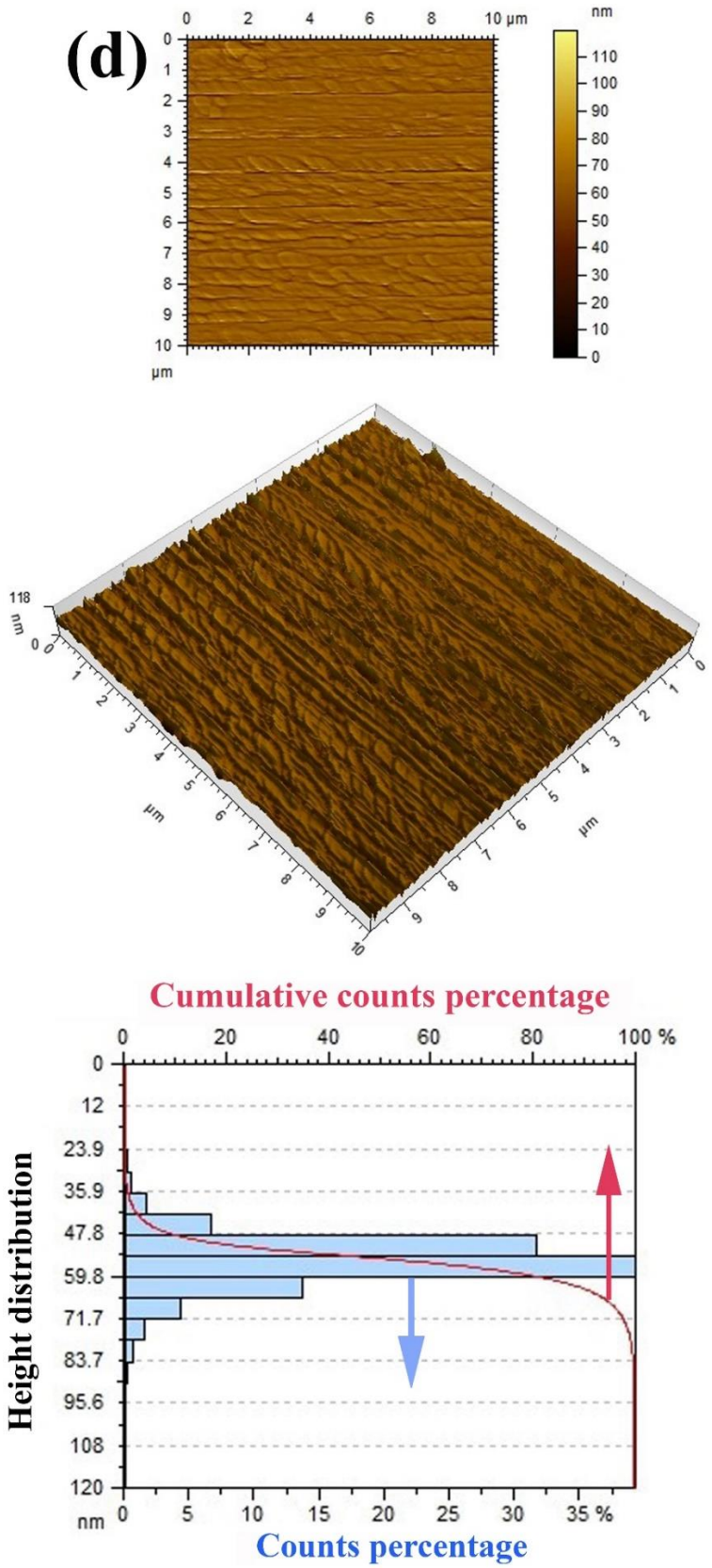

Fig. S7.3d. AFM images and analysis of the 150 nm coated substrate.

Table S7.1. Contact angle measurements data.

DIW temperature (°C)	DIW pH value	Stainless steel substrate surface information	Highest CA (degree)	Lowest CA (degree)	ACA (degree)
20	4	Uncoated	126.5	122.5	124.9
30	4	Uncoated	120.6	119.4	119.8
40	4	Uncoated	106.5	106.2	106.3
50	4	Uncoated	110.3	110.1	110.2
60	4	Uncoated	112.7	112.1	112.3
20	7	Uncoated	132.8	130.9	131.7
30	7	Uncoated	122.5	119.5	120.6
40	7	Uncoated	115.8	115.6	115.7
50	7	Uncoated	115.2	114.5	114.8
60	7	Uncoated	115.3	114.8	115.1
20	9	Uncoated	117.8	116.7	117.4
30	9	Uncoated	115.7	114.8	115.3
40	9	Uncoated	108.3	108.0	108.1
50	9	Uncoated	112.7	112.1	112.3
60	9	Uncoated	107.4	106.8	107.1
20	4	50 nm SS film	121.0	117.8	119.5
30	4	50 nm SS film	110.8	110.4	110.6
40	4	50 nm SS film	104.2	103.8	104.0
50	4	50 nm SS film	110.1	108.7	109.3
60	4	50 nm SS film	110.7	110.2	110.4
20	7	50 nm SS film	131.3	130.1	130.9
30	7	50 nm SS film	116.7	114.8	115.8
40	7	50 nm SS film	105.1	104.9	105.0
50	7	50 nm SS film	104.6	104.1	104.4
60	7	50 nm SS film	101.3	100.8	101.1
20	9	50 nm SS film	109.6	108.7	109.2
30	9	50 nm SS film	106.6	106.4	106.5
40	9	50 nm SS film	108.7	107.4	108.1
50	9	50 nm SS film	100.6	99.0	99.7
60	9	50 nm SS film	105.0	104.9	104.9
20	4	100 nm SS film	117.4	115.8	116.7
30	4	100 nm SS film	104.0	103.5	103.8
40	4	100 nm SS film	103.8	103.3	103.5
50	4	100 nm SS film	99.0	98.1	98.5

60	4	100 nm SS film	102.1	101.3	101.7
20	7	100 nm SS film	128.3	128.1	128.2
30	7	100 nm SS film	109.6	108.8	109.3
40	7	100 nm SS film	103.4	102.8	103.0
50	7	100 nm SS film	103.3	102.7	102.9
60	7	100 nm SS film	100.6	99.0	99.9
20	9	100 nm SS film	103.3	103.0	103.2
30	9	100 nm SS film	103.4	103.2	103.3
40	9	100 nm SS film	106.2	105.1	105.7
50	9	100 nm SS film	99.7	98.1	98.8
60	9	100 nm SS film	98.4	97.5	98.1
20	4	150 nm SS film	111.0	110.6	110.9
30	4	150 nm SS film	99.8	98.1	99.0
40	4	150 nm SS film	102.8	102.0	102.5
50	4	150 nm SS film	94.4	92.1	93.1
60	4	150 nm SS film	88.7	88.4	88.5
20	7	150 nm SS film	122.6	121.0	122.0
30	7	150 nm SS film	106.7	106.4	106.6
40	7	150 nm SS film	102.9	102.5	102.7
50	7	150 nm SS film	95.8	95.1	95.5
60	7	150 nm SS film	95.5	94.7	95.2
20	9	150 nm SS film	95.0	94.2	94.5
30	9	150 nm SS film	101.3	100.9	101.0
40	9	150 nm SS film	103.4	102.9	103.2
50	9	150 nm SS film	97.5	96.2	97.0
60	9	150 nm SS film	97.4	96.7	97.0